MATERIALS AND MICROFABRICATION APPROACHES FOR COMPLETELY BIODEGRADABLE WIRELESS MICROMACHINED SENSORS

A Thesis
Presented to
The Academic Faculty

by

Mengdi Luo

In Partial Fulfillment
of the Requirements for the Degree
Doctor of Philosophy in the
School of Materials Science and Engineering

Georgia Institute of Technology
December 2014

MATERIALS AND MICROFABRICATION APPROACHES FOR COMPLETELY BIODEGRADABLE WIRELESS MICROMACHINED SENSORS

Approved by:

Dr. Mark G. Allen, Advisor
School of Electrical and Computer Engineering
Georgia Institute of Technology

Dr. Oliver Brand
School of Electrical and Computer Engineering
Georgia Institute of Technology

Dr. Zhiqun Lin
School of Materials Science and Engineering
Georgia Institute of Technology

Dr. Preet Singh
School of Materials Science and Engineering
Georgia Institute of Technology

Dr. Donggang Yao
School of Materials Science and Engineering
Georgia Institute of Technology

Date Approved: Nov 7, 2014

To my parents and Martin,

for sharing the bumpy ride.

ACKNOWLEDGEMENTS

First and foremost, I would like to express my sincere gratitude to my adviser Dr. Mark G. Allen for his faith, patience and encouragement of me, his mental and financial support of me, as well as his vision and extensive technical guidance on my research projects throughout these years. I thank Dr. Allen for giving me the opportunity to work together with him, to broaden my knowledge and experience in MEMS technology, to explore and work on many exciting, interdisciplinary and very challenging projects with inspired creative ideas. I am deeply impressed by his professional research attitudes, solid and broad knowledge, sharp mind and big vision, creativity, leadership, management and communication skills. He would be a role model for me to learn from.

I would also like to thank Dr. Oliver Brand, Dr. Zhiqun Lin, Dr. Preet Singh and Dr. Donggang Yao for being my thesis committee members and dedicating their time and efforts on evaluating and guiding my work. Their suggestions and support are important and very valuable for me to accomplish this work and achieve the PhD degree.

I would like to gratefully acknowledge everyone that I have been work with in MSMA (Microsensors and Microactuators) group. I really enjoy being part of this very talented, friendly and supporting group. Thank Dr. Seong-Hyok Kim, Dr. Florian Herrault, and Dr. Zhan Liu for helping me early on my graduate career in MSMA for their guidance and support. Thank Dr. Seung-Joon Paik, Dr. Wen Shen, Dr. Po-Chun Wang, Dr. Adam Martinez, Dr. Chao Song, Dr. Andac Armutlulu, and Dr. Xuehong Yu, Jooncheol Kim, Minsoo Kim, Melissa Tsang, Yuan Li, and Brock Peterson, for their friendship, advice and support. Special thanks go to Ms. Purnima

Sharma and Mr. Richard Shafer, without them the group and the lab would not be able to be running smoothly and efficiently. They have been important to every MSMA group member.

Finally I would like to express my sincerely thanks to my parents Wei Luo and Xucang Zhang, for their great love, mentally and finacially supporting me throughout years of my college education that seems never ending. I would also like to thank my cousin Jingjing Qu, my aunt Hong Luo and uncle Yongnian Qu for their help of taking care of my parents when I am studying in US. Lastly, I would like to thank my fiance Martin F. Mueller for his great support during the last two years of my PhD research, and his willingness to share his future life with me when I was going through a very difficult time.

TABLE OF CONTENTS

LIST OF TABLES

LIST OF FIGURES

LIST OF SYMBOLS & ABBREVIATIONS

Abbreviations

AC	Alternating current
Al	Aluminum
AMD	Arithmetic mean distance
AMSD	Arithmetic mean square distance
Ca	Calcium
Ce	Cerium
Co	Cobalt
CO_2	Carbon dioxide
CTE	Coefficients of thermal expansion
Cu	Copper
DC	Direct current
DCM	Dichloromethane
DI	Deionized
Dy	Dysprosium
EDM	Electric discharge machining
EDX	Energy dispersive X-ray
FDA	Food and drug administration
Fe	Iron
GMD	Geometric mean distance
HCl	Hydrochloric acid
HF	Hydroluric acid
IC	Integrated circuits
ICP	Intracranial pressure
IOP	Intra-ocular pressure

IR	Infrared
IV	Inherent viscosity
KOH	Potassium hydroxide
LC	Inductive-capacitive
MEMS	Microelectromechanical systems
Mg	Magnesium
MgO	Magnesium oxide
Mn	Manganese
MST	Microsystem technlogy
NaCl	Sodium chloride
Nd	Neodymium
NEMS	Nanoelectromechanical systems
NH_4F	Ammonium fluoride
PCL	Poly(ϵ-caprolactone
Pd	Palladium
PDLLA	Poly(D, L-lactic acid)
PGA	Poly(glycolic acid)
PGS	Poly(glycerol sebacate)
PLA	Poly(lactic acid)
PLGA	Poly(lactic-co-glycolic acid)
PLLA	Poly(L-lactic acid)
PMMA	Poly(methyl methacrylate)
PPy	Polypyrrole
PSA	Poly(sebacic anhydride)
Pt	Platimum
PTFE	Polytetrafluoroethylene
PVA	Poly (vinyl alcohol)

PVAc	Poly (vinyl acetate)
RDA	Recommended dietary allowance
RF	Radio frequency
RIE	Reactive ion etching
RLC	Resistor-inductor-capacitor
ROP	Ring-opening polymerization
SEC	Saturated calomel electrode
SEM	Scanning electron microscope
Si NMs	Silicon nanomembranes
Ti	Titanium
VP-SEM	Variable pressure scanning electron microscopy
Zn	Zinc
ZnO	Zinc oxide

Symbols

C_{par}	Planar spiral inductor parasitic capacitance
C_S	Analytical model equivalent sensor circuit capacitance
d_0	Center deflection of capacitor plate
D_n	Effective flexural rigidity
E	Young's modulus
E_{corr}	Metal corrosion potential
f_0	Resonant frequency
f_{min}	Minimum phase frequency
g_0	Distance between two capacitor plates
I_{corr}	Metal corrosion current
k	Coupling coeffcient between the sensor and the external coil
k_m	coupling coeffcient between two planar spiral inductors

L_E	External coil inductance
L_S	Analytical model equivalent sensor circuit inductance
L_{ss}	Planar spiral inductor inductance
ll	Total length of spiral inductor
l_t	Line thickness of planar spiral inductor
M_w	Molecular weight
Q	Quality-factor
s	Line spacing of planar spiral inductor
T_m	Melting temperature
T_g	Glass transition temperature
t_m	Bending plate thickness
w	Line width of planar spiral inductor
z_n	Neutral surface for bending
ν	Poisson's ratio

SUMMARY

Implantable sensors have been extensively investigated to facilitate diagnosis or to provide a means to generated closed loop control of therapy by yielding *in vivo* measurements of physical, chemical and biological signals. MEMS technology has demonstrated significant value in this application mainly due to its micro-scale size, low weight, low power consumption, potential for low fabrication cost, superior functionality or performance, and ability to be combined with biotechnology and molecular biology. Among those, biodegradable sensors which degrade gradually after they are no longer functionally needed exhibit great potential in acute or shorter-term medical diagnostic and sensing applications due to the advantages of (a) exclusion of the need to a secondary surgery for sensor removal, and (b) reduction of the risk of long-term infection.

The objective of this research is to design and characterize microfabricated RF wireless pressure sensors that are made of completely biodegradable materials and degrade at time-controlled manner. This will be achieved by means of investigation of appropriate biodegradable materials and development of appropriate fabrication processes for these non-standard MEMS materials. To achieve this goal, four subareas of research will be performed: (1) design of sensors that operate wirelessly and are made of biodegradable materials; (2) investigation of the biodegradable materials in the application of implantable biodegradable wireless sensors to achieve controllable degradation lifetimes; (3) development of new fabrication processes that allow the handling of delicate biodegradable materials; and (4) testing the pressure response functionality and studying the degradation behavior of the wireless biodegradable pressure sensors.

The structure of the wireless sensor consists a very compact and relatively simple design of passive LC resonant circuits embedded in a polymer dielectric package. A sensing cavity, which is bounded by two metal plates, forms a variable capacitor and is interconnected with planar inductor coil(s). The inductor and the capacitor can be either connected with a conducting via, or can be capacitively and inductively coupled without a conducting via. When pressure is applied to the sensor, the gap between the two capacitive electrodes is reduced and the capacitor value increases. The resulting pressure-induced LC resonant frequency change can be measured wirelessly using an external coil. To design the sensor with a particular resonant frequency range, the inductance and capacitance of the sensor is predicted using an analytical model based on the literature. An electromagnetic model of the sensor is also developed to analyze the wireless sensing mechanism. A mechanical model for circular plate bending is also presented to understand the deflection of the capacitor plates. Then, the electromagnetic and mechanical models are integrated to predict the pressure-dependent capacitance change. The geometry of the sensor is finally established based on the analytical and finite element simulations results.

Among various biodegradable materials, including both polymers and metals that have been reviewed for biomedical applications, only FDA-approved and commercialized biodegradable polymers are considered as candidates in this pioneer work of completely biodegradable wireless sensors. To explore the feasibility of both slow degradation sensors (expected degradation time on the order of years), and rapid degradation sensors (expected degredation time on the order of months), poly(L-lactic acid) (semi-crystalline, degradation time $>$ 2 years) and a "shell-core" structure of poly(lactic-co-glycolic acid) (amorphous, degradation time $<$ 1 month) and polyvinyl alcohol (water soluble) are utilized as the dielectric package. To form the required electrical conductors, biodegradable metallic zinc and zinc/iron couples with appropriate electrical properties (e.g., conductivity and AC resistance) and ease of

fabrication are chosen. In the metallic couples, a bulk biodegradable metal (zinc) that degrades relatively slowly is electrically connected to a small amount of more active biodegradable metal (iron). This approach allows acceleration and tailoring of the degradation rate of the entire metal by galvanic corrosion. The *in vitro* degradation rate of the pure zinc and zinc/iron-couples with different metal surface area ratio are studied through both electrochemical testing and physical weight loss measurements. Further, due to the absence of degradation data of poly(lactic-co-glycolic acid) utilized in the degradable sensor, the degradation behavior of this polymer is studied *in vitro*.

To exploit the advantages of microelectromechanical systems (MEMS) technology in fabricating miniaturized devices, while protecting vulnerable biodegradable materials from the strong and/or hazardous chemicals that are commonly used in conventional MEMS fabrication process, novel fabrication processes that combine conventional MEMS technology with non-wet processes have been developed in this study. These new processes enable the fabrication of biocompatible and biodegradable 3-D devices with embedded, near-hermetic cavities. The bulk metal conductors are electrodeposited through photoresist molds; for the case of the metal couples, a thin layer of more active metal is either evaporated or electrodeposted on this bulk conductor. The metal conductor is then embossed into biodegradable polymer sheets, followed by multilayer polymer lamination with or without folding to create the final devices with or without a conducting via.

The fabricated biodegradable pressure sensors are characterized wirelessly in air and through a long-term immersion test *in vitro* until no resonance can be detected by the external coil. During the entire *in vitro* functionality measurements, the impedance phase and magnitude of individual sensors without applied pressure are recorded to determine the resonant frequency and quality factor, and pressure response tests are performed intermittently to determine the sensitivity. *In vitro*

degradation tests continue after the sensor stops resonating with the external coil and last for 7 months for the slow degradation sensors, and less than 35 days for the rapid degradation sensors. All the sensors exhibit three stages of behavior *in vitro*: equilibration, functional lifetime, and performance degradation. During the functional lifetime, most sensors exhibit fully stable functionality: relatively steady resonant frequency and slight decrease of quality factor with zero applied pressure, as well as comparable sensitivities at different time points. The slow degradation sensors exhibit functional lifetimes of several days and show no significant total weight loss but do show an obvious physical appearance change of the metal-couple conductors within 7 months. These slow degradation sensors are expected to fully degrade after 2 years, based on the degradation of the polymer package. The rapid degradation sensors exhibit functional lifetimes of no more than 1 day and can degrade completely within 26 days. Compared with that of slow degradation sensors, the rapid degradation sensors present improved functional time ratio (functional lifetime/degradation lifetime $\times 100\%$) of 2.7% to 4.0%.

CHAPTER I

INTRODUCTION

1.1 In Situ Sensors For Biomedical Application

1.1.1 Biomaterials

Generally speaking, biomaterials refer to that class of materials that are used in contact with biological systems. To be more specific, the most accepted definition of biomaterials is currently the one employed by the American National Institute of Health that describes a biomaterial as "any substance or combination of substances, other than drugs, synthetic or natural in origin, which can be used for any period of time, which augments or replaces partially or totally any tissue, organ or function of the body, in order to maintain or improve the quality of life of the individual" [6]. Metals, metallic alloys, synthetic or natural polymers, ceramics, and mineral compounds are all currently being used as biomaterials by modern surgeons [146].

One of the big concerns for applying those foreign materials in the body, especially for an extended period of time, is the rejection response from the delicate human body system. Therefore, one of the essential prerequisites for biomaterials is to be biocompatible. Biocompatiblity is defined as "ability of a biomaterial to perform its desired function with respect to a medical therapy, without eliciting any undesirable local or systemic effects in the recipient or beneficiary of that therapy, but generating the most appropriate beneficial cellular or tissue response to that specific situation, and optimizing the clinically relevant performance of that therapy" [156]. The concept includes all aspects of the interfacial reaction between the biomaterial and body tissues: initial events at the interface, material changes over time (degradation), and the fate of its degradation products. Excellent biocompatible materials must meet a

number of requirements during the entire lifetime that they remain in the body [26]:

- Non-toxic
- Non-cancerogenic
- Non-mutagenic
- Non-allergenic
- Free from contaminants (e.g., additives, solvents, and synthesis residues)
- No adverse immunological responses

Typical applications of biomaterials in medicine are for disposable products (e.g. syringe, blood bag, and catheter), materials supporting surgical operation (e.g. suture, adhesive, and sealant), prostheses for tissue replacements (e.g. intraocular lens, dental implant, and breast implant), and artificial organs for temporary or permanent assist (e.g. artificial kidney, artificial heart, and vascular graft) [61]. The global market of biomaterials was estimated as 150200 billion US dollars in 2012, including all diagnostic and therapeutic equipments. The ten largest markets are US, Japan, Germany, France, Italy, UK, Brazil, China, Canada and Spain. The growth of US market share is 9% per year being the leading market in the world followed by Europe, with 25% market share, and Japan. The largest market for biomaterial based products is orthopedic biomaterials followed by cardiovascular and drug delivery materials [6].

1.1.2 MEMS-based Wireless Implants

Microelectromechanical Systems (MEMS) technology refers to using microfabrication technology to create functional structures with critical features on the nano- to micro scale. Sometimes, devices with nano-scale dimensions are classified as nanoelectromechanical systems (NEMS). MEMS is also referred to as micromachines (mainly in Japan) or microsystem technology (MST) (mainly in Europe). MEMS technology has become a huge industry with a total sales of MEMS manufacturers exceeding

5 billion US dollars in 2007, and continuously growing, with main applications in automotive, communication and electronics markets [119].

In modern biomedical and health care fields, the concept of biomaterials has gradually shifted from purely mechanical replacement implants/transplants towards true biological solutions [154]. Implantable sensors have been extensively investigated to facilitate diagnosis or to provide a means to generate closed-loop control of therapy by yielding *in vivo* measurements of physical, chemical and biological signals (e.g. pressure, strain, force, glucose level, etc.)[77, 154]. In this application, MEMS technology attracts great interest mainly due to its micro-scale size, low weight, low power consumption, potential for low fabrication cost, superior functionality or performance, and capability of being combined with biotechnology and molecular biology [119, 25]. Sensing strategies for MEMS-based sensors include optical [94], mechanical [34] , magnetic [47], electrochemical [151] detection methods, and combinations of the above.

To reduce the risk of infection resulting from transcutaneous wires breaching the skin and also to reduce user discomfort, wireless operation of implantable sensors is more desired [4]. But the challenges in designing and fabricating is thereby increased. The majority of wireless biomedical implantable sensors are composed of an implantable *in vivo* device and one or more external *ex vivo* electronics that control and/or collect the data provided by the internal implants. The implant either (a) telemeters data externally, (b) receives and executes commands from an external electronics or (c) performs both operations [10]. The choice of designing the implant and the external electronics depends on many factors, including the implant size, its location in the body and the desired sensitivity. From the point of telemetry, wireless sensors can be divided into active and passive telemetry. For active telemetry, integrated power supplies are utilized to power the integrated circuits (IC) [117]. Further transmission distance could be achieved, however the entire system is relatively complex, higher packaging requirements are needed to isolate the active

circuitry from harsh environments while allowing the capacitive transducer to interact with the surrounding environment. The lifetime of the system depends on the power supply which might need constant replacement or recharging [3, 124]. All these constraints add challenges on the design and fabrication of active sensors in the implantable biomedical application. On the contrary, passive telemetry relying on the inductive coupling between the coil in the implant and the external coil eliminates the complexity and reduces risk by placing the power supplies and active circuitry on external electronics. But telemetry by inductive coupling can be used only for short distances, because the magnetic field strength along the coil axis decreases as the third power of distance [4].

The pressure sensor is one of the most common types of implantable sensors nowadays. The most typical structure includes a suspended mechanical membrane that deflects according to environmental pressure variations. This deflection can be transduced wirelessly with the help of conductors on both sides of the gap or piezoresistors on the high strain areas of the membrane and appropriate electronic circuitry. Implantable pressure sensors have been widely utilized in the following biomedical applications *in vivo* [119]:

(a) Intra-ocular pressure sensor. Elevated intra-ocular pressure (IOP) is one of the risk factors for glaucoma, which is vision loss due to pressure-induced optic nerve damage. Therefore, long-term (continuous) IOP measurements can offer new perspectives for patients suffering from glaucoma.

(b) Intra-cranial pressure sensors. An increase in intracranial pressure (ICP) can be found in patients who suffer from head injury or diseases such as chronic hydrocephalus, brain tumors or abscesses. Continuous measurement using a wireless implanted system offers opportunities of increasing mobility over catheter-based systems, reducing the mortality risk of intensive care patients, and allowing the monitoring of the ICP of patients after surgery to treat obstructive hydrocephalus.

(c) Cardio vascular pressure sensors. Blood pressure at various anatomical positions contains clinically relevant information when the heart pumps blood through the bodys vascular system. Continuous monitoring of pressure for cardiovascular applications using wireless implantable micro sensors offers additional advantages of better therapies and increased quality of life for several conditions including coronary artery disease, heart failure, aneurysm, hypertension and arrhythmias.

(d) Pressure sensors for urology. Urodynamic testing is the most reliable current diagnosis method for urinary incontinence, typically by inserting catheters in an outpatient procedure allowing for ambulatory pressure measurements. Implantable pressure sensors increase the attractiveness of ambulatory monitoring by eliminating catheters and enabling measurements under close to normal life circumstances for the patients.

1.1.3 Toward Biodegradable Sensors

As biodegradable materials have been greatly developed and are being used in biomedical applications (e.g. drug delivery system, stent, orthopedic devices) [26, 113, 95], the idea of biodegradable sensors has been brought forward. Similar to biodegradable non-sensing implants, biodegradable sensors are expected to "do their job and disappear" [148]. There are two main advantages of biodegradable sensors:

(a) Exclude the need to perform a secondary surgery for sensor removal. In some acute or shorter-term medical applications, the sensor's functionality is required only for a limited time. In these cases, utilizing biodegradable sensors that can be functional for a desired time and disappear gradually is preferable [89, 10].

(b) Reduce the risk of long term infection. Due to the limitation of biomaterials, even those materials generally considered to be biocompatible would engender some degree of tissue response, especially in long-term implantation [45]. Up to now, all implants have limited life time and there are many levels of ethical and technical issues

associated with revision surgeries of those existing "permanent" implants [51, 85]. Therefore, biodegradable sensors with adjustable functional lifetime and degradation time may be a solution to overcome current limitations of long-term biocompatibility.

1.2 Thesis Outline

Chapter 2 introduces the biodegradable materials and a current literature review on research related to implantable biodegradable sensors. Biodegradable polymers are first introduced, with explanation of the common degradation mechanisms and the difference between bulk and surface erodible polymers. Several most intensively studied bulk and surface erodible biodegradable polymers are listed with a brief illustration of their developments, physical properties, and possible applications. The *in vitro* as well as *in vivo* performance of three major biodegradable metals, iron (Fe), magnesium (Mg), and zinc (Zn), as well as their alloys, are preseted together with their performance in the current clinical application. Finally, several studies related to biodegradable sensors currently in the literature are demonstrated.

Chapter 3 presents the sensor concept, design, and modeling. The research objective for designing and studying the completely biodegradable wireless pressure sensor is first proposed. The sensor utilized in this work consists a passive LC resonant circuit embedded into a dielectric package. A parallel-plate capacitor is interconnected with planar spiral inductor(s) to form the LC resonator. The electromagnetic model of the LC resonant circuit is presented to calculate the inductance and capacitance. Biodegradable polymers are utilized as the dielectric (package and spacers). The mechanical theory is also presented for a circular plate in order to develop a sensor plate mechanical deflection model. In addition, the metal and polymer materials selection for the biodegradable sensor is demonstrated. Finally, the geometry of the sensor is developed by utilizing the models and the capacitance change (and ultimately the resonant frequency change) of the sensor as a function of applied pressure guided by

finite element simulations (COMSOL 4.2).

Chapter 4 demonstrates the *in vitro* degradation study of the polymer and metals utilized in the sensor. Due to the lack of the degradation data, an *in vitro* degradation study of the PLGA (5004A) which is proposed to be applied in the rapid degradable sensor is performed. The physical weight and appearance change of PLGA films are recorded until the polymer degrades completely. Galvanic corrosion is utilized to accelerate the degradation of metal conductors. The degradation of biodegradable Zn and Zn/Fe couple rectangular specimens are studied through both electrochemical means and weight loss measurement. The degradation rates are calculated; several parameters that might affect degradation rate during the measurement are also discussed.

Chapter 5 presents the fabrication process of the biodegradable sensors including sensors with and without conducting vias. The fabrication process of conductors for all the sensors with different polymer dielectrics is the same: electroplating Zn through a photoresist mold on a flexible and chemically resistant membrane (Kapton®), and extra steps of either electroplating or evaporating Fe for Zn/Fe-couple conductors. The polymers are prepared using solvent casting and laser micromachining. The sensor assembly steps that involve embossing, folding and lamination are illustrated.

Chapter 6 presents the characterization of the inductors and performance of the sensors in air and *in vitro*. The pressure response and short-term stability of the sensor is first tested wirelessly in air to confirm the success of the fabricated sensors. Then the sensors are tested wirelessly in a prolonged immersion test in saline (0.9%) until no resonance with the external coil can be observed. The resonant frequency (f_0) and quality factor (Q) of the sensors with zero applied pressure during the entire test are recorded and calculated. The pressure response of the sensors are performed intermittently to obtain the sensitivity. The performance of all the sensors are compared and the possible failure mechanisms are also discussed. Differences between

performance predicted by the models and the observed behavior are discussed and explained.

Chapter 7 demonstrates the prolonged *in vitro* degradation of the sensors after they stop being functional. The pictorial histories as well as the weight change of all fabricated sensors are presented. Due to the time limit, the degradation tests for PLLA-based sensors last for approximately 7 months, and terminate without observing complete degradation of the sensors. For rapidly degradable PLGA-based sensors, the entire degradation processes of less than 40 days is recorded for those with non-PLLA spacers and PVA embossing temperature of 130°C. Finally, the functional lifetimes of these sensors are compared with their degradation lifetimes.

Chapter 8 presents the conclusion, contributions, and future outlook of this work.

CHAPTER II

BIODEGRADABLE MATERIALS AND SENSORS

Broadly speaking, the term "biodegradable materials" can refer to both materials that will degrade in a ecological environment where biological processes are occurring, and materials that degrade by biochemical reactions upon contact with living tissue [78, 146].

For biomedical application, biodegradable materials (sometimes being called bioresorbable or absorable) refer to biomaterials that are not only biocompatible but also can degrade into products that can be eliminated from body by either natural pathways or involved normally in a metabolic pathway [146]. Biodegradable materials are intended for temporary aids, such as temporary surgical products (e.g. for suturing, fixation, covering and adhesion), pharmaceutical use (drug delivery systems) and tissue engineering (scaffolds, stent) [61].

In this chapter, the two main categories of biodegradable materials, biodegradable polymers and biodegradable metals are introduced first, then current studies on biodegradable sensors in the literature are listed.

2.1 Biodegradable Polymers

Biodegradable polymers can be either natural or synthetic biodegradable polymers. Natural origin biodegradable polymers include modified polysaccharides (cellulose, starch, dextran, chitin etc.) and modified proteins (collagen, casein, fibrin, etc.) [146]. The widely studied synthetic biodegradable polymers include aliphatic polyesters, polyols, polycarbonates and miscellaneous [61]. Significant interest has been focused on synthetic biodegradable polymers, mainly due to their versatility with respect to mechanical and physicochemical property adjustments by various means, such

as additives, polymerization, chemical modification, polymer blending, and composites [146, 103]. The degradation rate of a polymer can be influenced by [78, 41, 23, 26]

- Polymer chemistry
- Molecular architecture
- Molecular weight
- Morphology
- Enzymes
- Surrounding conditions (e.g., pH and temperature)

Synthetic biodegradable polymers in medical applications are typically degraded by hydrolysis [82, 103]. The entire degradation process of biodegradable polymers involves the chain scission process caused as the water penetrates into the polymer matrix, i.e., degradation, and the physical disintegration during which the degradation products (monomers and oligomers) leave the polymer matrix, i.e., erosion [41, 136]. During the entire degradation process, some polymer properties would change, including loss of molecular weight and mechanical strength, crystallization, monomer formation, morphological changes, etc. [41, 136].

Based on the erosion mechanism, biodegradable polymers can undergo either bulk erosion or surface erosion, as illustrated in Figure 1. In bulk erosion, the water penetrates faster than the matrix erodes, consequently, degradation and erosion occur throughout the entire polymer volume. In the ideal case, the size of the polymer remains consistent for a considerable portion of time while the micro-structure within the volume changes. The erosion rate depends on the total amount of materials and will decrease as the material is consumed. In contrast, in surface erosion, water penetrates more slowly than the erosion, and the size of the polymer decreases gradually due to mass loss from the exterior surface. In the ideal case, the erosion rate is directly proportional to the surface area [41, 136, 26].

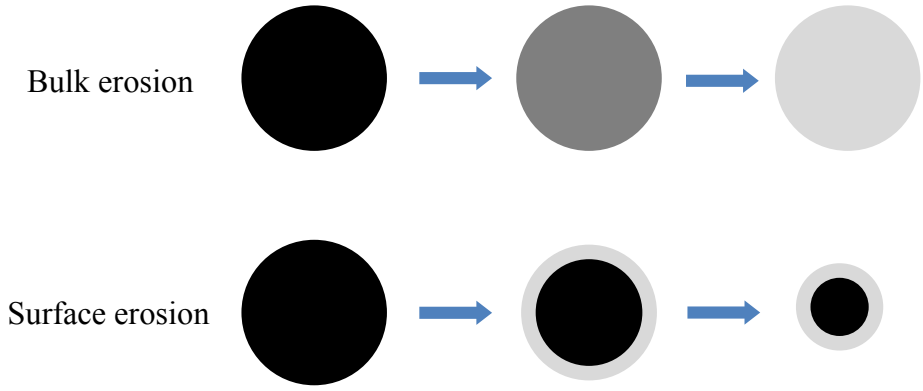

Figure 1: Schematic illustration of bulk erosion and surface erosion

2.1.1 Aliphatic Polyesters

The family of aliphatic polyesters is one of the first synthetic and by far the most popular class of biodegradable polymers [82, 57]. Poly(glycolic acid) (PGA), poly(lactic acid) (PLA) , poly(ϵ-caprolactone) (PCL), poly(glycerol sebacate) (PGS) and their co-polymers have been widely investigated. The molecular structure of some these polymers are shown in Figure 2.

Theoretically, all polyesters are degradable because esterification is a chemically reversible process; however, only aliphatic polyesters with reasonably short aliphatic chains between ester bonds can degrade over the time frame required for most biomedical applications [103]. The degradation of aliphatic polyesters is mainly due to the

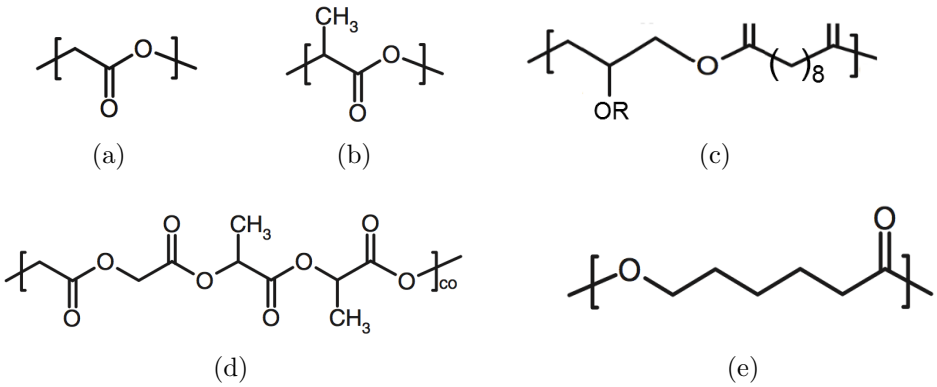

Figure 2: The molecular structures of some aliphatic polyesters: (a) PGA, (b) PLA, (c) PGS, (d) PLGA, and (e) PCL

hydrolytic cleavage of the backbone ester bonds [82, 70, 46, 141] or by enzymatic promotion [157, 61]. Hydrolysis can be catalyzed by either acids or bases [82]. A typical hydrolysis process of aliphatic polyesters is schematically demonstrated in Figure 3 utilizing PLA as an example [26]. The phenomenon of autocatalysis is observed sometimes during the degradation due to the carboxylic end groups formed during chain scission, which can enhance the rate of further hydrolysis [116]. This autocatalysis mechanism makes polyester matrices truly bulk eroding [82, 42].

Polyesters can be synthesized by step (condensation) polymerization of hydroxy acids or of diols and diacids, or by addition (chain) polymerization including ring-opening polymerization (ROP) of the cyclic lactone [146, 82, 70]. Generally, ring-opening polymerization is the preferred route to synthesize polyesters with high molecular weight, due to the milder conditions and shorter reaction times that can be used [86, 139]. A condensation process is usually used to prepare a variety of hydrolytically sensitive polymers, such as polyanhydrides and polyurethanes [103, 71]. Enzyme-catalyzed polyester synthesis has also attracted great interest recently from the point of view of molecular architecture. Biocompatible, pure, and well-defined

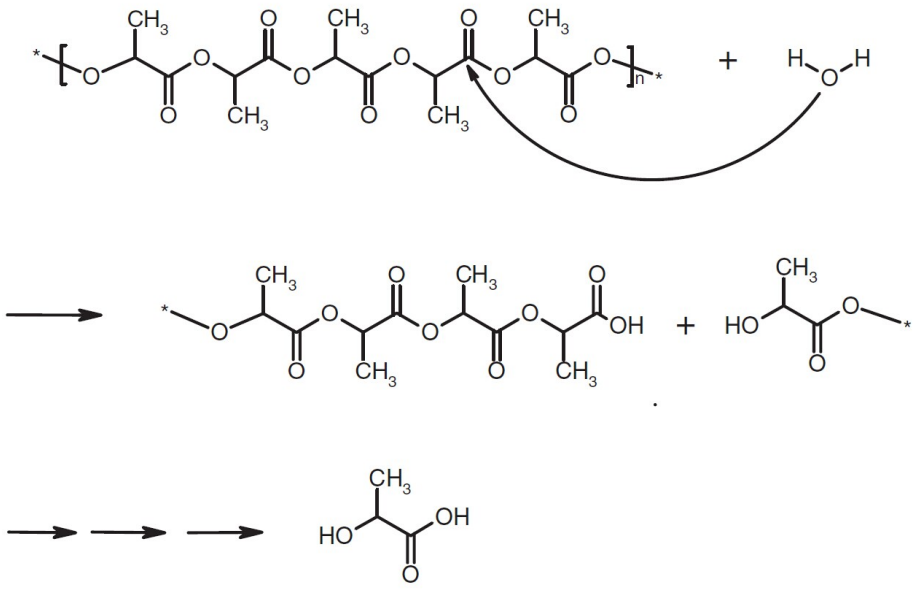

Figure 3: Schematic illustration of hydrolytic degradation of PLA

polymer structures may be obtained as the method is highly selective and proceeds without side-reactions under mild conditions [69, 73]. Since all the biodegradable polymers utilized in this work are purchased as commercialized product, no details of the synthesis procedures are introduced here.

(1) Poly(glycolic acid) (PGA)

PGA is a very stiff, highly crystalline polymer, yet degrades rapidly 100% within 3 months) [93, 24, 39]. PGA has excellent fiber-forming properties and was commercially introduced in 1969 as the first synthetic absorbable suture under the trade name DEXON® and approved by the United States (US) Food and Drug Administration (FDA) [39]. PGA is one of the stiffest biodegradable polymers: a self reinforced form exhibits a modulus of approximately 12.5 GPa [87]. Due to its excellent mechanical properties, PGA has been utilized in the application area of bone internal fixation devices (Biofix®). However, its poor solubility in most common solvents, high melting temperature (T_m) (approximately 225 °C) and tendency of causing inflammation in the surrounding tissues due to rapid degradation limits its biomedical application [93]. Several copolymers containing glycolide units have been developed to overcome the inherent disadvantages of PGA.

(2) poly(lactic acid) (PLA)

PLA is one of the most popular biodegradable polymers, due to its excellent properties: good processability, excellent biocompatibility, and degradation into non-toxic products [82, 9, 141]. PLA has been approved by the FDA for medical use and is commercially available in a variety of grades. It has been widely applied in the medical field, for use in sutures, drug delivery devices, prosthetics, scaffolds, vascular grafts, as well as bone screws and pins and plates for temporary internal fracture fixation [5, 115, 14, 9, 93]. PLA is soluble in halogenated hydrocarbons, ethyl acetate, tetrahydrofuran, dioxane, and several other solvents [61]

With two asymmetric carbons, lactide exists as the optically active *L*- form and

D-forms or as the racemic D,L-form. Naturally occurring pure enantiomeric poly(L-lactic acid) (PLLA) is semicrystalline due to its stereoregular structure; the degree of crystallinity of PLLA depends on the molecular weight and polymer processing parameters [103]. PLLA is a relatively hard material with high modulus (2.5 to 4.8 GPa), good tensile strength, and low extension. It has crystalline T_m in the range of 170 - 180 °C and a glass transition temperature (T_g) of approximately 60 - 67 °C [61, 95]. Since PLLA has glass transition temperatures above body temperature, these matrices are stiff with little elasticity in the body and are somewhat brittle at room temperature [27, 38] Being considered as hydrophobic, the degradation of PLLA is relatively slow. Even PLLA would lose its strength in approximately 6 months when hydrolyzed, it takes from 2 to 5.6 years for complete resorption in-vivo depending on the degree of crystalinity and porosity of the polymer matrix [95, 7, 103].

The Poly(D,L-lactic acid) (PDLLA) can be synthesized by polymerization of the diastereoisomer (D,L-v) or a racemic mixture of D,D-lactic acid/L,L-lactic acid [70, 146]. PDLLA is amorphous and has a T_g in the region of 50 - 60 °C [26]. Compared to PLLA, PDLLA exhibits much lower strength (approximately 1.9 GPa) due to its amorphous structure. PDLLA loses its strength within 1 - 2 months when hydrolyzed and degrades completely within 12 - 16 months [93].

(3) Poly(lactic-co-glycolic acid) (PLGA)

PLGA is under the most intense and thorough study among all the co-polymers that are biodegradable, and has been approved by the FDA for a number of clinical applications [158, 40, 120]. The degradation rate and mechanical properties are affected by a number of factors: molecular weight, the ratio of lactide to glycolide, and the degree of crystallinity [82, 96]. Generally, PLGA is less stiff and degrades faster than both PLA and PGA, with the 50:50 composition exhibiting the most rapid degradation rate [96, 120]. The degradation time is approximately 1 to 2 months for 50:50 PLGA, 4 to 5 months for 75:25 PLGA, and 5 to 6 months for 85:15 PLGA. PLGA with

compositions between 25 and 70% GA are amorphous and the crystallinity decreases with increase in the content of either co-monomer [40]. PLGA is soluble in a wide range of common solvents including chlorinated solvents, tetrahydofuran, acetone or ethyl acetate [144], and demonstrates good cell adhesion and proliferation [88, 8].

(4) Poly(ϵ-caprolactone) (PCL)

Poly ϵ-caprolactone (PCL) is a semicrystaline polyester and degrades much more slowly than PLA and PGA. One of the interesting properties is that PCL has a very low Tg (-60 °C) and low melting temperature (60 °C). Therefore, PCL is in the rubbery state and exhibits high permeability to low molecular weight species at body temperature [82, 103]. PCL is highly processable due to its low melting point and good solubility in a wide range of organic solvents [26, 103]. PCL has low tensile strength (approximately 23 MPa) but an extremely high elongation at breakage (>700%) [48]. PCL is also remarkably compatible with numerous other polymers [131, 26]. Due to its slow degradation, high permeability to many drugs, non-toxicity, and excellent biocompatibility, PCL is widely used as a long-term drug/vaccine delivery vehicle and scaffold [102]. PCL is also commercialized in varies grades and is approved by the FDA for several medical applications.

(5) Poly(glycerol sebacate) (PGS)

PGS is a relatively new and fast-developing member of polyester biodegradable polymers, first reported in 2002 as a tough biodegradable elastomer synthesized by polycondensation of glycerol and sebacic acid [150]. Unlike all the other polyesters introduced above, PGS is a soft thermoset elastomeric polymer and undergoes surface erosion [67, 18]. Conventionally, PGS is synthesized by a two-step method of prepolycondensatioan and crossliking [150]. Photopolymerization of PGS prepolymer with reactive acrylate moieties is also introduced to avoid the harsh conditions involved in the conventional polymerization of PGS [107]. The mechanical properties and degradation rate of PGS can be modified by controlling the curing time,

curing temperature, reactant concentrations and the degree of acrylation in acrylated PGS [118]. PGS materials have average Young's modulus (E) in the range of 0.025 to 1.2 MPa, ultimate tensile strength more than 0.5 MPa and strain to failure greater than 330% [150, 17, 134]. PGS is a semi-crystalline polymer being completely amorphous above 37 °C, and the degree of crystallization decreases significantly with increasing curing time and curing temperature [62]. PGS has also been shown to exhibit shape memory behavior, in which the three-dimensional network of PGS acts as the fixed phase and the amorphous phase acts as the reversible phase. [16]. PGS has been under investigation for biomedical applications in drug delivery and soft-tissue engineering including cardiac, vascular, cartilage, retinal, nerve and repair of tympanic membrane perforations [118].

2.1.2 Polyanhydrides

Polyanhydrides can be considered as the most extensively investigated biodegradable surface eroding polymers specifically designed and developed for drug delivery applications [103]. Polyanhydride-based biodegradable polymers have hydrophobic backbone with hydrolytically labile anhydride linkages such that hydrolytic degradation can be controlled by manipulation of the polymer composition. Aliphatic polyanhydrides degrade within days or weeks while the erosion of aromatic polyanhydrides ranges from several months to years [71]. Schematic hydrolytic degradation of an alphatic polyanhydride is shown in Figure 4. Polyanhydrides are generally considered surface eroding because they undergo a linear mass loss during erosion, but would change to bulk erosion once the dimension drops below a critical limit [43]. They degrade *in vitro* as well as *in vivo* to their acid counterparts as non-mutagenic and non-cytotoxic products, and show no evidence of inflammatory [125, 80]. Many polyanhydrides have fairly low melting points and are soluble in common organic solvents. These properties make polyanhydrides popular candidates for controlled

release application [103, 26].

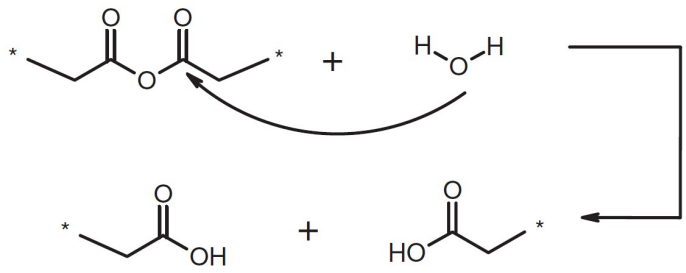

Figure 4: Schematic hydrolytic degradation of an alphatic polyanhydride

The limitations of aliphatic homo-polyanhydrides such as poly(sebacic anhydride) (PSA), however, are their super hydrolytic instability (in that they will undergo spontaneous depolymerization to low molecular weight polymers in organic solutions or upon storage at moisture room temperatures and above), low mechanical strength, and film or fiber forming properties [71]. Therefore, copolymers of sebacic anhydride and hydrophobic aromatic monomers are usually utilized. Polyanhydrides based on a variety of aromatic and aliphatic dicarboxylic acids were investigated as drug-carrier matrices and approved by the FDA in 1996 [79, 103]. Poly((carboxy phenoxy propane)-(sebacic acid)) (P(CPP-SA)) with the structure shown in Figure 5 is also approved by the FDA for use as a localized delivery vehicle [74, 103]

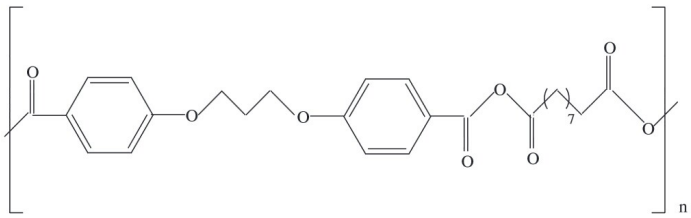

Figure 5: Stucture of poly((carboxy phenoxy propane)-(sebacic acid)) (P(CPP-SA))

2.1.3 Poly(vinyl alcohol) (PVA)

Unlike the other biodegradable polymers presented above, PVA is a vinyl polymer with carbon backhones which are generally not susceptible to hydrolysis. It is considerded biodegradable in the ecological enviroment because it can be easily biodegraded

by microorganisms as well as enzymes [152]. In the biomedical field, it is sometimes included as a biodegradable polymer mainly due to its water-soluble and non-toxic properties [111]. Commercial PVA is typically made by polymerization of vinyl acetate to poly (vinyl acetate) (PVAc) followed by hydrolysis of PVAc [92]. PVA with different degrees of hydrolysis can be obtained by alternating the extent of the hydrolysis reaction. Generally, the hydrolysis reaction cannot reach completion without more drastic treatment; all PVA typically has some residual acetate groups [32].

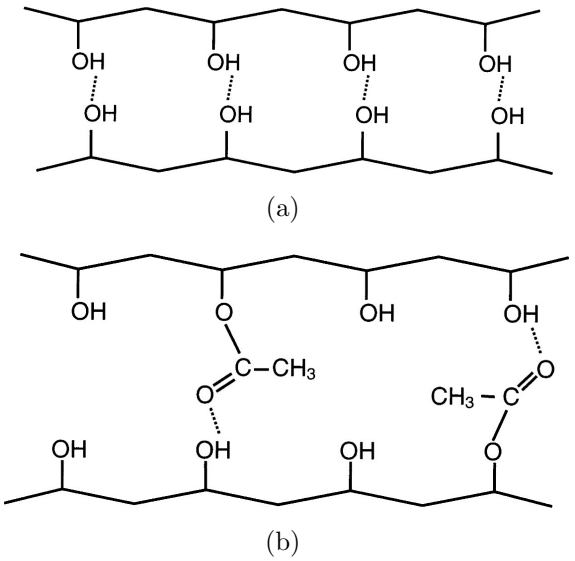

Figure 6: Hydrogen bonding in commercial PVA (a) many inter chain hydrogen bonds can be established between two high hydrolysis PVA chains, and (b) acetate groups act as spacers and restrict the level of hydrogen bonding between two low hydrolysis PVA chains [30]

The solubility of PVA in water is determined by the extent of both inter and intra chain hydrogen bonding, together with the PVA-water hydrogen bonding. As shown in Figure 6(a), when the PVA chains are highly hydrolyzed, many interchain hydrogen bonds can be established, while in Figure 6(b), the interchain hydrogen bond is limited due to the bulky size and hydrophobic character of unhydrolyzed acetate groups [30].

Therefore, the hydrolysis degree, molecular weight (M_w) and solution temperature

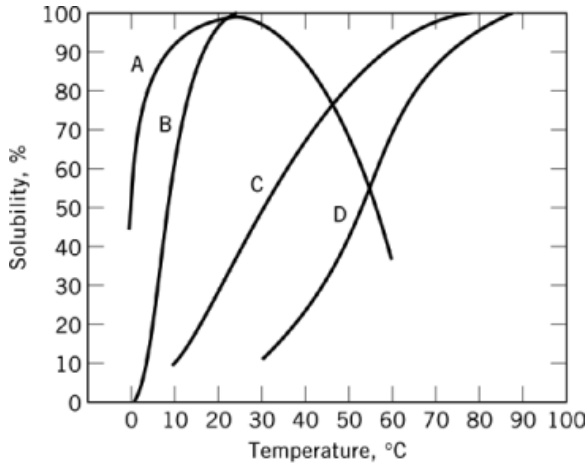

Figure 7: Solubility of PVA in water as a function of temperature: (a) 78 - 81% hydrolyzed, M_w = 160,000 - 168,000, (b) 87 - 89% hydrolyzed, M_w = 40,000 - 48,000, (c) 98 - 99% hydrolyzed, M_w = 40,000 - 48,000, and (d) 98 - 99% hydrolyzed, M_w = 136,000 - 144,000 [15]

together determine the solubility of PVA in water by affecting the degree and character of hydrogen bonds of PVA in aqueous solution [32]. The solubility of some PVA with different degrees of hydrolysis and molecular weight as a function of temperature is shown in Figure 7.

2.2 Biodegradable Metals

Nowadays, with the advent of tissue engineering, biomaterials are envisaged to actively interact with the body. Metallic biomaterials are not necessarily required to be inert but they should be able to assist and promote the healing process. In many cases, they should do their job and step away thereafter [53]. The corrosion of metal, a normally undesirable phenomenon in metallurgy engineering application, however, can be utilized as a useful property for certain metals in biodegradable applications. Magnesium (Mg), Mg alloy, and iron (Fe) are the most well-known biocompatible and biodegradable metals due to their combination of high mechanical strength, fracture toughness, and non-toxicity. Their main medical applications up to now are biodegradable stents, a small mesh-like tubular scaffold which is placed

and then expanded inside the coronary arteries to keep the lumen open, and bone implants [161, 148, 99]. An example of a magnesium coronary stent is shown in Figure 8.

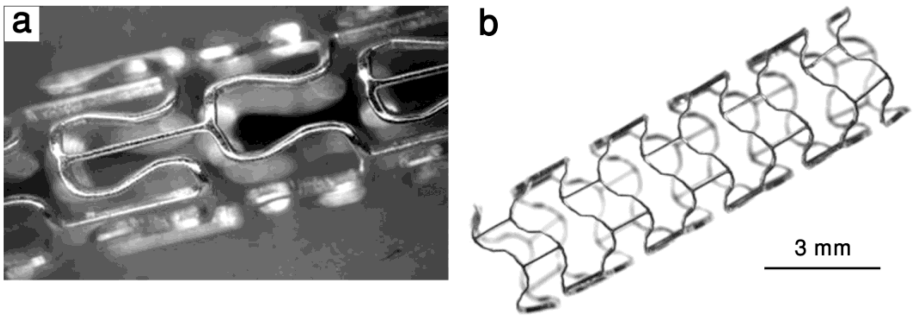

Figure 8: (a) Non-expanded, and (b) expanded view of a magnesium coronary stent (MAGIC, biotronik)

2.2.1 Iron (Fe) and alloy

Iron can interconvert between ferric (Fe^{2+}) and ferrous (Fe^{3+}) ions by accepting and donating electrons quite readily, which makes it a useful component for cytochromes, oxygen-binding molecules (hemoglobin and myoglobin), and many enzymes [99]. Fe has a high radial strength because of its higher elastic modulus, which can be helpful in making stents with thinner struts. Iron also has high ductility which can be helpful during the implantation of stents when the stent is plastically deformed [90]. Armco® iron (Fe > 99.8%) is the first biodegradable metal that has been utilized as a biodegradable metallic stent in 2001 [113]. In the *in vivo* degradation study of a pure Fe stent in the native descending aorta of New Zealand white rabbits and the tail of mice for prolonged times (> 6 months), no significant neointimal proliferation, pronounced inflammatory response, or systemic toxicity based on organ examination were observed. Further, the degradation product of Fe is metabolically inactive and can accumulate in diverse organs of the body [113, 114, 100].

However, pure Fe degrades very slowly *in vivo*; the Armco® iron stent did not corrode compeletely after a prolonged time (> 18 months) [113, 114]. Therefore, to

increase the corrosion rate of Fe-based stents, means of physical design modification including increasing the surface area of the stent and reducing the strut thickness of the stent [113, 114], microstructure modification [98, 106], and alloying Fe with other elements including manganese (Mn), palladium (Pd), cobalt (Co) and aluminum (Al) [54, 128, 84] are proposed and investigated showing positive results.

2.2.2 Magnesium (Mg) and alloy

Mg is another attractive metal for biodegradable implants because of its low density, low thrombogenicity, and well-known biocompatibility [90]. However, pure Mg degrades too rapidly at physiological pH (7.4 7.6) and in the high chloride environment of the physiological system: it loses mechanical integrity before the tissue heals sufficiently. Further, the rate of production of hydrogen gas (a degradation product) during the corrosion process can be too rapid for the host tissue to tolerate [132]. Therefore, Mg-based implants are usually utilized in the alloy form to reduce the degradation rate as well as increase the mechanical integrity. The studied alloy elements include zinc (Zn), aluminum (Al), manganese (Mn), calcium (Ca), and rare earth elements (neodymium (Nd), cerium (Ce), dysprosium (Dy)). Positive *in vitro* results have been reported with a total degradation time around one to six months [132, 159]. Biodegradable polymeric layers including PLGA and PLLA are also applied to the surface of Mg alloy stents to further control the degradation rate [149, 68]. Generally, magnesium alloys have lower Young's modulus and faster degradation than iron-based alloys [90]. Implantations of Mg-based metal stents in humans have been performed in the left pulmonary artery of a preterm baby with a congenital heart disease and in the coronary arteries of 63 patients. The stents degraded within approximately 4 to 5 months, showing no major in-stent obstruction or neointimal hypertrophy [164, 28].

2.2.3 Zinc (Zn) and Alloys

From a biological point of view, Zn is also an essential element for basic biological function that is involved in various aspects of cellular metabolism [50], and also exhibits strong antiatherogenic properties [52]. The recommended dietary allowance (RDA) and recommended upper limit for Zn are 15 and 40 mg/day, respectively; however, Zn consumption in amounts higher than these values is generally considered relatively non-toxic, and amounts approaching 100 mg/day can be tolerated for some time [36].

Compared to Fe and Mg, the application of Zn and Zn alloys as biodegradable metals is relatively new. Zn-Mg alloys with Mg concentration ranging from 1 to 3 wt% have been investigated in vitro for bone fixation applications. Zn-Mg alloys show good mechanical properties comparable with that of bone, as well as better corrosion resistance and low rate of pH value increase and hydrogen evolution during in vitro degradation compared with Mg alloys. The quantity of zinc ions released from the implants is negligible compared with RDA and recommended upper limits for Zn [147]. Patrick *et al.* utilized Zn wires as biodegradable cardiac stent materials and tested them in the abdominal aorta of rats for 6 months, and demonstrated that though the mechanical property of pure Zn is not sufficient for the application of stents, it shows favorable degradation behavior: *in vivo* longevity comparable to Fe with the harmless bioresponse comparable to Mg [13]. The results of those preliminary research strongly support the utilization of Zn and its alloys as biodegradable metals.

2.3 Literature Review of Biodegradable Sensors

Up to now, a number of researchers have proposed approaches to implantable biodegradable sensor; however, no fully functional completely biodegradable sensor has been reported.

(1) Implantable Strain Sensor Utilizing Ultrasound Read-out [145]

The concept of a wireless implantable strain sensors that utilizes an external ultrasound read-out system for the in-situ measurement of small strains on implants, bones or fixation systems was proposed by Umbrecht *et al.* . The schematic working principle of this sensor together with a demonstrator sensor unit are shown in Figure 9. A compressible fluid reservoir filled with incompressible liquid is attached to a microchannel. Due to the high ratio between the diameter of the reservoir and the diameter of the microchannel, an amplified filling level change can be introduced by a small load applied to the reservoir. A external ultrasound imaging technology can be utilized to read out the filling level. The demonstrator sensor unit is made of biocompatible polymer poly(methyl methacrylate) (PMMA), and they proposed that the whole sensor could be biodegradable if using solely bioresorbable polymers such as PCL and Degrapol®. The Degrapol® is a polyester-urethane and is made from two polyester diols linked through a diisocynate unit. P(HB-co-CL) (poly3-(R-hydroxybutirrate)-co-(β-caprolactone)-diol) is the crystalline domain (hard segment), while the amorphous domain (soft Segment) consist of poly(β-caprolactone-co-glycolide)-diol. But the fact that this system requires ultra-sound reading could be limiting compared to RF readout.

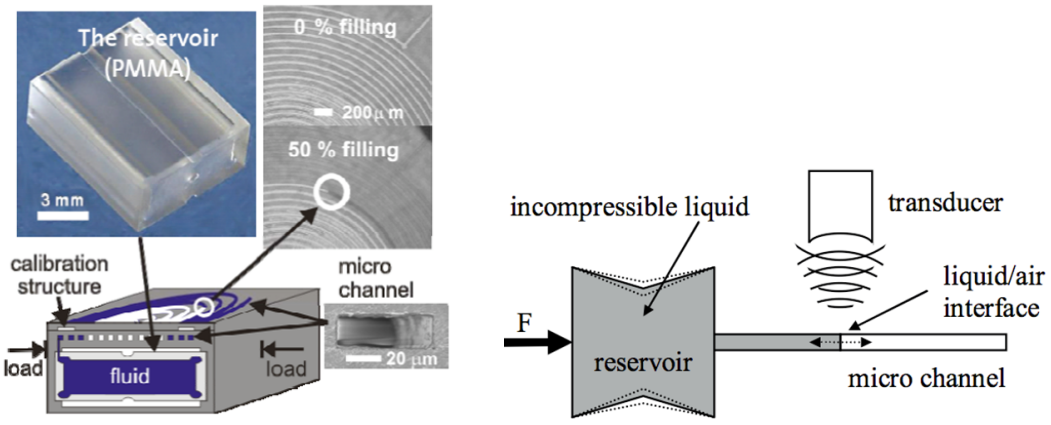

(a) (b)

Figure 9: A wireless strain sensor that utilizing an external ultrasound read-out system (a) schematic of the sensor principle, and (b) a demonstrator sensor unit(cross-cut) fabricated from poly(methyl methacrylate) (PMMA).

(2) Implantable Biodegradable Stimulator [31]

Implantable biodegradable stimulators that exploit RF coupling have been proposed as an approach to promote bone growth. The resistor-inductor-capacitor (RLC) circuit was fabricated using conventional micromilling of biodegradable magnesium alloy sheets with thickness of 0.01 inch, and packaged with 70:30 poly L: D/L-lactide (PDLA) by lamination, as shown in Figure 10. In future work, they proposed to utilize biodegradable ZnO-based transistors or an ultraminiature, non-degradable IC which would have minimal impact in vivo as the RF rectifier and constant current source. The ultimate stimulator is expected to provide a constant current of 60 μA, while sustaining a serviceable life *in vivo* sufficient for the duration of spinal fusion (about 24 weeks).

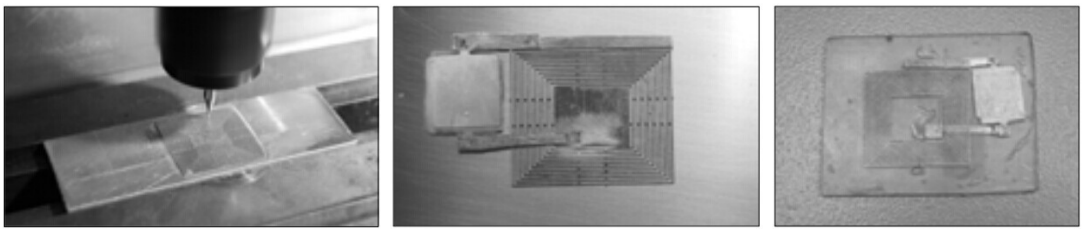

(a) (b) (c)

Figure 10: An implantable biodegradable stimulator prototype (a) micromilling of coil, (b) assembled coil and capacitor, and (c) RF circuit embedded in PDLA

(3) Miniaturized RLC Resonators [12, 11]

Miniaturized RLC resonators with sizes of approximately 10-17 mm were fabricated using biodegradable materials and proposed as an RF component of wireless biosensors; some examples are shown in Figure 11. The metal resonators made of Mg, Fe, Mg- and Fe-alloys were fabricated by electric discharge machining (EDM) from 3 mm thick plates. The polymer resonators were made of PLLA-PPy (polypyrrole) and PCL-PPy polymer composites by compression molding and laser cutting. The polymer composites are prepared by emulsion polymerization of conductive pyrrole

nanoparticles in the matrix of PLLA or PCL followed by precipitation. Unloaded resonant frequency ($f_{unloaded}$) and quality factor ($Q_{unloaded}$) were measured to be 0.5-1 GHz and 8-410 for the metal resonators, and 2.0-3.4 GHz and 6-19 for the polymer resonators, respectively. The proposed fully biodegradable sensor sensor is shown in Figure 12, by attaching this RLC resonator with a sensing layer on the surface that is sensitive to a stimulus (e.g. the permittivity varying with glucose level) , a shift and/or a damping of the resonant frequency (f_0) can be detected wirelessly by an external coil inductively coupled to the resonator.

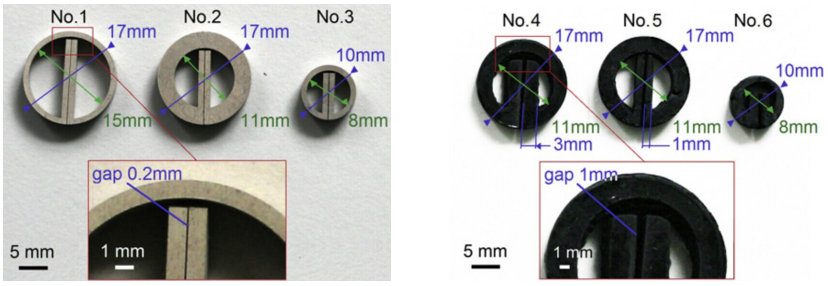

(a) (b)

Figure 11: *RLC* resonators made of (a) biodegradable metal (Fe), and (b) biodegradable polymer composite(PCL-PPy)

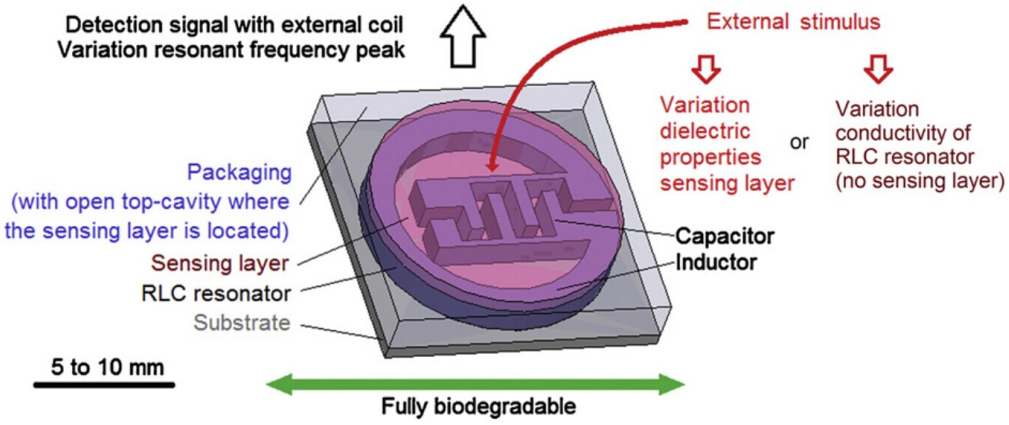

Figure 12: Concept of a fully biodegradable sensor based on an RLC resonator(short-range wireless telemetry with inductive link)

(4) Water Soluble Electronics [60]

Recently, "transient electronics" made of water soluble electronic elements including a resistor, inductor, capacitor, transistor and diode on water soluble silk was demonstrated Figure 13. Thin layers of conductive Mg, dielectric magnesium oxide (MgO) and silicon dioxide (SiO_2) are fabricated by physical vapor deposition. Monocrystalline silicon nanomembranes (Si NMs) as semiconductors were fabricated by transfer printing. The whole structure was demonstrated to be dissolved in DI water within 10 minutes, shown in Figure 14. The transience times for NM-based electronic components can be increased, in controlled amounts, by adding transient encapsulating layers and packaging materials (silk), or reduced by decreasing the critical dimensions or by physically structuring the materials in a way that accelerates dissolution by disintegration. A resonant frequency of 1.8 GHz and initial quality factor of approximately 7 was obtained for an implanted transient RF material structure. The solubility of silk is also programmed, over several orders of magnitude, through the control of crystallinity [58]. Inductive coils of Mg combined with resistive microheaters of doped Si NMs, integrated in silk packages, that provide transient thermal therapy to control surgical site infections was also demonstrated in vivo under the skin of a Sprague-Dawley rat. A localized increase temperature of approximately 5 °C was observed, and device has functional time scale of 15 days.

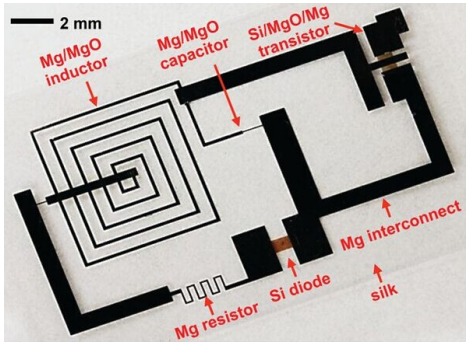

Figure 13: Image of water soluble electronics including transistors, diodes, inductors, capacitors, and resistors, with interconnects and interlayer dielectrics, all on a thin silk substrate.

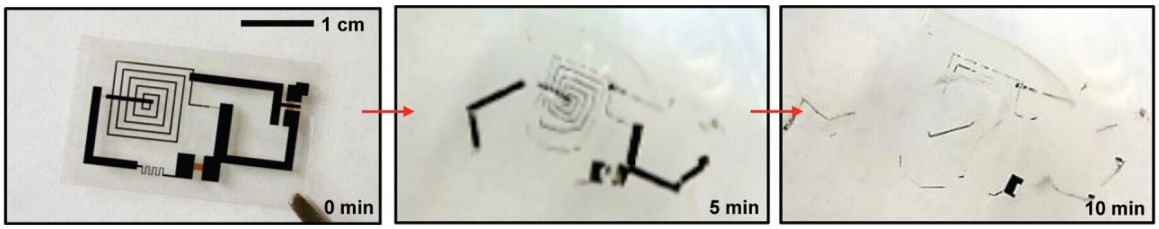

Figure 14: Images showing the time sequence of dissolution the water soluble electronics in DI water

CHAPTER III

BIODEGRADABLE PRESSURE SENSOR DESIGN AND MODELING

3.1 Research Objectives and Sensor Concept

The research objectives for designing and studying the completely biodegradable wireless pressure sensor in this work are summarized below:

- Implement passive LC resonant circuits for wireless telemetry.
- Develop compact-structure design(s) with sensor total area less than 1.5 cm^2.
- Achieve fabrication of the device using completely biocampatible and biodegradable materials.
- Design sensors with resonant frequencies ranging from 20 to 60 MHz and reasonable sensitivity.
- Design sensors with quality factor high enough to achieve wireless testing at distance of at least 3 mm.
- Develop reliable microfabrication processes that avoid any non-biocampatible contamination or residues.
- Design sensors with different degradation life times.
- Demonstrate device functionality and degradation *in vitro*.

In this work, a very compact and simple design of a passive wireless pressure sensor is adopted. This sensor concept is first proposed by Collins in 1967 for intraocular and other physiological pressures measurements [22]. It utilized the self- and mutual inductance and associated distributed capacitance of a pair of spaced apart planar

spiral coils to form a resonant LC circuit, and magnetic coupling with an external loop to realize the wireless telemetry of the pressure-modulated frequency. Though the miniature device was not completely successful due to the limitations of micro-fabrication techniques of the time, many successfully microfabricated RF pressure sensors have been developed using the same mechanism since then [126, 35, 2].

The general concept of such passive pressure sensors is schematically illustrated in Figure 15. The pressure sensor consists of a sensing cavity, which is bounded by two metal plates forming the variable capacitor and interconnected with planar spiral inductor(s). All the conductors (inductors, capacitors, and electrical via) are integrated and embedded into a dielectric package. The inductor coil not only acts as an essential component of the resonant sensor, but also provides means for magnetic coupling the sensor to an external (e.g., outside the body) coil. When pressure is applied to the sensor, the gap between the two capacitive electrodes is reduced and the capacitor value increases. The resulting pressure induced change in the LC resonant frequency can be measured wirelessly using an external coil.

The inductor and the capacitor can be either connected with a conducting via Figure 15(a), or be capacitively and inductively coupled without a conducting via Figure 15(b). In the sensor with conducting via, a single planar spiral inductor is

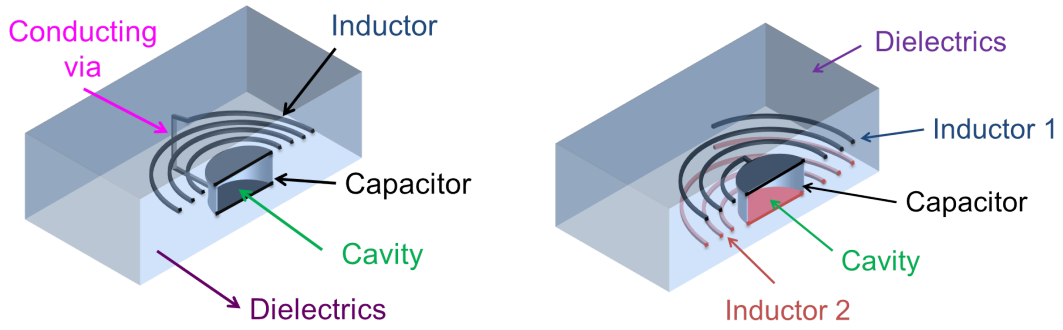

(a) (b)

Figure 15: Passive LC resonating pressure sensor concept (a) with conducting via, and (b) without conducting via

conductively connected to the capacitor by means of a vertical via trace. For the sensor without conducting via, two parallel planar inductors are each connected with a corresponding central capacitor plate, and the circuit is completed by exploiting the parasitic capacitances and mutual inductances between the layers.

In the following sections, the electromagnetic model of the LC resonant circuit is discussed. The mechanical theory is also presented for a circular plate in order to develop a mechanical deflection model. In addition, the materials selection for the biodegradable sensor is presented. Finally, the geometric design of the sensor as well as the simulation result combines the deflection with the capacitance change under applied pressure using COMSOL is demonstrated to help in predicting the sensor sensitivity.

3.2 Sensor Electromagnetic theory

To further understand the electromagnetic behavior of the sensor and its interaction with the external loop coil, both analytical and finite element models are used to help design the geometry of the device as well as predict the device behavior as it relates to the readout telemetry.

3.2.1 Sensor Analytical Modeling

3.2.1.1 Inductance of Planar Spiral Inductors

The single planar spiral inductor can be analyzed by a π equivalent circuit with series inductance L_{ss}, series resistance R_{ss}, and parasitic capacitance C_{par}, shown in Figure 16. C_{par} is the parasitic winding-to-winding capacitance. The substrate impedance is neglected.

The planar spiral impedance accordingly is:

$$Z_{spiral} = \frac{R_{ss} + j[L_s\omega - C_{par}R_{ss}^2\omega - C_{par}L_{ss}^2\omega^3]}{1 - 2C_{par}L_{ss}\omega^2 + (C_{par}L_{ss})^2\omega^4}, \quad (1)$$

The self-resonance of the planar spiral and quality factor can be calculated from

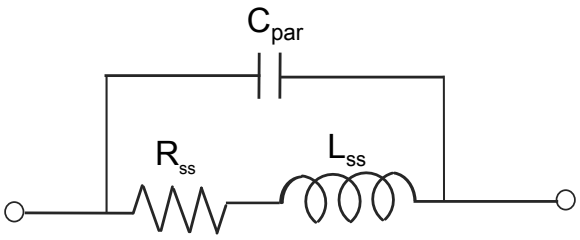

Figure 16: Schematic illustration of cross-sectional view of the deflectable region of the biodegradable pressure sensor

Eq. (1) as:

$$f_{0\ Spiral} = \frac{1}{2\pi\sqrt{L_{ss}C_{par}}}\sqrt{1 - \frac{C_{par}R_{ss}^2}{L_{ss}}} \tag{2}$$

and

$$Q_{spiral} = \frac{I_m[Z_{spiral}]}{R_e[Z_{spiral}]} = \frac{\omega L_{ss}}{R_{ss}}\left[1 - \frac{C_{par}R_{ss}^2}{L_{ss}} - C_{par}L_{ss}\omega^2\right]. \tag{3}$$

Many approaches have been developed in the literature to calculate the inductance of planar spirals [155, 162, 123, 97]. Among them, the current sheet approximation deduced from [97] is utilized in this work to predict the inductance. This approach has been utilized to calculate the inductance of planar spiral inductors with of square, hexagonal, octagonal and circular shapes. Only the result of the circular shape, which is the same as the inductor of this work, is presented below.

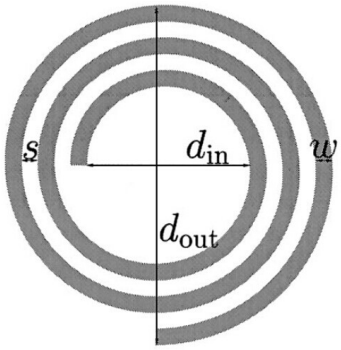

Figure 17: Schematic illustration of circular planar spiral inductor

As shown in Figure 17, a single layer planar spiral inductor with circular shape can be completely specified by the line weidth w, line spacing s, the number of turns n together with either the inner diameter d_{in} or the outer diameter d_{out}. The average

diameter d_{avg} is defined as:

$$d_{avg} = \frac{d_{in} + d_{out}}{2}, \tag{4}$$

and the fill ratio ρ which indicates how 'hollow' the inductor is can be expressed as:

$$\rho = \frac{d_{in} - d_{out}}{d_{in} + d_{out}}. \tag{5}$$

In the current sheet approximation, the inductance of the planar spiral is obtained by approximating the sides of the spirals by symmetrical current sheets of equivalent current densities. By evaluating the self and mutual inductances using the concepts of geometric mean distance (GMD), arithmetic mean distance (AMD), and arithmetic mean square distance (AMSD), the inductance is given by:

$$L_{ss} = \frac{\mu n^2 d_{avg} C_1}{2} \left[ln\frac{C_2}{\rho} + C_3\rho + C_4\rho^2 \right], \tag{6}$$

where μ is the material permeability, and C_i are the layout dependent coefficients. For the circular planar spiral, $C_1 = 1.00$, $C_2 = 2.46$, $C_3 = 0.00$, and $C_4 = 0.20$.

The frequency-dependent inductance of the planar spiral circuit in Figure 17 is calculated from [130] as:

$$L_{eq}(f) = \frac{L_{ss}}{1 - L_{ss}C_{par}(2\pi f)^2}, \tag{7}$$

where C_{par} is the inductor parasitic self-capacitance. The entire parasitic capacitance of a planar spiral consists the capacitance between the lines (parasitic self-capacitance) and the capacitance between the lines and substrates/environment [105, 64]. Parasitic self-capacitance is very complex to analytically calculate because of its distributed nature, and is sometimes neglected in the literature due to its much smaller value compared to substrate loss for inductors built on silicon [163, 105]. The simplified simulated result from [33] is adopted here due to design similarity with that work. The result is presented below.

By modeling the capacitance for several structures of interest using FastCap and a curve fitting approach, the parasitic self-capacitance of a planar spiral inductor on

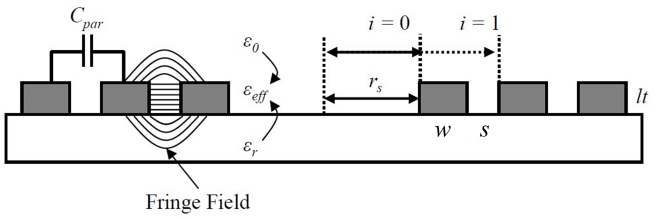

Figure 18: Geometry used to estimate the the parasitic self-capacitance of a planar spiral inductor in [33].

a substrate (shown in Figure 18) exhibits independence of the thickness of the line l_t for $l_t < 80\mu$m, and when the total length of the lines is more than 3 mm. The parasitic self-capacitance can be calculated roughly as:

$$C_{par} = \epsilon_0 \epsilon_{eff} ll_{eff} \frac{1}{n^K}, \tag{8}$$

where ϵ_0 is the vacuum permittivity, ϵ_{eff} is the effective relative permittivity, n is the number of turns, K is a fitting variable, which is a function of the starting radius r_s, pitch p_s (the total width of one line and one space, $w + s$), and total effective length ll_{eff}, which is defined as:

$$ll_{eff} = ll - \frac{ll_1 + ll_n}{8}, \tag{9}$$

where ll is the total length of the inductor, ll_1 and ll_n are the lengths of the first and last turn of the inductor. The reason ll_1 and ll_n are partially subtracted from the effective length is due to the fact that the first and last turn do not contribute much to the parasitic self-capacitance. K can be found using curve fitting. Although Eq. (8) has no real physical meaning, it can be utilized to predict the C_{par} of a planar inductor. Since C_{par} is generally very small compared to the capacitance of the capacitor, it will not affect the modeling result that is utilized for the geometric design.

3.2.1.2 Capacitance of the Sensor

(1) Capacitance of Parallel Plate Capacitor

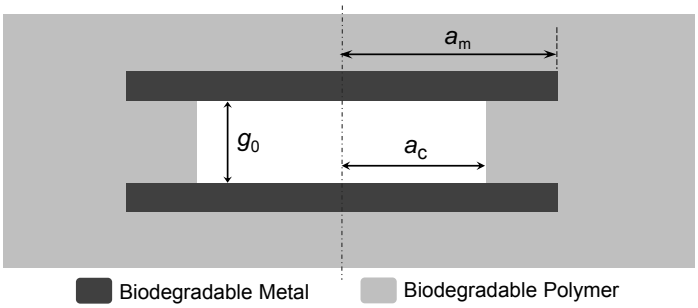

Figure 19: Schematic illustration of cross-sectional view of the capacitor in the biodegradable pressure sensor

The cross-sectional view of the capacitor that is embedded inside the dielectrics is shown in Figure 19. The two capacitor plates are separated by a cavity in the center and biodegradable polymer spacer on the edge. The capacitance of the circular parallel plate capacitor can be simply calculated by:

$$C_{plate} = C_{cavity} + C_{spacer} = \frac{\epsilon_0 \pi a_c^2}{g_0} + \frac{\epsilon_0 \epsilon_p \pi (a_m^2 - a_c^2)}{g_0}, \tag{10}$$

where ϵ_0 is the vacuum permittivity (8.854 pF/m), ϵ_p is the relative permittivity (dielectric constant) of the polymer spacer, g_0 is the distance between the two metal plates, and a_c and a_m are the radius of the cavity and capacitor plate, respectively.

(2) Overlap Capacitance of Two Planar Spiral Inductors

In the case of the sensor without conducting via (Figure 15(b)), two planar spiral inductors overlap with each other and result in overlap capacitance C_{ove}. C_{ove} can be calculated using parallel plate theory as:

$$C_{plate} = \frac{\epsilon_0 \epsilon_p \pi A_{ove}}{g_0}, \tag{11}$$

where A_{ove} is the overlap area between two planar spirals. Counter rotation of the two spirals is required for constructive mutual coupling of the sensor. For perfectly aligned overlapping inductors, the A_{ove} has been deduced in [33], the value can be approximately calculated as:

$$A_{ove} = 0.45 \cdot w \cdot ll, \tag{12}$$

where w is the line width and ll is the total spiral length for inductors with more than 8 turns.

3.2.2 Sensor Lumped Element Model

3.2.2.1 Generalized Sensor Circuit Model

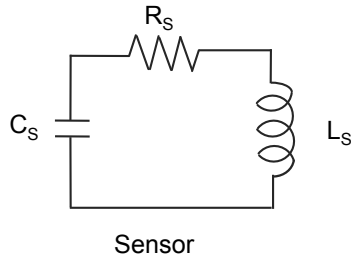

Figure 20: Electromagnetic lumped element model for an generalized LC resonant circuit

The lumped element model of a generalized sensor circuit that includes a series inductance L_S, series capacitance C_S and a series resistance R_S is shown in Figure 20. The resonant frequency of the sensor circuit is given by:

$$f_0 = \frac{1}{2\pi\sqrt{L_S C_S}} \tag{13}$$

and the quality factor Q is [129]

$$Q = \frac{1}{2\pi f_0 \sqrt{L_S C_S}}. \tag{14}$$

When the sensor is magnetically coupled to an external coil, the resonance frequency of the sensor can be detected wirelessly. The sensor resonance and its coupling to an external coil is modeled from a two-port network using transformer theory, as shown in Figure 21 [133].

Analysis of the circuit in Figure 21 using transformer network theory and Kirchhoffs voltage law, phase notation ($s = j\omega = j2\pi f_0$), yields the loop equations

$$V_1(s) = sL_E I_1 + sL_C I_2 \tag{15}$$

$$V_2(s) = sL_C I_1 + sL_S I_2 \tag{16}$$

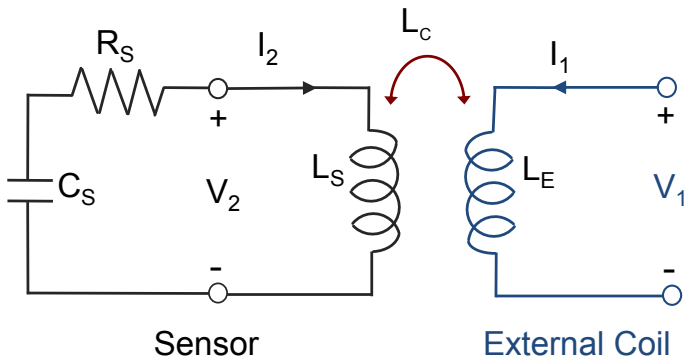

Figure 21: Lumped element model for an inductively coupled system containing a loop coil and LC resonant circuit

and

$$-R_S I_2 - V_2 - \frac{1}{sC_S} I_2 = 0. \tag{17}$$

where V_1, V_2, I_1 and I_1 are the transformer voltages and currents, respectively.

By defining the coupling coefficient k between the sensor and the external coil, which is proportional to the mutual inductance L_C and given by:

$$k = \frac{L_C}{\sqrt{L_S L_E}}, \tag{18}$$

and substituting f_0 from Eq. (13) and Q from Eq. (14), the input impedance Z_1 looking into the external coil is given by: [33]

$$Z_1 = \frac{V_1}{I_1} = j2\pi f L_e \left[1 + k^2 \frac{\left(\frac{f}{f_0}\right)^2}{1 - \left(\frac{f}{f_0}\right)^2 + \frac{j}{Q}\left(\frac{f}{f_0}\right)} \right]. \tag{19}$$

In Eq. (53), the the resonance frequency f_0, quality factor Q, and coupling coefficient k are related to the impedance of the external coil Z_1, which can be expressed in terms of its measured impedance magnitude and phase [33]. The general impedance for a circuit is defined as:

$$Z = R + jX \tag{20}$$

where R is the real part of the impedance and X is the imaginary part, defined as

$$R_e(Z) = R = |Z| cos\theta \tag{21}$$

and

$$I_m(Z) = X = |Z| sin\theta. \tag{22}$$

The magnitude and phase of the impedance Z are defined as:

$$|Z| = \sqrt{(R_e(Z))^2 + (I_m(Z))^2} \tag{23}$$

and

$$\angle Z = arctan\left[\frac{I_m(Z)}{R_e(Z)}\right] \tag{24}$$

Therefore, by separating the real part and imaginary part of the impedance Z_1 in Eq. (53) and substituting into Eq. (23) and Eq. (24), and defining $\Omega = f/f_0$, the magnitude and phase of impedance Z_1 are given by:

$$|Z_1| = \sqrt{\left[2\pi f L_E\left(1 + \frac{k^2Q^2\Omega^2(1-\Omega^2)}{Q^2(1-\Omega^2)^2 + \Omega^2}\right)\right]^2 + \left[\frac{2\pi f L_e k^2\Omega^3 Q}{Q^2(1-\Omega^2)^2 + \Omega^2}\right]^2} \tag{25}$$

and

$$\angle Z_1 = arctan\left[\frac{\Omega^2 + Q^2(1-\Omega^2)^2 + K^2\Omega^2Q^2(1-\Omega^2)}{k^2Q\Omega^3}\right]. \tag{26}$$

3.2.2.2 Circuit Model for Sensor with Conducting Via

In the case of the wireless pressure sensor with conducting via to connect the capacitor and single planar inductor shown in Figure 15(a), the equivalent circuit model is shown in Figure 22.

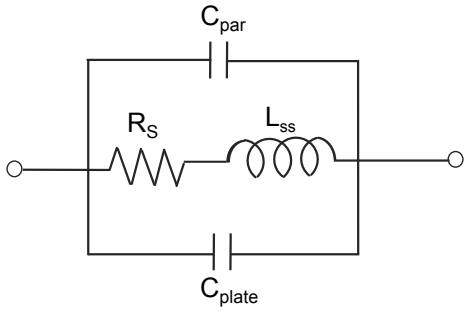

Figure 22: Circuit model for a sensor with conducting via

The sensor includes a series inductance, a series resistance and two parallel capacitances. The inductance L_S and capacitance C_S of the sensor can be calculated as:

$$L_S = L_{ss} \tag{27}$$

and

$$C_S = C_{plate} + C_{par} \tag{28}$$

where L_ss is the inductance of the planar spiral inductor, C_{plate} is the capacitance of the capacitor, and C_{par} is parasitic capacitance of the spiral inductor.

3.2.2.3 Circuit Model for Sensor Without Conducting Via

In the case of wireless pressure sensor with two planar inductors that are capacitively and inductively coupled without conducting via shown in Figure 15(b), the equivalent circuit becomes more complicated (Figure 23).

This circuit is analyzed in [33] by rearranging the circuit to a equivalent circuit that splits the two inductors; the analyzed result adopted from [33] is present below.

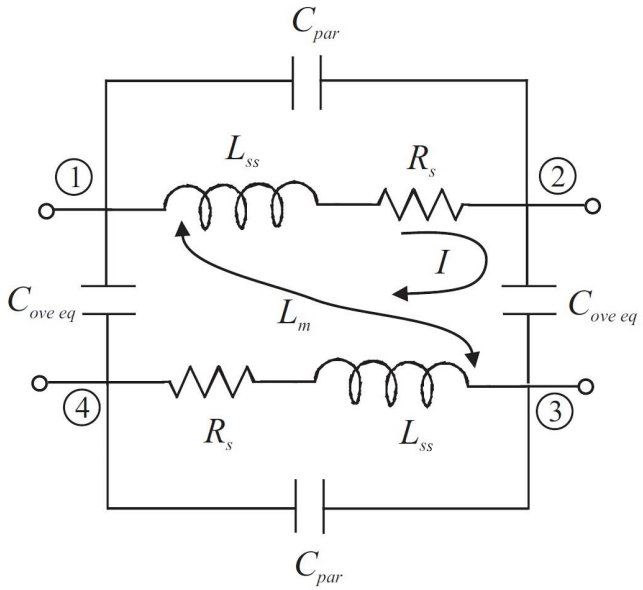

Figure 23: Circuit model for a sensor without conducting via (the two planar spiral inductors that are capacitively and inductively coupled)

The total capacitance C_S and inductance L_S of the sensor are:

$$C_S = \frac{1}{2}(C_{ove} + C_{plate}) + C_{par} + C_{sub} \tag{29}$$

and:

$$L_S = L_{ss}(1 + k_m), \tag{30}$$

where C_{sub} is the substrate and environmental impedance and assumed as an ideal capacitor, and k_m is the coupling coefficient between the two planar spiral inductors. The factor of $\frac{1}{2}$ in Eq. (29) is due to the fact that the total capacitance is split into two separate distributed elements. The impedance of the external coil coupled with this sensor is given by:

$$Z_{1\ nv} = j2\pi f L_e \left[1 + k^2 \left(\frac{2}{1 + k_m} \right) \frac{\left(\frac{f}{f_0} \right)^2}{1 - \left(\frac{f}{f_0} \right)^2 + \frac{j}{Q} \left(\frac{f}{f_0} \right)} \right]. \tag{31}$$

Compared with Eq. (53), the factor of $\frac{2}{1+k_m}$ next to the coupling coefficient between the inductors and the external coil is due to the external coil being coupled to two planar spiral inductors. When the two planar spirals are strongly coupled (effectively almost becoming one single inductor $L_s = L_{ss} + k_m L_{ss}$), the factor $2/(1 + k_m)$ approaches unity as k_m approaches unity. When the two spirals are poorly coupled (the spirals are closer to individual inductors of inductance L_{ss}), the factor approaches 2 as k_m approaches zero.

3.3 Sensor Mechanical theory

In this work, the capacitance change of the sensor is due to the pressure-induced deflection of the two capacitor plates. Therefore, it is essential to understand the deflection of the circular mechanical plates to be able to effectively design and analyze sensor performance.

The simplified schematic cross-sectional view of the deflectable region of the sensor is shown in Figure 24. Both the metal capacitor plates and the polymer package film

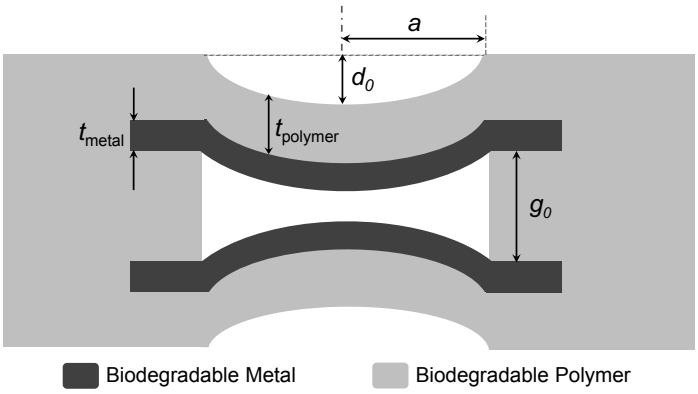

Figure 24: Schematic illustration of cross-sectional view of the deflectable region of the biodegradable pressure sensor

will undergo deflection under applied pressure, with the deflectable radius a and center deflection of d_0. The thicknesses of the polymer and metal plate are $t_{polymer}$ and t_{metal}, respectively. The two plates are separated by a gap of g_0, which also determines the maximum total center deflection of the two plates. The boundary condition can be viewed as clamped at the edge if the metal and the polymer are perfectly laminated.

3.3.1 Plate Flexural Rigidity

The flexural rigidity defines the bending stiffness of a plate when a mechanical load is applied. For the case of a single plate with one uniform material, the flexural rigidity is given by:

$$D = \frac{Et_m^3}{12(1-\nu^2)} \tag{32}$$

where E is the Young's modulus, ν is the Poisson's ratio and t_m is the thickness of the plate. For a plate consisting of multiple layers, as shown in Figure 25, the analytical equations of the effective flexural rigidity D_n and effective total thickness h_n for a plate with n layers were derived in [59], presented below for reference. The bottom surface of layer 1 is located at start point of the z - axis ($z = 0$), the interface between layer i and $i+1$ is located at h_i, and the top surface of layer n is located at

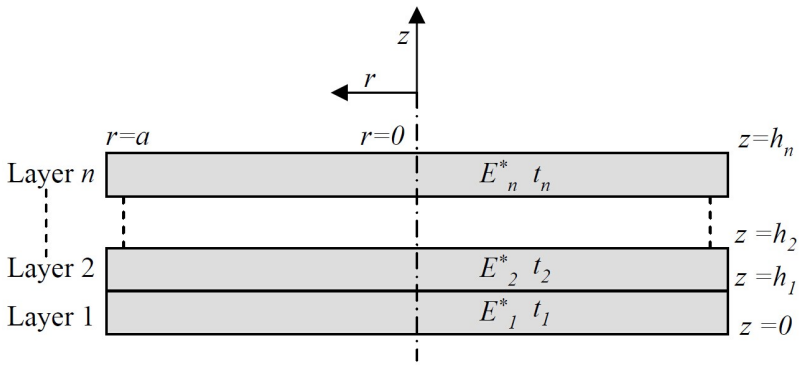

Figure 25: Schematic illustration of a multilayered plate (cross-section)

$z = h_n$. The relation between h_n and the thickness of i^{th} layer t_i can be described by:

$$h_i = \sum_{j=1}^{i} t_j, \tag{33}$$

where i=1-n for Eq. (33). z_n is defined as the neutral surface for bending

$$z_n = \frac{\sum_{i=1}^{n} E_i^* t_i \left(h_{i-1} + \frac{t_i}{2}\right)}{\sum_{i=1}^{n} E_i^* t_i}, \tag{34}$$

where E_i^* is the plane-strain modulus redefined as:

$$E_i^* = \frac{E_i}{1 - \nu_i^2}. \tag{35}$$

The flexural rigidity of the multilayered plate D_n is given by

$$D_n = \sum_{i=1}^{n} E_i^* t_i \left[h_{i-1}^2 + h_{i-1} t_i + \frac{t_i^2}{3} - \left(h_{i-1} + \frac{t_i}{/} 2 \right) z_n \right]. \tag{36}$$

For a monolayered plate with uniform material properties, Eq. (35) and Eq. (36) can be simplified to:

$$z_n = \frac{h_n}{2} \tag{37}$$

and

$$D_n = \frac{E^* t_n^3}{12}. \tag{38}$$

In this way, Eq. (36) is equivalent to Eq. (32).

Two special cases of interest for the effective flexural rigidity are n = 2 and n = 3. For a bilayer plate (n=2),Eq. (34) and Eq. (36) can be simplified to:

$$z_n = \frac{E_1^* t_1^2 + E_2^* t_2 (2t_1 + t_2)}{2(E_1^* t_1 + E_2^* t_2)} \tag{39}$$

and

$$D_n = E_1^* t_1^2 \left(\frac{t_1}{3} - \frac{z_n}{2} \right) + E_2^* t_2 \left[t_1^2 + t_1 t_2 + \frac{t_2^2}{3} - \left(t_1 + \frac{t_2}{2} \right) z_n \right]. \tag{40}$$

When $t_1 \gg t_2$ (e.g. a thin film/thick substrate system), Eq. (39) and Eq. (40) can be simplified to:

$$z_n = \frac{t_1}{2} + \frac{E_2^* t_2}{2E_1^*} \tag{41}$$

and

$$D_n = \frac{E_1^* t_1^3}{12} + \frac{E_2^* t_1^2 t_2}{4}. \tag{42}$$

Eq. (42) can be used to determine the modulus of the thin film E_2^* by measuring the difference between the flexural rigidity between the substrate and the film/substrate system.

For a trilayer plate (n=3), Eq. (34) and Eq. (36) can be simplified to:

$$z_n = \frac{E_1^* t_1^2 + E_2^* t_2 (2t_1 + t_2) + E_3^* t_3 (2t_1 + 2t_2 + t3)}{2(E_1^* t_1 + E_2^* t_2 + E_3^* t_3)} \tag{43}$$

and

$$\begin{aligned} D_n = E_1^* t_1^2 \left(\frac{t_1}{3} - \frac{z_n}{2} \right) + E_2^* t_2 \left[t_1^2 + t_1 t_2 + \frac{t_2^2}{3} - \left(t_1 + \frac{t_2}{2} \right) z_n \right] \\ + E_3^* t_3 \left[t_1^2 + t_2^2 + t_1 t_3 + t_2 t_3 + \frac{t_3^2}{3} - \left(t_1 + t_2 + \frac{t_3}{2} \right) z_n \right]. \end{aligned} \tag{44}$$

3.3.2 Circular Plate Theory

The deflection of a circular plate with clamped edges under a uniform vertical (i.e., lateral) load is schematically shown in Figure 26. By using cylindrical coordinates along the center of the plate, the deflection of the circular plate at radial axis position r is: [138]

$$d(r) = d_0 \left(1 - \frac{r^2}{a^2} \right)^2, \tag{45}$$

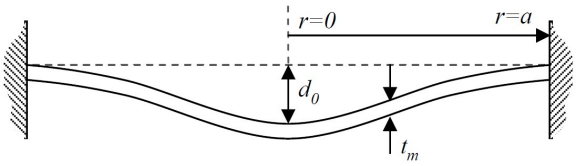

Figure 26: Schematic illustration of the cross-sectional view of a circular plate with clamped edges

where d_0 is the center (also the maximum) deflection. By using the energy method, an approximate expression for the center deflection of a thin plate under a uniform load is derived and given by: [138]

$$d_0 = \frac{Pa^4}{64D} \frac{1}{1 + 0.488 \left(\frac{d_0}{t_m}\right)^2}, \tag{46}$$

where P is the uniformly applied pressure, t_m is the plate thickness and D is the flexural rigidity. In Eq. (46), both bending and stretching of the plate is included. The last term in the Eq. (46) represents the stretching effect of the middle surface of the deflection. When the deflection is small compared to the plate thickness ($d_0 \ll t_m$), the stretching factor can be neglected, and Eq. (46) can be simplified to:

$$d_0 = \frac{Pa^4}{64D}. \tag{47}$$

Alternatively, if the deflection becomes large compared to the plate thickness ($d_0 \gg t_m$), Eq. (46) can be simplified to:

$$d_0 = 0.622a \sqrt[3]{\frac{Pa}{Et_m}}. \tag{48}$$

3.4 Biodegradable Materials Selection

From the point of view of the degradation lifetime, two kinds of sensors are proposed in this pioneer work of completely biodegradable wireless sensors: a slowly degrading sensor which is expected to degrade completely within 1-2 years, and a rapidly degrading sensor which is expected to degrade within 1-2 months. The degradation lifetime of sensors will obviously depend on the materials that are utilized.

3.4.1 Biodegradable Conductors

For sensing applications, especially for microfabricated devices, electrical performance as well as the fabrication facility of the metal are both important factors to consider when choosing biodegradable metal candidates.

3.4.1.1 Galvanic Corrosion

When two dissimilar metals are electrically connected and immersed in electrolyte, the more electrochemically "active" metal will corrode preferably to the other metal due to the electrode potential difference. This phenomenon is termed galvanic corrosion; the more active metal that corrodes is the galvanic anode or sacrificial anode, and the metal under protection is the cathode [109].

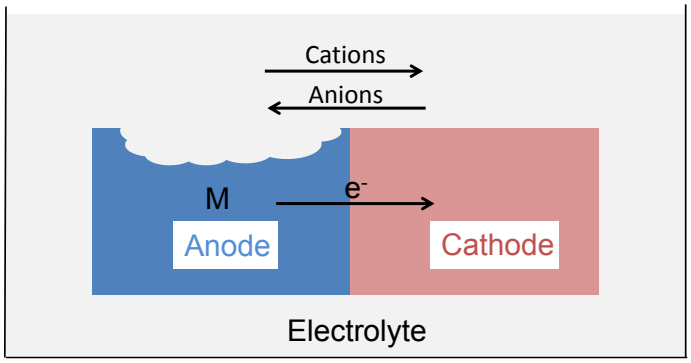

Figure 27: Galvanic corrosion electrochemical process with oxygen reduction on cathode

As shown in Figure 27, the anodic reaction is the metal dissolution:

$$M \rightarrow M^{n+} + ne^{-} \tag{49}$$

and the cathodic reaction is mainly either oxygen reduction (Eq. (50)), or hydrogen evolution (Eq. (51)), or a combination of both.

$$2H^{+} + 2e^{-} \rightarrow H_2 \tag{50}$$

$$O_2 + 2H_2O + 4e^{-} \rightarrow 4OH^{-} \tag{51}$$

The electrolytes, either liquid or solids, are ionically conductive. The electrons given up by the metal ions at the anodic site are carried to the cathodic site by the metallic conductor. For a given metallic couple, the factors that affect galvanic corrosion include: [165]:

- **Geometric factors:**

  area, distance, position, shape, orientation;

- **Electrolyte properties:**

  ionic species, pH, conductivity, temperature, volume, flow rate;

- **Surface condition of the metal:**

  surface treatment, passive film, corrosion product;

- **Environment effects:**

  forms of moisture, cyclic wet/dry, solar radiation, climate, seasonal variations.

Galvanic corrosion can obviously be utilized as a galvanic cell. In industry applications, sacrificial anodes have been used to protect metallic structures (e.g. steel water or fuel pipelines and storage tanks, as well as ship and boat hulls) in various environments. On the other hand, galvanic corrosion can also be utilized to accelerate the dissolution of the anode material. The factors that affect the corrosion rate of the galvanic anode in an bimetal couple include anode/cathode area ratio, electrolyte conductivity, temperature, etc.

3.4.1.2 Materials of Conductors

As mentioned in Section 2.2, there are three good candidate biodegradable metals: Mg, Fe, and Zn. Mg and its alloys possess excellent electrical properties, however, reasonable thick films of Mg are challenging to deposit, e.g., through ventional electrodeposition from aqueous solution. Due to its high magnetic permeability, Fe alone cannot be used in RF sensing due to poor AC conductivity. On the other hand, Zn

has good conductivity with bulk resistivity only 3.5 times higher than that of Cu, and can be readily electroplated to a relatively large thickness (more than 50 μm). Therefore, Zn is chosen as the main biodegradable metal of conductors in the sensors.

For the rapidly degrading sensors, a certain quantity of pure Fe is employed together with the Zn to form Zn/Fe-couple conductors. This small amount of Fe can promote accelerated degradation of Zn by galvanic corrosion, and itself degrade once the Zn has completely dissolved. Even though the bulk Fe degrades very slowly *in vivo* [113, 114], by limiting the total volume utilized in the conductors, the entire conductor is expected to exhibit an accelerated degradation. Moreover, the degradation rate of the conductors is expected to be adjustable by changing the area ratio of Zn : Fe exposed to the electrolyte. The detailed degradation rate study of Zn/Fe-couple with different Zn : Fe area ratio is presented in Section 4.2.

3.4.2 Biodegradable Dielectrics

One of the main objectives of this work is to explore the feasibility of fabricating and characterizing completely biodegradable wireless sensors; therefore, only commercialized and FDA approved biodegradable polymers are under consideration here.

Because of its good mechanical property and processability, PLLA is utilized as the main dielectric (package) and thin dielectric layers that enable separation of the two capacitor plates (spacer) for the slowly degrading sensors. After comparing the processability (polymer dissolving time, film casting and film embossing feasibility) and mechanical properties of three samples (M_w = 221 000, 674 000 and 1 465 000) provided, PLLA with inherent viscosity (IV) of 3.8 dL/g (labelled as PL 38, M_w = 674 000) from Purac (Netherlands) is utilized. A small amount of PCL is also utilized as a bonding agent during lamination due to its low melting temperature. PCL with IV of 0.65 - 0.85 dL/g (labelled as B6003-1) is purchased from LACTEL Absorbable Polymer (USA).

For the rapid degradation sensors, a PLGA/PVA "shell-core" bilayer structure is proposed as the package. Among all the commercialized biodegradable polymers, PLGA with 50:50 (DL:PLG) mole ratio exhibits the most rapid degradation rate (complete dissolution within 2 months) [96]. However, PLGA is amorphous with a T_g of 40 - 47 °C. Therefore, it is difficult for PLGA to maintain stable and appropriate mechanical properties at the body temperature of 37 °C. Therefore, PVA is adopted here as the main mechanical support in the sensor package. In this PLGA/PVA bilayer package structure, the PLGA is located outermost, in direct contact with the environment, and performs the functions of defining the degradation time of the sensor as well as protecting the water soluble PVA inside propr to the PLGA dissolution. The PVA is encapsulated inside the sensor and performs the functions of supporting the PLGA and defining the deflection of the polymer membranes before they are dissolved in saline/body fluid.

To obtain the most rapid degradation rate of the sensor, two types of acid-terminated PLGA 50:50 (DL:PLG) with IV of 0.2 dL/g (labelled as PDLG 5002A, $M_w = 17\,000$) and 0.4 dL/g (labelled as PDLG 5004A, $M_w = 44\,000$) that exhibit the most rapid degradation rate on the data sheet (5002A: 0.5-1 month; 5004A: 0.75-1 month) are purchased from Purac (Netherlands). Upon testing, due to its very low molecular weight, PDLG 5002A is very unstable and the cast film is too brittle to handle. On the other hand, PDLG 5004A exhibited excellent processbility and a satisfying degradation rate. Therefore, PDLG 5004A is utilized in the rapid degradation sensor. Based on the solubility of PVA in water shown in Figure 7, to achieve 100% dissolution of PVA under 37 °C ultimately, 87 -89% hydrolyzed PVA with average M_w = 31 - 50kg/mol (Sigma-Aldrich) is utilized in this work.

The summary of the properties of the biodegradable polymers utilized in this study are listed in Table 1. The properties of all the polymers except PVA are obtained from the data sheet provided by the manufacturer. The degradation time refers to

the time period for the polymer to achieve complete mass loss, and it depends on processing method, device geometry, and implantation site.

Table 1: Biodegradable polymers utilized in this work

Sensor Application	**Slow Degrading Sensor**		**Rapid Degrading Sensor**	
Polymers	**PLLA**	**PCL**	**PLGA**	**PVA**
$\mathbf{M}_w$ **(kg/mol)**	674	37	44	31 − 50
$\mathbf{T}_g$ **(°C)**	60 − 65	-65 − -60	42 − 47	85
$\mathbf{T}_m$ **(°C)**	185 − 195	58 − 63	Amorphous	200
$\boldsymbol{E}$ **(GPa)**	3.0 − 3.7	0.2 − 0.4	3.4 − 3.5	3.5
Degradation Time	> 2 years	> 2 years	3 − 4 weeks	Soluble

3.5 Sensor Design and Simulation

Generally speaking, wireless sensors with interlayer conducting vias that connect the upper and lower portions of the sensor conductors exhibit higher quality factor due to reduced energy loss. Therefore, most of the fabrication and characterization in this work is concentrated on sensors with a conducting via. The geometry of the sensors without a conducting via can be found in the end of the sensor fabrication Section 5.2 with two demos.

To meet the size requirement of the sensor, the outer radius of the planar spiral inductor is set to be 0.5 mm. To achieve a sensor resonant frequency f_0 between 20 to 60 MHz and quality factor of more than 20, the dimensions of the planar inductor, the capacitor and the polymer spacer (which defines the dimension of the cavity and distance between the two capacitor plates) are finalized based on the calculation results using the models discussed above, as well as fabrication feasibility considerations. The dimension of the planar inductor and capacitor plates are the same for all the wireless sensors with conducting via, while the thicknesses of both polymer spacer and packages are different to achieve different f_0 and sensitivity. It is

also interesting to learn whether the functional lifetime and/or degradation behavior of the sensor would be affected by the thickness of the polymer package.

To determine the proper thickness range of the polymer package that would implement reasonable sensitivity, the capacitance change (and ultimately the resonant frequency change) of the sensor as a function of applied pressure is simulated by finite element simulations (COMSOL 4.2). The metal electrical interconnects between the inductor and the capacitor plates are not depicted. Electrostatic analysis and solid-mechanical analysis are coupled by adopting moving mesh method. A two-dimensional axisymmetric model was used. The geometry of the simulation was simplified by neglecting the inductor coil and via structures. The properties required for simulation of the polymer and metal are adopted from that of PLLA and Zn, shown in Table 2.

Table 2: Materials properties value for COMSOL simulation

	Polymer (PLLA)	Metal (Zn)
Young's modulus E (Gpa)	3.1	100 [76]
Poisson's ratio ν	0.35 [65]	0.25 [76]
Dielectric constant	3 [104]	-

Three different radii of deflecting diaphragm (cavity radius) and two different polymer diaphragm thicknesses, chosen with fabrication constraints as well as desired

Table 3: Dimensions of the sensor designs for simulation

Design Name	Cavity radius (mm)	Polymer thickness (μm)
$A-200$	1.8	200
$B-200$	2.1	200
$B-400$	2.1	400
$C-200$	2.4	200
$C-400$	2.4	400

performance in mind, were selected for detailed modeling (Table 3). The initial gap between capacitor plates and the thickness of the metal plates are set at 30 μm and 65 μm. The radius of the cavity, which ultimately defines the radius of the deflecting diaphragm, is set smaller than the radius of the capacitor plate (2.5 mm). Applied pressures ranging from 0 to 20 kPa were simulated, and the capacitance (C) and maximum/center deflection (d_0) at each applied pressure is generated by COMSOL simulation. The simulated C and d_0 of design A-200 is shown in Figure 28. As the pressure increases, the center deflection of the plates increases linearly, and the capacitance also increases accordingly.

The normalized simulated capacitance change of all the geometric designs in Table 3 is presented in Figure 29. The capacitance change is determined by both the cavity radius and the polymer thickness. When the polymer thickness is the same, the smaller the radius of the cavity, the smaller the capacitance change (design A-200 $<$ B-200 $<$ C-200). The thinner PLLA sheet exhibits a higher capacitance change than the thicker PLLA sheet for the same cavity radius because of larger deflection (design B-200 $>$ B-400, design C-200 $>$ C-400). The capacitance shows a linear change as a function of applied pressure, due to the relatively small deflection of the plates compared to their thickness, as well as the gap. A maximum $\Delta C/C$ value of

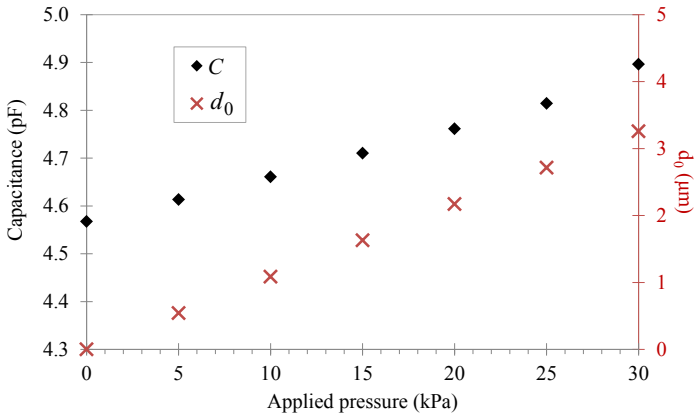

Figure 28: Simulation result of capacitance (C) and maximum/center deflection (d_0) as functions of applied pressure of sensor with design A-200

5.6% is exhibited for the design $C - 200$ under an applied pressure of 20 kPa.

The calculations and simulations presented above provide a toolkit for the design of sensors with specific performance for a variety of application areas. Based on the application areas of interest here (measurement of physiologically-relevant pressures with reasonable pressure sensitivity and small overall sensor size), feasible geometric designs of sensors that meet these requirements for a wireless biodegradable pressure sensor with conducting via are presented in Table 4. The predicted electrical (inductance and capacitance), and overall (initial resonant frequency, predicted sensitivity) performance parameters of the sensors for these selected designs are shown in Table 5. These calculated results will be used as a basis for fabrication, measurement, and comparison with experimental results to be discussed in Chapter 6.

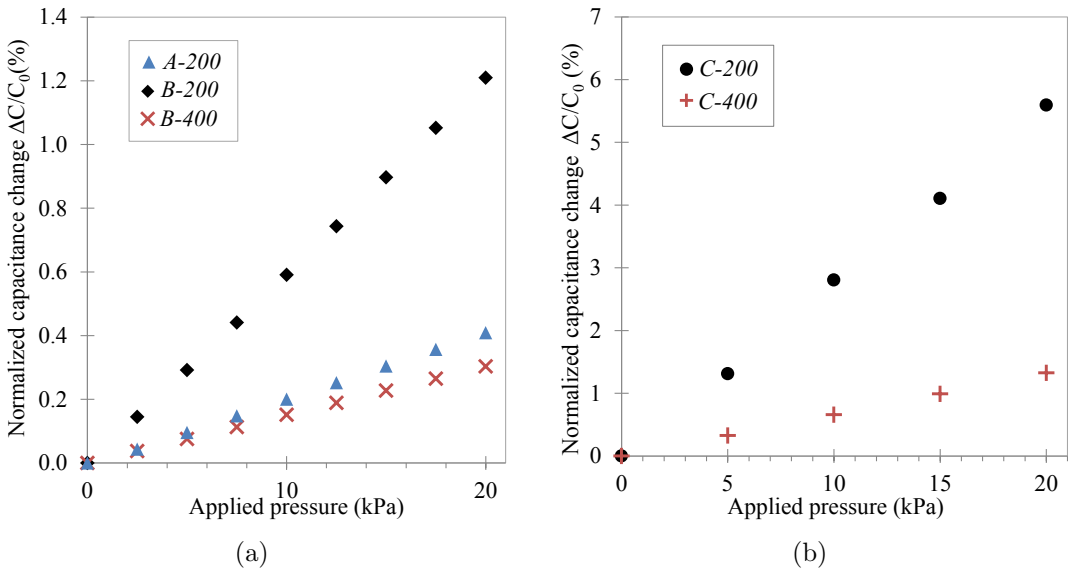

Figure 29: Normalized capacitance change as a function of applied pressure for the simplified sensor structure of different geometric designs in Table 3

Table 4: Design of biodegradable wireless pressure sensor with conducting via

Senor Component	**Parameters**	**value**
Planar Spiral Inductor	Line width (μm)	70
	Line space (μm)	70
	Number of turns	14
	Thickness (μm)	50 - 80
	Starting radius (mm)	2.75
Capacitor	Plate radius (mm)	2.5
	Thickness (μm)	50 - 80
Conducting via	Width (μm)	300
Polymer Spacer	Cavity radius (mm)	2.1
	Thickness (μm)	20 - 40
Polymer Package	Thickness (μm)	150 - 400

Table 5: Calculated sensor functionality of PLLA-based sensors with 65 μm-thickness Zn conductor and different PLLA thickness (T_{PLLA}) and cavity gap thickness (T_{gap})

Calculated Sensor Functionality	T_{gap} = 30 μm T_{PLLA} =130 μm	T_{gap} =30 μm T_{PLLA} =200 μm	T_{gap} = 45 μm T_{PLLA} = 300 μm
Inductance	2 μH	2 μH	2 μH
Total capacitance	10.98 pF	10.98 pF	7.91 pF
f_0 under 0 pressure	34.0 MHz	34.0 MHz	40.0 MHz
Sensitivity (0-25kPa)	-15.3 kHz/kPa	-9.2 kHz/kPa	-2.5 kHz/kPa

CHAPTER IV

IN VITRO DEGRADATION STUDY OF PLGA AND ZN BASED METAL(S)

The biodegradable sensors in this work consist of biodegradable polymers PLLA and PLGA and water soluble polymer PVA as the dielectric materials, and bioderadable metal(s) Zn and Zn/Fe-couple as conductors. It is therefore necessary to understand the biodegradability of these materials. Although the degradation rates of biodegradable polymers have been studied previously [146, 167, 82, 78, 26] there is less information available for biodegradable metals in biodegradable sensor applications. The degradation data of this particular PLGA (5004-A) that was utilized in this work was also not found in the literature. Therefore, in this chapter, both the *in vitro* degradation behaviors of PLGA films and biodegradable metal Zn and Zn/Fe-couples are studied.

4.1 In Vitro Degradation of PLGA Films

Two PLGA films with thicknesses of approximately 100 μm and 200 μm are solvent-cast from dichloromethane (DCM) solution on a polytetrafluoroethylene (PTFE) Petri dish. After drying under room temperature for 3 days, the films are peeled off the substrate carefully with tweezers, and further dried at 37 °C for 1 day. Then each piece of film is trimmed into two pieces with shape and volume similar to the ones utilized in the sensor. Each of these four PLGA films is placed in one glass vial (the weight of the vials and the films are measured individually), and approximately 20 mL of 37 °C saline is added in the vial. The glass vial containing the PLGA immersed in saline is placed in an incubator at 37 $\pm$0.5°C with gentle agitation on a

shaker at 30 rpm. Intermittently during the *in-vitro* degradation test, the glass vial containing the PLGA is removed from the incubator. The saline inside the vial is drained carefully, and the PLGA film inside the vial is rinsed with DI water in excess of 4 times. The PLGA is then dried at 37 $\pm$0.5°C for 24 hours before the weight is measured. PLGA is very sticky, especially at the final stage of the degradation, and will adhere to the substrate during drying; therefore, the PLGA film is not removed from the glass vial during the weighing step. Instead, the weight is subtracted from the original weight of the vial, polymer, and saline; in this fashion, the accuracy of the weight measurement during the entire process is improved.

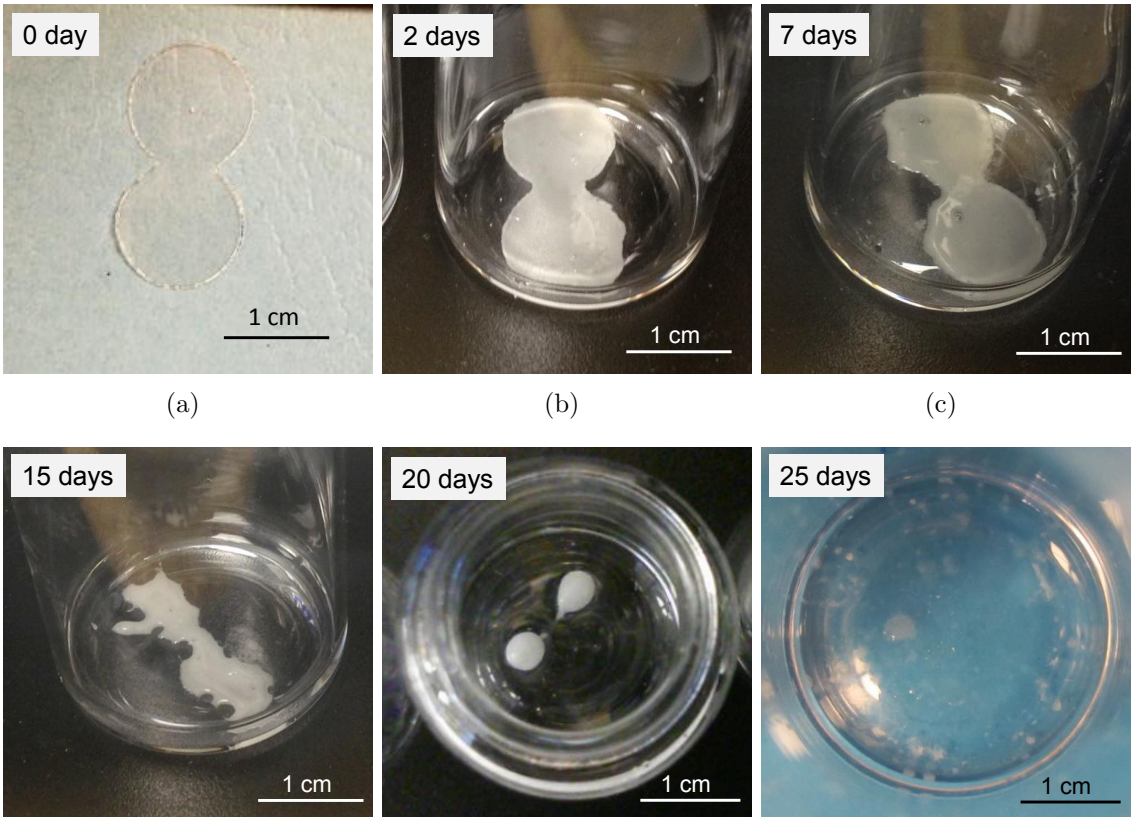

Figure 30: Pictorial history of a PLGA film *in-vitro* degradation study of (a) 0 day, (b) 2 days, (c) 7 days. (d) 15days, (e) 20 days, (f) 25 days.

A pictorial history of one of the PLGA films before and during the entire *in-vitro* degradation study is shown in Figure 30. Except for the picture of the PLGA

specimen before the degradation study, all the other pictures are taken before the film is dried, because while PLGA turns opaque white when hydrated in saline, it returns to completely transparent after drying and therefore would be difficult to be distinguished in the photo.

For the first seven days of the degradation test of the PLGA specimen, the shape and materials of the polymer appear relatively unchanged. After the PLGA has been degraded *in vitro* for 15 days, signicant transformation in shape and loss of material is observed. As the degradation continued, the quantity of remaining polymer continued to be reduced, and by the end of 25 days, only trace polymer residues were found in the vial.

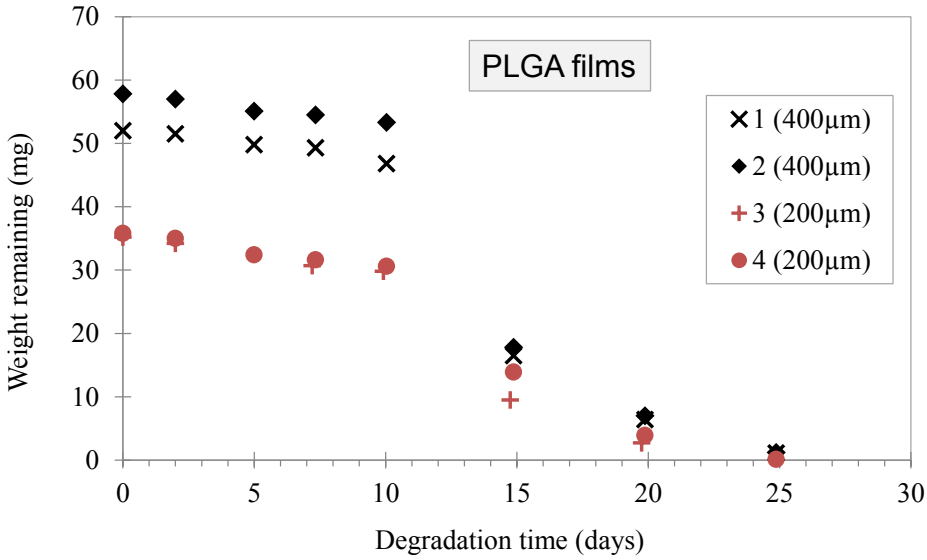

Figure 31: The remaining weight of the PLGA-film specimens during the *in-vitro* degradation

The remaining weight of each specimen during the degradation test is presented in Figure 31. The weight change behavior of all four specimens are indentical dispite the different thickness. The weight of the PLGA remains relatively constant during the first 10 days, suddenly decreases dramatically between 10 and 15 days, and continues diminishing rapidly until almost all the materials are degraded at 25 days. This behavior agrees with the physical appearance change of the PLGA films observed in

Figure 30. It is a very typical weight loss behavior of biodegradable polymers that undergo bulk erosion [41]. During the first stage, water penetrates into the PLGA polymer matrix and hydrolyzes the polymer chains, while the size of the polymer remains relatively stable (before 10 days). Then as molecule chains fragment, the monomers and oligomers will leave the PLGA matrix, and the weight of the polymer is reduced rapidly. By calculating the remaining weight percentage of all the four specimens, the weight loss in the first 10 days in less than 15%, while by day 15, the weight loss is more than 60%. After the PLGA films are degraded for 25 days, less than 2% of the original weight remains. Therefore, it can be concluded that the degradation life time (the time period for the polymer to degrade completely) is approximately 25 days.

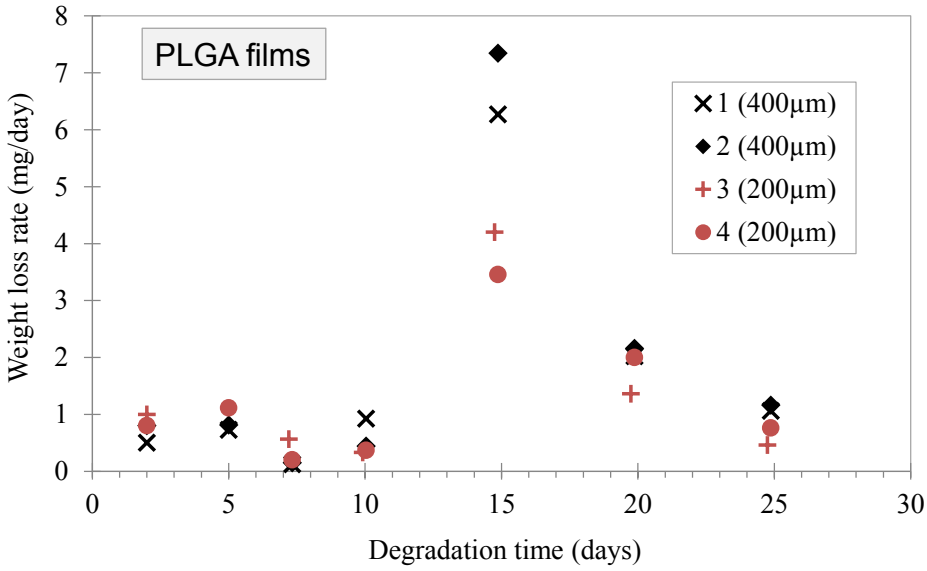

Figure 32: Weight loss rate of he PLGA-film specimens during the *in-vitro* degradation

The weight loss rate at each time point is calcuated by dividing the weight loss between this time point and the previous time point by the time period. The result of the weight loss rate for each specimen is plotted as a function of degradation time in Figure 32. A dramatic increase of the degradation rate is observed at day 15, with a maximum value of approximately 7.3 mg/day. The high degradation rate afer 15

hours corresponds to the stage that the polymer loses its shape and volume. In the application of biodegradable sensors, the degradation rate is less important than the degradation lifetime of the polymers. Therefore, no detailed study is performed to explain the exact degradation rate.

4.2 Degradation Behavior of Biodegradable Metal Zn and Zn/Fe-couple

The corrosion rate of metal and metal couples can be measured by means of electrochemical techniques and physical loss measurements [110, 37]. The main advantages of electrochemical techniques include sensitivity to low corrosion rate, short experimental duration, and well-established theoretical understanding [110]. However, measurement of the physical weight loss can provide direct corrosion rate results and real-time appearance change of the metals, which would be useful in the study of the degradation of the sesor. Therefore, single metal Zn and Zn/Fe-couple are studied using both electrochemical techniques and physical loss measurement.

4.2.1 Electrochemical Study of Degradation of Zn and Zn/Fe-couples

Electrochemical techniques for corrosion studies usually involve polarization. Polarization describes the potential change from the equilibrium potential caused by applying a net current to or from an electode [122]. In the ideal case, where there is only one anodic and one cathodic reaction on the corroding surface, a linear relationship between potential (E) and logarithmic current ($LogI$) can be found when the electrode is polarized to sufficient polarization both in the anodic and cathodic directions. The linear regions are denoted Tafel regions, mathematically expressed as [66, 37, 110]:

$$I_{net} = I_{corr}\left\{exp\left[\frac{2.303(E-E_{corr})}{\beta_a}\right] - exp\left[-\frac{2.303(E-E_{corr})}{\beta_c}\right]\right\} \qquad (52)$$

where I_{net} is the current, I_{corr} is the current at corrosion potential E_{corr}, and E is the applied potental. β_a and β_c are the Tafel constants (the anodic and cathodic slopes

of the $E - logI$ plot of the Tafel regions). An example of the plot of a corroding metal showing Tafel behavior under polarization is shown in Figure 33 [110]. The corrosion current I_{corr} and potential E_{corr} can be determined by the extrapolation of either anodic or cathodic or both Tafel regions.

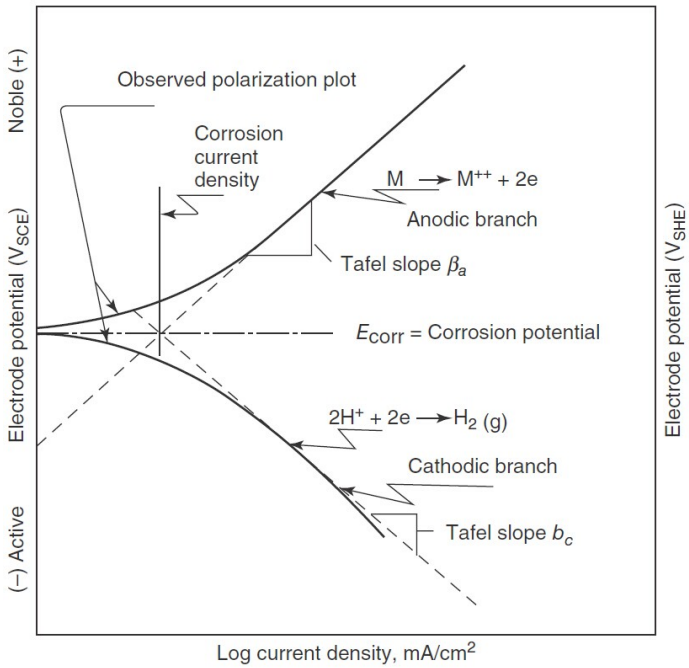

Figure 33: Hypothetical cathodic and anodic Tafel Polarization diagram

Potential dynamic polarization is utilized in this work to obtain the polarization $E - logI$ plot. In the potential dynamic polarization measurement, the continuesly changing potential is impressed on the working electrode (the sample to be measured) and a counter electrode (platimum, Pt) at constant rate to polarize them in the opposite direction. A reference electrode (Saturated Calomel electrode, SEC) is connected to the working electrode through a high-impedance voltmeter, to prevent any current passing through the reference electrode. The current and potential (compared with the reference electrode) of the measured metal are recorded simultaneously.

A Zn specimen with thickness exceeding 100 μm is fabricated by electroplating on a Kapton® film with Ti-Cu-Ti seed layer through a photoresist mold, followed by

peeling off the Kapton® and removing the seed layer (details can be found in Chapter 5). The freestanding metal piece is connected to the electrode with all but 1.2 cm^2 on the surface covered by electroplater's tape (eletricity and water proof). In the biodegradable sensors in this work, Fe is eveporated on Zn; therefore direct measurement of the electrochemical data of the evaporated Fe itself would be desirable. However, during the testing, it is observed that evaporated Fe would delaminate from the substrate and fragment during the polarzation experiment, mainly due to the intense andodic polarization, therefore disturbing the current data as well as altering the Fe surface area of the Fe. Different substrates including glass, Si wafers, Kapton® films, and wafers with parylene coating were utilized without success. Therefore, a pellet (diameter = 3 mm) ordinarily used as a source for E-beam evaporation is utilized as the Fe specimen; this material is connected to a conducting wire and mounted to a thick epoxy chunk prior to immersion in solution. The scan rate is 0.5 mV/s, and the electrolyte is 0.9% saline. To achieve a similar set-up to that used in in-vitro degradation, the saline is preheated to 37 °C and placed in the water bath under 37 °C during the entire polarization measurement. The recorded potentialdynamic polarization diagrams of Zn and Fe are shown in Figure 34.

The corrosion current density of Zn is between 10 to 20 μA/cm^2, and the corrosion potential is approximately -1.04 V (vs. SCE). This result is slightly smaller than the results of Zn in 3.5% NaCl solution presented in [166, 135, 81] (30-60 μA/cm^2), presumably due to the lower concentration of NaCl investigated here.

The galvanic corrosion rate of two metals can be roughly predicted by superimposing the polarization curves of the anodic and cathodic metals; the point at which these curves cross yields the expected corrosion current [63, 56, 137]. This prediction is fairly accurate when the open circuit potential of the anode and cathode are relatively far apart (more than roughly 120 mV depending on the slopes of the curves) [49]. To obtain the current density for the galvanic couple when the area

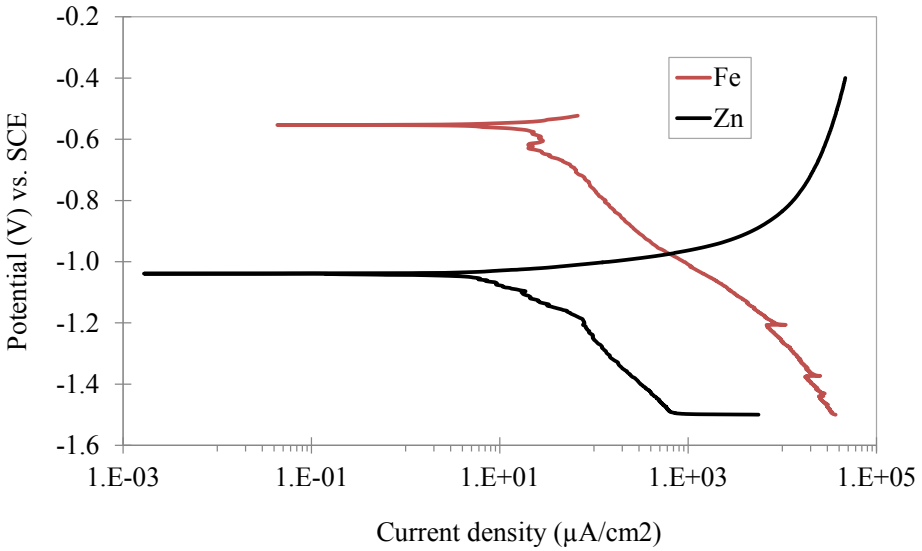

Figure 34: Potentialdynamic polarization diagrams of Zn and Fe in 0.9% NaCl under 37°C.

ratio is not 1 : 1, the polarization curves of anodic and cathodic materials can be multiplied by their respective wetted surface area. The predicted corrosion current and exact corrosion potential then correspond to the intersection of the anodic and cathodic curves [49, 56, 63]. The polarization curves were tranformed by this means utilizing the result of Figure 34, with Zn area maintained at 1 cm^2, and Fe area of 0.1 cm^2, 0.2 cm^2, 0.5 cm^2 and 1 cm^2. The results are plotted in Figure 35. Note that the current rather than current density is used for the x-axes in this polarization diagram.

Assuming anodic reactions occur only on Zn surfaces, the corrosion current density (where the current density is calculated based on the area of exposed Zn) of Zn/Fe-couples with different Fe : Zn area ratio (from 0.1 to 2) is plotted in Figure 36. It is noted that the corrosion current is not linearly dependent on the Zn : Fe area ratio. One possible reason for this nonlinearity is that based on the point at which the two curves cross for a given area ratio, the corrosion does not occur in the Tafel region of both metals. In this case, the relationship between the corrosion current and the area ratio would not be linear; instead, the corrsion rate is at least in part controlled

by Fe diffusion [91, 165].

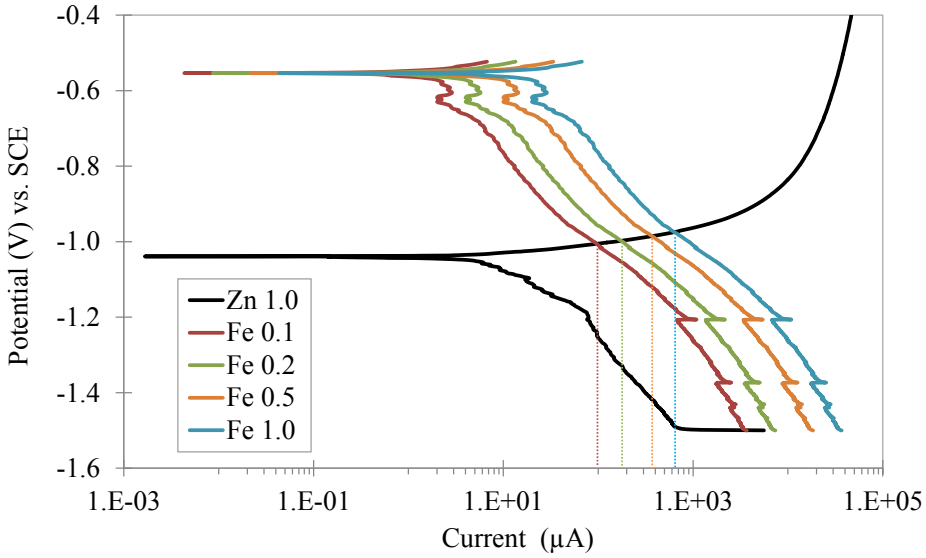

Figure 35: Superimposed polarization diagrams of Zn (0.1 cm^2) with Fe (0.1 cm^2, 0.2 cm^2, 0.5 cm^2 and 1 cm^2) in 0.9% NaCl at 37°C

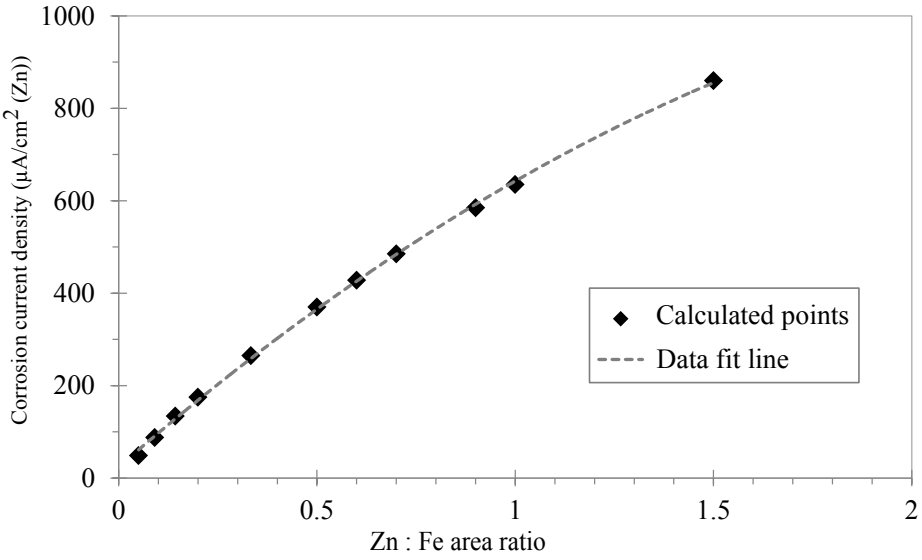

Figure 36: Predicted galvanic corrosion current density (based on Zn area) calculated by superimposing polarization diagrams as a function of the Fe : Zn area ratio

4.2.2 Weight-loss Measurement of Zn and Zn/Fe-couples *In Vitro*

The weight loss measurement is performed by immersing each freestanding electroplated metal specimen in approximately 20 mL of saline (0.9% NaCl, pH 6.8), and placing the immersed specimen in an incubator at a temperature of 37±0.5°C with gentle mechanical agitation. The agitation is achieved by placing the container of the specimen on a shaker at 30 to 60 rpm. The weight of each specimen is measured every four hours over the first 56 hours, and approximately every 12 hours over the subsequent 120 hours. Each specimen is rinsed with approximately 50 mL deionized (DI) water for at least 3 times and dried thoroughly in a 37±0.5°C oven overnight before the weight measurements. After the specimen breaks into smaller pieces, filter paper with pore size of 20 μm is used to collect the remaining debris for weighing, and the debris is transferred to a weighing paper for measurement. After measuring the weight, each specimen (including debris) is placed back to the incubator under saline. The saline is refreshed approximately every 8 hours.

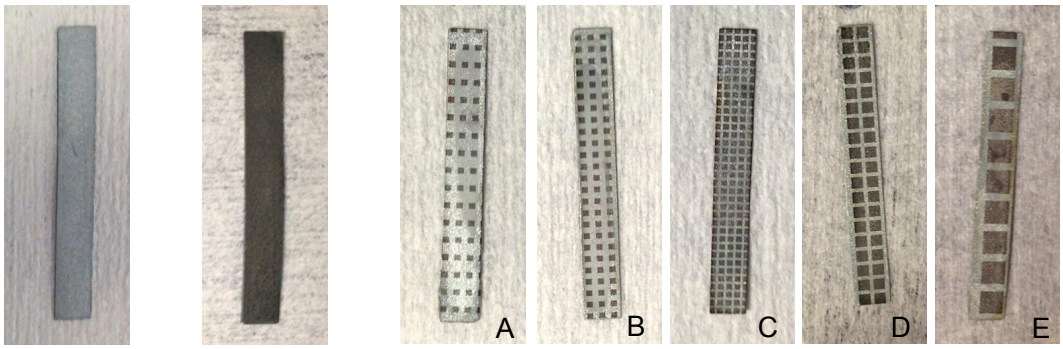

Figure 37: Metal specimens for *in vitro* degradation (weight-loss) measurement: (a) electroplated pure Zn, (b)Zn/Fe(bilayer), and (c) Zn/Fe(checkers).

Two types of freestanding rectangular (0.3 × 2.5 cm) specimens are prepared: pure Zn and Zn/Fe-couples. Zn specimens are prepared by electroplating through

photoresist molds on Ti-Cu metallized Kapton® films, peeling off the resultant rectangular metal pieces from the Kapton® film, and removing the remaining Ti-Cu seed layer by micro-polishing. The thickness of the specimens ranges from 60 to 100 μm. Zn/Fe-couple specimens are prepared by depositing Fe on the electroplated Zn using an E-beam evaporator (Denton Explorer). 400-700 nm of pure Fe is evaporated on the surface of the Zn with a deposition rate of 0.05 nm/s and a chamber pressure less than 1×10^{-6} $torr$. To prevent any oxidation of the metal, the chamber is not vented until at least one hour after the evaporation concludes, thereby ensuring that the chamber is completely cooled down. To obtain different area ratios of Fe : Zn, Zn/Fe(bilayer) specimens with Fe evaporated entirely on one side, and Zn/Fe(checker) specimens with Fe evaporated partially on the Zn surface in a checkerboard pattern through an appropriate shadow mask are prepared. Shadow masks with arrays of square holes are fabricated from 0.127 mm-thick blue tempered shim stock (Precision Brand©) using an IR laser. The electroplated Zn, Zn/Fe(bilayer) and Zn/Fe(checker) specimens are shown in Figure 37 with the demensions of the different checker designs listed in Table 6. Distinct color differeces can be observed between the region covered by Fe (dark gray/black) and the exposed Zn (light gray/white).

Table 6: Dimension of evaporated Fe with different checker designs

Parameters	**Checker pattern**				
	A	**B**	**C**	**D**	**E**
Fe box side length (mm)	0.5	0.5	0.5	1	2
Distance between boxes (mm)	0.5, 1	0.5	0.21	0.41	1.41
Fe surface coverage (single side)	16.7%	25%	50%	48%	50%
Total Fe : Zn(exposed) area ratio	9.0%	14.3%	33.3%	31.6%	33.3%

After the rectangular specimen has been immersed in saline for 12 hours or less, a signicifant amount of oxidized material is obversed on the surface of the Zn/Fe couple specimens, as shown in Figure 38. Some of the residue is loosely attached

to specimen and can be removed by rinsing the specimen in deionized water. There are also some oxides observed in the pure Zn specimens in later time stages of the degradation experiment.

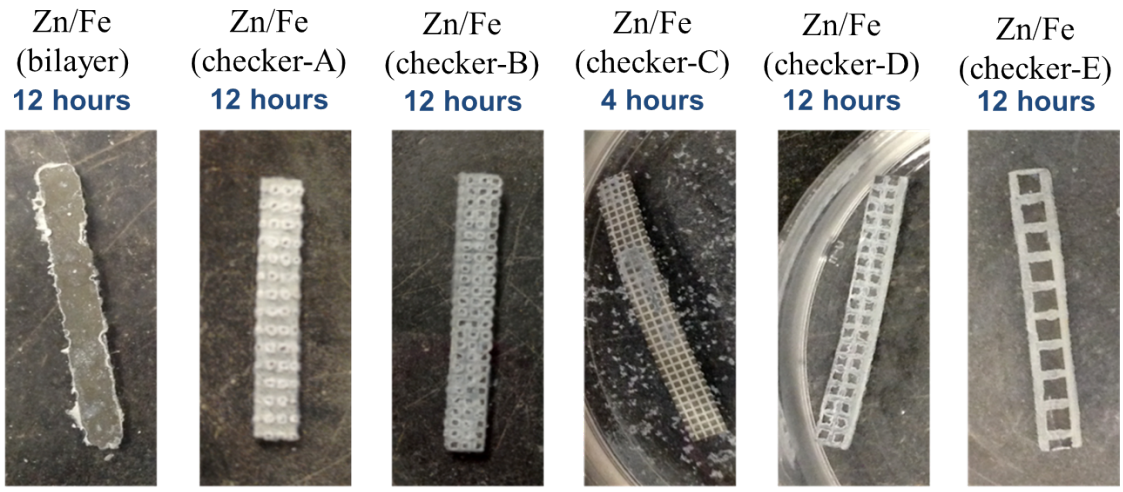

Figure 38: Zn/Fe(bilayer) and Zn/Fe(checker) specimens after *in-vitro* degradation test of 4 to 12 hours (immersed in saline before washing and weighing)

Scanning electron microscope (Hitachi S-3700N VP-SEM) pictures of the Zn/Fe-couple specimen before and after (4 hours, 8 hours, and 12 hours) the degradation test are shown in Figure 39, with the energy dispersive X-ray (EDX) element atomic percentage listed in Table 7. Before degradation, the surface area with and without Fe coverage can be distiguished in the SEM pictures by contrast difference; 100% Fe and 100% (atomic%) Zn are also confirmed in these regions by EDX spectroscopy. After the *in vitro* degradation, significant surface morphology differences are exhibited between the area with and without Fe coverage, with the exposed Zn area undergoing much more severe corrosion. A significant amount of oxygen is detected in the Zn area. According to the mechanism of galvanic corrosion, Fe, which is the cathode in the Zn/Fe galvanic couple, should be protected by the sacrificial anode Zn. However, mild oxidation of Fe is observed in the SEM pictures, and the percentage of iron in the EDX also shows a decreasing trend with time. Possible reasons include: (1) the efficiency of the galvanic protection is less than 100%; (2) there are very likely

some defects on the thin Fe films since the evaporation of these films takes place on electroplated Zn that has a relatively rough surface compared to the iron thickness. Such defects may expose the Zn beneath the Fe to the electrolyte during degradation, leading to local galvanic corrosion, and expending the defects; (3) Fe can be oxidized while drying the specimen before weight measurements. However, even with this unexpected comsumption of Fe, there is still a sufficient amount of Fe preserved to enable the prolonged corrosion degradation of the Zn/Fe couple.

Table 7: EDX element atomic percentage of Zn/Fe(checker) specimen after textitin-vitro degradation for 4, 8 and 12 hours

Region	**Element**	**Degradation time**		
		4 hours	**8 hours**	**12 hours**
Area with Fe coverage	Fe (%)	31	26	20
	O (%)	39	42	44
	Zn (%)	30	32	36
Exposed Zn area	Zn (%)	35	30	33
	O (%)	63	68	67
	Cl (%)	2	2	-

Pictorial histories of the Zn-Fe-checker and Zn-Fe-bilayer specimens over the 200-hour experiment duration are shown in Figure 40. Initially, a white oxidation product is observed, consistent with Zn oxidation [21], Fe also remains detectable by its dark gray/black color. As the degradation of the Zn/Fe couple continued, the specimens gradually lost their physical integrity. The fragmentations begin with the Zn region without Fe-coverage for the Zn/Fe(checker) specimens and the edge for the Zn/Fe(bilayer) specimens. Then the specimens gradually break into smaller fragments, and brown/red iron oxides begin to be observed, consistent with iron oxidation [98]. The breaking regions are the Fe-Zn junctions where Fe is directly in contact with Zn, possessing minimum resistance, which therefore experience the

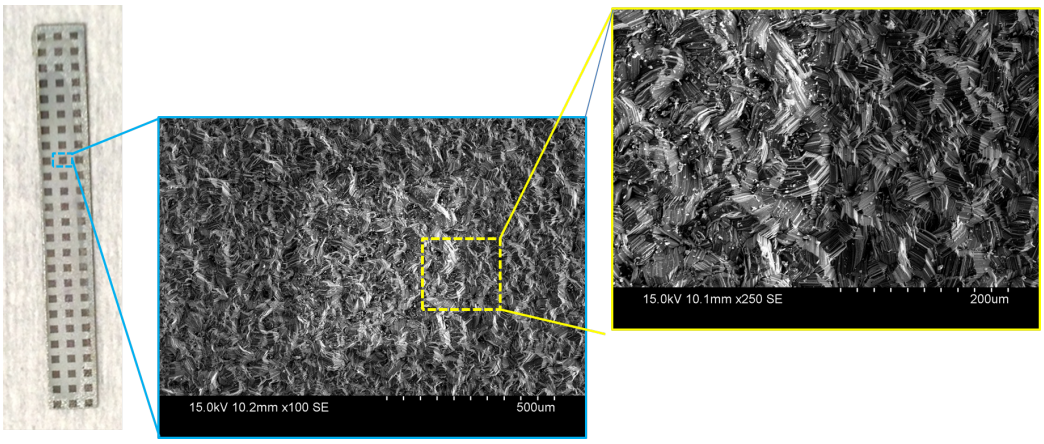

(a)

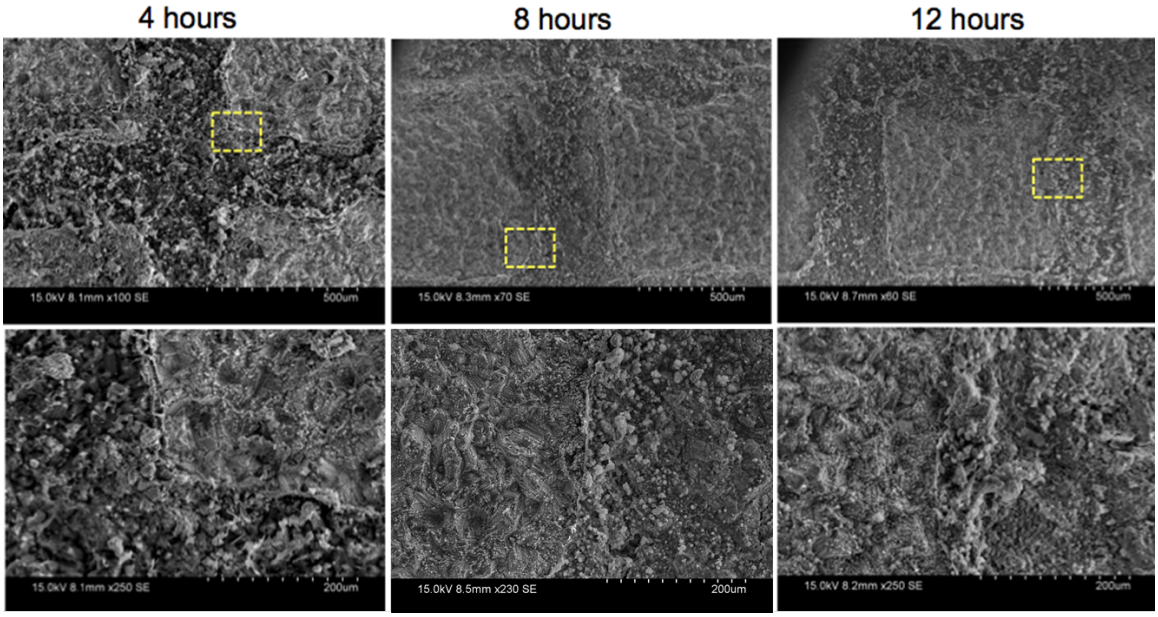

(b)

Figure 39: SEM picture of Zn/Fe/(checker) specimen (a) before degradation test , and (b)after *in vitro* degradation of 4 hours, 8 hours and 12 hours, with zoomed-in image of the area in the yellow box shown in the bottom row)

strongest galvanic corrosion. This ralatively controllable fragmentation can be utilized in designing the metal-couple to achieve certain shape/dimension during degradation. Meanwhile, such fragmentation is not observed in Zn specimens within 300 hours of *in-vitro* degradation; most of the Zn specimens maintain their physical integrity, with a few specimens breaking into two or three sections. For the corrosion of Zn, simple oxidation products including ZnO, $Zn(OH)_2$ will be produced, and these simple

products will slowly be converted to zinc hydroxycarbonates (i.e. $Zn_4CO_3(OH)_6{\cdot}H_2O$ and $Zn_5(CO_3)_2(OH)_6$) and zinc hydroxychloride ($Zn_5(OH)_8Cl_2{\cdot}H_2O$) in the presence of CO_2 and chloride species with minutes or hours [44, 83]. Generally, zinc hydroxycarbonates are widely accepted as a insoluble passive film, while oxidation products containing simple oxides and chloride species are more soluble [19].

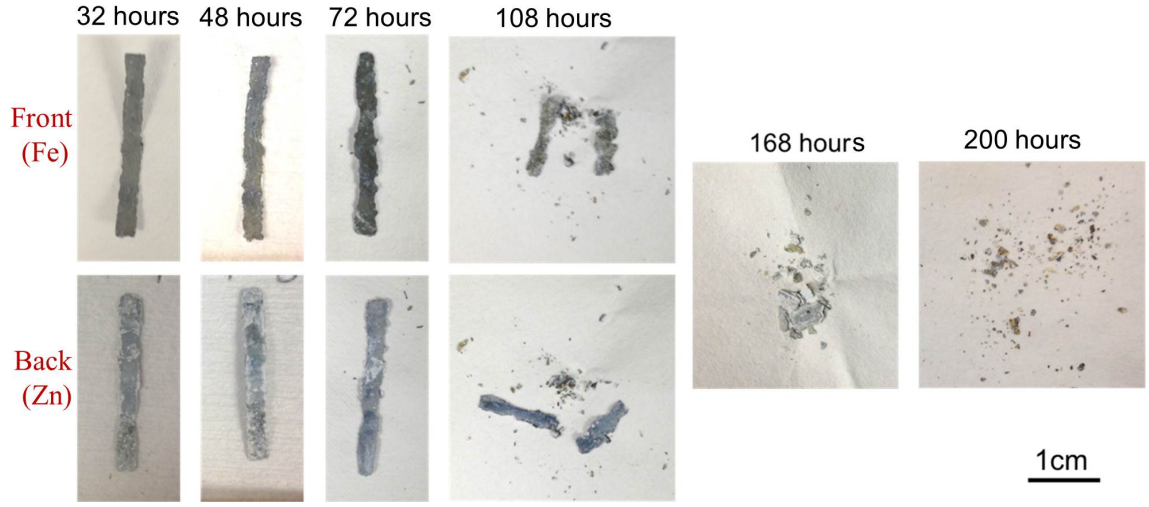

(a)

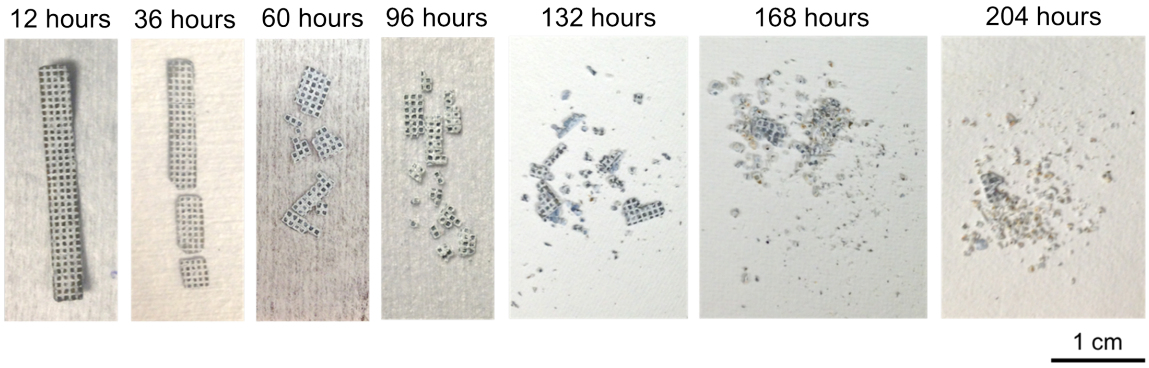

(b)

Figure 40: Pictorial histories of the Zn/Fe-couple specimens (a)Zn/Fe(bilayer), and (b) Zn/Fe(checker-C) over the 204-hour experiment duration

Because the specimens studied in this work vary in thickness, exposed Zn area and Fe area, it is challenging to compare the absolute weight change between different kinds of specimens. If assuming only Zn is degraded until the end stage of the degradation, the weight loss of the specimen (i.e. the Zn weight loss) can be

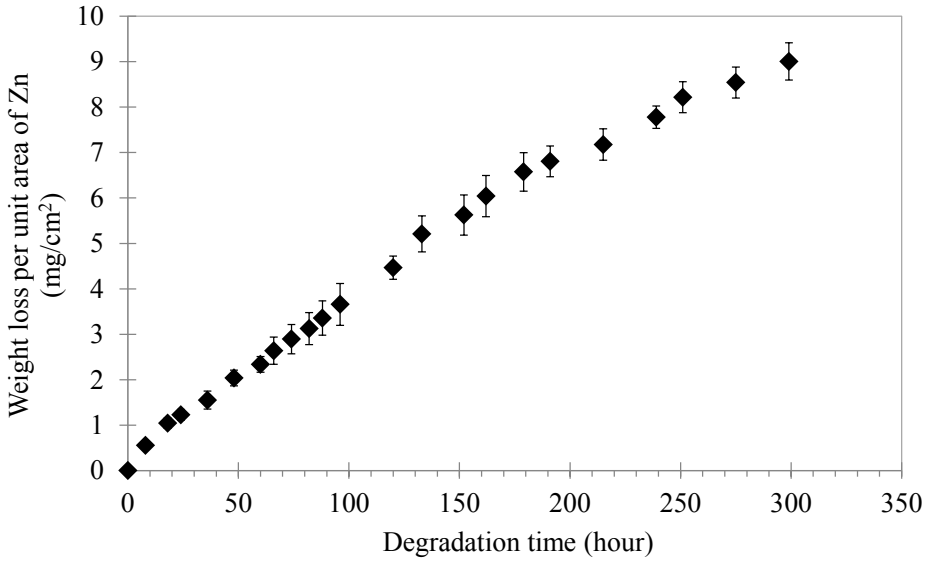

(a)

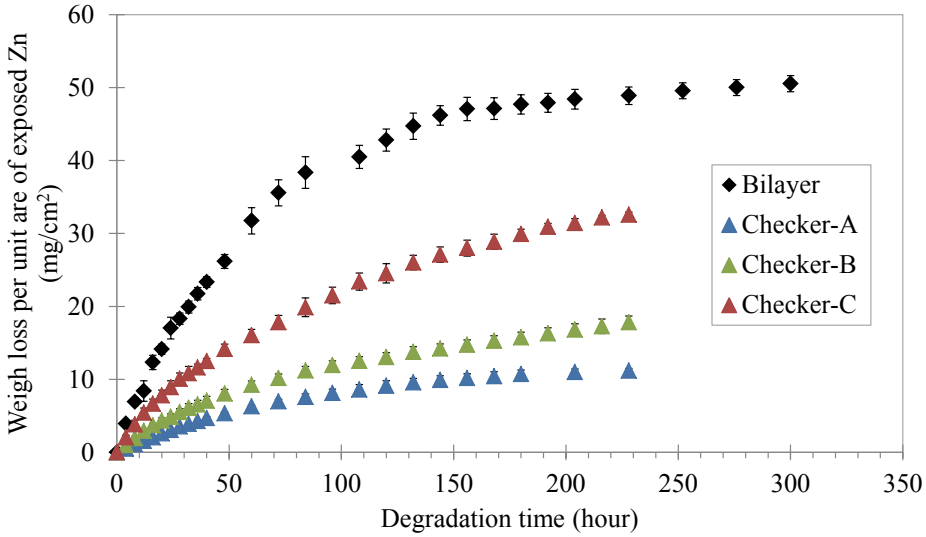

(b)

Figure 41: Weight loss per unit area of initial exposed Zn as a function of degradation time of (a)pure Zn, and (b) Zn/Fe-couple

normalized by the area of the Zn. However, after the specimen fragments, the exact area of the Zn is difficult to determine. Therefore, the initial exposed Zn areas are utilized here as the normalizing area; this approximation will become less valid as fragmentation proceeds. The weight losses of pure Zn and Zn/Fe-couples normalized by the initial exposed Zn areas are plotted as a function of the degradation time in

Figure 41. The results of at least three specimens of each design are collected and analyzed for calculation of the average value and the standard deviation.

During a 300-hour degradation time period *in vitro*, the Zn weight loss per unit area increases approximately linearly with the degradation time (Figure 41(a)), indicating that the degradaon rate of the Zn maintains relatively constant. However, a slight slope decrease and shift are observed within the initial 24 hours and between 191 and 215 hours; this might be due to the formation of localized passive films [101, 20] on the Zn surface. During the entire *in vitro* degradation of Zn in this study, the average degradation rate (i.e.,the slope of the weight loss per unit area vs. degradation time curve) is 0.062 $mg/(cm^2 \cdot hour)$, which corresponds to a average degradation thickness of 2.08 μm/day. After 300 hours of degradation, the average weight loss per unit area of Zn is apprximataly 16.5 ± 0.7 mg/cm^2.

For Zn/Fe-couple specimens in Figure 41(b), for each type of Zn/Fe-couple specimen, the degradation follows similar behavior: within an initial short period of time (before apprximately 50 hours), the weight loss per unit area increases almost linearly with degradation time. After this initial period, the weight loss per unit area still increases as the degradation test continues; however, the rate of increase gradully slows down. This is very likely due to two reasons: (1) when the specimens degrade and loss physical integrity, the total area of the exposed Zn changes, too. As shown in Figure 40: after 48 to 60 hours, a noticeable amount of metal has degraded; after 108 to 132 hours, significant amounts of material have been consumed. Therefore, the total area of Zn has decreased significantly, while the weight loss per unit area of Zn is still calculated by dividing the absolute weight loss by the initial Zn area; (2) the galvanic corrosion speed is reduced due to the fact that Fe is partially oxidized unexpectedly as discussed above.

For different Zn/Fe-couple specimens, the degradation rate decreases as the Fe converage area decreases: Zn/Fe-bilayer > Zn/Fe(checker-C) > Zn/Fe(checker-B) >

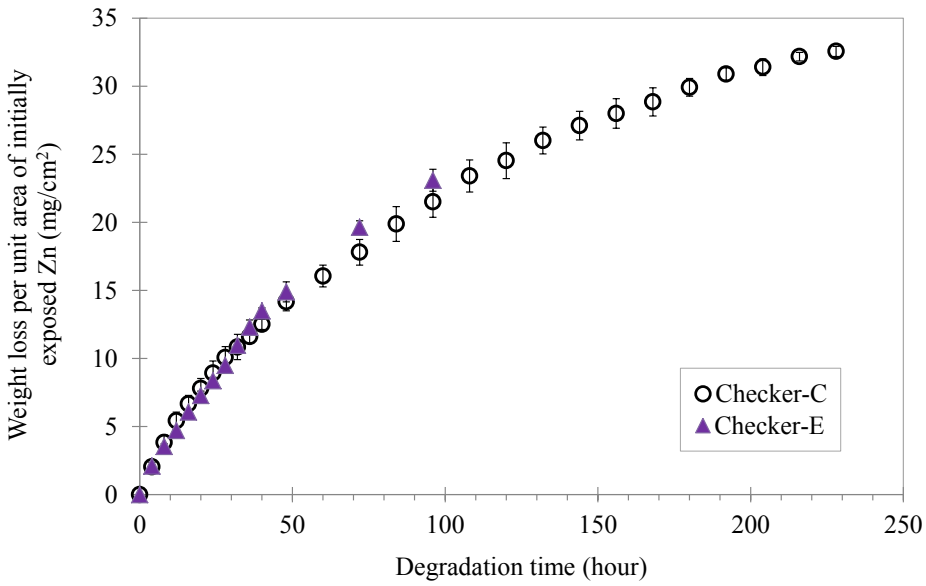

Figure 42: Weight loss per unit are of initial exposed Zn as a function of degradation time of Zn/Fe(checker-C) and Zn/Fe(checker-E)

Zn/Fe(checker-A). This is due to the mechanism of galvanic corrosion: during the galvanic corrosion of the Zn/Fe-couple, electrons transfer from Zn to Fe to protect the Fe from being oxidized. The greater the area of Fe that is in contact with the electrolyte, the more electrons it requires to avoid corrosion; therefore, the greater the rate of consumption of Zn. Initially, it was suspected that the degradation rate might also correlate to the total perimeters of the Fe checker 'boxes', where the galvanic corrosion occurs most dramatically. To test this hypothesis, the degradation of Zn/Fe(checker-C)and Zn/Fe(checker-E) that possess similar Fe/Zn area ratio but with different Fe perimeters are studied. The specimen weight loss per unit area of Zn plotted as function of degradation time of these two types of Zn/Fe(checker) specimens is shown in Figure 42. Identical degradation curves are observed among the Zn/Fe(checker) specimens with C and E design. Therefore, the impact of the Fe perimeters on the degradation rate of Zn/Fe-couples can be excluded based on this result.

To further analyze the numerical relationship between the degradation rate and

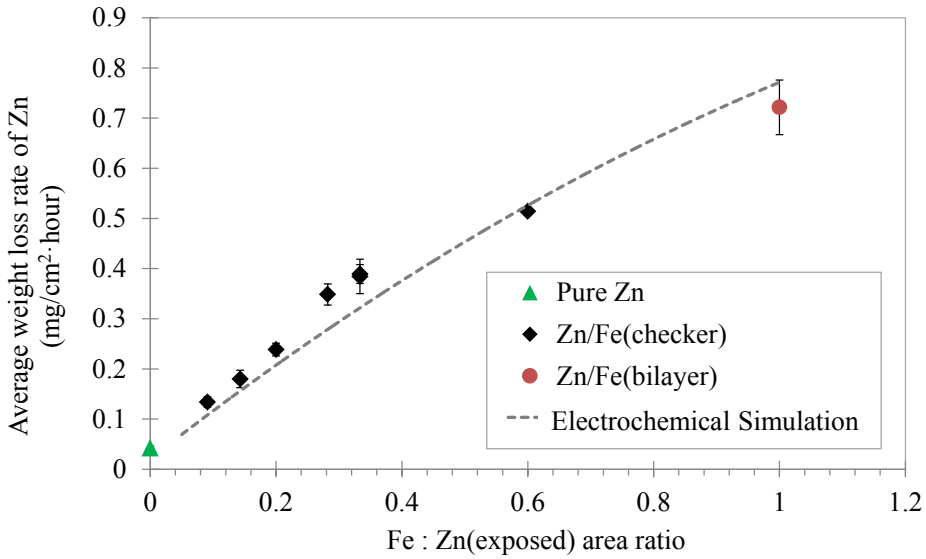

Figure 43: Degradation rate using weight loss of Zn for Zn and Zn/Fe-couple rectangular specimens in the first 24 hours of *in vitro* degradation compared with the simulated degradation rate based on electrochecmical testing

the Fe:Zn area ratio, the average degradation rate of each kind of sample based on the first 24 hours are collected and analyzed. Utilizing the result of the initial 24 hours rather than that of a longer period of degradation time is expected to minimize the effects of reduced specimen area and consumption of Fe. The results of at least three specimens for each area ratio are included, except for specimens with checker-patterned Fe covered on both sides of the Zn (with design of checkers-B-B (two specimens included) and checkers-A-C (one spceimen included)). The slope of the weight loss per unit area of Zn as a function of the degradation time is utilized as the degradation rate for each specimen, and the data among specimens is calculated as the average and standard deviation of this slope. This calculation is then repeated for each area ratio of Fe:Zn. The calculated degradation rate result is plotted as a function of the Fe/exposed Zn area ratio, and compared with the simulated result based on electrochecmical testing, shown in Figure 43. The simulated result based on electrochecmical testing of Zn and Fe is obtained by converting the Zn corrosion current density in Figure 36 to the equivalent weight change rate of Zn (100 μA (Zn)

$\rightarrow$ 0.122 mg/hour) by means of Faraday's law.

The corrosion rate obtained by weight loss of the Zn/Fe couple and superimposed polarzation diagram of Zn and Fe agree fairly well when the Fe: Zn area ratio is less than 0.25 and higher than 0.5. The reasons for the relatively higher degradation rate obtained by weight loss (mainly Checkers B and C) are still under further investigation.

4.2.2.1 Effects of Zn Surface Morphology on Depgradation Rate of Metals

As discussed above, the surface area of both exposed Zn and Fe are important parameters to determine the *in vitro* degradation rate of biodegradable metals. Electroplated Zn does not have a perfectly smooth surface, the microscopic surface area is different from the macroscopic area. Therefore, the possible effect of Zn surface morphology on the degradation rate of Zn/Fe-couples is studied here.

Three different Zn surfaces were prepared that ultimately acted as substrates for the evaporation of iron. The first surface (Surface I) comprised the electroplated Zn without any subsequent modification; this surface was identical to the surfaces described above. The second surface (Surface II) comprised the electroplated Zn that was subsequently polished using 2000 grit sandpaper; this resulted in a significantly smoother surface but did preserve large numbers of concavities in the surface. The third surface (Surface III) was the Zn surface that had initially been in contact with the seed layer, i.e., the bottom side of the electroplated Zn layer. Since the roughness of Surface III is dictated by the roughness of the substrate and seed layer (both of which are relatively smooth), this surface was also correspondingly smooth. SEM pictures of these three Zn surface mophologiesprior to the evaporation of Fe are shown in Figure 44.

Approximately 500 - 700nm of Fe is evaporated in different checker and bilayer patterns onto specimens bearing Surfaces I, II, or III. After Fe evaporation, degradation

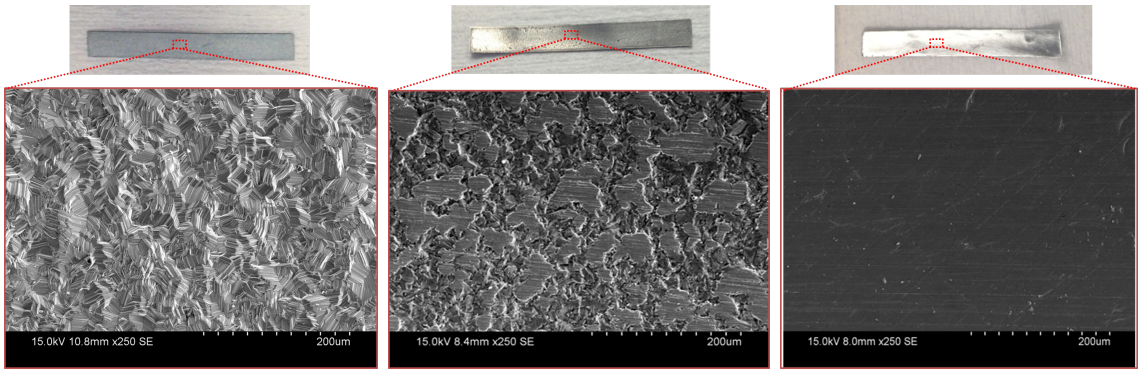

(a) (b) (c)

Figure 44: SEM pictures of (a) top surface of electroplated Zn without polishing (Surface I), (b) polished top-surface of Zn (Surface II), and (c) back-surface of Zn (Surface III)

tests for 4, 12 and 24 hours are performed as described above. After the specimens are rinsed with DI water and dried throughly, one specimen of each surface type is selected and characterized using SEM and EDX. SEM pictures of Zn/Fe(checker) specimens on Surfaces II and III are shown in Figure 45 and Figure 46, with the EDX element atomic percentage listed in Table 8. Similar to the Surface I behavior described previously, significant corrosion of the exposed Zn region between the Fe covered regions is observed in both Surface II and III specimens. For all surface types, Fe-covered regions remain well-protected during the first 4 hours, and start to mildly degrade after 12 hours. Overall, in the SEM pictures, the corrosion of the specimens with Fe on Surface II appears more extensive than Surface III. However, the element atomic percentages as determined by EDX of these two specimen types do not exhibit significant differences. In Figure 45(b), significant amounts of Zn oxidation products are preserved on Surface II after being washed and dried at 24 hours.

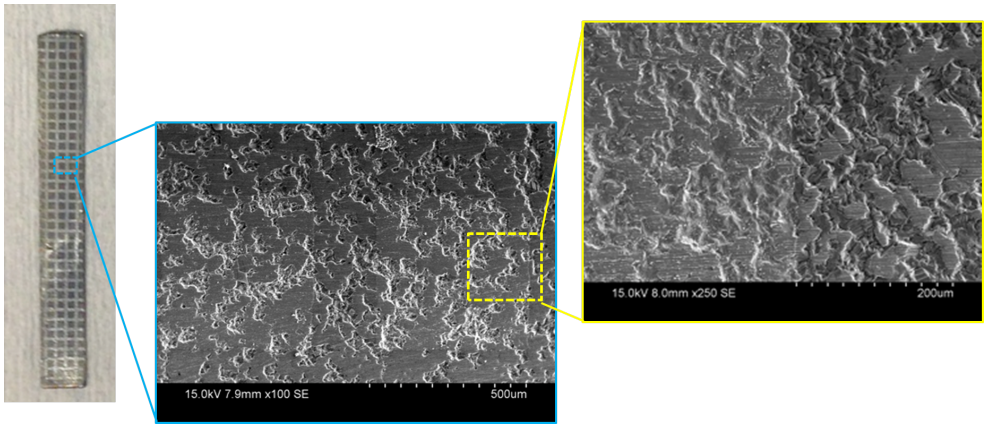

(a)

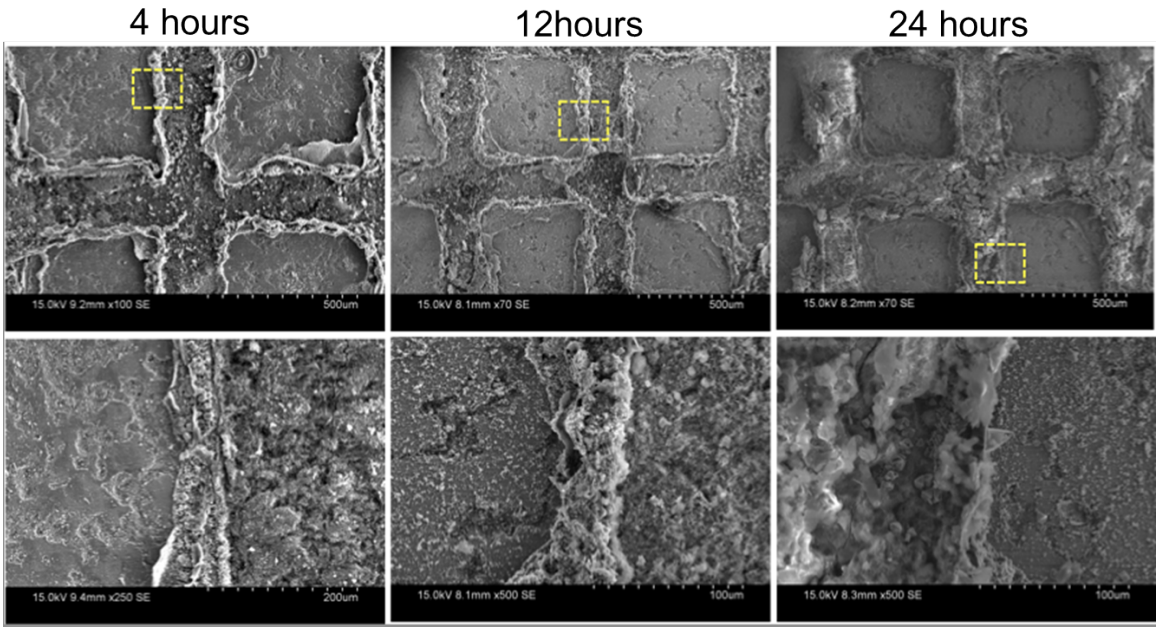

(b)

Figure 45: SEM pictures of Zn/Fe(checker) specimen with Fe evaporated on Surface II: (a) before degradation test, and (b) 4, 12, 24 hours after degradation test

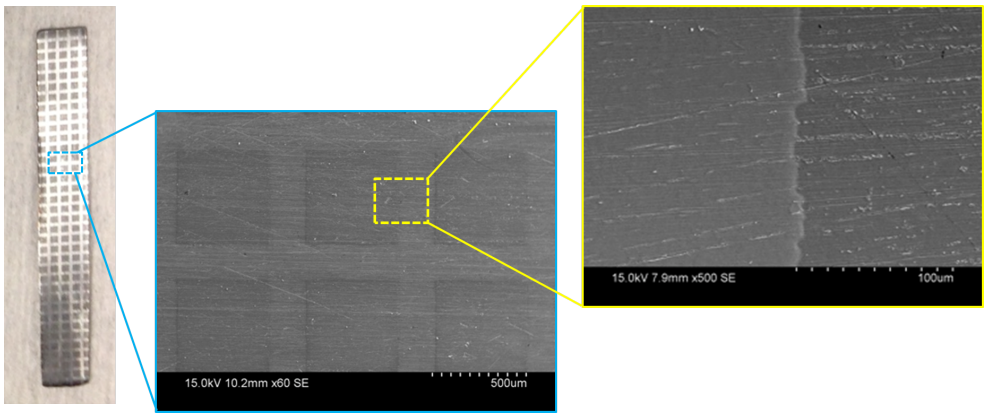

(a)

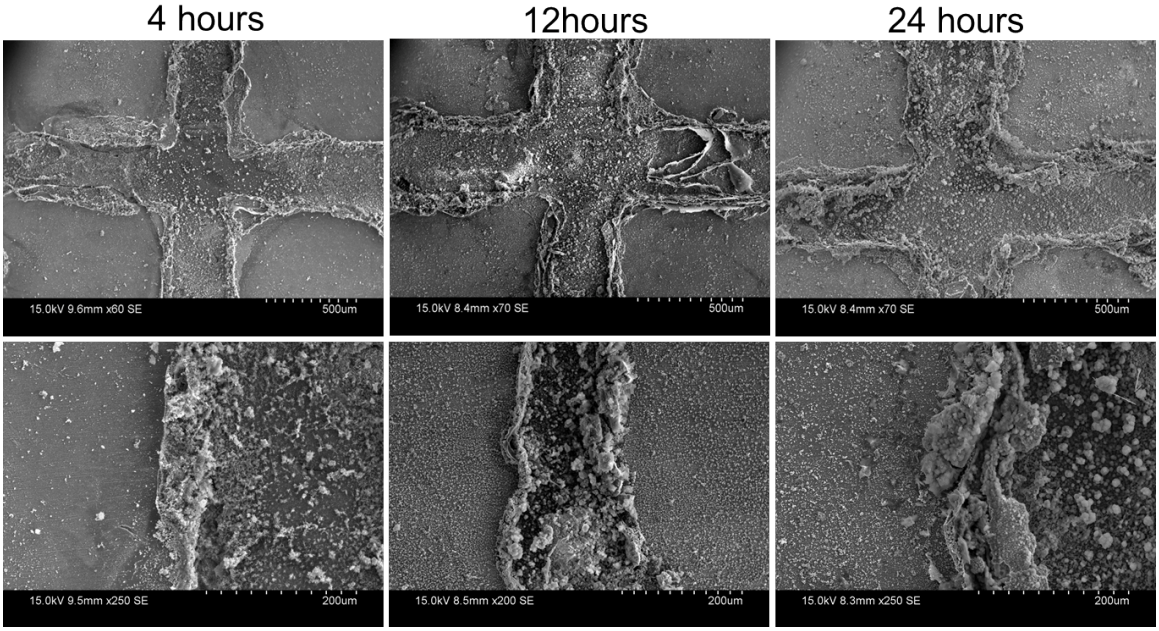

(b)

Figure 46: SEM pictures of Zn/Fe(checker) specimen with Fe evaporated on Surface III: (a) before degradation test, and (b) 4, 12, 24 hours after degradation test

Table 8: EDX element atomic percentage of Zn/Fe(checker) specimens with Fe evaporated on Surfaces II and III after textitin-vitro degradation for 4, 12 and 24 hours

Specimen	Time (hours)	Area with Fe coverage			Exposed Zn area		
		Fe (%)	O (%)	Zn(%)	Zn(%)	O (%)	Cl(%)
Fe on Surface II	4	66	24	10	45	55	-
	12	38	31	31	33	65	2
	24	22	43	35	30	69	1
Fe on Surface III	4	55	29	16	37	62	1
	12	28	45	27	31	68	1
	24	18	46	36	30	67	2

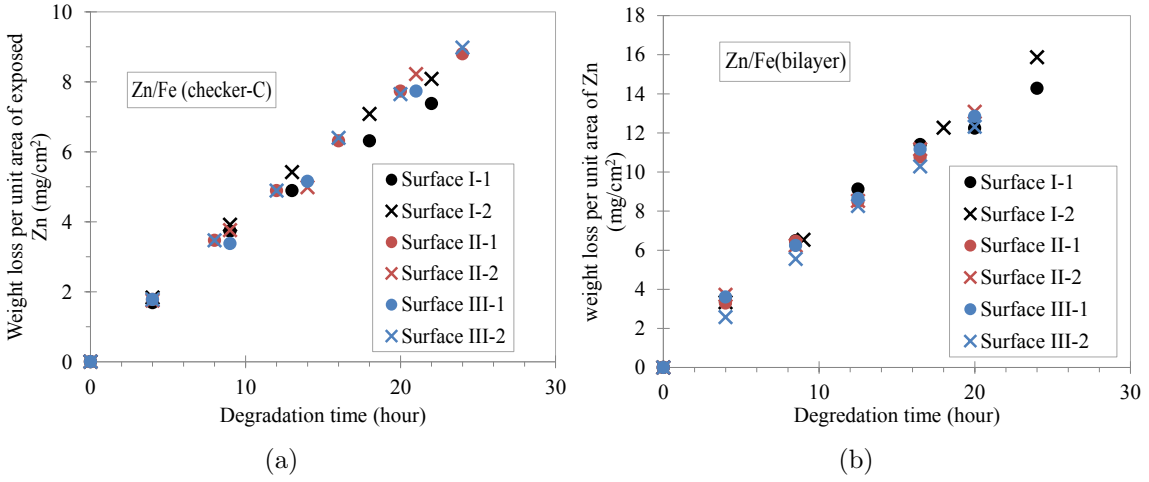

Figure 47: Weight loss per unit area of exposed Zn as a function of degradation time of rectangular metal specimens of (a) Zn/Fe(checker-C), and (b) Zn/Fe(bilayer), parameterized by surface type

In addition to analyzing the atomic composition of degradation products on various surface types, it is also instructive to determine whether the corrosion rate of Zn/Fe couples is affected by the these different Zn surface morphologies. To determine this effect, an experiment was performed in which three different Zn:Fe area ratios, Zn/Fe(checker-A), Zn/Fe(checker-B) and Zn/Fe(bilayer), were prepared on each of the surface morphologies. The degradation rate of each surface type, with the same

Fe:Zn area ratios on each type, are compared. The result of the measurements, i.e., weight loss per unit area of exposed Zn as a function of degradation time for two of the area ratios, parameterized by the three different surface morphologies, for the initial 24 hours of degradation are plotted in Figure 47. No significant differences are observed among specimens with Fe on different surface morphologies.

4.2.2.2 Effects of the Volume of Saline and Agitation on the Degradation Rate of Metal(s)

As the metal(s) degrade in saline, the concentration of the various ions present as well as the pH of the electrolyte will gradually change, and the degradation rate of the immersed metal may be affected accordingly. However, if the electrolyte volume is infinite, the ion concentration and pH can be considered constant. Therefore, for engineering purposes it is instructive to consider where there exists a volume threshold of the electrolyte above which the electrolyte can be considered "infinite", and in which previous metal dissolution does not affect the subsequent degradation rate of the specimens.

To characterize the effects of volume and gentle machanical agitation (shaker with rate of less than 50 rpm) on the *in vitro* degradation rate of the metal(s), plated pure Zn and Zn/Fe-couple (using the checker-C design as an example) specimens are placed in different degradation enviroments (i.e, differing saline volume, with or without agitation). To minimize the the effect of individual specimen degradation fluctuation, each specimen is also placed in different degradation enviroments set-up sequentially as described below; this allowed the tests to be carried out using fewer samples. At least three weight measurements are performed for each specimen under each degradation enviroment. The pH of the saline environment is also monitored during the entire set of degradation tests.

(1) Electroplated Pure Zn Specimens

For pure Zn specimens, the weight of each specimen is measured every 8 hours,

a weight loss rate is calculated every eight hours, and the saline is refreshed every 8 hours. The selected enviroments for the degradation tests are 20 mL saline, 70 mL saline (with and without agitation), 150 mL saline , 200 mL saline (with and without agitation), a total of six environments. The pH of the saline solutions are measured during the degradation tests; it was observed that the pH remained between 6.5 and 7.8 during the entire set of degradation tests.

The degradation rates of eight Zn specimens in different degradation enviroment set-ups are shown as functions of degradation time in Figure 48. The color of the column represents the degradation enviroment. The degradation rate during each enviroment is extracted from the slope of the weight loss per unit of exposed Zn area vs. degradation time. Three such measurements were taken for each environment at times of 8, 16, and 24 hours. The height of the vertical bar is given by the mean of these three measurements, and the error bar is the root-mean-square deviation of these three measurements for a particular enviroment. As an example, consider the specimen $Zn-1$ in Figure 48: $Zn-1$ is first placed in 20 mL saline with agitation at 37 $\pm$0.5°C for 24 hours (with measurements of weight loss being performed at 8, 16, and 24 hours during this first degradation), then $Zn-1$ is placed in a 70 mL saline with agitation environment at 37 $\pm$0.5°C for an additional 24 hours (with measurements of weight loss being performed at 8, 16, and 24 hours during this second degradation). In this manner, during the entire degradation test, the weight of the $Zn-1$ specimen is measured every 8 hours. The saline is also refreshed every 8 hours. The degradation rate of $Zn-1$ is 0.0829 $\pm$ 0.007 $mg/(cm^2 \cdot hour)$ during the initial 24 hours (20 mL saline) and 0.0803 $\pm$ 0.009 $mg/(cm^2 \cdot hour)$ during the second 24 hours (70 mL saline). These numbers represent the means and standard deviations of the weight loss rates measured between 0-8, 8-16, and 16-24 hours for each environment. The average degradation rate of Zn in each enviroment is compared in Figure 49. Note that in the case where there are multiple specimens subjected to

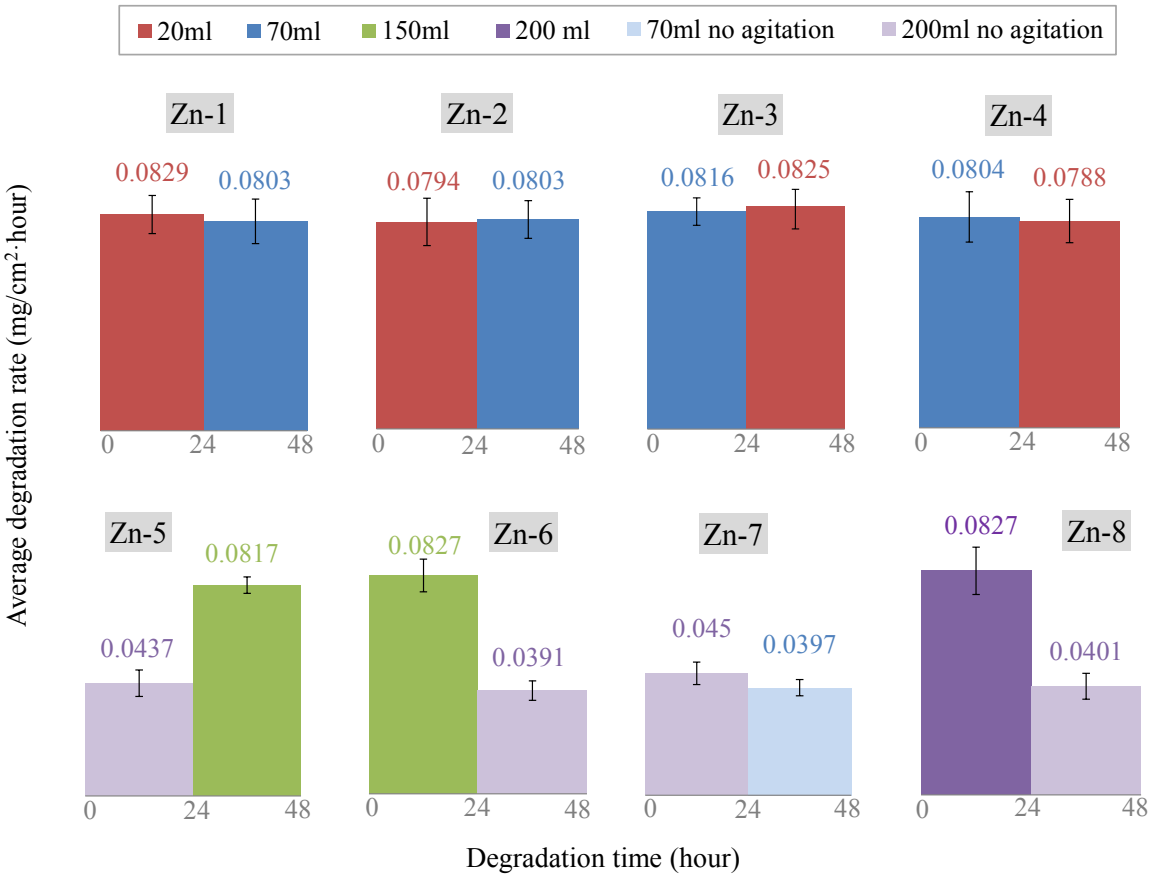

Figure 48: *In vitro* degradation rate as a function of degradation time of eight electroplated Zn specimens in different degradation enviroments. Agitation was employed unless 'no agitation' is specified.

the same environments (for example, the red bars indicating the 20 ml with agitation environment which exist for specimens Zn-1, Zn-2, Zn-3, and Zn-4), the summary red bar in Figure 49 represents the mean and standard deviation of these four bars. In the case of only a single sample is subjected to an environment (for example, the 70 ml with no agitation environment which exists only for specimen Zn-7), the summary light blue bar in Figure 49 is taken directly from Figure 48.

Based on the degradation results in Figure 48 and Figure 49, significant degradation rate differences are observed between the degradation enviroments that employ mechanical agitation and those that do not. For both the 70 mL and 200 mL environments, holding the saline volume constant and varying only the presence or absence of

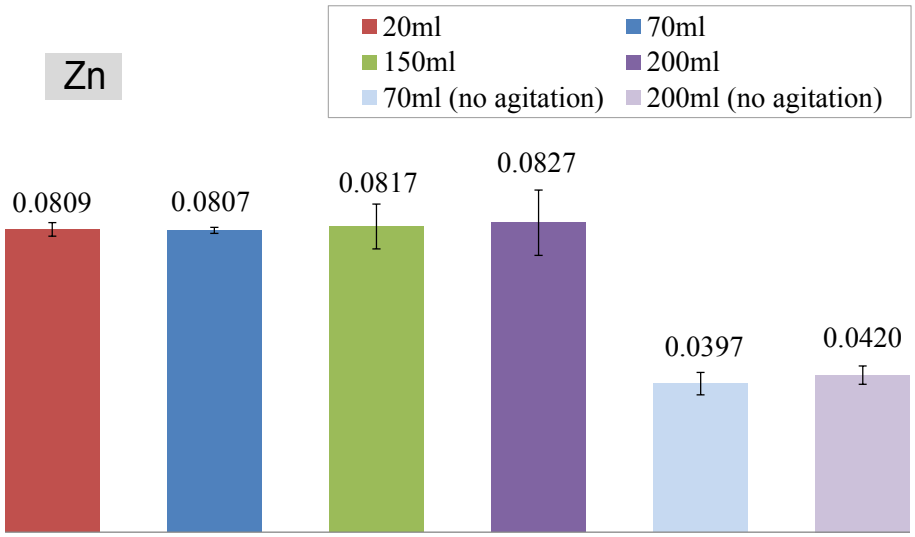

Figure 49: Summary of *In vitro* degradation rate of Zn in different degradation enviroments

agitation resulted in a dramatic decrease of degradation for the cases of no agitation. This effect, consistent across all Zn samples, can also be seen in Figure 48 when a sample moves from an agitation to a non-agitation environment even with a change in saline volume. One potential explanation for this could be local concentration accumulation: without the agitation, the ions move much slower (through diffusion rather than convection); therefore the ions consumed or generated near the corrosion site cannot be as rapidly exchanged with the ions in the electrolyte far away. The local ion concentration and pH near the corrosion site will change significantly and slow down the further degradation of Zn. This explanation could be strengthened by comparing the magnitudes of the diffusion flux of ions to the generation flux of ions during degradation; this was not performed. However, it was observed that un-agitated 200 mL saline had a significantly lower degradatin rate than agitated 20 mL saline, presumably due to elimination of this local concentration accumulation through convection.

With agitation, the degradation rates of Zn in the saline environments of more than 20 mL remain constant at $0.0815 \pm 0.009\ mg/(cm^2 \cdot hour)$, independent of the

total volume of the saline. This degradation rate agrees with the degradation rate deduced above. This justifies the conclusion that agitated 20 mL saline with refresh frequency of 8 hours (the protocol utilized to study the degradation rate of metal(s) in Section 4.2.2) exceeds the volume threshold defined earlier so as to not affect the *in vitro* degradation rate of Zn.

(2) Zn/Fe(checker-C) Specimens

Six Zn/Fe(checker-C) specimens are studied in this section. The weight of each specimen is measured every 4 hours, and the saline is refreshed every 8 hours. The degradation enviroments are 20 mL (with and without agitation), 70 mL (with and without agitation), 150 mL, and 200 mL (without agitation). The pH of the saline remains between 6.7 and 7.9 during the entire degradation test. The degradation rate of each specimen as a function of degradation time is shown in Figure 50.

One phenomenon observed in the degradation rate results of Zn/Fe-couples and not in that of pure Zn (Figure 48 is time dependency. All specimens (except C-1) that begin their degradation histories in agitated saline show degradation rate decreases as degradation time continues. This might be an artifact caused by the Fe consumption and area loss as discussed in the previous section (Section 4.2.2). However, in specimens C-5 and C-6, it is observed that the effect of adding agitation to the system overcomes this prolonged degradation rate decrease phenomenon. For example, consider specimen C-5. From 12-24 hours, C-5 is in an environment of 200 ml saline with no agitation. Subsequent immersion in 70 ml saline with agitation results in a higher degraration rate, even though this sample is now in its third degradation environment.

To exclude the time dependence of the degradation rate comparison among different enviroments, only the degradation rate of each specimen during the first 24 hours are collected for further analysis, consistent with the analysis of Section 4.2.2. In this way, for each enviroment, there are an equal number of degradation rates

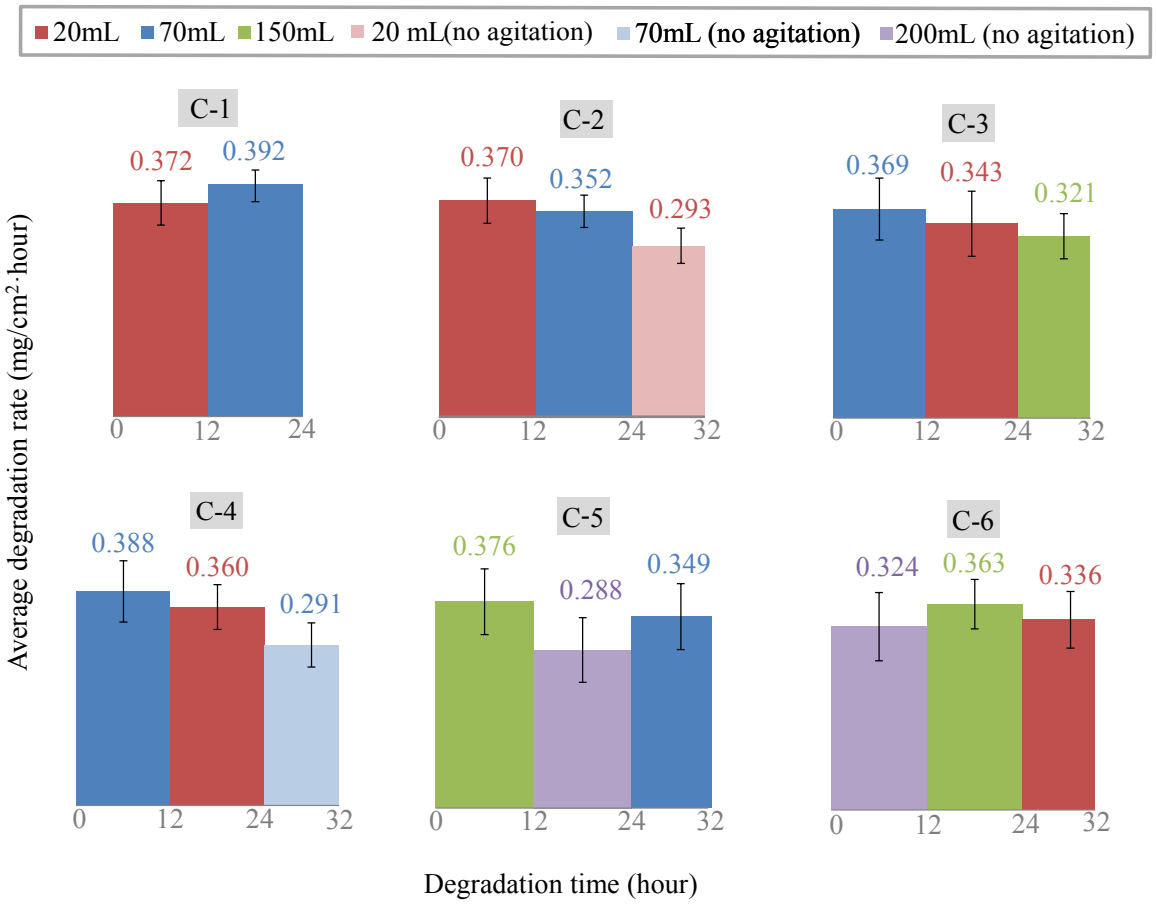

Figure 50: *In vitro* degradation rate as a function of degradation time for six electroplated Zn/Fe(checker-C) specimens in different degradation enviroments. Agitation is applied unless otherwise specified.

collected during the first 12 hours and the second 12 hours. The average degradation rates of Zn/Fe(checker-C) together with the root-mean-square deviation are listed in Figure 51. Similar to the resulf of pure Zn, the degradation rate of Zn/Fe(chekcer-C) in agitated saline with volume from 20 mL to 150 mL remains constant at 0.367 $\pm$ 0.012 $mg/(cm^2 \cdot hour)$. This degradation rate also agrees with the model proposed in Figure 43. Therefore, agitated 20 mL saline with refreshing frequency of 8 hours (the protocol utilized to study the degradation rate of metal(s) in Section 4.2.2) exceeds the threshold volume for Zn/Fe-couple degradation and will not affect the degradation rate.

Based on these results, it can be concluded that by utilizing the protocol in this

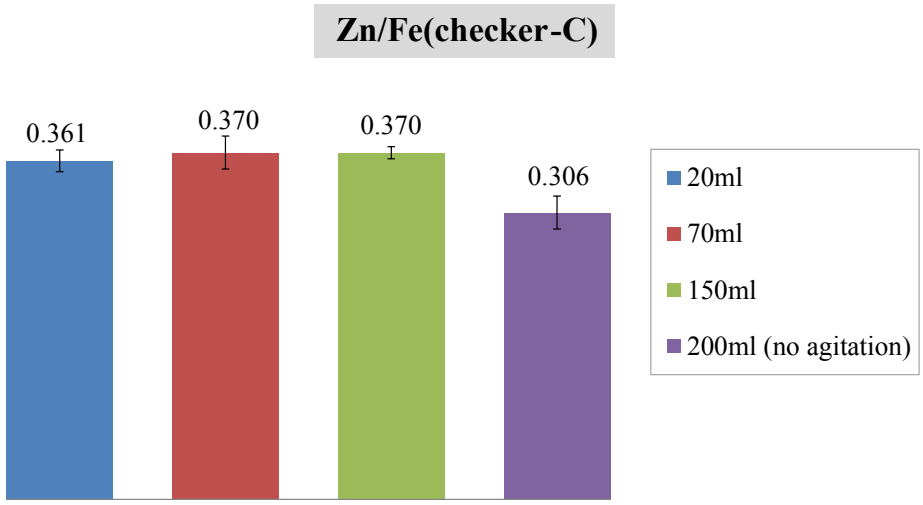

Figure 51: Summary of *In vitro* degradation rate of Zn/Fe(checker-C) under different degradation enviroments. Agitation was utilized unless otherwise specified.

study of degradation rate of biodegradable metal(s) (i.e., immersing each specimen in 20 mL saline, and refreshing the saline every 8 hours) corresponded to the use of an ïnfiniteämount of saline. In other words, the use of a limited volume of saline which might otherwise lead to concentration accumulation and/or pH change in the vicinity of the degradation site will not be a factor for the reduced degradation rate in this metal degradation study if the above protocol is used.

CHAPTER V

MICROFABRICATION OF THE COMPLETELY BIODEGRADABLE WIRELESS PRESSURE SENSOR

As introduced in Chapter 1, MEMS technology has great potential in biomedical applications. However, conventional MEMS fabrication processes, which are usually utilized on silicon wafers and inorganic films, normally involve strong and/or hazardous chemicals. (e.g., hydrofluoric acid (HF), hydrochloric acid (HCl), potassium hydroxide (KOH), ammonium fluoride (NH_4F). For implantable applications, it is critical for these sensors to be completely free of toxic residues. Furthermore, the implantable sensors presented in this work are not only biocompatible, but also biodegradable. Biodegradable materials are naturally more vulnerable to harsh environments and/or chemicals. Therefore, any chemicals or processes that might introduce toxic chemicals to the device or damage the biodegradable materials must be excluded.

In this work, novel fabrication processes that combine conventional MEMS technology with non-wet processes have been developed. Wireless pressure sensors both with and without interlayer conducting vias (see section X) are fabricated using these new processes.

5.1 Fabrication Process of Biodegradable Wireless Pressure Sensor with Conducting Via

The wireless pressure sensor with conducting via is composed of a single planar spiral inductor electrically interconnected with a parallel plate capacitor, shown in Figure 52. The conductor embedded in the polymer structure relies on metal electroplating followed by polymer embossing. A folding technique coupled with polymer

multilayer lamination is utilized after embossing to create the final 3-D device structure with embedded pressure reference cavity and appropriately-positioned conductor elements.

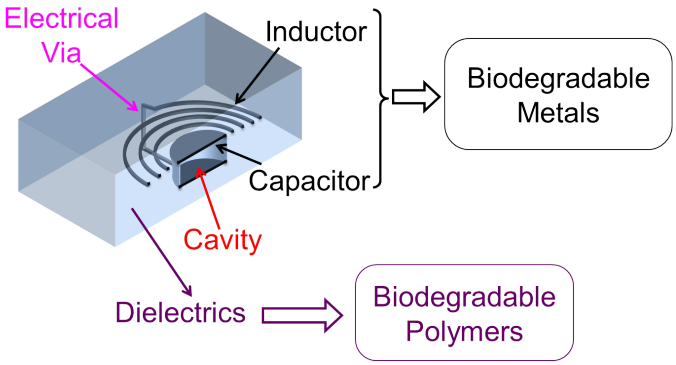

Figure 52: Schematic structure and composition of wireless pressure sensor with conducting via.

The entire fabrication process for the wireless pressure sensors with conducting via can be roughly divided into three parts: (a) building metal conductors, (b) preparing the polymer dielectrics, and (c) assembling the metal and polymer to form the device. The fabrication process for forming metal conductors for all types of fabricated sensors does not vary from sensor to sensor, while the processes involving fabrication of the biodegradable polymers do vary, because of the the dissimilar mechanical and physical properties of these different biodegradable polymers. Biodegradable sensors in this work can be divided into two types based on the main dielectric materials utilized (package materials): PLLA based sensors and PLGA/PVA based sensors. In the following sections, detailed fabrication processes for fabricating pure Zn conductors as well as the additional procedures for Zn/Fe couple conductors is described, followed by the fabrication processes of polymer preparation and sensor assembly of PLLA- and PLGA/PVA-based pressure sensors, respectively.

5.1.1 Fabrication Process of Zn Conductors

The Zn conductors are a planar structure comprising a single planar spiral inductor connected to two capacitor plates. The entire conductor is built on a simultaneous through-photoresist electrodeposition on a flexible and chemically-resistant polymer film (Kapton®) substrate. The detailed fabrication process is schematically depicted in Figure 53.

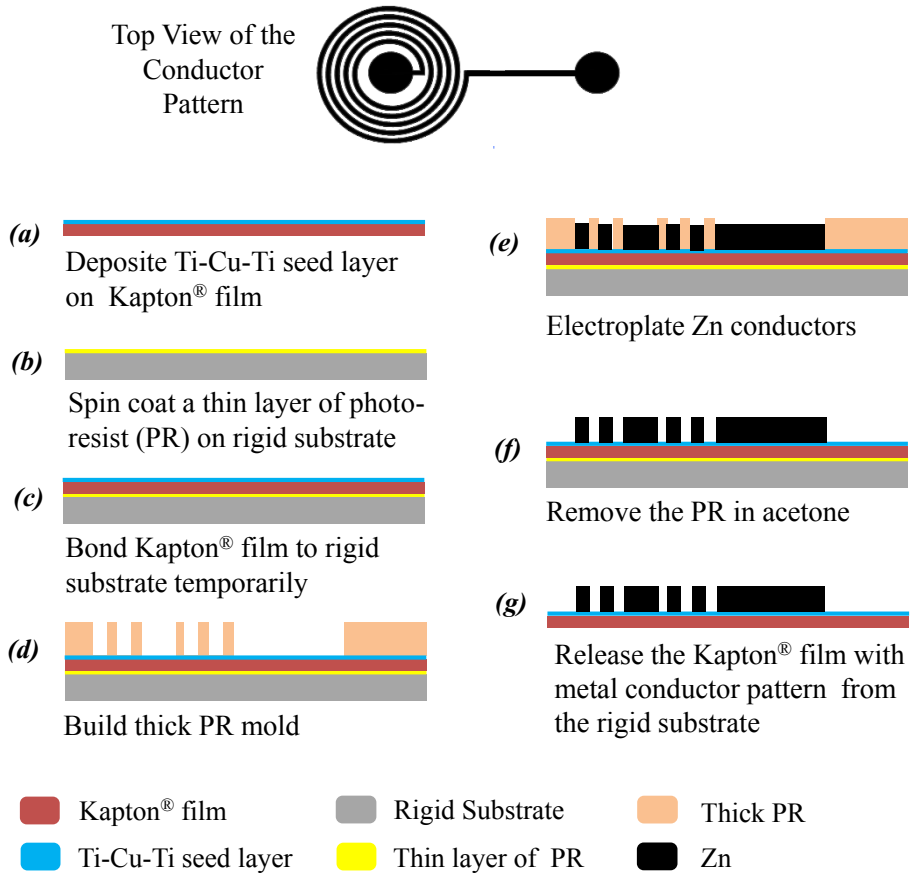

Figure 53: Fabrication process of building Zn conductors on Kapton® film.

The process starts with sputtering a Ti-Cu-Ti seed layer on a pre-cleaned Kapton® film with thickness of 80 μm using a CVC DC sputter (Figure 53(a)). After a thin layer (less than 10 μm) of negative photoresist NR9-1500PY (Futurres, Inc.) is spin coated on to a rigid substrate (silicon wafer) as glue, the Kapton® film with seed layer is temporarily bonded to the wafer (Figure 53(b,c))(the detailed recipe can be found

in Appendix A). The rigid substrate is utilized here as a temporary support to build the photoresist mold for electroplating. Kapton® tape with an approximate thickness of 60 μm is applied on the edge of the Kapton® film occasionally to reenforce the bonding between the Kapton® film and the wafer.

Afterwards, a thick photoresist mold is built on the Kapton® film using photolithography (Figure 53(d)). Zn conductors are subsequently electroplated via pulse reverse electroplating in the mold(Figure 53(e)). Upon completion of electroplating, the photoresist is removed thoroughly in acetone(Figure 53(f)). Depending on the desired thickness of the metal conductor, the thickness range of the mold is from approximately 40 μm to 90 μm. Negative photoresist NR21-20000P (Futurrex, Inc.) and NR22-20000P (Futurrex, Inc.) are used. Both oven and hotplate recipes are used in this work, the details of the recipe can be found in Appendix A. The average current density of electroplating of Zn is 6 mA/cm^2. The electroplating process takes 4 to 10 hours depending on the designed final thickness. Figure 54 shows images of one batch of the electroplated Zn conductors on metalized Kapton® film after the thick photoresist mold has been removed.

The Kapton® film bearing the microfabricated metal conductor patterns is then separated from the rigid substrate (Figure 53(g)). The separation step is readily realized by placing the wafer on a hotplate (110 °C) and using tweezers to peel the Kapton® film off when the thin layer of photoresist (NR9-1500PY) is melted (usually in less than 1 minute). The residue of thin layer of photoresist (NR9-1500PY) beneath the Kapton® film is wiped clean with acetone.

5.1.2 Additional Processes for Zn/Fe-Couple Conductors

As shown in the result of the metal degradation study in Section 4.2, Zn/Fe-couples degrade much more rapidly than pure Zn. Therefore, if a rapid degradation rate is demanded, Zn/Fe-couple conductors, rather than Zn conductors, are preferable.

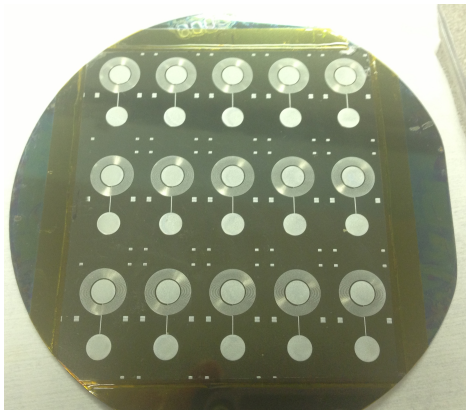

Figure 54: Electroplated Zn conductors on metalized Kapton® film after removing the photoresist and before being released from the rigid substrate.

Some additional processes need to be added prior to assembling the metal conductor with the polymer dielectrics in this case.

5.1.2.1 Electroplate Zn/Fe(bilayer) Conductor

In MEMS fabrication processes, electroplating is generally used to obtain relatively thick metal layers. In the case that more than 1 μm of Fe is required for the Zn/Fe(bilayer) couple conductor, electroplating of Fe and Zn are utilized. To be more specific: in the electroplating step described in Figure 53(e), the specimen is first placed in an Fe bath and the desired thickness of Fe is deposited using direct current electroplating with current density of 5 mA/cm^2. The sample is rinsed in DI water, and then Zn is deposited from a Zn bath using pulse reverse electroplating with average current density of 6 mA/cm^2. Figure 55 shows images of the electroplated Zn Figure 55(a) and Zn/Fe(bilayer) inductor Figure 55(b) on metalized Kapton® film with a close tilted view of the windings. For the Zn/Fe(bilayer) inductor (Figure 55(b)), two metal layers can be clearly seen in the upper right scanning electron microscopy (SEM) image: a thinner, bottom-most Fe layer and a thicker Zn layer with a larger grain size on top.

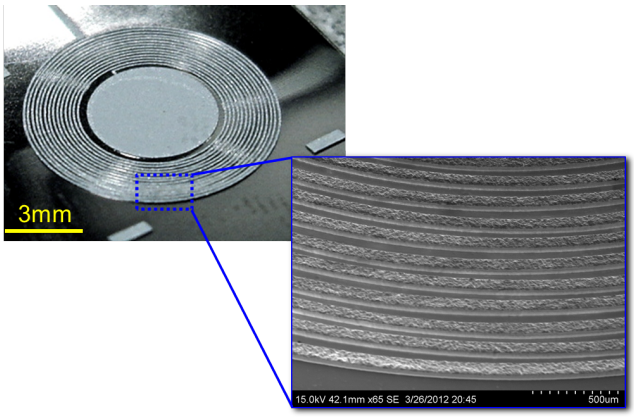

(a)

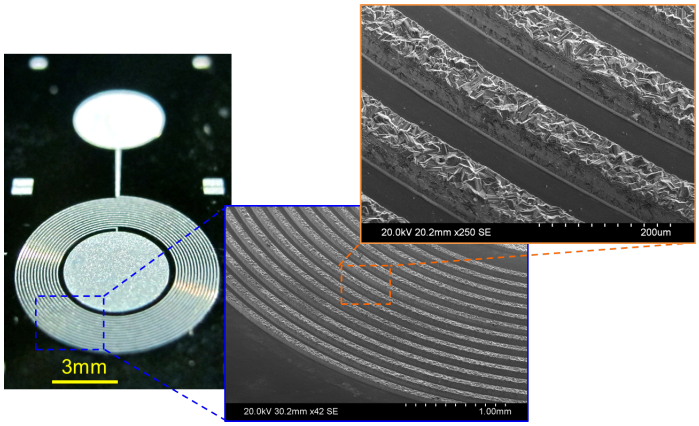

(b)

Figure 55: Electroplated (a)Zn and, (b)Zn/Fe bilayer on metalized Kapton® film

5.1.2.2 Evaporation of Thin Fe on Zn Surface

For the biodegradable sensors that comprise Zn/Fe-couple conductors with either complete or partial coverage of Fe on a single side of Zn, an additional step of evaporating Fe on the Zn surface is required after the Kapton® film bearing the microfabricated Zn conductor is separated from the rigid substrate (step Figure 53(g)). The Kapton® film bearing the microfabricated Zn conductor is placed in the chamber of a E-beam Evaporator (Denton Explorer), and 400 - 700 *nm* of pure Fe is evaporated on the surface of the Zn. The evaporation process and shadow mask design for Fe checker pattern can be found in Section 4.2. After Fe evaporation, the specimen is gently blown using a nitrogen air gun to remove any loose flakes on the Kapton®

surface and between the windings of the inductor coils.

5.1.3 Polymer Preparation and Sensor Assembly of PLLA-based Pressure Sensor

Once the biodegradable conductor patterns have been built on the Kapton® film, the steps to incorporate these patterns into the PLLA based pressure sensor is shown in Figure 56.

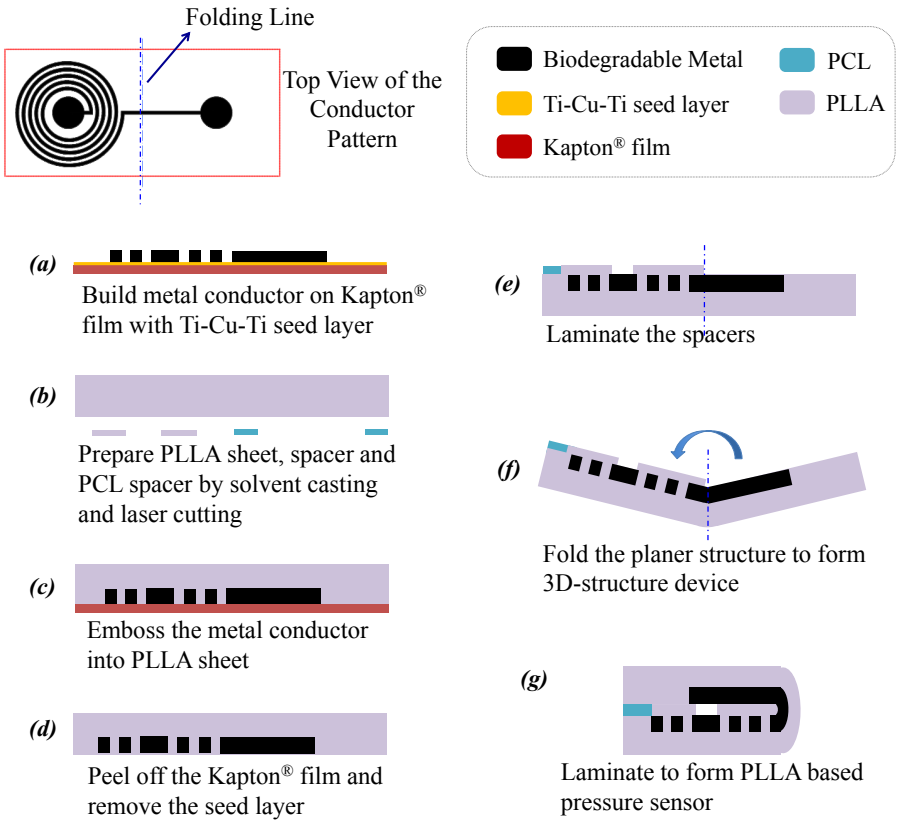

Figure 56: Fabrication process of PLLA-based biodegradable wireless pressure sensor

The polymeric portions of the PLLA-based pressure sensor are comprised of three polymer films: embossing PLLA film, PLLA spacer, and PCL spacer. PLLA and PCL are dissolved in DCM and solvent casted onto a polytetrafluoroethylene (PTFE) petri dish to obtain films with different desired thicknesses at room temperature. After drying completely at room temperature, the polymer films are carefully peeled off

from the substrate. The spacers are patterned as appropriate using a CO_2 laser (Figure 56(b)). The embossing film made of PLLA with a thickness of 200 - 400 μm, will be used to support the entire metal conductor. PLLA spacers with a thickness of 20 - 40 μm are patterned into a toroidal ring to define the sensor cavity. A PCL spacer with a thickness of 40 - 50 μm is patterned to almost completely concentrically surround the outside of the PLLA spacer. Photos of the fabricated PLLA and PCL spacers are shown in Figure 57(a).

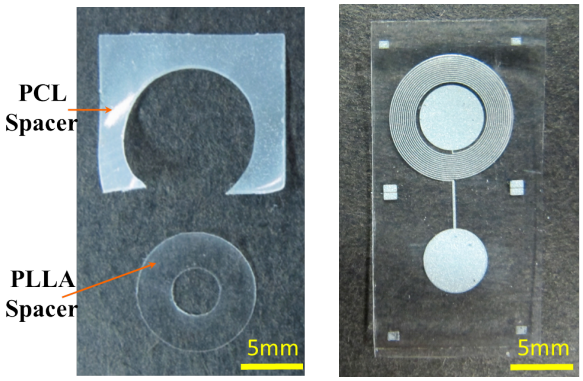

(a) (b)

Figure 57: (a) Spacers made of biodegradable polymers PLLA and PCL, and (b) embossing PLLA film bearing the metal pattern

After the biodegradable polymers are prepared, the Kapton® film with electroplated metal conductors and the embossing PLLA film are laminated under 15-bar pressure at 175 °C for 5 minutes and cooled down to 30°C (using circulatory water to cool down the stage) using a nano-imprinter (Obduct) (Figure 56(c)). After being removed from the nanoimprinter, the specimen is further cooled down under ambient conditions for at least 1 hour. After cooling, the Kapton® film is peeled off carefully from the PLLA embossing film, into which the metal conductors have now been embossed. Any remaining nonbiodegradable seed layer originally existing between the Kapton® and the electroplated metal is removed by micro-polishing, thereby limiting the number of wet processing steps (Figure 56(d)). An example of the resulting structure consisting of 200-μm-thick embossing film bearing the embedded Zn conductor

patterns is shown in Figure 57(b).

The embossing film bearing the metal conductor is then prepared for assembly and lamination. The film is spray-coated with a thin layer of PCL in the regions external to the capacitor plates. The concentration of the PCL in DCM solution for spray coating is 2% wt, and the resultant thickness of the PCL is less than 1μm. The ring-shaped PLLA spacer and the PCL spacer are then solvent bonded to the embossing film consecutively by means of a very small quantity of DCM (Figure 56(e)). Since PLLA film is rigid at room temperature and soft above its T_g, the embossing film bearing the embedded metal and the bonded spacers is then swiftly folded by selectively heating up the folding line to approximately 60 °C (Figure 56(f)). Afterwards, the folded specimen is laminated under approximately 1 bar at 55 °C for less than 1 minute to form the PLLA-based pressure sensor (Figure 56(g)). Finally, the outer device shape is defined and further sealed by CO_2 laser micromachining along the edge of the inductor. The folding technique, adapted from [55] enables the microfabrication of a 3-D device with multiple metal layers and electrical interconnects using a single electrodeposition step. This is particularly favorable when the metallic and polymeric materials are sensitive to chemicals used in conventional microfabrication techniques. In the folding step, it is very critical that the folding line of the PLLA film is neither under heated nor over heated. Otherwise, the embossing film bearing the embedded metal will be either not be soft enough to bend, or will be too soft to mechanically support the conducting via during folding, resulting in breaking of the via. During the final lamination, the PCL spacer together with the thin PCL layer sprayed on the embossing PLLA sheet softened and sealed the cavity. An example of a fully-fabricated and functional 10-mm-diameter device, together with a detailed photomicrograph of the via section, are shown in Figure 58. The design parameters of this device are presented in Table 4.

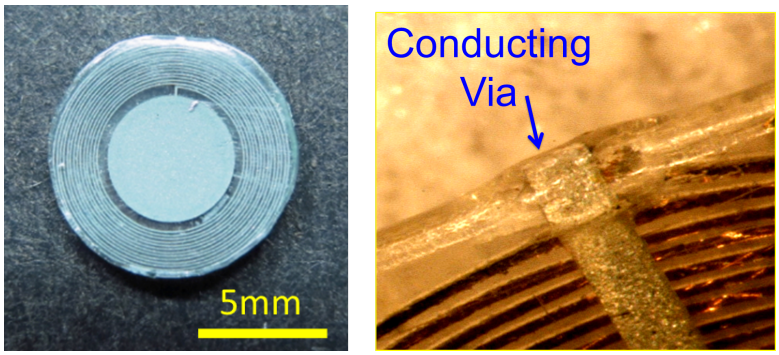

(a) (b)

Figure 58: (a) A functional microfabricated PLLA-Zn RF pressure sensor, and (b) detail view of the conducting via portion

5.1.4 Polymer Preparation and Sensor Assembly of PLGA/PVA Based Pressure Sensor

Biodegradable pressure sensors using a PLGA and PVA "shell-core" stucture as package are designed to degrade much more rapidly than the PLLA-based sensors. Unlike PLLA, PLGA is an amorphous polymer that exhibits no melting point. Therefore the metal conductor pattern cannot be simply embossed into a PLGA/PVA-bilayer polymer sheet in the same manner as PLLA. Several modifications must be made to enable a PLGA fabrication process, as shown in Figure 59.

Generally, there are three polymer films in the PLGA/PVA-based pressure sensor: an outer most PLGA shell film, an embossing PVA film, and a polymer spacer. For the latter films, PLLA inner-spacers and PCL outer-spacers, the same as the PLLA and PCL spacers utilized in PLLA based pressure sensors, were considered initially. However, after studying the performance (Chapter 6) and device degradation (Chapter 7) of the PLGA/PVA sensors with different spacers, the PVA/PLGA-spacer combination and pure PLGA spacer exhibit equally good, if not better, sealing performance, and furthermore degrade more rapidly. Therefore, PVA/PLGA combinations and PLGA spacers are utilized in most of this work.

Similar to the polymer preparation of PLLA-based sensors in Section 5.1.3, all

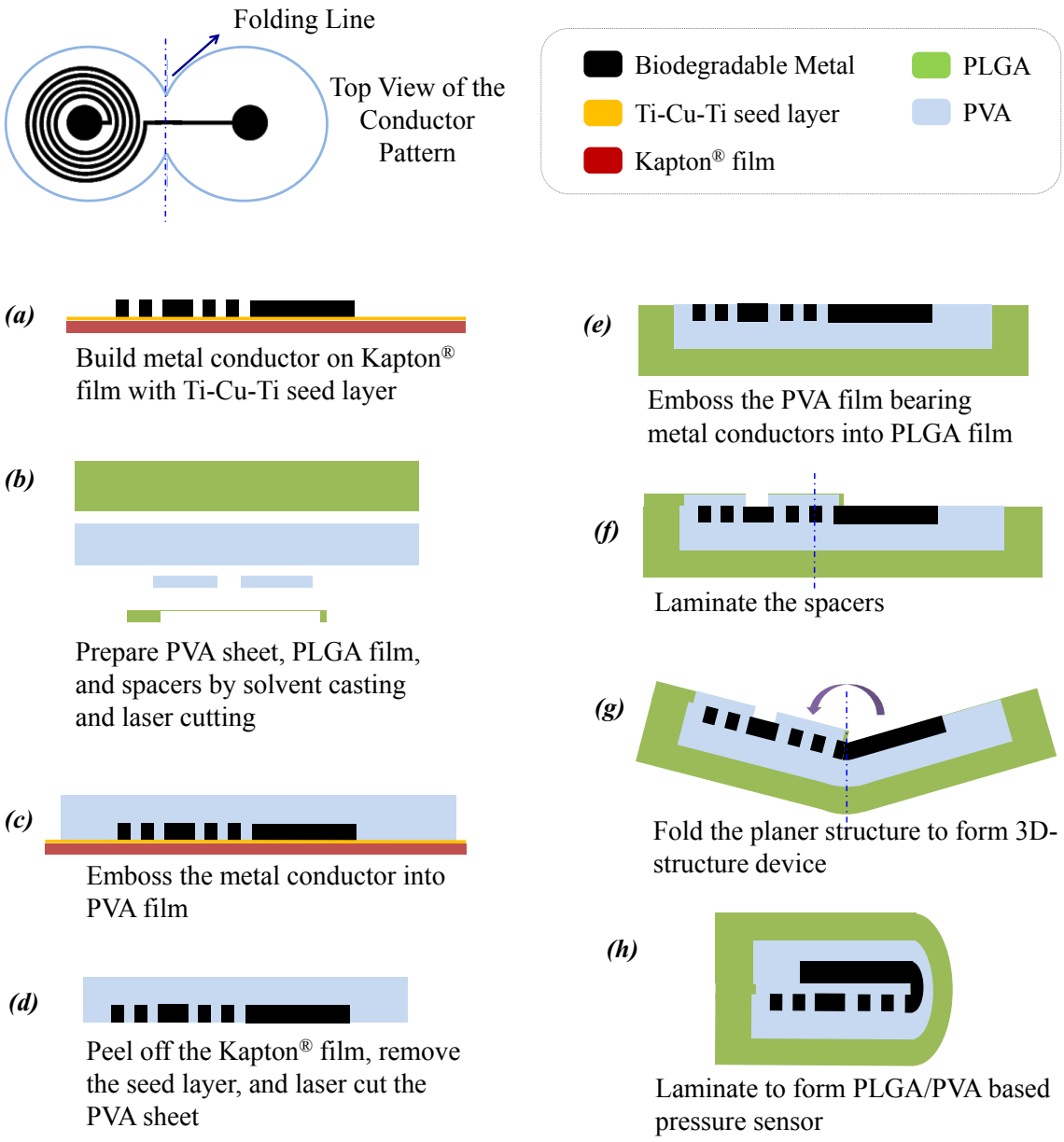

Figure 59: Fabrication process of PLGA/PVA-based biodegradable wireless pressure sensor

the polymer films are solvent cast, and the spacers are patterned into appropriate shapes using a CO_2 laser (Figure 59(b)). PLGA, PLLA and PCL are dissolved in DCM at room temperature, solvent cast in a PTFE petri dish, and dried under room temperature for more than 48 hours. PVA is dissolved in DI water under 80 ∘C for 4 hours to obtain a transparent solution. After cooling down to room temperature, the PVA solution is cast on a piece of glass and dried overnight. After complete drying,

the polymer films are carefully peeled off from the glass substrate. The thicknesses of the PLGA shell film and embossing PVA film are from 200 to 400 μm. The thickness of the spacers is 30 to 50 μm. PVA spacers are dip-coated with PCL in 4 wt% PCL DCM solution. Examples of a fabricated PVA spacer and a PLGA spacer for a PVA/PLGA spacer combination are shown in Figure 60.

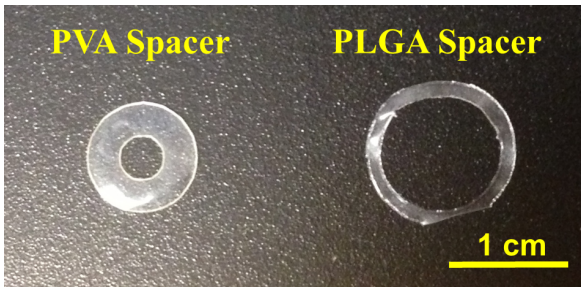

Figure 60: Fabricated PVA spacer (left) and PLGA spacer (right) for PLGA/PVA spacer combination

To form the rest of the sensor, the metal conductor is embossed into the embossing PVA film (Figure 59(c)). After the film is cooled down and relaxed for at least 2 hours, the Kapton® film substrate is peeled off from the PVA embossing film bearing the the metal conductors, and any remaining non-biodegradable seed layer is removed by micro-polishing. Then the PVA embossing film bearing the metal conductors is trimmed by CO_2 laser (Figure 59(d)). Initially, the lamination condition utilized for embossing metal conductor to PVA film is a pressure of 10 bar, a temperature of 165 °C , and a time of 5 minutes. However it has been found in subsequent sensor degradation tests (Chapter 7 that PVA will be cross-linked at such high temperature (165 °C) and is not completely soluble in water under 37 °C. Therefore, a lamination condition of 30 bar pressure, temperature of 130 °C and time of 10 minutes is utilized ultimately. The specimen is cooled down to 32 °C under 30-bar pressure, and further cooled down to room temperature after the pressure is released. A schematic top view of the shape of the resultant PVA embossing film bearing the metal conductors is shown in the top left of Figure 59.

This trimmed PVA embossing film bearing the the metal conductors is then laminated with a PLGA shell film possessing a larger area (Figure 59(e)). The lamination occurs in a nano-imprinter under 10-bar pressure at 60 °C for 4 minutes. It was observed that bubbles are easily trapped during this lamination step. Processes that may help in reducing the chance of bubble formation include: preheating the PLGA film at 65 °C for 1 hour and cooling down to room temperature to further dry the film, and placing the trimmed PVA embossing film bearing the metal conductors on top of the PLGA shell film prior to lamination. However, bubbles were still observed in some sensors. As shown in the pictures of the final PLGA based pressure sensors in Figure 61, very few small air bubbles are trapped in Figure 61(a), several large bubbles are present in Figure 61(b), while barely any bubbles are found in Figure 61(c).

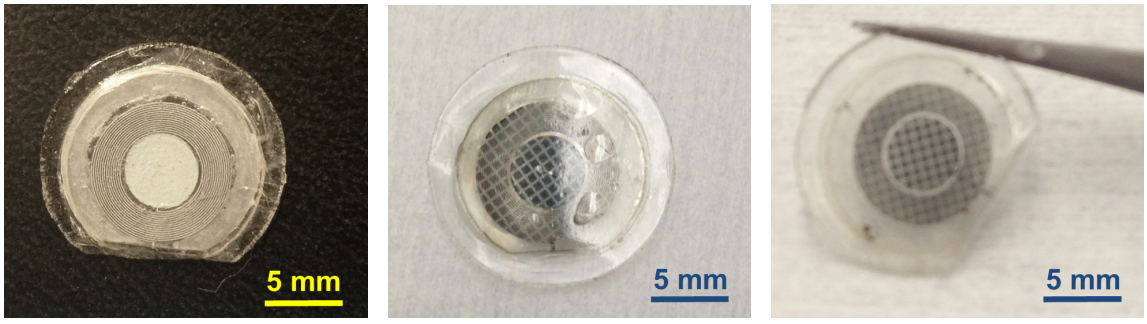

(a) (b) (c)

Figure 61: Examples of fabricated biodegradable PLGA/PVA-based pressure sensors with: (a) Zn conductor and PLLA-PCL spacers, (b) Zn/Fe conductor and PLLA-PCL spacers, and (c) Zn/Fe conductor and PVA-PLGA spacers

The embossing film bearing the metal conductor is then prepared for assembly and lamination. The PVA spacer and the PLGA spacer (or the PLLA-PCL spacers) are solvent bonded to the embossing PVA film consecutively by means of wetting the surface of the embossing film with a very small quantity of water (Figure 59(f)). Then the whole structure is folded swiftly by selectively heating up the folding line

(Figure 59(g)), and laminating to form the PLGA/PVA-based pressure sensor (Figure 59(h)). In this folding step, it is especially critical that the folding line is neither under-heated nor over-heated, since there are two layers of polymer film with distinctive thermal and physical properties that need to be bent at the same time. Upon testing, a temperature of 55 to 58 °C is ideal for the bending step. An extra small piece of PLGA is usually required to be added to the folding area during the folding step to prevent the breaking of the PLGA shell film at this line (this can be seen at the bottom of the sensor shown in Figure 61(a), and the similar asymmetric features in all of the sensors in Figure 61. The proper temperature for the final lamination step is approximately 55 °C for device with PLGA outer-spacer, and 60 °C for device with PCL-outer-spacer.

Finally, the outer device shape was defined by CO_2 laser micromachining. Examples of three fully-fabricated and functional PLGA/PVA based pressure sensors are shown in Figure 61. The PCL spacer appears opaque at room temperature, while both PVA and PLGA appear completely transparent. Based on the sharp boundary of the PCL spacer (i.e., lack of apparent PCL flow) in the sensor shown in Figure 61(a), it can be concluded that sometimes the PCL spacer is not completely melted during the final lamination step. However the sensor is sealed on the edge by the PLGA shell film.

5.2 Fabrication Process of Biodegradable Wireless Pressure Sensor Without Conducting Via

Wireless pressure sensors without a conducting via are composed of two single planar spiral inductors connected with a capacitor plate in the center, and positioned such that the inductors and capacitor plates on respective layers overlap each other. The two inductors are capacitively and inductively coupled, shown in Figure 62.

Similar to that of wireless sensor with conducting via, the fabrication process of the sensors without conducting via can be divided into three parts: fabricating

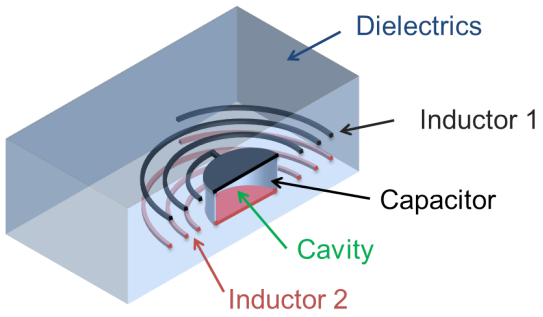

Figure 62: Schematic structure of wireless pressure sensor without conducting via.

biodegradable metal conductors, preparing biodegradable polymer films, and assembling the device. Because there is no vertical conducting via that connects the top and bottom metal conductors, the device can be assembled by lamination of three layers: top and bottom polymer film bearing metal conductors with a spacer film in between. The metal of the conductor in the sensor can be either pure Zn or a Zn/Fe couple, and the dielectric polymer can be either PLLA or PLGA/PVA "shell-core" structure. Only PLVA/PVA-based wireless sensors without conducting via are fabricated and studied in this work due to their relatively rapid degradation rate. The fabrication process is shown in Figure 63.

The fabrication processes of building metal conductors (Figure 63(1)), preparing PLGA and PVA films (Figure 63(2)) and and embossing metal conductors into PVA embossing film (Figure 63(3-a,b)) are the same as that of sensors with conducting via, except that the design and thickness of the metal inductor are different. The detailed process can be found in Section 5.1.1 and Section 5.1.4. Then PVA and PLGA spacers are laminated on the surface of one PVA embossing film bearing metal conductors by wetting the PVA surface with moisture (Figure 63(3-c)). Then another piece of PVA film bearing metal conductors is laminated on the top of the the spacers under approximately a 1 bar pressure and a temperature of 65 °C for 1 minute (Figure 63(3-d)). Afterwards, the specimens are laminated with two PLGA films, one piece on the top and one piece in the bottom, under a pressure of approximately 1 bar at 55 °C

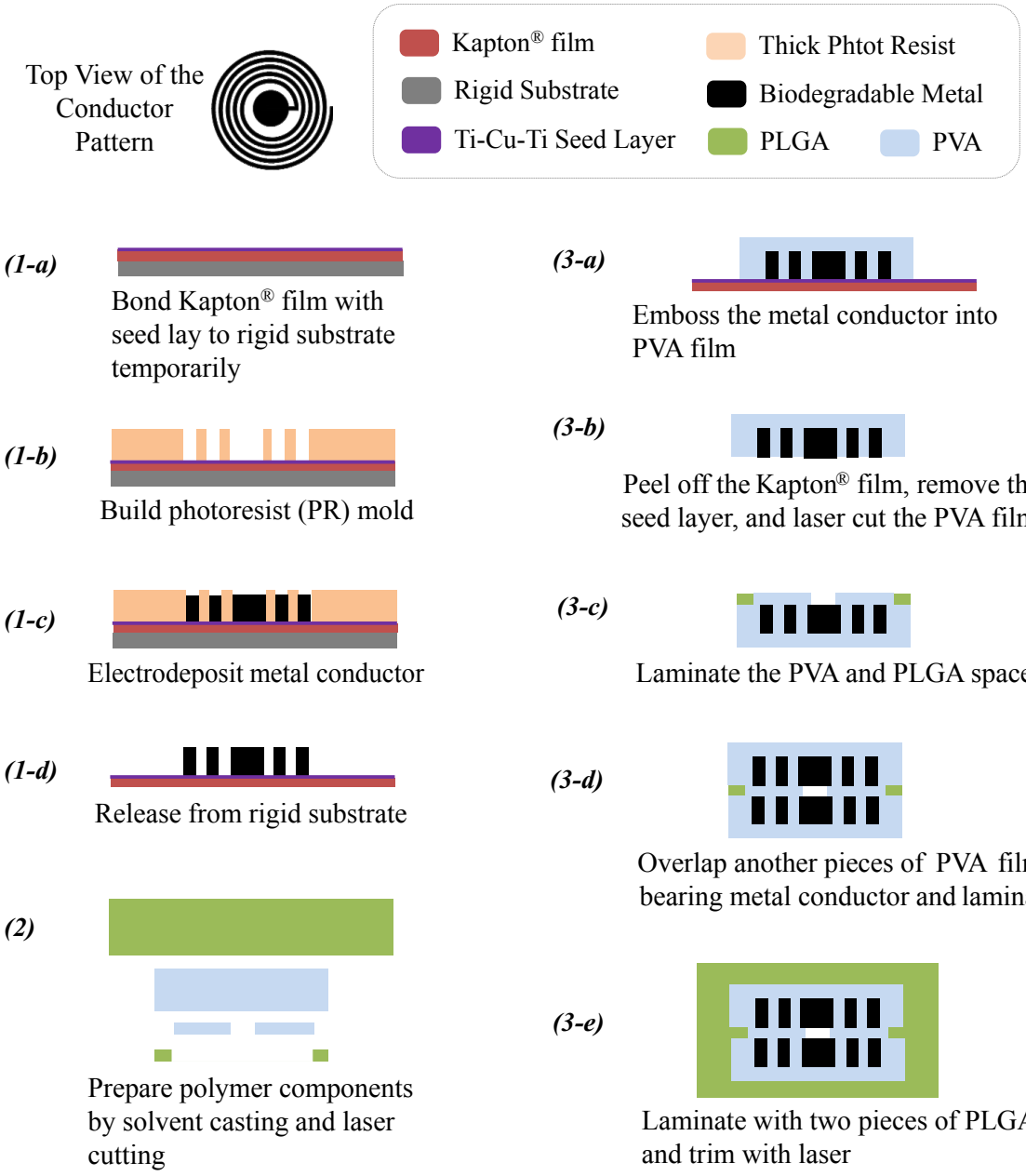

Figure 63: Fabrication process of PLGA/PVA based wireless pressure sensor without conducting via

for 1 minute. After cooldown, the sensor is trimmed by CO_2 laser micromachining to define the final outer shape (Figure 63(3-e)). Markers, which are designed on the mask for photolithography and plated simultaneously with the conductors, are used to align the top and bottom conductors during the lamination of the two PVA films bearing metal conductors. These markers are trimmed away together with the edge

of the sensors during the laser micromachining. Examples of fabricated PLGA/PVA based pressure sensors without conducting via are shown in Figure 64. Figure 64(a) is a semi-complete pressure sensor with Zn conductor design *A* after step (Figure 63(3-d)). Figure 64(a) is a fully fabricated biodegradable sensor with Zn conductor design *B*. The parameters of the design *A* and *B* are shown in Table 9

Table 9: Conductor design of the sensors with no conducting via

Component	Parameter	Design A	Design B
Inductor	Number of turns	13	12
	Line width (μm)	80	120
	Line spacing (μm)	70	25
	Inner radius (mm)	2.9	3.8
	Thickness (μm)	2.9	3.8
Capacitor plate	area (mm^2)	22.9	13.1

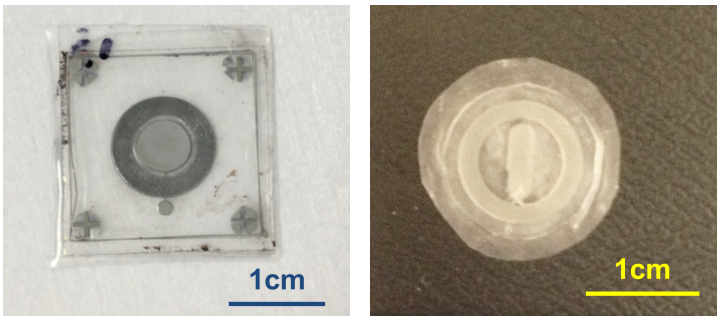

(a) (b)

Figure 64: Examples of fabricated biodegradable Zn-PLGA/PVA pressure sensors without conducting via: (a) with conductor design *A* before laser micromachining, and (b) with conductor design *B*

CHAPTER VI

FUNCTIONALITY STUDY OF THE BIODEGRADABLE PRESSURE SENSORS

6.1 Metal Inductor Characterization

As discussed in Chapter 3, the inductance of the metal conductor together with the variable capacitance define the resonant frequency f_0, whereas the quality factor Q affects the wireless detecting distance of the sensor. Therefore, it is very important to measure the inductance and Q. Prior to folding and laminating the embossing film bearing the metal inductor and capacitor plates, the inductance and Q values of the inductor pattern of all the sensors are measured directly using an impedance analyzer. Referring to Figure 57(b), the impedance analyzer probes are placed on the two capacitor plates.

The inductance and Q of pure Zn and Zn/Fe-couple inductors are compared. Figure 65 shows the measured inductance and Q of the pure Zn and plated Zn/Fe-bilayer inductor as a function of frequency and parameterized by Fe thickness. The dimension of the inductors can be found in Table 4 in Chapter 3. The total metal thickness of the inductors was held constant at approximately 65 μm. An inductance of approximately 1.9 μH was observed at frequencies below 50 MHz independent of the relative thicknesses of Zn and Fe; this result agrees with the value calculated by the current sheet model in Chapter 3. At higher frequencies, Q decreases as the relative thickness of Fe increases, due to the well-known poor AC conductance of Fe at higher frequencies. Therefore, to obtain a wireless sensor with high Q, the use of thick and continuous Fe as the metal conductor is not favorable. However, as shown in the degradation result of the metals in Section 4.2, the existence of Fe is necessary

for accelerated degradation.

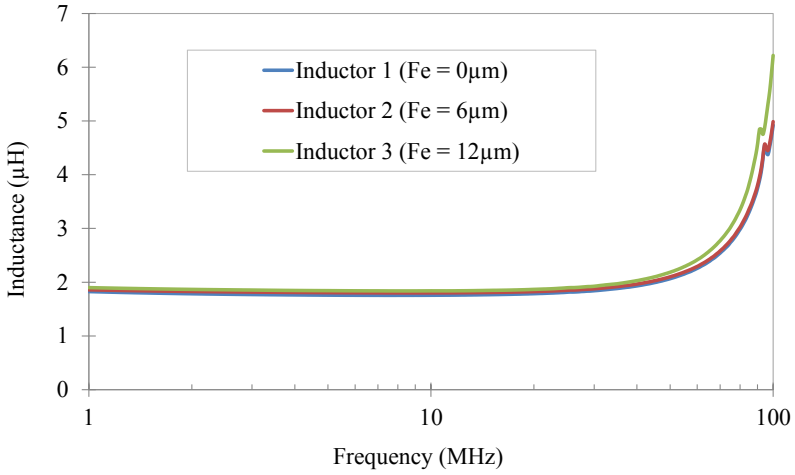

(a)

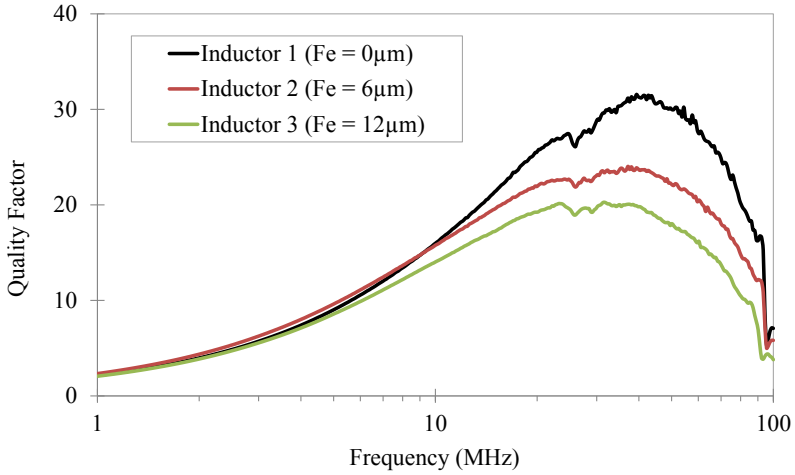

(b)

Figure 65: (a) Inductance, and (b) Q-factor of the Zn-only inductor (inductor #1) and Zn-Fe bilayer inductors with different Fe thickness (inductors #2 and #3). Total metal thickness (Zn + Fe) was held to a nominal 65 μm total.

Therefore, to achieve rapid degradation without sacrificing Q, Zn/Fe-couple inductors with partial Fe coverage on one side (referred to as Zn/Fe(checker) inductors) are fabricated and characterized. The measured inductance and Q of Zn/Fe(checker) inductors with different Fe : Zn area ratios on a single surface are compared with that of pure Zn inductor in Figure 66. The electrical performance of the Zn/Fe(checker) inductor is identical to that of the pure Zn inductor. An inductance of approximately 1.9

μH was observed at frequencies below 70 MHz for all three inductors (Figure 66(a)). All the inductors exhibit Q above 25 between 20 to 90 MHz independent of the Fe coverage ratio (Figure 66(a)).

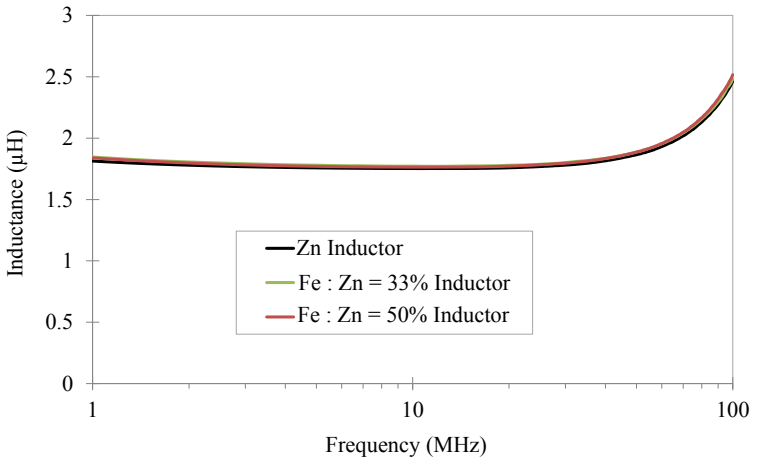

(a)

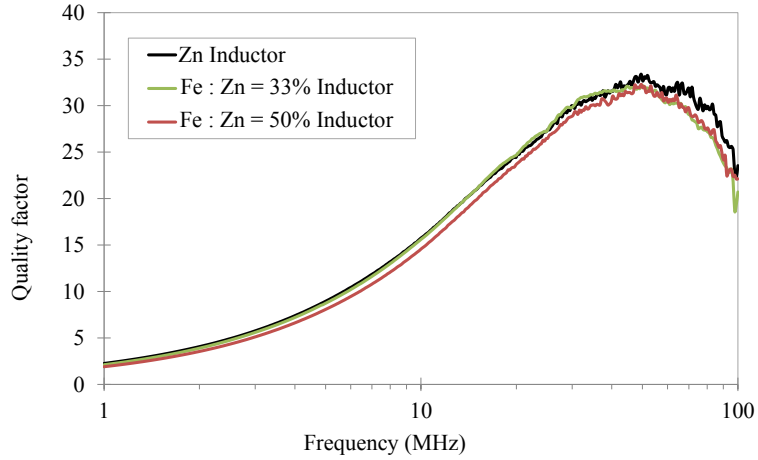

(b)

Figure 66: (a) Inductance, and (b) Q of the pure Zn inductor and Zn/Fe(checker) inductors with different Fe : Zn area ratio on single surface

6.2 Experimental Set-up for Wireless Characterization of Biodegradable Pressure Sensors

All the fabricated pressure sensors are characterized wirelessly by inductive coupling with an external coil that is connected to an impedance analyzer (Figure 67). The measuring distance is approximately 3 mm, and the impedance phase and magnitude

are recorded as functions of frequency.

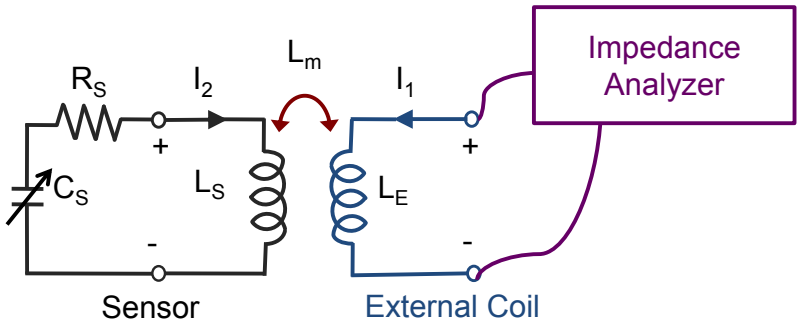

Figure 67: Equivalent circuit electrical model for a sensor coupled with an external coil

6.2.1 Resonant Frequency f_0

The external coil (5 turns, diameter = 1 cm) has a measured inductance (L_e) of 4.3 μH below 80 MHz and Q more than 200, and shows no self-resonances in the measurement frequency range of 1 to 100 MHz. As discussed in Chapter 3, the input impedance of the antenna Z_1 can be expressed in terms of the parameters of the coupled sensor by Eq. (53):

$$Z_1 = \frac{V_1}{I_1} = j2\pi f L_E \left[1 + k^2 \frac{\left(\frac{f}{f_0}\right)^2}{1 - \left(\frac{f}{f_0}\right)^2 + \frac{j}{Q}\left(\frac{f}{f_0}\right)} \right] \tag{53}$$

where the f is the frequency, L_E is the inductance of the external coil, k is the coupling coefficient, Q is the quality factor and f_0 is the resonant frequency.

By using this model, f_0, Q, and k can be extracted from the measured Z_1 as a function of f by curve fitting. An example of the results of impedance measurement and simulation use curve fitting of a PLLA-Zn sensor is graphed in Figure 68.

At resonance, the sensor induces a change in the impedance phase and magnitude of the external coil. The minimum of the phase f_{min} occurs at 32.92 MHz. The Q, k, and f_0 obtained from the fitting result are 24.52, 0.1576 and 32.71 MHz respectively. The f_{min} is only 0.64% higher than the acutal f_0. Based on the discussion in Chapter 3, for small values of k and large values of Q, the relationship between f_{min} and

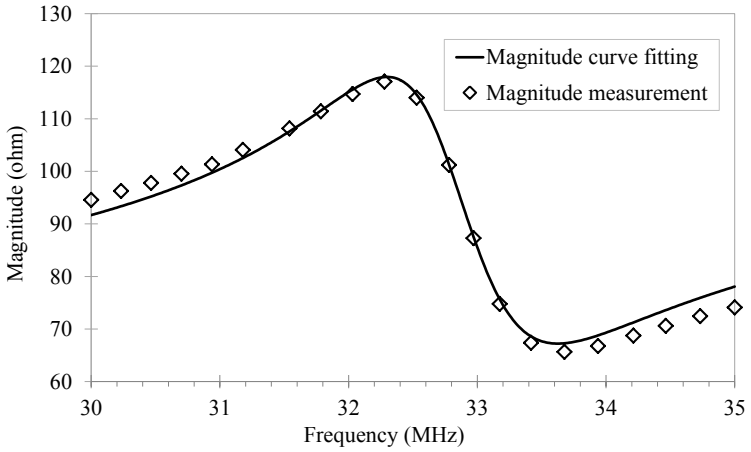

(a)

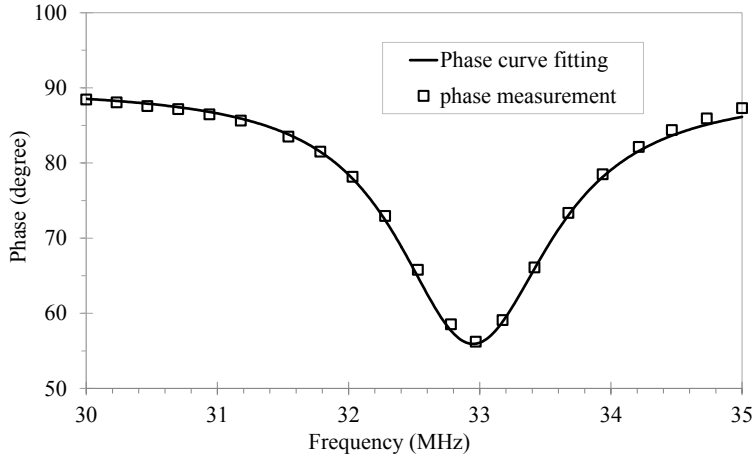

(b)

Figure 68: Measured and simulated curve fitting (a) impedance magnitude, and (b) impedance phase of a PLLA-Zn biodegradable wireless pressure sensor

f_0 can be shown to be [33]:

$$f_{\min} = f_0 \left(1 + \frac{k^2}{4} + \frac{1}{8Q^2}\right) \tag{54}$$

With k less than 0.2 and Q larger than 5, the difference between f_{min} and f_0 is smaller than 1.5%. Therefore, in the following sections of sensor characterization, the value of f_{min} obtained from the phase of measured impedance is used as the resonant frequency f_0 of the sensor.

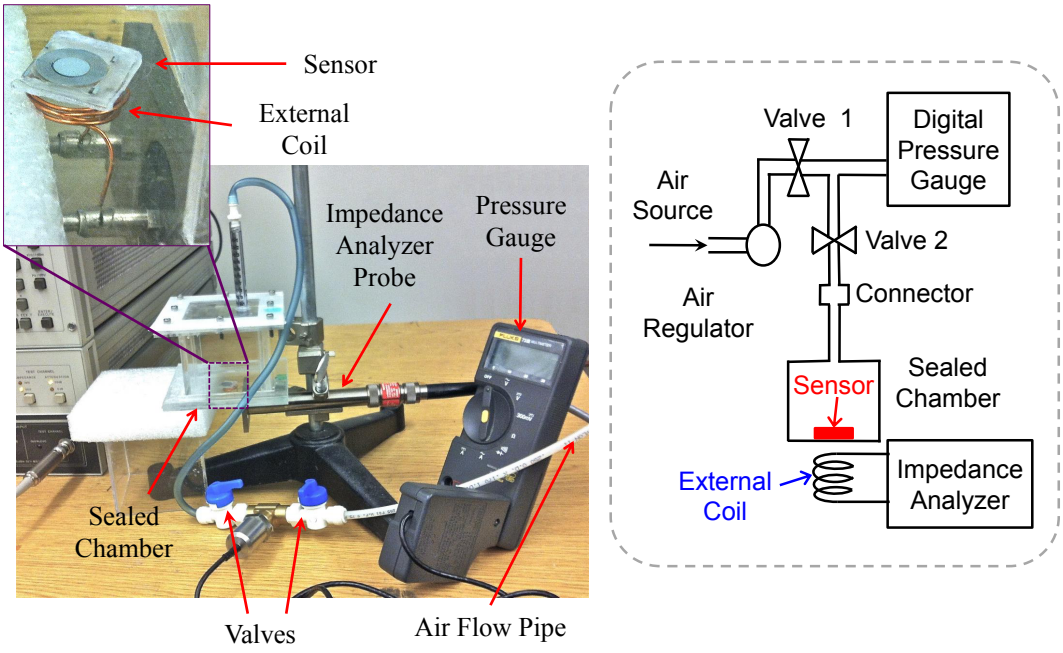

Figure 69: Pressure sensor test measurement setup. (a) photograph of apparatus; (b) schematic drawing of apparatus

6.2.2 Pressure Sensitivity

To determine the pressure sensitivity of the fabricated sensor, the sensor is placed in a sealed chamber instrumented with a pressure gauge (Figure 69). The internal pressure of the chamber was controlled by application of compressed air via an external source. The air regulator controls the flow of the air into the chamber. After the chamber with the sensor placed inside is closed and sealed, a connector is used to connect the pressure delivery components to the chamber. To apply pressure to the sensor, both valves are opened, the air regulator is turned on and adjusted to control the applied pressure, and the pressure value can be read from the attached digital pressure gauge. When the pressure reaches and is stabilized at the value set for the measurement, valve 1 is closed to prevent possible air flow to the sensor during measurement. After the impedance phase and magnitude is recorded for this pressure value, value 1 is opened again and pressure is changed to next set-value. This acrylic chamber, machined

from acrylic sheet by CO_2 laser and glued by epoxy, has low leakage (as evidenced by its ability to maintain a constant pressure as read by the gauge with valve 1 closed over the duration of a measurement), and was tested up to 50 kPa air pressure without bursting. Aqueous environments could also be maintained in this apparatus by partially filling the sealed chamber containing the sensor with liquid.

The pressure response of the sensor was measured at multiple discrete pressure values from 0 to 30 kPa, corresponding to typical physiological pressure ranges found in the body [127, 121]. At each pressure value, the impedance phase as a function of frequency is recorded. Examples of impedance phase as a function of frequency at different pressure values of a fabricated PLLA-Zn device are shown in Figure 70. As the applied pressure is increased, the frequency at which the phase minimum occurs shifts monotonically to lower frequencies. The frequency shift is due to the pressure-induced deflection of the PLLA/metal sensor plates, resulting in a decrease in the capacitor gap, and therefore an increase in capacitance and decrease in f_0.

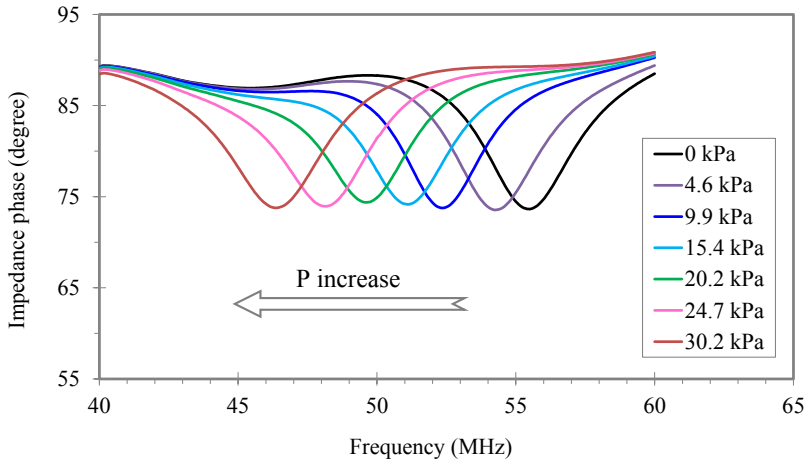

Figure 70: Impedance phase data as a function of frequency for several applied pressures of a PLLA-Zn biodegradable pressure sensor

The impedance measurements for microfabricated RF pressure sensors are repeated several times under multiple pressure conditions. f_0 at each pressure is plotted

as a function of pressure applied, and the slope is taken as the sensitivity of the pressure sensor. The f_0 as a function of applied pressure of the same PLLA-Zn pressure sensor mentioned above in both air and DI water environment is plotted in Figure 71. A sensitivity of - 290 kHz/kPa is measured in air, with comparable sensitivity in water.

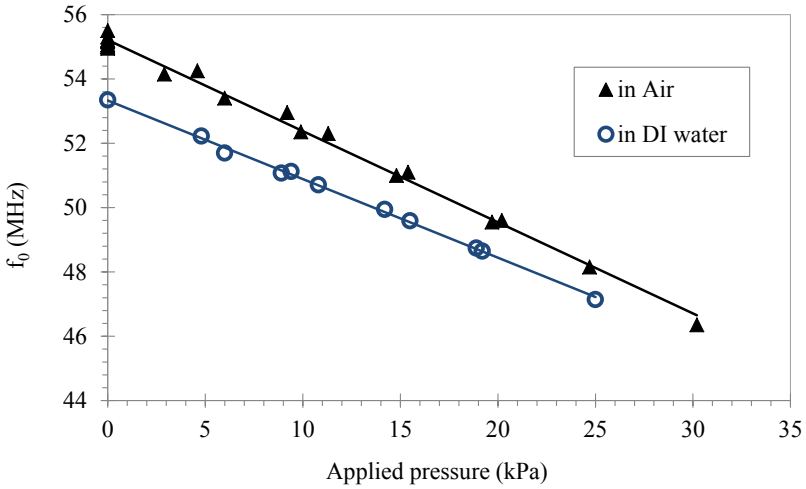

Figure 71: Resonant frequency $f_0$as a function of applied pressure of a PLLA-Zn biodegradable pressure sensor in air and DI water

6.3 Functionality Characterization of Biodegradable Pressure Sensors with Conducting Via

6.3.1 Functionality Measurement of PLLA-based Pressure Sensor in Air and *In Vitro*

The short-term performance stability of a fabricated PLLA-based sensor is first characterized. Initially, there is no extra pressure applied to the sensor, then 10 kPa pressure is applied and maintained for approximately 60 minutes and then released. The impedance is recorded through the entire process and f_0 is extracted and plotted as a function of time, as shown in Figure 72. f_0 decreases from approximately 55.2 MHz to 52.5 MHz when 10 kPa is applied, and remains relatively stable. When the pressure is released, f_0 responses instantly and stabilizes back at 55.2 MHz. Based

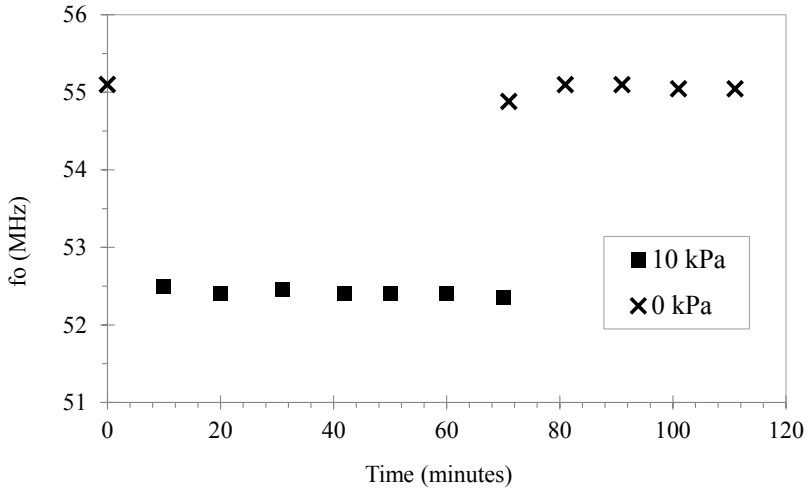

Figure 72: Short term performance stability of the fabricated PLLA-based pressure sensor

on this result, it can be concluded that the pressure/frequency response of the micro-fabricated PLLA-Zn biodegradable pressure sensor does not significantly drift in the short term.

The PLLA-Zn/Fe sensors contain PLLA embossing film with thickness of 200 to 400 μm as the main dielectric (package), and electroplated Zn/Fe bilayers with 60 μm-thick Zn and approximately 5 μm-thick Fe as conductors.

The sensor is first measured in an air enviroment with an applied pressure range of 0 to 25 kPa. Then the chamber is filled with DI water to a depth of approximately 5 mm. The sensor is immersed in DI water, and the pressure-response measurement is performed after the chamber is sealed. Following this, the sensor is taken out and wiped dry with tissue, and the chamber is cleaned and filled with a saline solution (0.9% NaCl in DI water) to a depth of approximately 5 mm. The sensor is immersed in saline, and pressure-response measurement is performed after the chamber is sealed. After this, without removing the sensor, a long-term immersion test under room temperature is performed to investigate the stability and functional lifetime of the sensor *in vitro* at room temperature. The test consisted of holding the sensor immersed in saline at zero applied pressure until no resonance can be observed. Intermittently

during this test, and while immersed in saline, pressure-response measurements are performed to assess sensor sensitivity. The performance study results of four PLLA-Zn/Fe sensors numbered as PLLA-Zn/Fe sensor 1, 2, 3 and 4 are presented here. These four sensors have similar design of the metal conductor, while the thickness of the PLLA package varies. The PLLA embossing film thickness of sensors 1, 2, 3 and 4 are approximately 200 μm, 200 μm, 130 μm, and 350 μm respectively.

6.3.1.1 PLLA-Zn/Fe Sensor 1

The measured phases of the external coil as a function of frequency for several applied pressure values of the PLLA-Zn/Fe sensor 1 in air and in 0.9% saline are shown in Figure 73. Then the resonant frequency of this sensor in air and saline is obtained from the respective impedance-frequency result and plotted as a function of applied pressure in Figure 74.

f_0 shifts to lower frequency as the applied pressure increases, due to the capacitance increase. In air, the sensor has a resonant frequency of 31.8 MHz at zero applied pressure, and a sensitivity of -39 MHz/kPa. Upon immersion of the sensor in saline, the sensor resonant frequency falls from 31.8 MHz to 30.5 MHz. A slightly decreased sensitivity (-34 kHz/kPa) of the sensor is also observed. This behavior is consistent with previous non-biodegradable devices [34] and is due to electrical interactions of the sensor with the embedding medium.

In the prolonged long-term immersion test, PLLA-Zn/Fe sensor 1 is kept immersed in saline at zero applied pressure for approximately 170 hours. Selected recorded phase behaviors as function of frequency are shown in Figure 75. It is very clear that once the sensor is placed in saline, the trough of the impedance phase becomes broader and shallower. As the sensor is kept in saline for longer times, the trough of the impedance phase continues become even broader and shallower, corresponding to a decrease of Q. After the sensor has been immersed in saline for 144 hours, only a very small

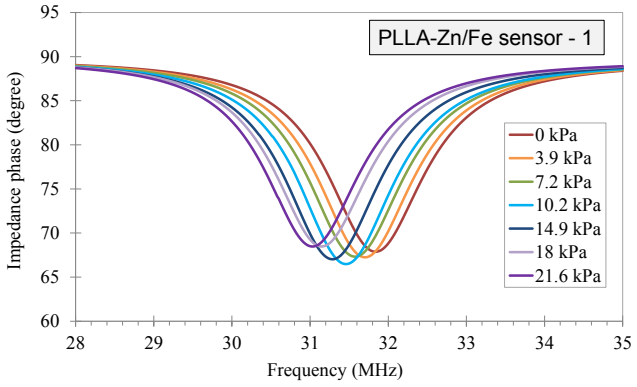

(a)

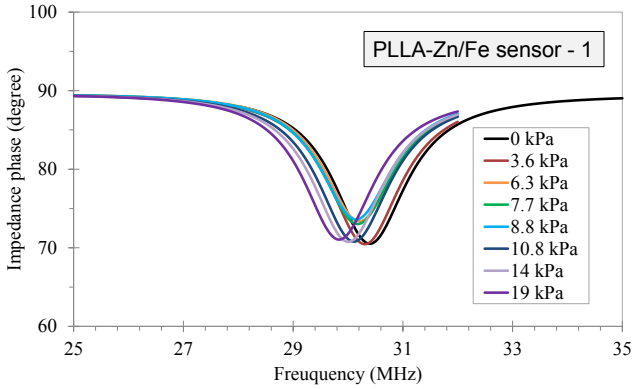

(b)

Figure 73: Measured impedance phase as a function of frequency at several applied pressures for PLLA-Zn/Fe sensor 1 in (a) air, and (b) saline (0.9% NaCl)

trough can be observed. The resonant frequency f_0 of the sensor during the entire long-term immersion test without applied pressure, together with the calculated Q, are plotted as functions of the immersion time in Figure 76.

The performance of the sensor can be divided into three stages. In stage one, within the first 21 hours of immersion for PLLA-Zn/Fe sensor 1, the sensor is observed to equilibrate with the immersion environment. f_0 increases rapidly from 30.5 MHz to 31.5 MHz within the first 6 hours and drops gradually to 30.7 MHz, while Q drops rapidly from 18.9 to approximately 10 within this time period. This stage can be referred to as the equilibration stage.

In stage two, between 21 to 107 hours, f_0 remains relatively constant at 30.7 ± 0.1

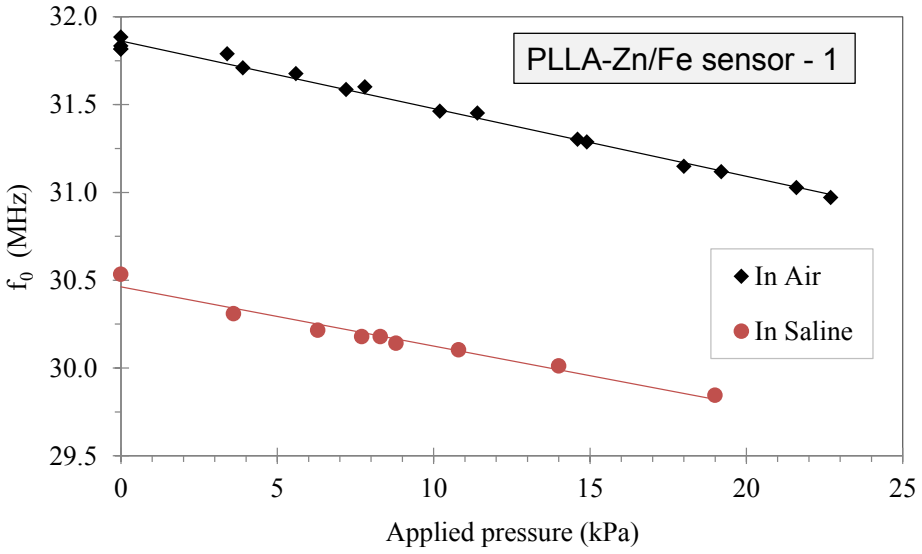

Figure 74: Resonant frequency (f_0) of the pressure sensor as a function of applied pressure of PLLA-Zn/Fe sensor 1 in air and 0.9% saline environments (within 30-minute immerse time).

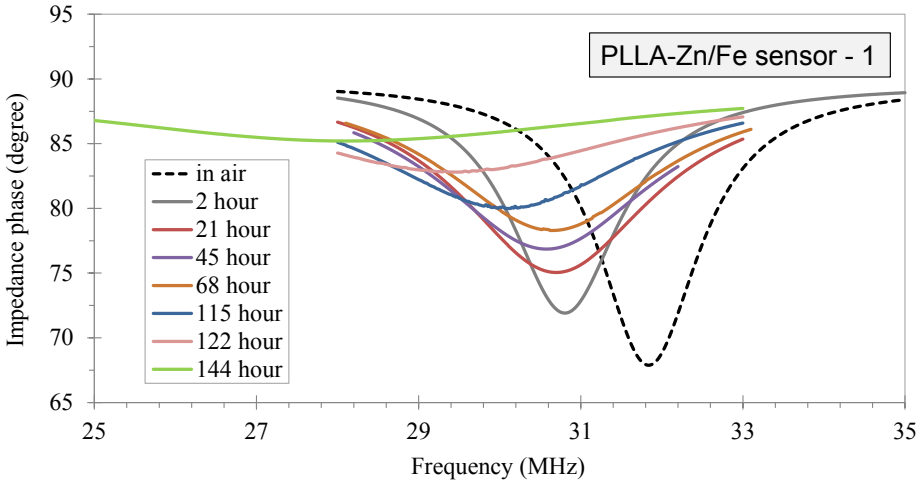

Figure 75: Impedance phase as a function of frequency of PLLA-Zn/Fe sensor 1 at selected immersion time points in saline.

MHz and the Q remains relatively stable above 9.0. Pressure-response measurements are taken at immersion times of 8 hours, 26 hours, 34 hours, 57 hours, 79 hours and 96 hours. Each resonant frequency f_0 together with that of 0 hours are plotted as a function of applied pressure, as shown in Figure 77. The sensitivity of the sensor at each immersion time, represented by the slope of each trend line in Figure 77, are

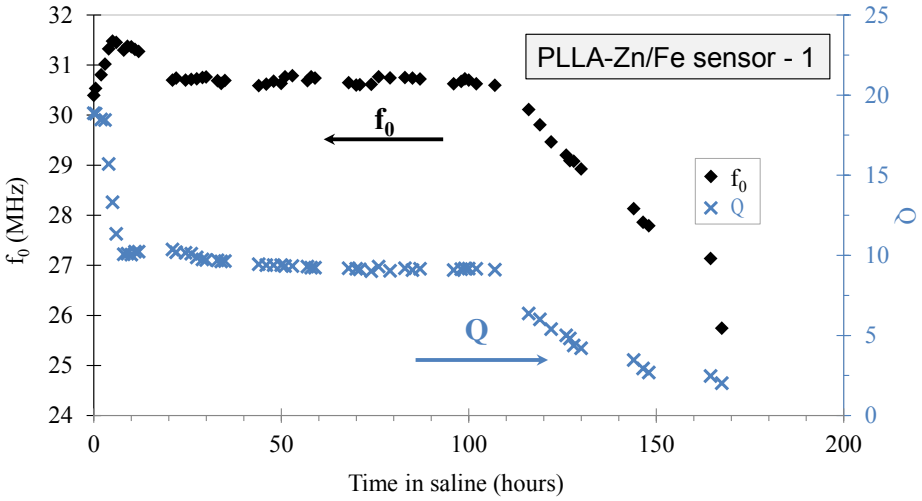

Figure 76: Measured resonant frequency (f_0) and calculated quality factor (Q) as functions of the immersion time of the PLLA-Zn/Fe sensor 1 in 0.9% saline without applying pressure

graphed as a function of the immersion time, and shown in Figure 78. The sensitivity during stage two also remains relatively stable at -54 ± 3 kHz/kPa. This sensitivity is slightly higher than that of in air and initially in saline, and is consistent with the observation of a small reduction of the Youngs modulus of PLLA after immersion in saline [143, 1, 160]. As both resonant frequency and sensitivity are relatively stable during stage two, this stage can be considered the functional lifetime during which the sensor can be utilized.

In the next stage, corresponding to the time after the sensor has been immersed in saline for 107 hours for the PLLA-Zn/Fe sensor 1, f_0 as well as Q of the sensor begins to drop rapidly. Very weak resonance between the sensor and the external coil is observed after 168 hours, making it difficult to determine the f_0. The calculated Q is less than 2. This stage is considered to be the performance degradation stage, when the sensor starts to fail and degrade.

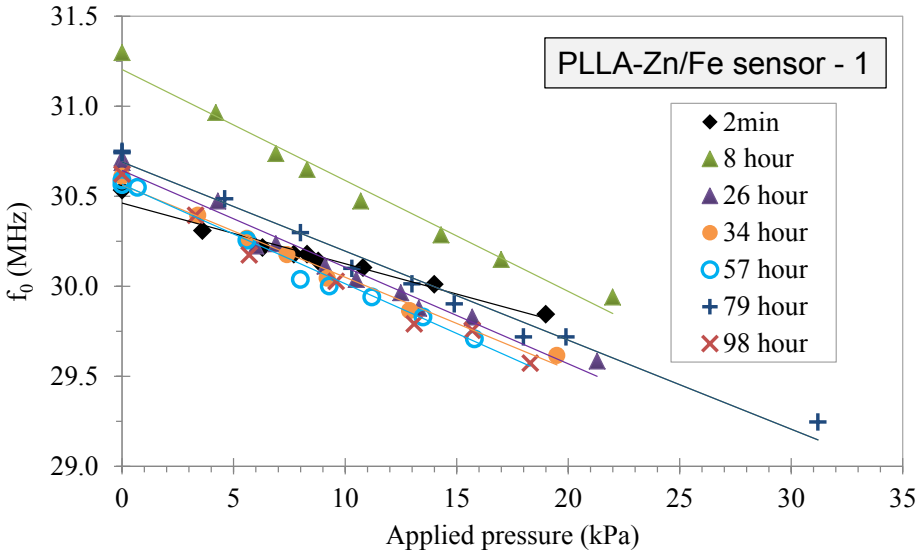

Figure 77: Resonant frequency f_0 as a function of applied pressure of PLLA-Zn/Fe sensor 1 after the sensor has been immersed in the saline for 0 hours, 8 hours, 26 hours, 34 hours, 57 hours, 79 hours and 96 hours.

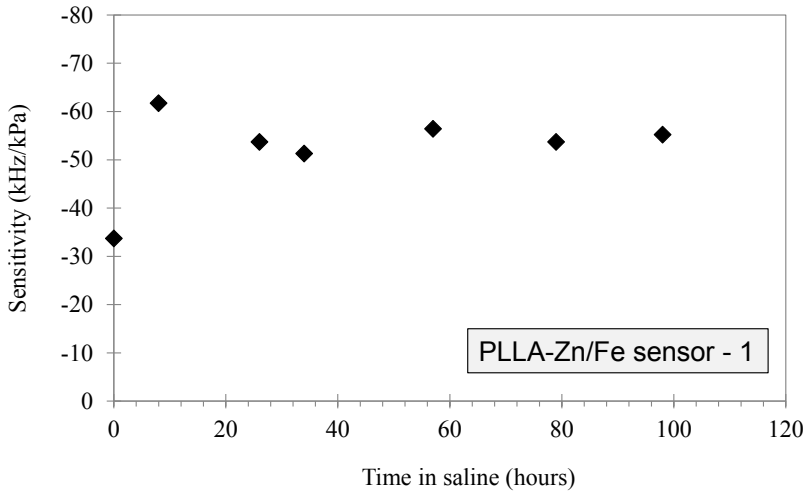

Figure 78: Measured pressure sensitivity of the PLLA-Zn/Fe sensor 1 after the sensor has been immersed in saline for 0 hours, 8 hours, 26 hours, 34 hours, 57 hours, 79 hours and 96 hours.

6.3.1.2 PLLA-Zn/Fe Sensor 2

The measured phases of the external coil as a function of frequency for several applied pressure values of the PLLA-Zn/Fe sensor 2 in air, in DI water, and in 0.9% saline are shown in Figure 79. Then the resonant frequency f_0 of this sensor in air, DI water

and saline is plotted as a function of applied pressure in Figure 80.

In air, the PLLA-Zn/fe sensor 2 has a resonant frequency of 32.9 MHz at zero applied pressure, and a sensitivity of -37 MHz/kPa. Upon immersion of the sensor in DI water, the sensor resonant frequency falls from 32.9 MHz to 32.2 MHz, with the same sensitivity of -37 MHz/kPa. When the sensor is immersed in saline, the resonant frequency falls further to 31.2 MHz with a slightly increased sensitivity of -39 kHz/kPa. This sensor, which has the exact same dimension of the PLLA-Zn/Fe sensor 1 presented above, shows very similar f_0 as well as sensitivity to that of PLLA-Zn/Fe sensor 1.

In a long-term immersion test, selected recorded phase behaviors as a function of frequency are shown in Figure 81. Similar to the behavior of the PLLA-Zn/Fe sensor 1, the trough of the impedance phase becomes much broader and shallower once the sensor is immersed in saline. As the sensor is kept in saline for longer, the the trough of the impedance phase continues to become even broader and shallower, corresponding to decreasing Q. The resonant frequency f_0 of the PLLA-Zn/Fe sensor 2 during the entire long-term immersion test without applied pressure, together with the calculated Q, are plotted as a function of the immersion time in Figure 82.

Similar to that of PLLA-Zn/Fe sensor 1, the performance of the PLLA-Zn/Fe sensor 2 can also be divided into three stages: equilibration stage, functional lifetime, and performance degradation stage. The equilibration stage for sensor 2 is approximately 22 hours. Unlike PLLA-Zn/Fe sensor 1, whose f_0 goes through the rapid increase and then decrease before it stabilizes, the f_0 of PLLA-Zn/Fe sensor 2 increases from 31.2 MHz to 33.1 MHz and stabilizes without dropping. The change of Q is similar: it drops from 19.0 to approximately 10. The functional lifetime of PLLA-Zn/Fe sensor 2 is approximately 68 hours (from 23 hours to 91 hours), with f_0 remaining relatively constant at 33.0 ± 0.2 MHz and Q remaining stable above 9.6. After being immersed in saline for 96 hours, the sensor enters the performance degradation stage: f_0 as well

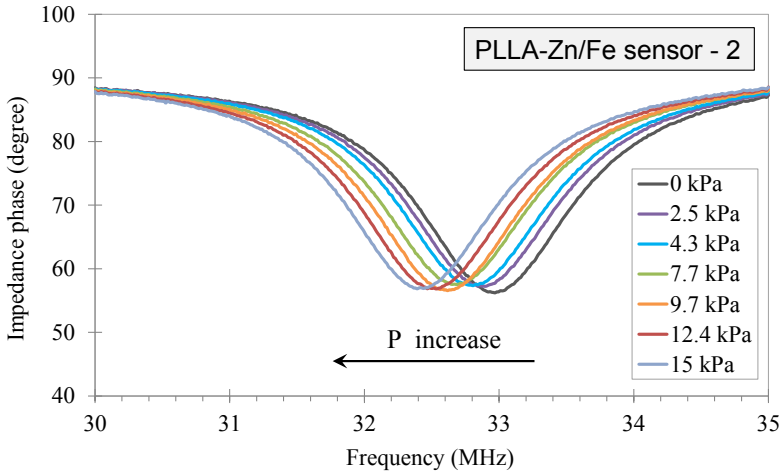

(a)

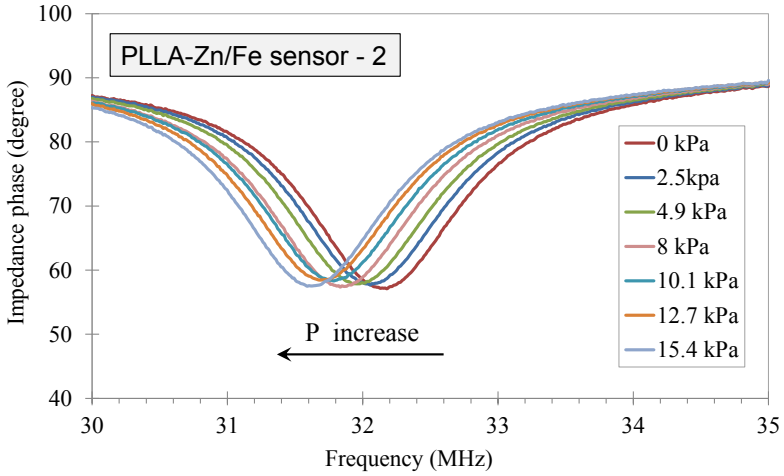

(b)

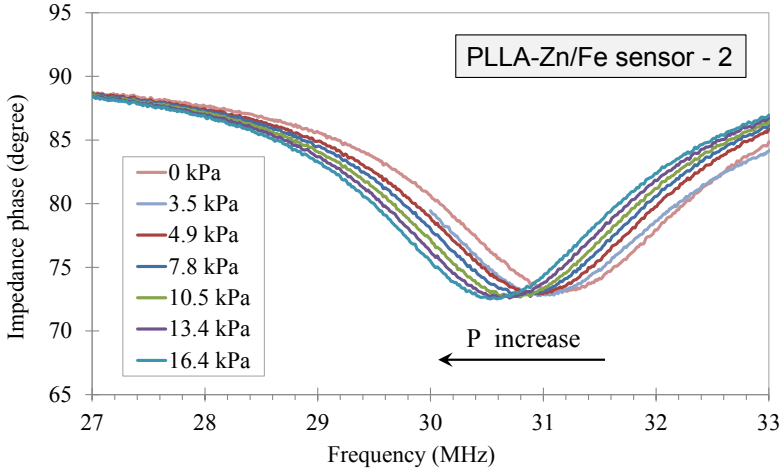

(c)

Figure 79: Measured impedance phase as a function of frequency at several applied pressures for PLLA-Zn/Fe sensor 2 in (a) air, (b) DI water and (c) saline (0.9% NaCl)

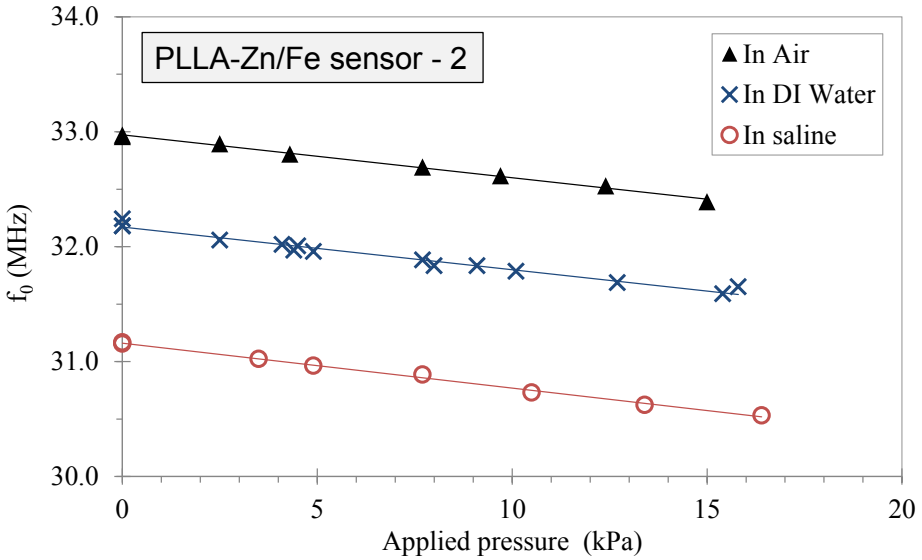

Figure 80: Resonant frequency (f_0) as a function of applied pressure of PLLA-Zn/Fe sensor 2 in air, DI water and 0.9% saline environments (for DI water and saline environments, measurements were performed within 30 minutes of immersion).

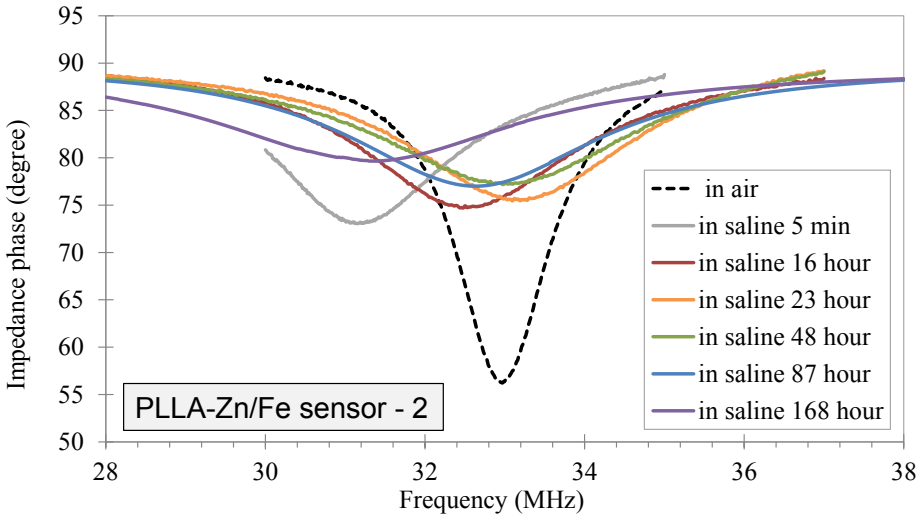

Figure 81: Impedance phase as a function of frequency of PLLA-Zn/Fe sensor 2 at selected immersion time points in saline.

as Q of the sensor starts to drop and very weak resonance between the sensor and the external coil is observed after 168 hours, making it difficult to determine f_0.

Pressure-response measurements of PLLA-Zn/Fe sensor 2 are performed at immersion times of 0 hours (3 min), 45 hours, 79 hours, and 102 hours. Each resonant frequency is plotted as a function of applied pressure in Figure 83. The sensitivities

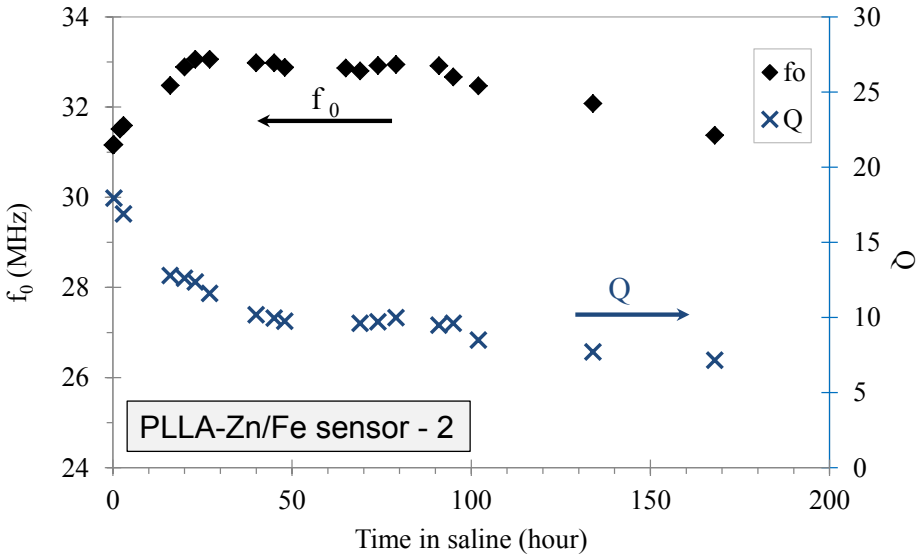

Figure 82: Measured resonant frequency (f_0) and calculated quality factor (Q) as a function of the immersion time of PLLA-Zn/Fe sensor 2 in 0.9% saline without applied pressure

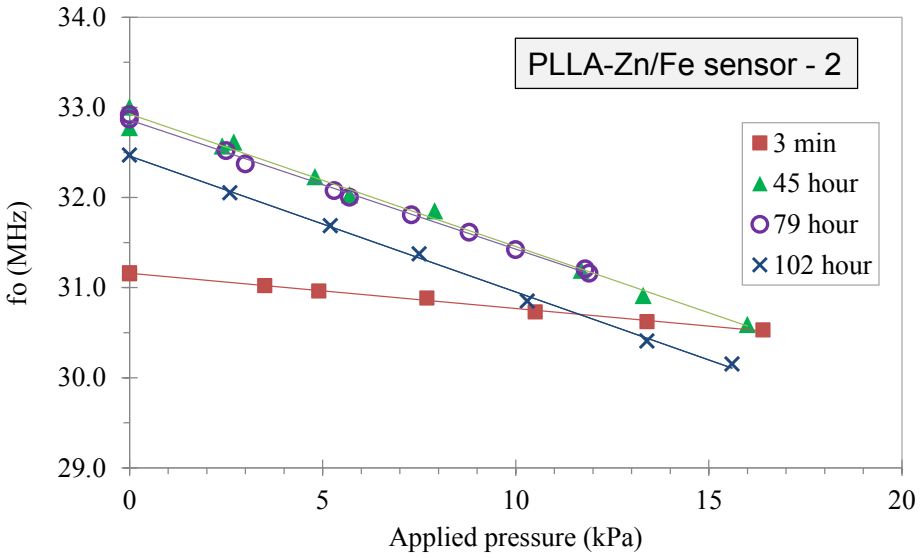

Figure 83: Resonant frequency f_0 as a function of applied pressure of PLLA-Zn/Fe sensor 2 after the sensor has been immersed in saline for 3 minutes, 45 hours, 79 hours and 102 hours.

at different time points are graphed as a function of the immersion time in Figure 84. The sensitivity during the functional lifetime stage also remains relatively stable at -146 ± 4 kHz/kPa. However, this sensitivity is much higher than that of the PLLA-Zn/Fe sensor 1, and can not be attributed only to the small reduction of the Youngs

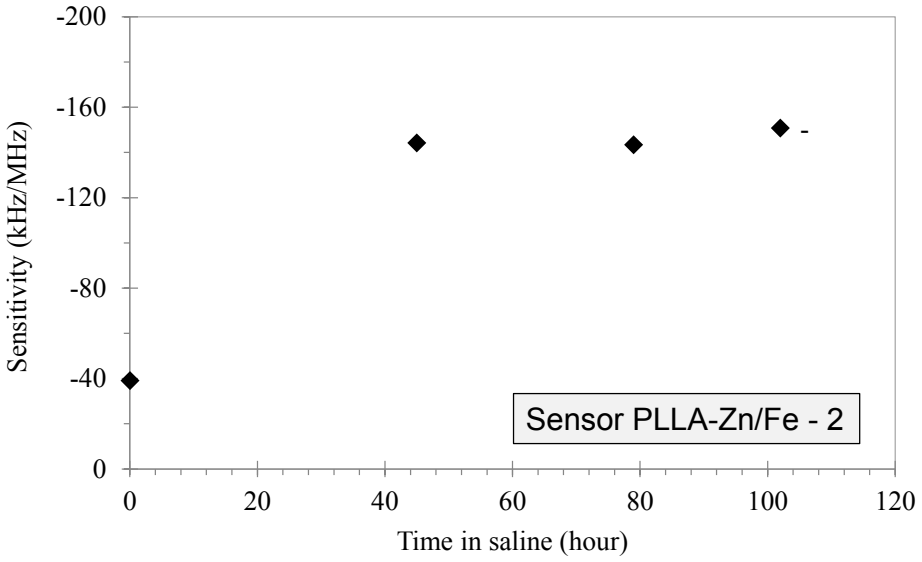

Figure 84: Measured pressure sensitivity of the PLLA-Zn/Fe sensor 2 after the sensor has been immersed in saline for 3 minutes, 45 hours, 79 hours and 102 hours.

modulus of PLLA after immersion in saline. While the exact reason is still under investigation, a possible explanation is that the PLLA spacer is partially delaminated from the two metal plates during immersion in the saline, resulting in a larger effective deflection diameter for the capacitor plates. This explanation can be supported by the behavior that f_0 with zero applied pressure does not drop during the equilibration stage in Figure 82.

6.3.1.3 PLLA-Zn/Fe Sensor 3

The resonant frequency of PLLA-Zn/Fe sensor 3 in air and saline extracted from the recorded impedance phase is plotted as a function of applied pressure in Figure 85. The sensitivity of the sensor in air and saline are -43.1 kHz/kPa and -39.4 kHz/kPa, respectively. PLLA-Zn/Fe sensor 3 exhibits higher sensitivity than that of PLLA-Zn/Fe sensor 1 and 2, due its smaller PLLA package thickness.

Selected recorded phase as function of frequency during the long-term immersion test of sensor 3 are shown in Figure 86. Similar to that of PLLA-Zn/Fe sensor 1 and 2, the trough of the impedance phase becomes broader and shallower as the immersion

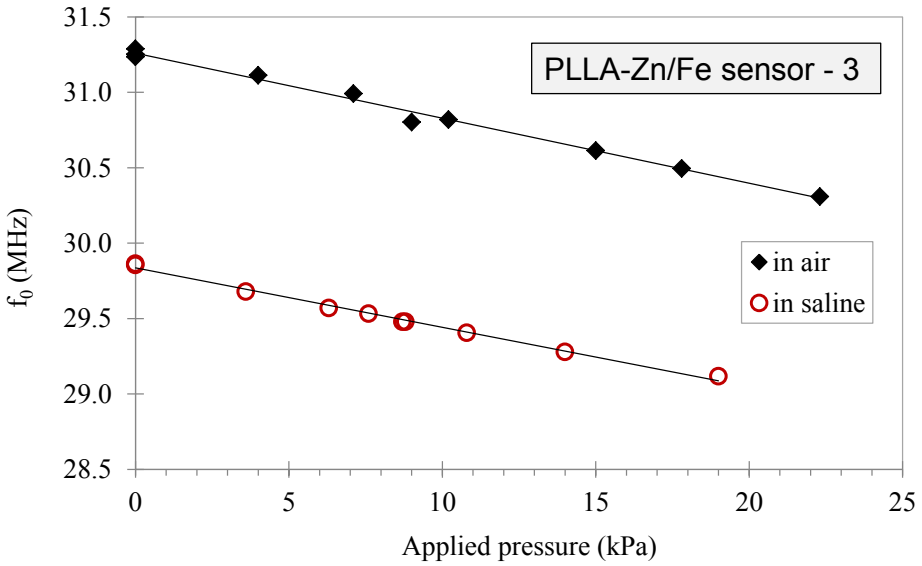

Figure 85: Resonant frequency (f_0) of the pressure sensor as a function of applied pressure of PLLA-Zn/Fe sensor 3 in air and 0.9% saline environments (for the saline environment, measurements were performed within 30 minutes of immersion).

time of the sensor increases. However, the change is more rapid: after 58 hours, there is only a very weak resonance observed in the impedance phase.

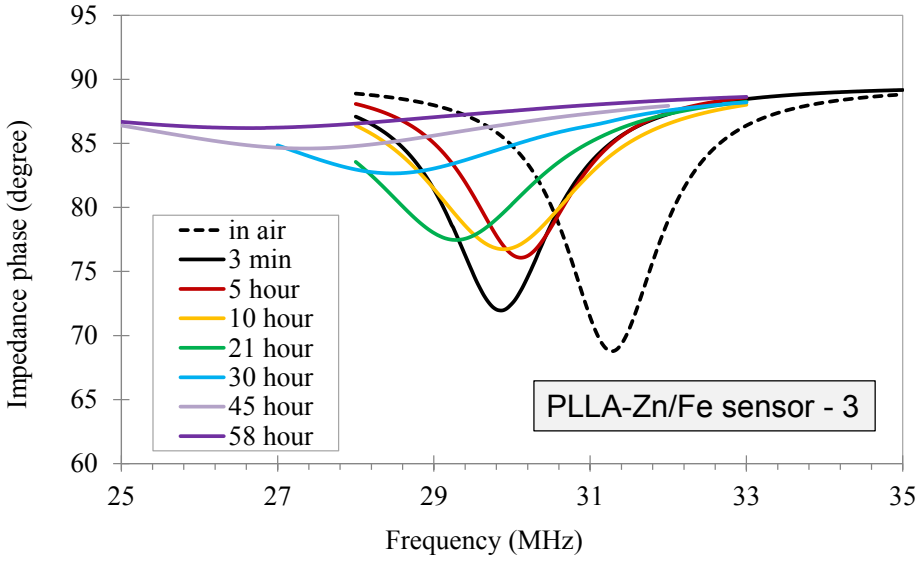

Figure 86: Impedance phase as a function of frequency of PLLA-Zn/Fe sensor 3 at selected immersion time points in saline.

The resonant frequency f_0 of sensor 3 during the entire long-term immersion test without applied pressure, together with the calculated Q are plotted as a function of

immersion time in Figure 87.

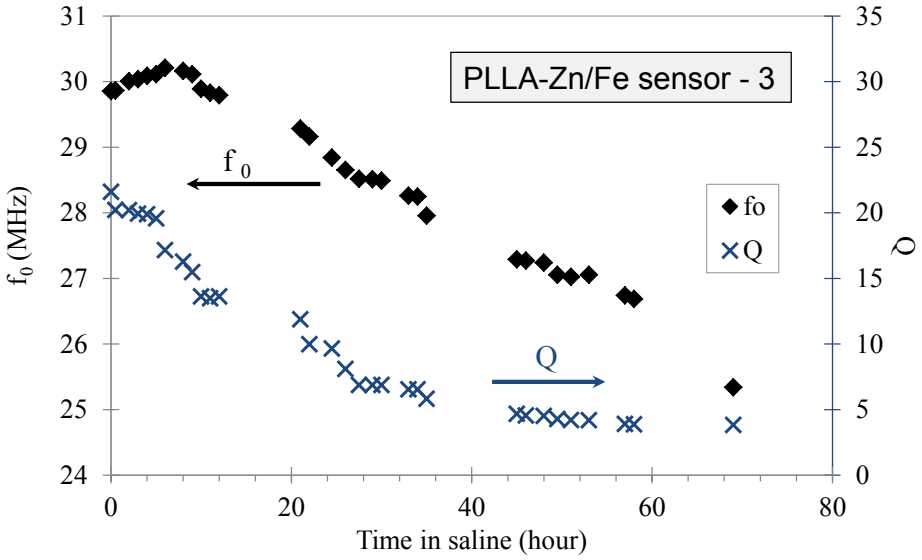

Figure 87: Measured resonant frequency (f_0) and calculated quality factor (Q) as a function of immersion time of PLLA-Zn/Fe sensor 3 in 0.9% saline without applying pressure

In the initial 5 hours, f_0 increases gradually from 29.9 MHz to 30.1 MHz, similar to the behavior of sensor 2 during the equilibration stage. However, after it reaches a maximum of 30.1 MHz at 6 hours, f_0 drops continuously with a steady speed of -72.4 kHz/hour until only a very weak resonance can be barely detected after 69 hours. Q drops rapidly from 21.6 to 6.9 within the first 28 hours, then gradually drops to approximately 3.8 after 69 hours. Therefore, this sensor failed to fully function in saline. One possible reason is that the PLLA package (130 μm is too thin to work as a stable barrier between the saline and the cavity between the two capacitor plates. Another possible reason is the observation of small cracks forming during the immersion, which is discussed later.

6.3.1.4 PLLA-Zn/Fe Sensor 4

The PLLA-Zn/Fe sensor 4 has a much thicker PLLA package than all the 3 sensors presented above. The resonant frequency of this sensor in air is shown in Figure 88.

A sensitivity of -8.8 MHz/kPa is obtained for this sensor. This sensitivity is about 4 times smaller than that of sensors 1 and 2.

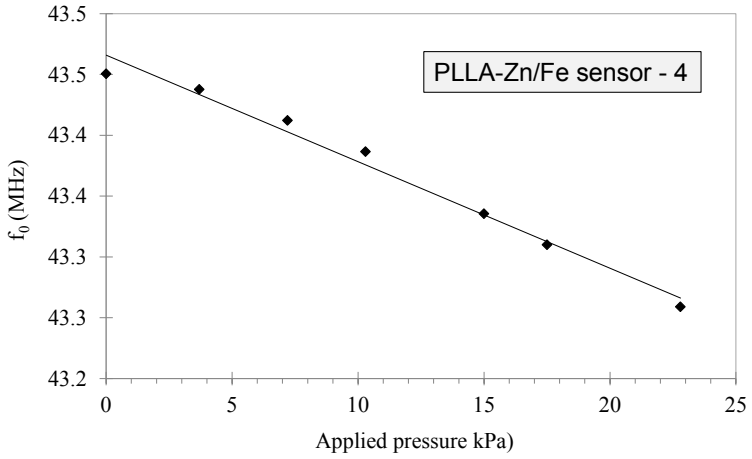

Figure 88: Resonant frequency (f_0) of the pressure sensor as a function of applied pressure of PLLA-Zn/Fe sensor 4 in air

Selected recorded phase as a function of frequency during the long-term immersion test of sensor 4 are shown in Figure 86. This sensor survives much longer than sensors 1, 2 and 3. The trough of the impedance phase becomes broader and shallower as expected as the immersion time of the sensor increases. A clear resonance still can be detected after the sensor is immersed in saline for 414 hours. The resonance became very weak after 439 hours.

f_0 and calculated Q of sensor 4 during the entire immersion test is shown in Figure 90. f_0 drops slightly to 40.4 MHz during the first 33 hours, then fluctuates at 42.1 ± 0.9 MHz from 33 to 214 hours. After being immersed in saline for 214 hours, f_0 remains relatively constant at 40.8 ± 0.5 MHz until 383 hours, when f_0 starts to drop rapidly. Q drops relatively rapidly to 15.8 in the first 21 hours, then decreases slowly and steadily to 12.8 at 383 hours, and then drops rapidly again to approximately 6.6 when the sensor no longer exhibits resonance at 459 hours. Based on the result of both f_0 and Q, the equilibration stage for sensor 4 is 33 hours, the functional life time is approximately 350 hours (from 33 hours to 383 hours), and after the sensor

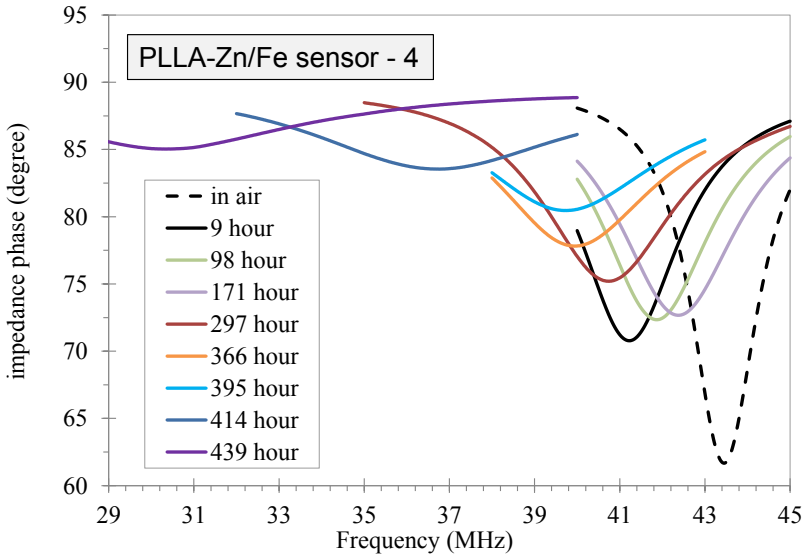

Figure 89: Impedance phase as a function of frequency of PLLA-Zn/Fe sensor 4 at selected immersion time points in saline.

has been immersed in saline for 383 hours, the sensor starts to fail. The functional lifetime is much longer than that of the sensor 1, 2 and 3, mainly due to the thicker PLLA. The reason for the large fluctuation in f_0 between 33 and 214 hours is still under investigation.

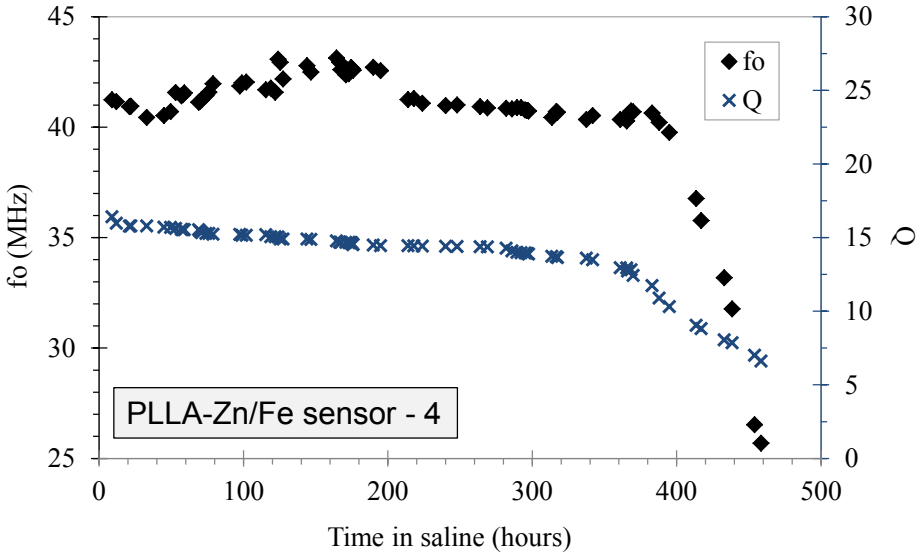

Figure 90: Measured resonant frequency (f_0) and calculated quality factor (Q) as a function of the immersion time of PLLA-Zn/Fe sensor 4 in 0.9% saline without applying pressure

6.3.1.5 *Investigation of Failure Mechanisms*

To investigate the mechanisms behind sensor failure, all PLLA-Zn/Fe sensors are removed from the saline after resonance is no longer detectable. Sensors 1, 3 and 4 are rinsed in DI water and dried in a sealed container with solid anhydrous drying agent at room temperature for three days immediately after removal from the saline, while sensor 2 is placed in air at room temperature for six months before being rinsed and similarly dried. Afterwards, the sensors are coupled with the external coil again, and all of them show resonance, as shown in Figure 91. The calculated Q of sensors 1, 2, 3 and 4 are 20, 6, 16 and 17, respectively. The Q of sensors 1, 3 and 4 after drying are only slightly smaller (between 2 to 8) than before they were placed in saline. This suggests minor, if any, corrosion of the Zn/Fe conductor during the long-term immersion test in saline. This excludes the corrosion of the metal as the reason of the sensor failure. However, if the sensor is held at room temperature for a prolonged time (e.g., six months for sensor 2) without intense drying, the Q drops strongly from 24 to 6, which could be indicative of degradation of the metal inside the sensor.

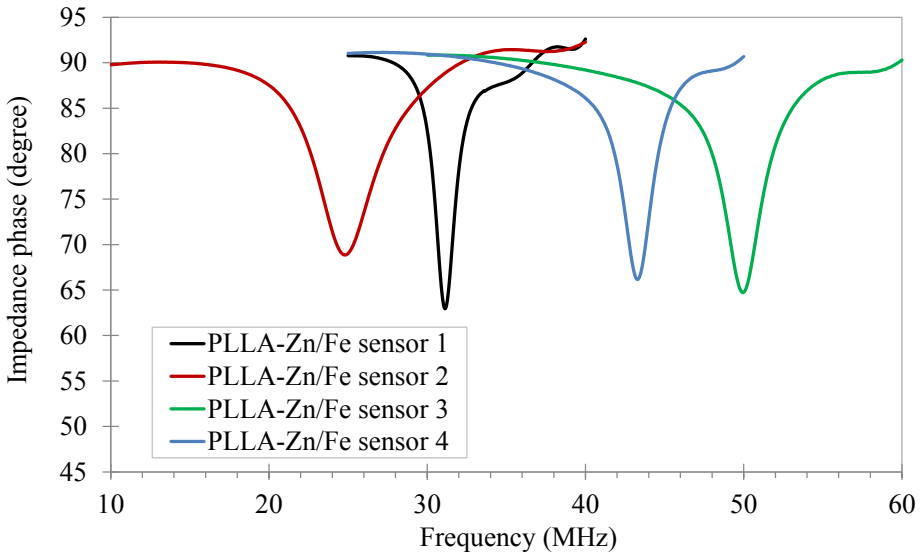

Figure 91: Impedance phase as a function of frequency of PLLA-Zn/Fe sensors after long-term immersion in saline test and drying

Upon examination, cracks were found in some of the sensors. Since PLLA exhibits brittle behavior at room temperature [38, 72], the formation of cracks is not unexpected as a failure pathway for these devices. One hypothesis for the failure of the sensors in saline during long-term immersion is that: once the sensor is placed in saline, water or water vapor begins to penetrate the polymers slowly; if there are micro-cracks, which might be formed either during fabrication or during the sensor going through pressure-response testing at room temperature, those cracks can accelerate water or water vapor penetration into the PLLA package, resulting in electrical shorts between the inductor windings. If the micro-cracks develop into macro-cracks that spread through the entire PLLA package, water or water vapor can easily penetrate into the cavity between the two capacitor plates and short or significantly change the dielectric environment of the capacitor. The existence of water or water vapor in the polymer and air inside the cavity will increase its dielectric constant at these frequencies [112, 140], and hence increase the total capacitance by increasing the parasitic capacitance between the inductor windings and capacitance of the parallel plates. This is consistent with the observation of the rapid f_0 drop during the performance degradation stage of the sensor. It is also interesting to note that although the Q of dried sensors returns to close to initial values in Figure 91, the f_0 of some of the sensors does not; this is also consistent with crack-induced irreversible deformations of the package as a result of the immersion testing in those sensors.

To further verify this hypothesis, pressure-response testing is applied to all the sensors in air. Sensors 2 and 3 show no f_0 shift upon pressure change, indicating the cavity is no longer sealed. This is consistent with the large cracks observed in these two sensors. Even with the few very small cracks observed in sensor 4, sensors 1 and 4 still show f_0 shifts as a function of applied pressure, as shown in Figure 92. For sensors 1 and 4, both the f_0 at zero applied pressure (31.1 MHz for sensor 1 and 43.3 MHz for sensor 4) and the sensitivity (-31.0 kHz/kPa for sensor 1 and -7.6 kHz/kPa

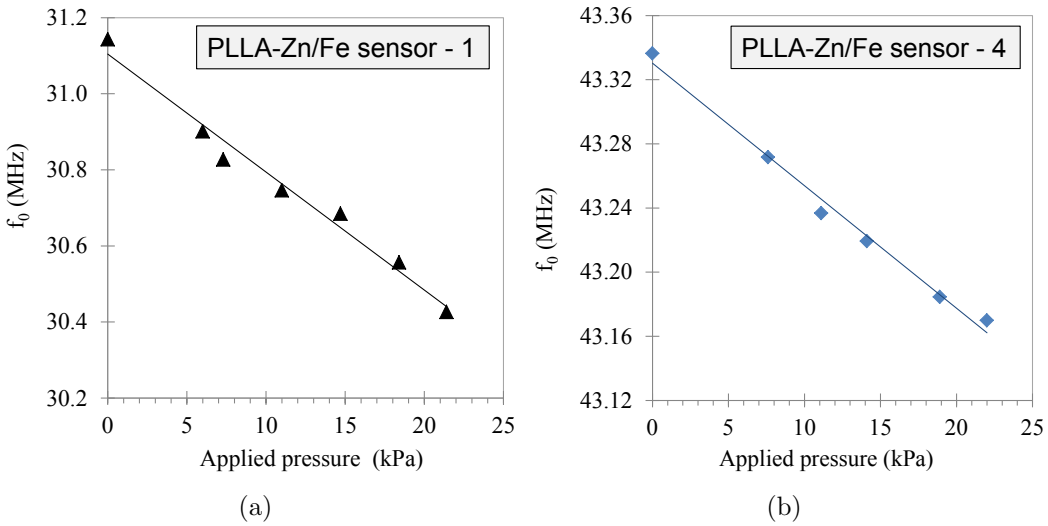

(a) (b)

Figure 92: Resonant frequency f_0 as a function of applied pressure of (a) PLLA-Zn/Fe sensor 1, and (b) PLLA-Zn/Fe sensor 4 in air (after long-term immersion in saline and drying)

for sensor 4) after the long-term immersion in saline and drying are similar to that before they were put in saline, indicating that the sensors are not damaged during the immersion in saline.

The summary of the performance of the PLLA-based sensor 1-4 are listed in Table 10

Based on the above observations, a preliminary overall mechanism for failure of these sensors can be proposed. Upon immersion in saline, the polymer packages absorb water, causing a change inthe dielectric environment of the sensor package as well as affecting to a small degree the Young's modulus and therefore the sensitivity of the sensor. Over time, additional water or water vapor penetrates the sensor and sensor cavity; in addition, the sensor package continues to be weakened by water infiltration. Should sensors have no major structural flaws and/or have sufficient mechanical robustness, no irreversible change in the sensor mechanical structure occurs. Instead, water vapor permeation continues until sufficient water has accumulated within the sensor to cause electrical failure. At this point, no resonances can be read

Table 10: Design and performance characterization summary for PLLA-based sensors

Environment	Properties	PLLA-Zn/Fe sensors			
		1	**2**	**3**	**4**
	PLLA thickness (μm)	200	200	130	350
In air	f_0 at 0 pressure (MHz)	31.8	33	31.3	43.5
	Sensitivity (kHz/kPa)	-38.5	-37.2	-43.1	-8.8
	Q	22.1	24	22.4	24.6
In saline	Equilibration time (hour)	21	23	6	33
In saline-*during stable functional lifetime*	Functional lifetime (hour)	86	79	N.A.	350
	f_0 at 0 pressure (MHz)	30.5±0.2	33.0±0.2	N.A.	40.8±0.5
	Sensitivity (kHz/kPa)	-54±3	-146±4	N.A.	-
	Q	10	10	N.A.	14
In air-*after drying*	f_0 at 0 pressure (MHz)	31.1	24.8	49.9	43.3
	Q	20	6	16	17
	Sensitivity (kHz/kPa)	-31	N.A.	N.A.	-7.6

and the sensor fails. For such sensors, upon drying, the water is removed and the sensor returns to its original state, with close to original Q, f_0, and pressure sensitivity. For sensors with insufficient mechanical robustness, large cracks occur which result in an irreversible change in the sensor. These large cracks permanently alter the f_0 of the sensor and, even upon drying and the restoration of resonant behavior, these cracked sensors cannot support a pressure difference across their mechanically deflecting portions and have no pressure sensitivity. For longer term immersion in ambient environments, the conductors themselves begin to corrode, resulting in an irreversible loss of Q and therefore functionality. These observations suggest a lower limit on the thickness and robustness of the sensor deflecting mechanism, and further suggest that improved moisture barriers could result in longer functional lifetimes for such more robust sensors.

6.3.2 Experimental Results vs. Simulation Results of PLLA-based Sensors

The LC resonant frequency f_0 under zero applied pressure as well as the sensitivity are the key functional parameters of the pressure sensor. As mentioned before, the resonant frequency f_0 is defined by the sensor inductance L_S and capacitance C_S

$$f_0 = \frac{1}{2\pi\sqrt{L_S C_S}}. \tag{55}$$

The shift of f_0 under different applied pressure is due to the capacitance change introduced by the deflection of the capacitor plates. However, the real time capacitance of the sensor cannot be measured directly becuase the capacitor is encapsulated in the polymer. Therefore, it is important to verify the simulation model of capacitance with the experimental results.

Experimental capacitance is calculated from the experimentally measured f_0 of the sensor and the inductance L_s of the Zn/Fe bilayer inductor before folding by

$$C_S = \frac{1}{(2\pi f_0)^2 L_S}. \tag{56}$$

The simulated capacitance value under zero applied pressure is calculated using Eq. (28), Eq. (10) and Eq. (8) in Chapter 3. The capacitance under certain applied pressure is directly obtained using COMSOL simulation. The simulated resonant frequencies are calculated using the simulated result of capacitance under each applied pressure, and the sensitivity between 0-20 kPa is calculated.

The experimental and simulated capacitance and sensitivity of the four PLLA-Zn/Fe sensors presented above are compared in Table 11 together with some of their critical design geometries.

Except for sensor 4, the capacitance calculated from experimental result of all the sensors are larger than that of the simulated result. Meanwhile, all the sensors exhibit much larger sensitivity than expected. There are two factors can contribute to these observed differences.

Table 11: Comparison of capacitance and sensitivity values of PLLA-Zn/Fe sensors using experimental results and simulation model in Chapter 3

Parameters	PLLA-Zn/Fe sensor			
	1	2	3	4
Cavity radius (mm)	2.1	2.1	2.1	2.1
Cativity thickness (μm)	30	30	25	45
PLLA thickness (μm)	200	200	130	350
Simulated capacitance (pF)	10.98	10.98	12.82	7.81
Experimental capacitance (pF)	13.13	12.24	13.6	7.05
Simulated sensitivity (kHz/kPa)	-9.5	-9.5	-13.7	-3.1
Experimental sensitivity (kHz/kPa)	-38.3	-37.2	-41.3	-8.8

(1) Imperfection of fabrication process.

The capacitance can be altered slightly due to fabrication imperfections, in that several geometries of the components cannot be precisely controlled or identical to the design. For instance, it is a challenge to precisely control the thickness of the solvent-cast polymer films to tolerances on the order of micrometers. The thickness of the spacer will affect the capacitance with zero applied pressure, while the thickness of the PLLA will affect the sensitivity of the sensor by affecting the deflection. Also, the linewidth of the spiral inductor usually appears a little wider than designed, due to the undercut of the thick photoresist. Therefore, the simulated result of the parasitic capacitance would not be accurate. The capacitance will also be altered if the two capacitor plates are not perfectly aligned during folding and lamination.

(2) Pre-bending of the capacitor plate

It is observed that the capacitor plates together with the attached polymer film are slightly bent inward after fabrication. This is very likely due to thermal mismatch between the polymer and the metal that possess distinct coefficients of thermal expansion (CTE) during the thermal embossing process.

To take this pre-bending of the plate into consideration, COMSOL is utilized to

build a relationship between the center deflection of the plate to an absolute applied pressure, in effect creating a fictitious pressure offset that mimics the plate curvature behavior. To achieve this goal, first a sensor structure with flat plate geometry is constructed in COMSOL. The simulation results of center deflection d_0 and capacitance of the capacitor at different applied pressures before d_0 reaches half of the cavity thickness are determined. Based on this result, the simulated f_0 is calculated at each applied pressure (center deflection). The simulated f_0 as a function of center deflection and applied absolute pressure of the sensor design identical to that of PLLA-Zn/Fe sensor 1 is shown in Figure 93. As the center deflection increases, the simulated f_0 decreases non-linearly, due to the non-linear increase of the capacitance over these deflections that are large compared with the capacitor gap.

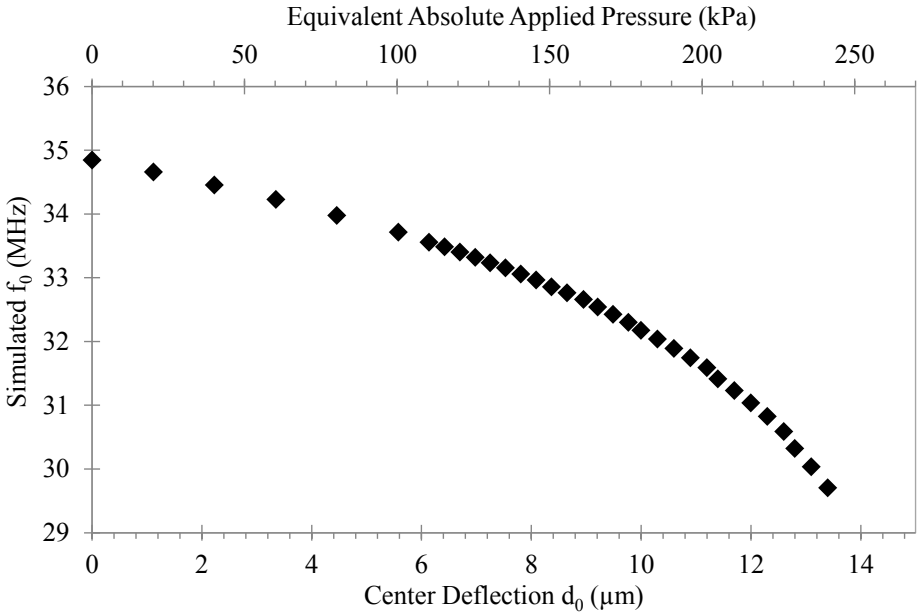

Figure 93: Simulated f_0 as a function of center deflection and equivlent applied absolute pressure of designed sensor structure identical to that of PLLA-Zn/Fe sensor 1

In order to simulate sensitivity of a sensor with pre-bent capacitor plate, the equivalent absolute pressure can be found at which the simulated center deflection is equal to the pre-bending center deflection. This value of equivalent absolute pressure

is then treated as the zero applied pressure; and the sensitivity is then the slope of the line tangent to the point of equivalent absolute pressure of Figure 93. From this figure it can be seen that the expected sensitivity of predeflected sensors will increase because the slope of the f_0 versus pressure line increases substantially at higher equivalent absolute pressures.

The experimental results of f_0 vs. applied pressure of PLLA-Zn/Fe sensors 1 and 3 are compared with the simulated results utilizing this approach with certain pre-bent center deflection value and identically designed geometries as PLLA-Zn/Fe sensors 1 and 3 in Figure 94 respectively.

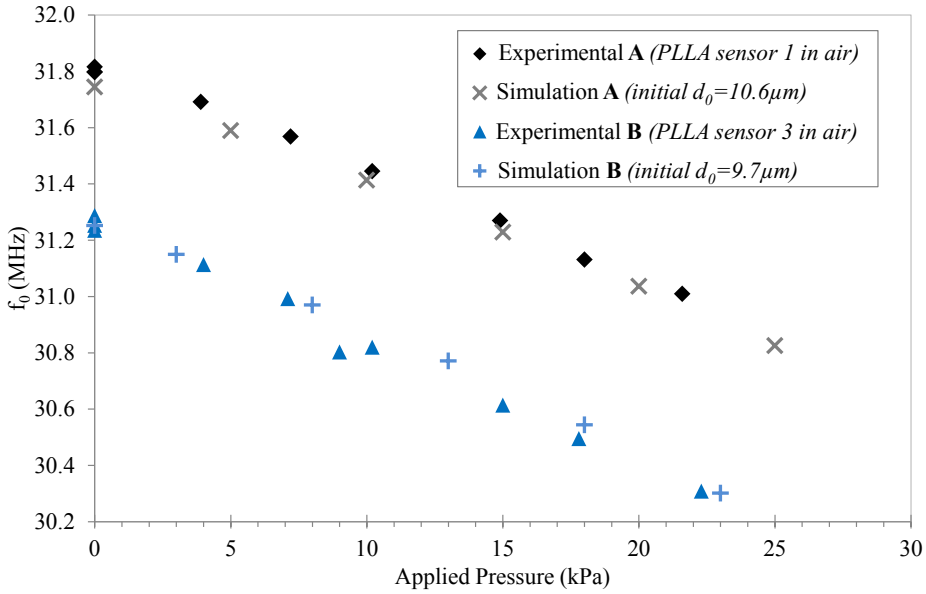

Figure 94: Experimental f_0 vs. applied pressure results of PLLA-Zn/Fe sensor 1 and 3, and simulated results using COMSOL with absolute pressure equivalent pre-bending center deflection corrections

With the equivalent pre-bent center deflection of 10.6 μm and 9.7 μm for simulated sensor geometry indentical to the design of PLLA-Zn/Fe sensors 1 and 3, the simulated results of f_0 vs. applied pressure are very close to that of the exprimental result. Note that this pre-bending value is relatively large, and can be the major reason for the mismatch of the experimental results and simulation results (using a flat plate) shown in Table 11.

To further verify this hypothesis, the plate bending value introduced by thermal mismatch of the polymer and metal are calculated. For a bilayer structure with schematic side view shown in Figure 95.

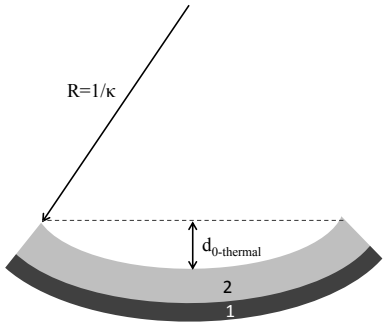

Figure 95: Schematic illustration of cross-sectional view of a bent bilayer plate undergoing curvature due to thermal mismatch between the plates

By defining

$$\xi = \frac{h_2}{h_1}, \Sigma = \frac{E_2(1-\nu_1)}{E_1(1-\nu_2)}, \sigma^{(T)} = \frac{E_2(\alpha_1-\alpha_2)}{1-\nu_2}\Delta T \tag{57}$$

where h_i is the plate thickness, E_i, ν_i and α_i are the Young's modulus, Poisson's ratio and coefficient of thermal expansion (CTE) of the i^{th} layer material, and ΔT is the temperature difference, the curvature of bilayer structure due to thermal mismatch can be calculated by [29]:

$$\kappa = \frac{6\xi^2(1+\xi)}{(\Sigma\xi^2-1)^2+4\Sigma\xi(\xi+1)^2}\left[\frac{(1-\nu_1)\sigma^{(T)}}{E_1 h_2}\right]. \tag{58}$$

The center deflection $f_{0-thermal}$ can thus be calculated by knowing the arc length (diameter of the bending plate), and the arc radius R.

The CTE of Zn, Fe and PLLA are 30.2 $\mu m/(m \cdot K)$ [153], 11.8 $\mu m/(m \cdot K)$ [108] and 78.5 $\mu m/(m \cdot K)$ ($T < T_g$) [75]. In the fabrication process, during the step of embossing metal into the PLLA, the 10 bar pressure is not released until the embossing stage is cooled down to 35 °C. Therefore, the bending should be introduced during the time that the PLLA embossing membrane bearing the metal on Kapton is cooled down from approximately 35 °C to room temperature. By simplifying the model

to a PLLA-Zn bilayer with a radius of 2.5 mm (the radius of the metal capacitor), the thermal-mismatch-induced center deflection ($d_{0-thermal}$) of the bilayer plate with identical geometry design of sensor 1 (Structure A) and 3 (Structure B) as a function of ΔT is shown in Figure 96. Note that the thickness designated PLLA* only includes the PLLA film thickness that is above the metal plate.

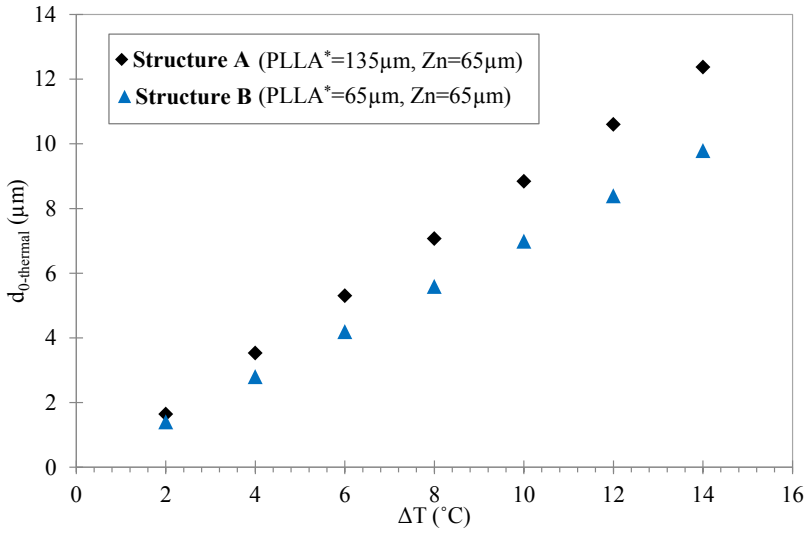

Figure 96: Calculated center deflection due to thermal mismatch of a simpified PLLA/Zn bilayer plate as a function of temperature difference. Plate radius = 2.5mm, thickness of Zn = 65 μm. Structure A: thickness of PLLA* = 135 μm. Structure B: thickness of PLLA* = 65 μm.

When the temperature difference (the temperature range during which the free standing samples are cooled down without pressure) is between 2 and 14 °C, calculated center deflections of the plate are 1.6 - 12.4 μm and 1.4 - 9.8 μm for structure A (sensor 1) and structure B (sensor 3), respectively. Based on the result shown in Figure 94, the simulated pre-bending center deflection for stucture A and B are 10.6 μm and 9.7 μm, corrosponding to 12 and 14 °C in ΔT. This is a very reasonable temperature difference between 35 °C and ambient room temperature in a cleanroom environment. A slight difference between the real center deflection and the calculated result is expected due to the fact that the real structure is not an ideal polymer/metal bilayer, and the thin layer of Fe ($< 4\mu m$) is neglected.

In summary, the pre-bending due the thermal mismatch of the metal and polymer of the plate is very likely to be the main reason that the flat plate model is not accurate in predicting the sensitivity of the sensor. By adding the concept of the absolute applied pressure to account for the pre-bent center deflection, the simulation result using COMSOL agrees very well with the experimental result. Therefore, by precisely controlling the cooling temperature range after releasing the embossing pressure, the sensitivity of the sensor can be designed more accurately.

6.3.3 Functionality Measurement of PLGA/PVA-based Pressure Sensor in Air and *In Vitro*

The fabricated PLGA/PVA-based pressure sensors are characterized first in air and then in saline. The measurement is air is at room temperature, while the measurement in saline is at 37 °C. Three categories of PLGA/PVA-based sensor are studied here: PLGA/PVA sensor with PLLA/PCL spacers; PLGA/PVA sensor with PVA/PLGA spacers; and PLGA/PVA sensor with pure PLGA spacers. The polymer designs of the sensors studied in the following section are listed in Table 12.

Table 12: Design parameters of polymers used for PLGA/PVA sensors 1, 2 and 3

Designs	**PLGA/PVA sensors**		
	1	**2**	**3**
PVA thickness (μm)	200 - 230	280 - 330	250 - 300
PLGA thickness(μm)	120 - 150	200	200
Spacer Materials	PLLA and PCL	PVA and PLGA	PLGA
Spacer thickness (μm)	25	35	45
PVA lamination temperature (°C)	165	130	130

In this study, a glass vial with cap machined to attach to an air connector is utilized as pressure box. The setup is shown in Figure 97. A machined O-ring made of red rubber (SBR) is added in the cap to prevent leakage. Upon testing, the glass

vial utilized can withstand up to 50 kPa without breaking or leaking. Each sensor is then kept individually in one glass vial. The advantages of using glass vials includes:

- Easy availability.
- Easy to attach and remove for pressure response testing.
- Enable multiple sensor testing simultaneously.
- Enable the testing be performed under 37 °C.
- Convenient for the subsequent sensor degradation test.

After the characterization of the PLGA/PVA-based pressure sensor in air, the sensor is placed into a test vial. Warm 0.9% saline that is pre-stored in an incubator at 37 ±0.5°C is filled into the vial to a height of 1 cm. The impedance phase behavior of the sensor is recorded immediately as immersion time 0-hour. Additional saline is added into the vial to fill it full (approximately 20 mL), and the vial together with the sensor inside is placed in the 37 ±0.5°C incubator. At intermediate times, the sensor is taken out of the incubator for testing: a portion of the saline is removed

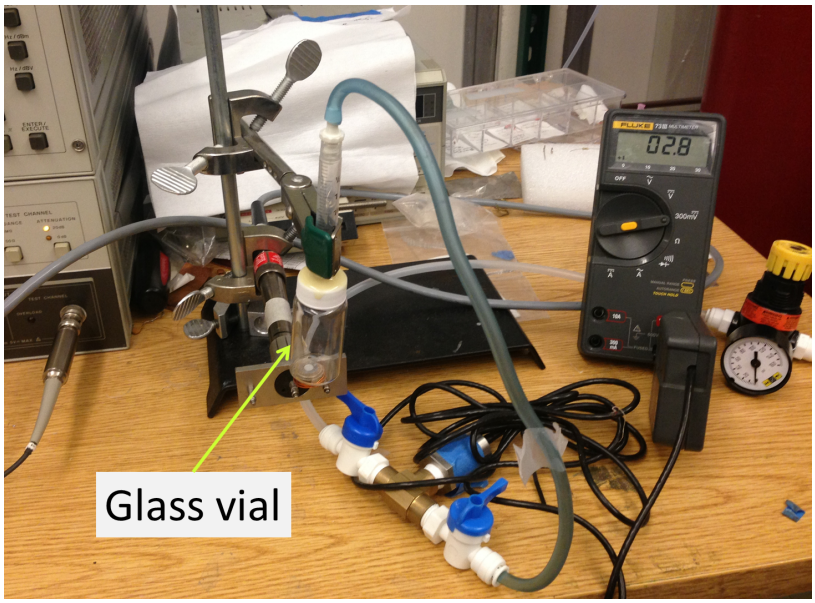

Figure 97: wireless characterization setup for PLGA/PVA-based biodegradable pressure sensors

temporarily, leaving saline with 1 cm in depth inside of the vial before the testing. After each test, the same saline that had been removed is filled back into the vial and the sensor is placed back into the incubator. Two kinds of characterizations are performed: measurement of the f_0 of the sensor with zero applied pressure every 20 to 30 minutes, and measurement of the pressure response of the sensor every few hours. The saline inside the vial is refreshed (i.e., completely replaced with fresh saline) every 72 hours.

6.3.3.1 PLGA/PVA Sensor 1 (PLLA/PCL Spacers)

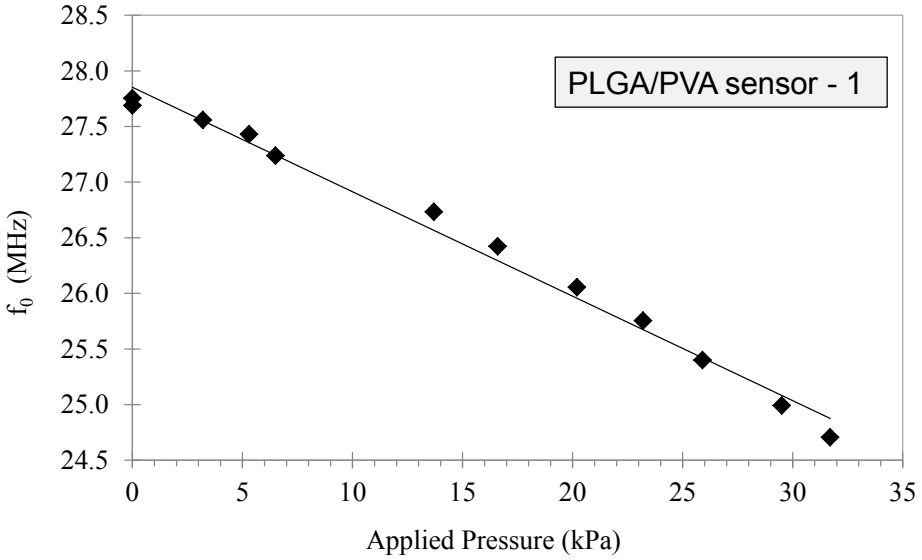

Figure 98: Measured f_0 as a function of applied pressure of PLGA/PVA sensor 1 in air at room temperature

PLGA/PVA sensor 1 contains a Zn/Fe couple conductor with 50% coverage of Fe on one side of the Zn surface (same pattern as checker-C shown in Figure 37(c) in Chapter 4). Pressure response measurement (0 to 32 kPa) in air under room temperature is first performed to confirm the functionality of the sensor. The result is plotted in Figure 98. A sensitivity of -93.9 kHz/kPa is exhibited. The relatively higher sensitivity indicates the center PLLA spacer is very likely not completely bonded with the two capacitor plates completely. The total capacitance of the sensor in air with

zero applied pressure calculated using f_0 (27.9 MHz), 17.1 pF, is 6.2 pF more than the calculation result using the designed dimension of the sensor. This is very likely due to the observed inward bending of the capacitor plates possibly introduced by the thermal mismatch during embossing the metal conductor to the polymer film. Similar behavior is also observed in the PLLA-based sensors discussed above.

Selected recorded impedance phase behavior as a function of frequency at different immersion times with zero applied pressure are shown in Figure 99. f_0 of the sensor in saline (37 °C) with zero applied pressure and calculated Q during the 12-hour immersion test are plotted in Figure 100.

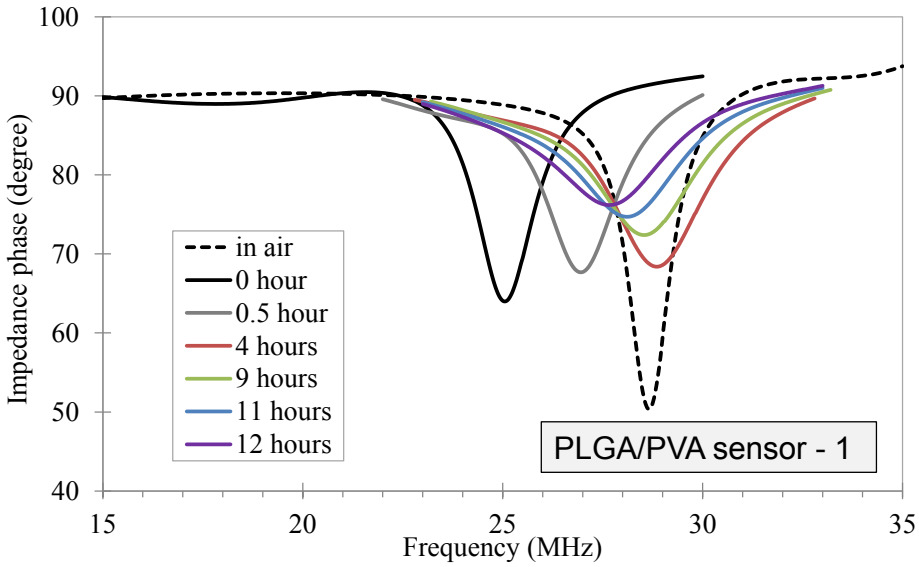

Figure 99: Impedance phase as function of frequency of the PLGA/PVA sensor 1 in air (room temperature) and in saline (37 °C) with zero applied pressure

As expected, the trough of the phase becomes shallower and broader as the immersion time increases, corresponding to decrease of Q. When the sensor has been immersed in saline for 12 hours, clear resonance still can be detected, however after the sensor has been placed in the incubator overnight, no resonance can be found in the next measurement. As shown in Figure 100, f_0 increases rapidly from 25.1 MHz to 28.9 MHz in the first 90 minutes, then begins to decrease at a rate of approximately -75.4 kHz/hour until the sensor has been immersed in saline at (37 °C) for 11.5 hours.

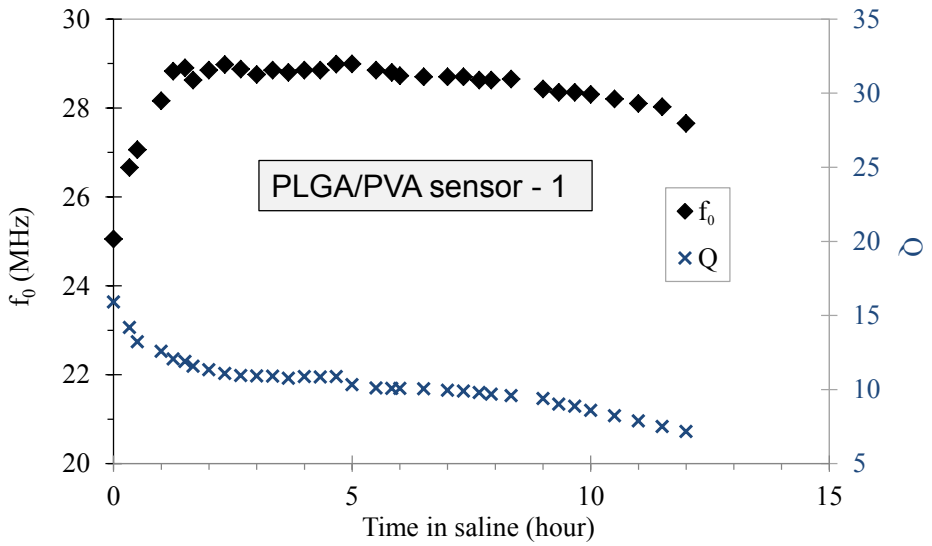

Figure 100: f_0 and calculated Q as functions of immersion time of the PLGA/PVA sensor 1 in saline (37 °C) with zero applied pressure

On the other hand, Q drops from 16 rapidly to 12 within the initial 90 minutes, then gradually decreases to 7 at 12 hours.

The pressure response of PLGA/PVA sensor 1 is measured at immersion time points of 0hours, 1.5 hours, 4 hours, and 9 hours, as shown in Figure 101. 0-20 kPa is applied during the pressure response measurement after then sensor has been immersed in saline. However, resonance disappears when the applied pressure exceeds certain values (15 kPa for immersion time point of 1.5 hours, 13.6 kPa for immersion time point of 4 hours, and 9.3 kPa for immersion time point of 9 hours). When the applied pressure is reduced to less than those thresholds, the resonance appears again. The resonant frequencies of the sensor corresponding to those pressure thresholds are all about 27 MHz. Therefore, the disappering of resonance is very likely due to the two parallel capacitor plates touching when too much pressure is applied.

The sensitivity of the sensor in air and in saline is plotted as a function of the immersion time in Figure 102. After the sensor is immersed in saline, the sensitivity increases slowly from -119.2 kHz/kPa at immersion time point 1.5 hours to -153.0 kHz/kPa at immersion time point 9 hours; the average rate of sensitivity increase is

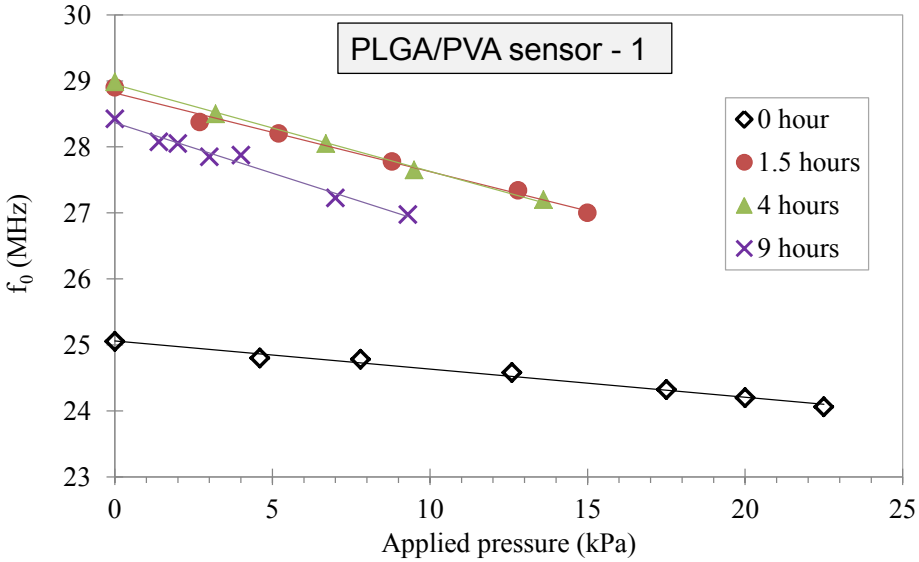

Figure 101: f_0 as a function of applied pressure in the pressure response measurements of PLGA/PVA sensor 1, (immersion time points: 0 hours, 1.5 hours, 4 hours, and 9 hours)

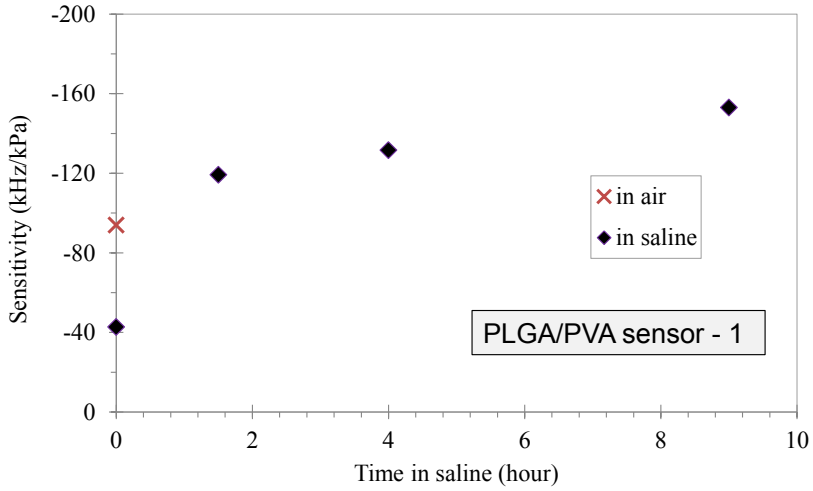

Figure 102: Calculated sensitivity of the PLGA/PVA sensor 1 in air (room temperature) and in saline (37 °C)

-4.5 kHz/(kPa·hour). The sudden reduction of sensitivity of the sensor from -93.9 kPa/kHz to -42.7 kPa/kHz when the sensor is placed in saline is very likely due to the extremely rapid f_0 increase during the initial stage of the immersion (Figure 100). Measurement of the sensitivity against the background of an equilibrating f_0 results in measurement artifacts and an artificially lowered sensitivity. Based on the result

of both Figure 100 and Figure 102, the equilibration stage of PLGA/PVA sensor 1 is the first 75 minutes, and the functional life time is the following 10 hours (from 1.5 to 11.5 hours).

6.3.3.2 PLGA/PVA Sensor 2 (PVA/PLGA Spacers)

PLGA/PVA sensor 2 with PVA-PLGA spacers is first characterized in air at room temperature by applying pressure from 0 to 30 kPa. The obtained f_0 is plotted as a function of applied pressure in Figure 103. The f_0 at zero applied pressure in air is 35.5 MHz, corresponding to a total capacitance of 10.6 pF. The sensitivity is -45.3 kHz/kPa.

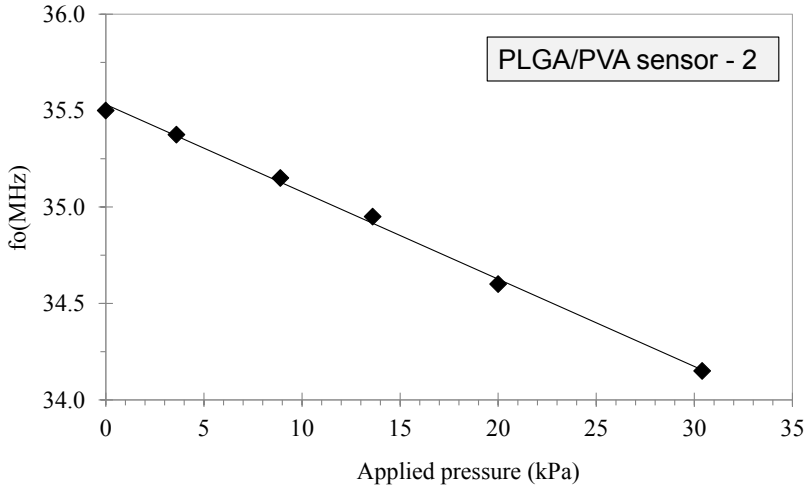

Figure 103: Measured f_0 as a function of applied pressure of PLGA/PVA sensor 2 in air at room temperature

Selected recorded impedance phase behavior as a function of frequency at different immersion times with zero applied pressure are shown in Figure 104. Similar to all the other sensors, the trough of the phase becomes shallower and broader as the immersion time increases, corresponding to decrease of Q. Clear resonance still can be detected when the sensor has been immersed in saline for 12.5 hours. However, after the sensor is placed in the incubator overnight, a very shallow and broad trough of phase behavior is detected at immersion time point 27 hours, and the phase plot

becomes almost flat at 30 hours, indicating very small Q.

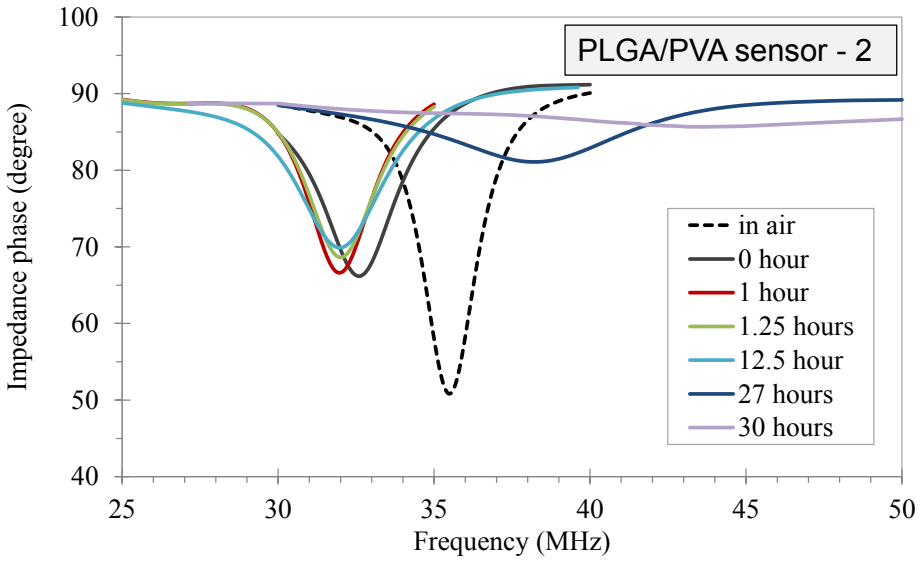

Figure 104: Impedance phase as a function of frequency of the PLGA/PVA sensor 2 in air (at room temperature) and in saline (at 37 °C) with zero applied pressure

f_0 and Q obtained from the measured impedance phase during the entire long-term immersion test are plotted as a function of immersion time in saline in Figure 105. The performance of the sensor in 37 °C can also be divided into three distinct stages: equilibration stage, functional lifetime, and performance degradation stage.

During the first 1.5 hours in saline, the f_0 of the PLGA/PVA sensor 2 decreases from 32.6 MHz to 32 MHz. This behavior is opposite to all the other sensors discussed previously (PLLA-Zn/Fe sensor 1-4 and PLGA sensor 1), but consistent with that of all the PLGA/PVA sensors with non-PLLA spacers (PLGA/PVA sensor 3 and 5). One hypothesis is that when the PLGA/PVA package swells in saline, the thin PLGA or PVA spacers, which are not as mechanically robust as the PLLA spacer, will be pressed inward slightly, resulting reduction of the distance between two capacitor plates and increase of the total inductance. The calculated capacitance increase is 0.5 pF.

During the functional lifetime of sensor 2 (beginning at 1.5 hours), f_0 increases with an average rate of 0.020 MHz/hour until some time between 12.5 hours to 27

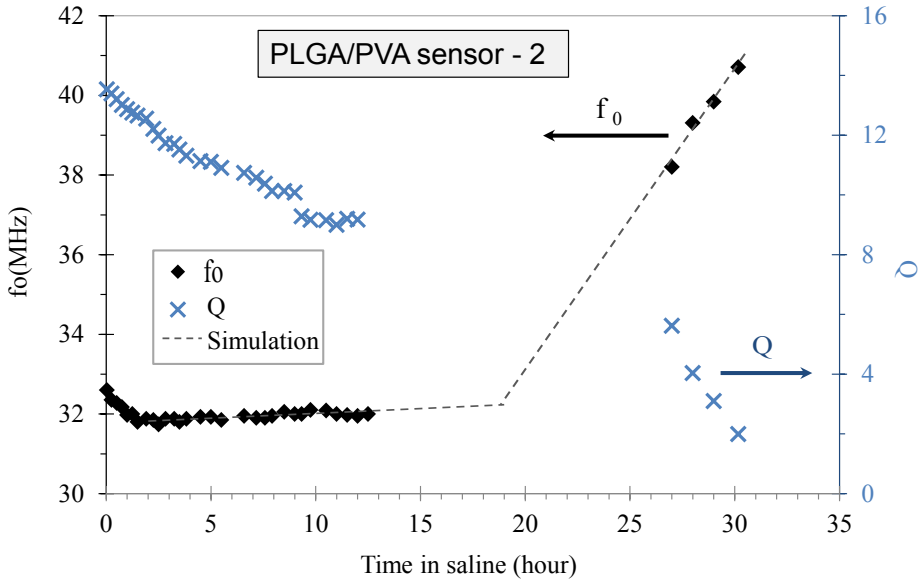

Figure 105: f_0 and calculated Q as a function of immersion time of the PLGA/PVA sensor 2 in saline (37 °C) with zero applied pressure

hours when the sensor begins to fail. The Q decreases slowly from 14 to 9 during the first two stages. During the performance degradation stage, f_0 increases rapidly at an approximately constant speed of 0.766 MHz/hour while Q decreases further to 2 when the sensor has been immersed in saline for 30 hours. No resonance can be detected afterwards. Unfortunately, due to the lack of data points during the night that the sensor is stored in the incubator, the exact time point that the sensor moves from functional lifetime to the performance degradation stage is not recorded. However, if linear increases of f_0 during the functional lifetime and performance degradation time are assumed (which is indicated by the recorded data), by extending the trend lines, the cross point that corresponds to the transition time point is approximately 19 hours. The rapid increase of the f_0 during the performance degradation stage is very likely due to the PVA film beneath the PLGA starting to swell/dissolve and pushing the capacitor plates further apart. The pictures of this sensor after being immersed in saline for 29 hours are presented in Figure 106. From the top view (Figure 106(a)), no obvious damage can be observed. But from the side view (Figure 106(b)), the

sensor is slightly twisted and the two capacitor plates are obviously pulled apart.

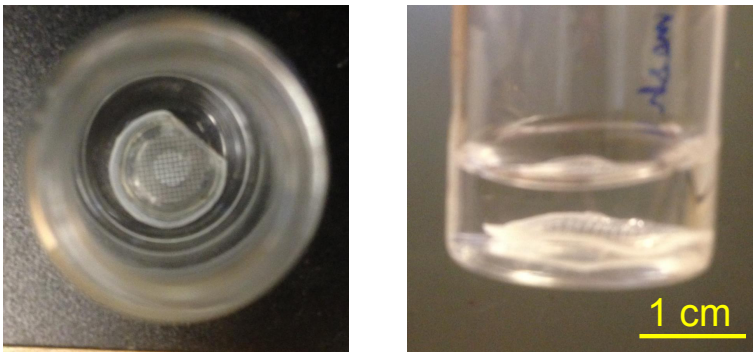

(a) (b)

Figure 106: (a) Top view, and (b) side view of PLGA/PVA sensor 2, after immersion in saline for 29 hours

Pressure response measurements of PLGA/PVA sensor 2 are performed at immersion time points of 2.25 hours, 5 hours, and 9 hours, as shown in Figure 107. The sensitivity of the sensor in air and in saline is plotted as a function of the immersion time in Figure 108. Before the sensor enters the performance degradation stage, the sensitivity of the PLGA/PVA sensor 2 remains relatively constant at 45.2 ± 1 kHz/kPa, which is comparable to the sensitivity in air.

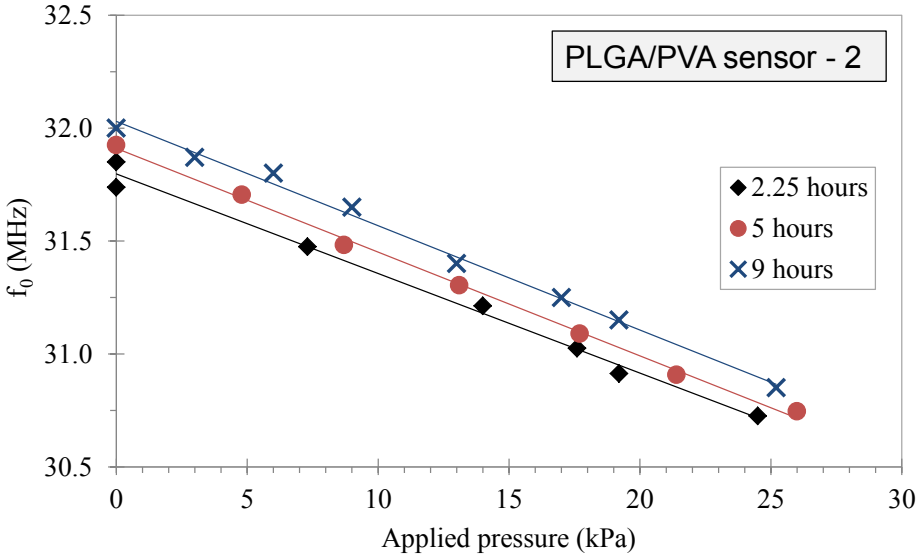

Figure 107: f_0 as a function of applied pressure of PLGA/PVA sensor 2 in saline (immersion time points: 2.25 hours, 5 hours, and 9shours)

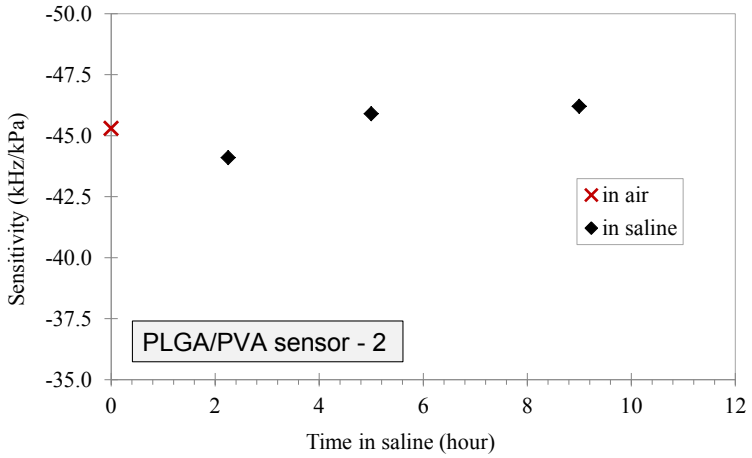

Figure 108: Calculated sensitivity of the PLGA/PVA sensor 2 in air (room temperature) and in saline (37 °C)

6.3.3.3 PLGA/PVA Sensor 3 (PLGA Spacer)

Similar to the characterization protocol of other sensors, pressure response measurements in air at room temperature (pressure range of 0 to 36 kPa) are first applied to PLGA/PVA sensor 3 to confirm its functionality. The result is plotted in Figure 109. A sensitivity of -43.3 kHz/kPa is exhibited, comparable to other sensors with similar design. The f_0 is 50.7 MHz in air with zero applied pressure. The calculated capacitance is 5.2 pF.

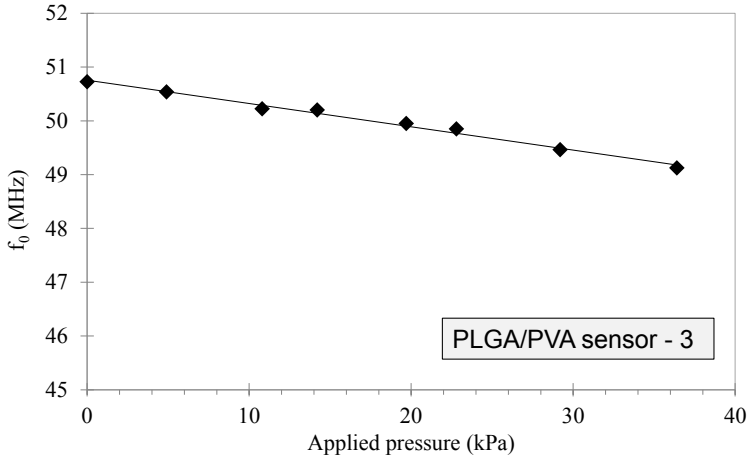

Figure 109: Measured f_0 as a function of applied pressure of PLGA/PVA sensor 3 in air at room temperature

Measured impedance behavior of the PLGA/PVA sensor 3 in air and in saline at zero applied pressure are shown in Figure 104. The f_0 and calculated Q during the entire immersion test are plotted as a function of immersion time in saline in Figure 100. The performance of the sensor in 37 °C can also be divided into three stages: equilibration stage (0 to 1.5 hours), functional lifetime (1.5 to 25 hours) and performance degradation stage (after 25 hours). The f_0 of PLGA/PVA sensor 3 drops dramatically from 47.3 MHz to 36.9 MHz in the equilibration stage, corresponding to a total capacitance change of 3.8 pF. This large decrease of f_0 might relate to the relatively thick PLGA package, but the precise reason is still under investigation. f_0 remains relatively stable at 31.7 ±0.3 MHz during the functional lifetime, and begins to increase rapidly when the sensor begins to fail after 25 hours. No obvious transition of Q can be found between the equilibration stage and the functional lifetime. Q remains above 12 before the sensor enters the performance degradation stage, and decreases rapidly to 5 at an immersion time of 27 hours. The phase is too flat to detect any resonance afterwards.

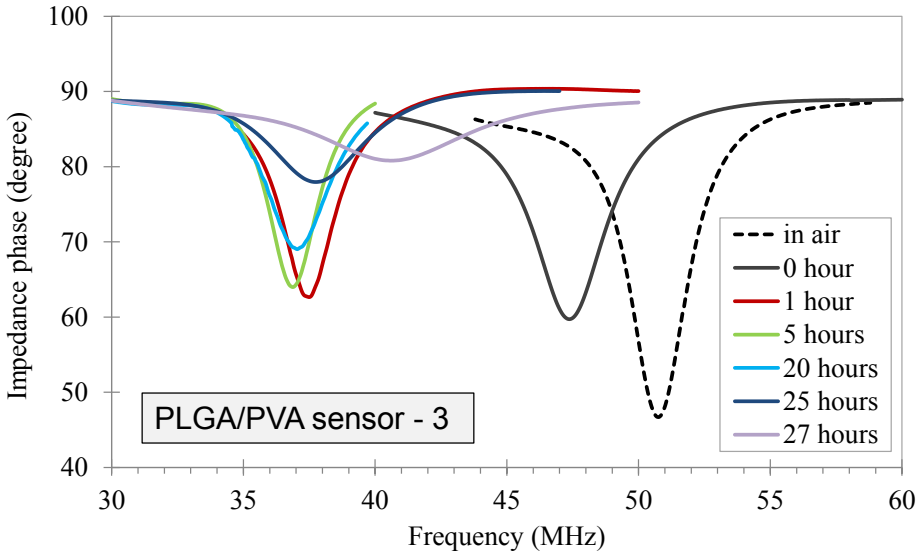

Figure 110: Impedance phase as function of frequency of PLGA/PVA sensor 3 in air (room temperature) and in saline (37 °C) with zero applied pressure

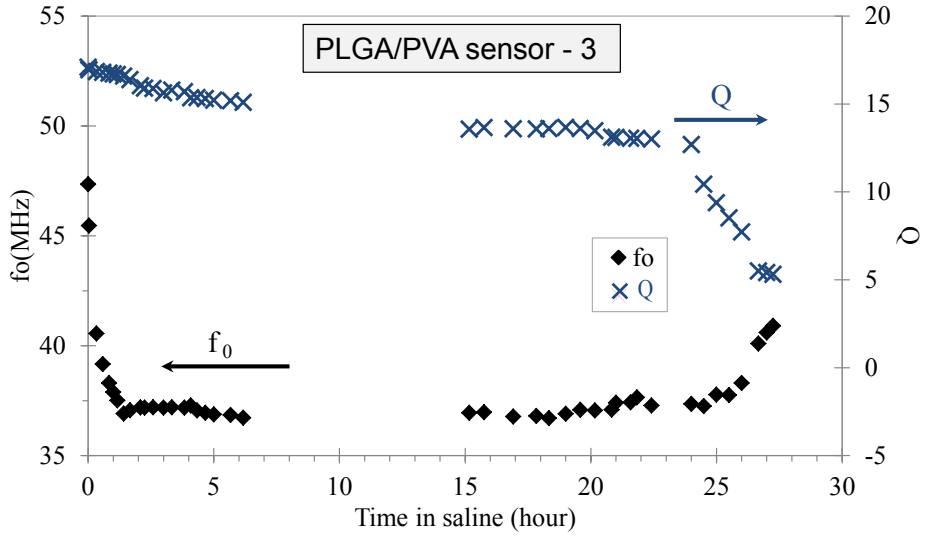

Figure 111: f_0 and calculated Q as functions of immersion time of the PLGA/PVA sensor 3 in saline (37 °C) with zero applied pressure

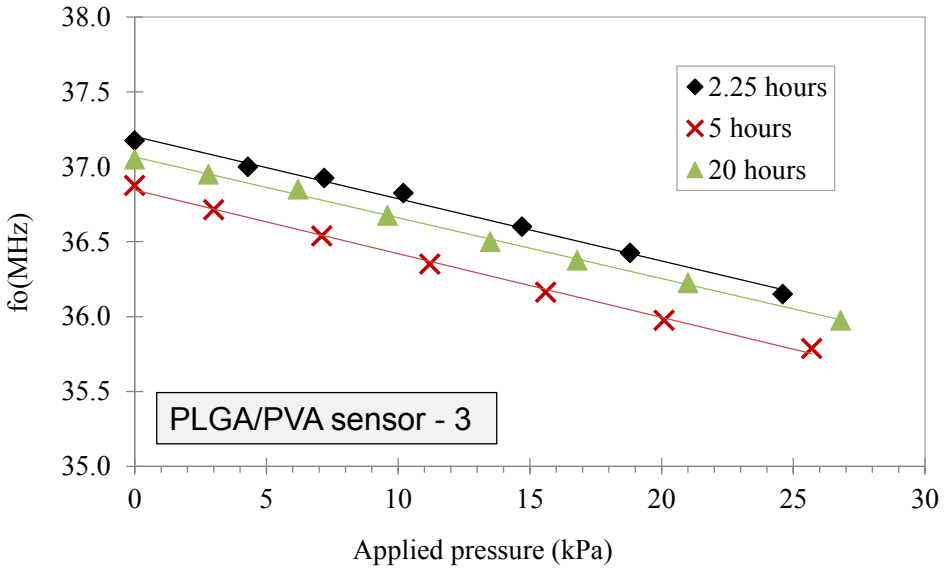

Figure 112: f_0 as a function of applied pressure of PLGA/PVA sensor 3 during immersion test in saline (immersion time points: 2.25 hours, 5 hours, and 22 hours).

Pressure response measurements of PLGA/PVA sensor 3 are performed at immersion time points of 2.25 hours, 5 hours and 20 hours, as shown in Figure 112. The sensitivity of the sensor in saline is calculated and presented together with the sensitivity in air (room temperature) in Figure 113. The sensitivity remains relatively

stable at 41.7 ± 0.6kHz/kPa in saline. These sensitivities in saline are also comparable to the sensitivity in air. This behavior is similar to that of the PLGA/PVA sensor 2 discussed above.

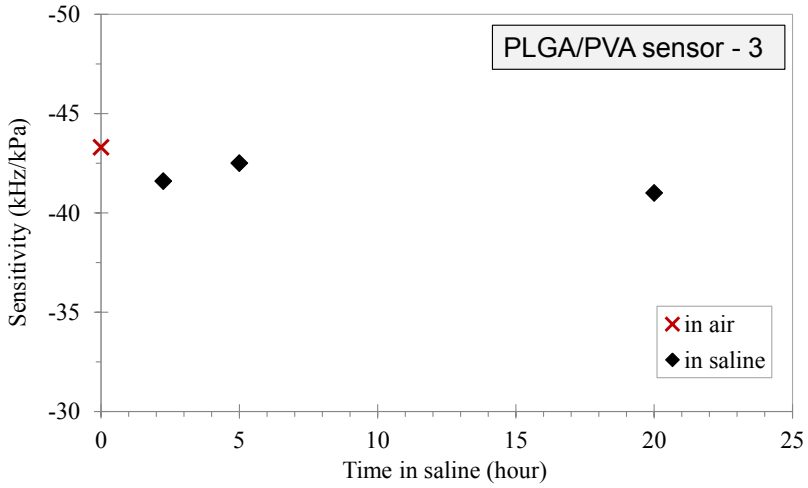

Figure 113: Calculated sensitivity of PLGA/PVA sensor 3 in air (room temperature) and in saline (37 °C)

6.3.3.4 Accelerated Degradation Due to Fabrication Defects of PLGA/PVA-based Sensors

During the characterization of PLGA/PVA sensors, it is found that some sensors, even with the same design as others and behaving normally during pressure response testing in air, fail much more rapidly than expected. PLGA/PVA sensors 4 and 5 are shown as such examples. The designs of these two sensors are listed in Table 13.

The results of the pressure response measurements of PLGA/PVA sensors 4 and 5 in air at room temperature are shown in Figure 114. Sensitivities of -78.9 kHz/kPa and -45.5 kHz/kPa are obtained for sensor 4 and 5 respectively.

The f_0 and calculated Q of PLGA/PVA sensors 4 and 5 during the long-term immersion test are plotted in Figure 115. Both of the sensors show no resonance after the last data point of each has been recorded (3 hours for sensor 4 and 5.67 hours for sensor 5). For PLGA/PVA sensor 4, almost no stable stage was observed between the equilibration stage and the performance degradation stage, during which

Table 13: Design of PLGA/PVA sensors 4 and 5

Samples	PLGA/PVA sensors	
	4	5
PVA thickness (μm)	200 - 230	250 -260
PLGA thickness(μm)	150	200
Spacer Materials	PLLA and PCL	PVA and PLGA
Spacer thickness (μm)	35	30
PVA lamination temperature °C	165	130

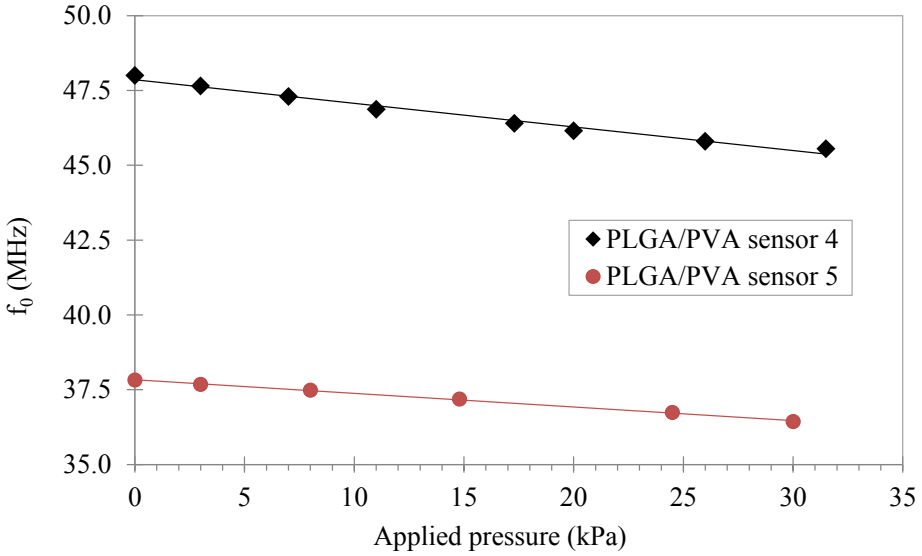

Figure 114: f_0 as a function of applied pressure of PLGA/PVA sensors 4 and 5 in air at room temperature

f_0 decreases rapidly accompanied with Q dropping to below 8. For PLGA/PVA sensor 5, a distinguishable equilibration stage (0 to 2.5 hours) and functional lifetime (2.5 to 5.33 hours) are exhibited. During the functional lifetime, f_0 remains constant at 32.66 $\pm$ 0.03 MHz, and Q decreases slowly from 14 to 11. However, resonance suddenly disappears when sensor 5 is taken out of the incubator for the next measurement at an immersion time point of 5.67 hours, even though no signs of performance degradation had been observed prior to this time point.

Upon observation, the reason for this accelerated failure is very likely due to

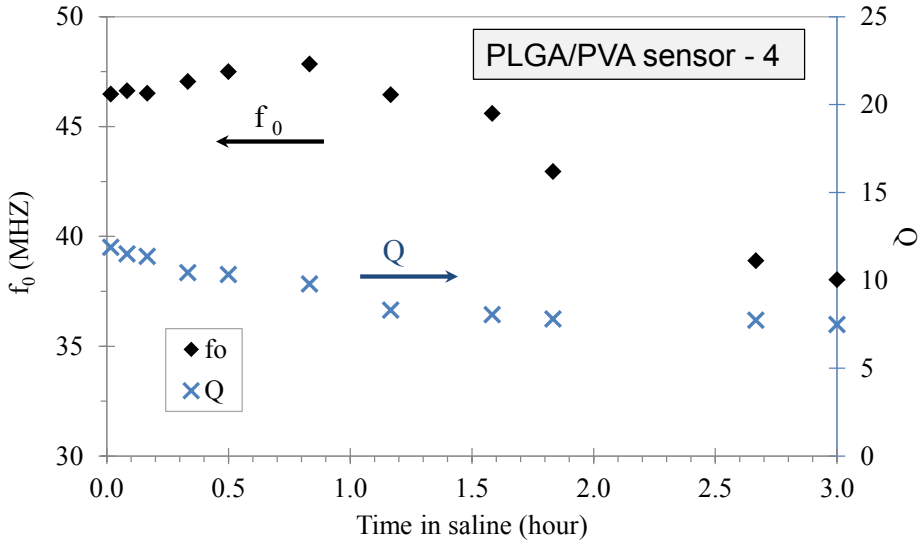

(a)

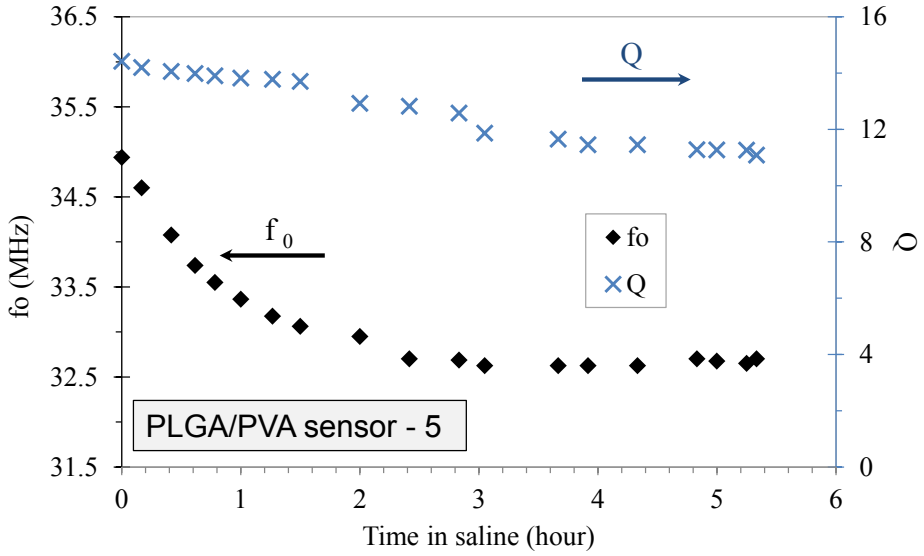

(b)

Figure 115: f_0 and calculated Q as a function of immersion time of (a) PLGA/PVA sensor 4, and (b) PLGA/PVA sensor 5, in saline (37 °C) with zero applied pressure

the previously-described bubbles that are trapped in the PLGA and/or between the PLGA and PVA films during lamination. These bubbles, especially the ones trapped close to the outer surface of the PLGA shell film, can dramatically reduce the functional lifetime of the sensor. These bubbles reduce the thickness of the PLGA shell package and make these points vulnerable to the invasion of water. The PVA core

film inside the PLGA shell film can be dissolved and force the breakage of the PLGA shell film. Then the sensor will fail rapidly once the water can penetrate directly into the sensor through these fractures. Pictures of PLGA/PVA sensor 4 before and during the long-term immersion test are presented in Figure 116. Compared with the well-functioning PLGA/PVA sensor 2 (Figure 106(a)) that appears white only on the PLGA edge upon failure at 29 hours, after PLGA/PVA sensor 4 has been immersed in saline for 1 hour, a white spot is observed as marked in Figure 116(b), indicating the swelling and/or dissolution of the PVA. As immersion continues, more damage points are detected surrounding the edge of the PVA core film. At the time point of 3.5 hours, which is 30 minutes after the sensor stops resonant behavior, the PVA core film beneath the PLGA shell film has been greatly damaged; an opening can be clearly seen from the side view in Figure 116(c).

A summary of the functionality measurements of PLGA/PVA-based sensors in air and *in vitro* are listed in Table 14.

Table 14: Functionality characterization summary for PLGA/PVA-based sensors

Environment	**Properties**	**PLGA/PVA sensors**		
		1	**2**	**3**
Spacer materials		PLLA/PCL	PVA/PLGA	PLGA
PVA embossing temperature		165 °C	130 °C	130°C
In air	f_0 at 0 pressure (MHz)	27.9	35.5	50.7
	Sensitivity (kHz/kPa)	-93.9	-45.3	-43.3
In vitro	Equilibration stage (hour)	1.5	1.5	1.5
In vitro-during functional lifetime	Functional lifetime (hour)	10	16.5	23.5
	f_0 at 0 pressure (MHz)	28.6±0.3	32.2±0.2	31.7±0.3
	Sensitivity (kHz/kPa)	-136.1± 16.9	-45.2±1	-41.7±0.6
	Q	>8	>8	14

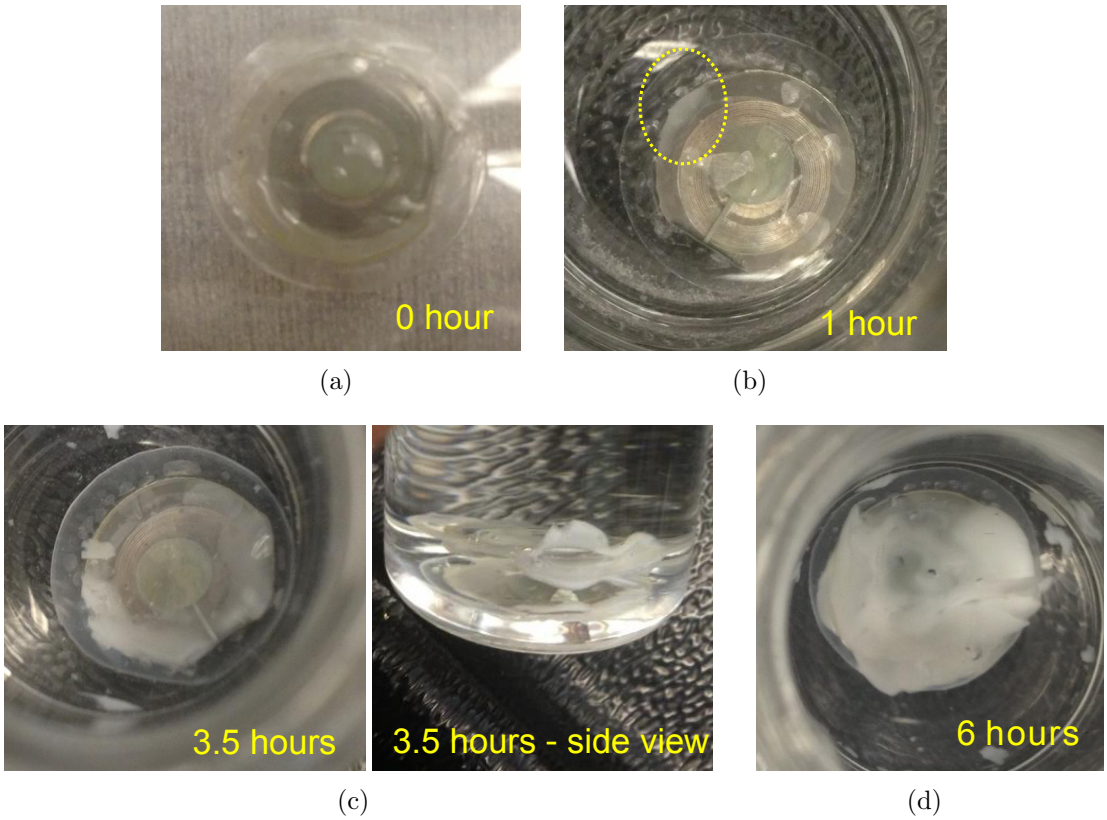

Figure 116: Time sequence pictures of PLGA/PVA sensor 4 (a) before, and (b-d) during the long-term immersion test in saline (37 °C) at immersion times of (b) 1 hour, (c) 3.5 hours, and (d) 6 hours

6.4 Functionality Characterization of Biodegradable Pressure Sensor Without Conducting Via

The biodegradable pressure sensor without conducting via, prepared for the functionality test presented here, consists of a PLGA/PVA "shell-core" stucture as package and PLLA/PCL as spacers. The dimensions of the Zn inductor and single plate capacitor are the same as that of the sensors with conducting via. The PVA embossing temperature is 165 °C.

6.4.1 Characterization in Air

The sensor is first characterized in air at room temperature. The pressure response measurement is performed, shown in Figure 117. Under zero applied pressure, the

f_0 of this sensor without conducting via is 73.3 MHz. A extremely high sensitivity of -341 kHz/kPa is observed. One possible reason is that the PLLA spacer is not completely laminated to the capacitor plates and/or polymer package film.

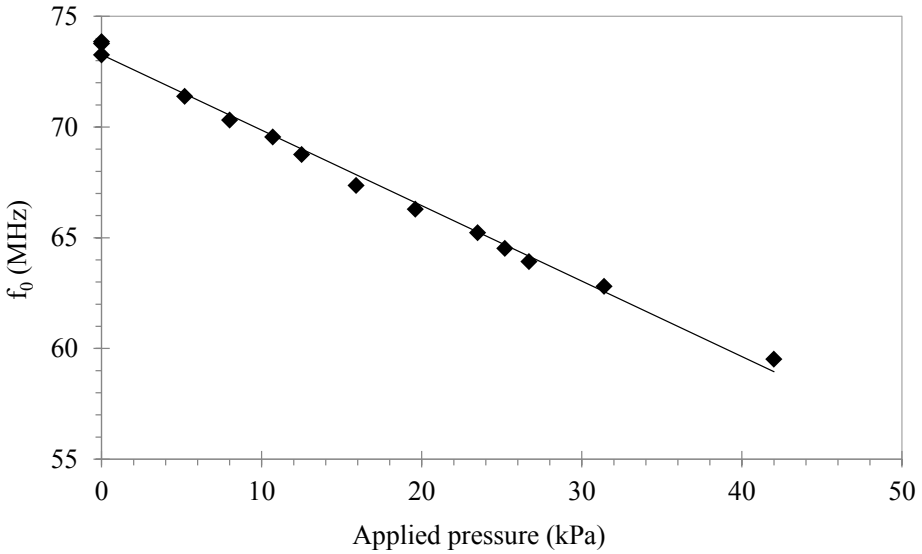

Figure 117: f_0 as a function of applied pressure for pressure sensor without conducting via in air

A short-term stability test is performed by applying constant pressure (10 kPa) to the sensor in air for approximately 42 hours. The f_0 recorded during the whole process is shown in Figure 118. f_0 decreases from 73.3 MHz to 68.9 MHz instantly upon 10 kPa pressure is applied and remains stable for the first 5 hours. A very slow increase of the f_0 from 68.9 MHz to 69.2 MHz from 5 hours to 43 hours is observed. This very slow shift of the f_0 under 10 kPa, however is not unacceptable for PLGA/PVA film which does not have perfect air-tightness.

6.4.2 *In Vitro* Characterization

The sensor withour conducting via is also placed in saline of 37 ° and characterized in a long-term immersion test. The detailed protocol is the same as the PLGA/PVA-based sensors with conducting via described in Section 6.3.3. The f_0 of the sensor with zero applied pressure and calculated Q are plotted as a function of immersion time in

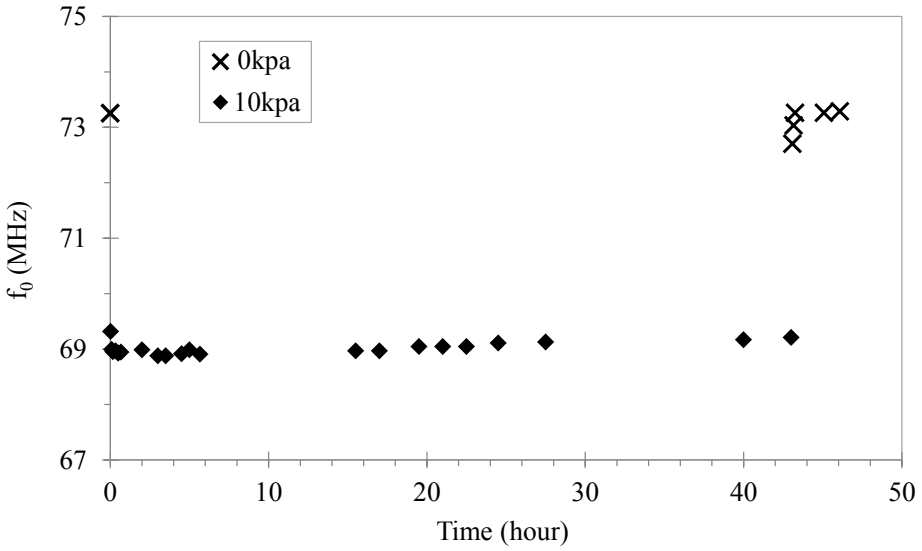

Figure 118: f_0 of the pressure sensor without conducting via before, during and after a constant pressure of 10 kPa is applied in air

Figure 119. The pictorial time history of the sensor is shown in Figure 120. During the equilibration stage (0 to 2.3 hours) f_0 increases rapidly from 60.9 MHz to 64.1, and Q decreases from 9 to approximately 5. From 2.3 hours to 8 hours, f_0 fluctuates around 64.1 MHz while Q remains above 3.5. This can be considered as the functional lifetime for this sensor. When the sensor transitions to the performance degradation stage, both f_0 and Q decrease rapidly and no resonance can be detected after the sensor has been immersed in saline for 13 hours. As expected, the PLGA/PVA sensor without via has a lower Q than sensors with conducting via, as discussed in Chapter 3. The edge (PLGA) of the sensor turns white, which has been also observed in other PLGA/PVA-based sensors after they fail.

This particular pressure sensor without conducting via does not show satisfying performance. Due to time restrictions, no additional devices without conducting via were fabricated and tested. However, based on this preliminary result, it is optimistic to expect that biodegradable pressure sensors without conducting via can achieve equally good performance as the sensors with via, allowing reduced complexity in sensor fabrication.

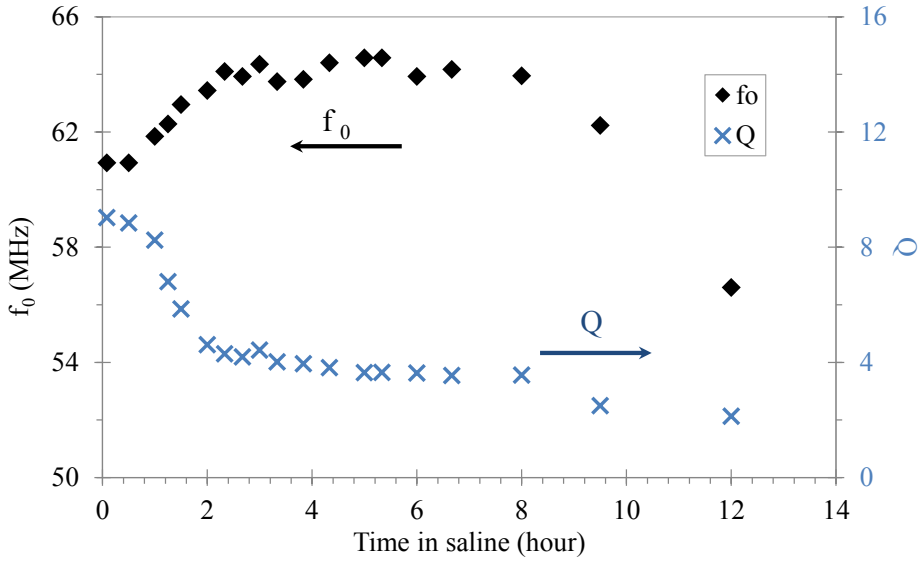

Figure 119: f_0 and calculated Q as functions of immersion time of pressure sensor without conducting via in saline (37 °C) with zero applied pressure

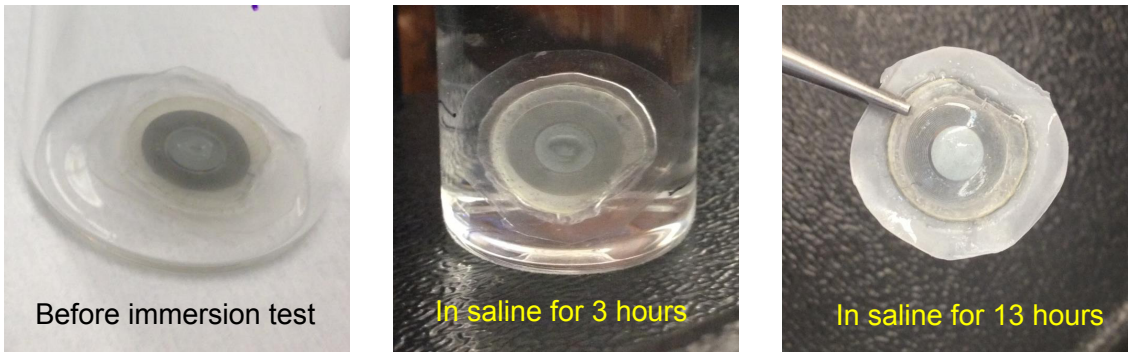

(a) (b) (c)

Figure 120: Pictorial time history of a PLGA/PVA-based sensor without conducting via: (a) before immersion test, (b) after immersion in 37°C for 3 hours, and (c) out of the saline after having been immersed for 13 hours

CHAPTER VII

IN VITRO DEGRADATION STUDY OF THE BIODEGRADABLE SENSORS

In Chapter 4, the degradation behaviors of the polymer and the metal materials of the sensor have been studied respectively. Those results can be utilized as guidance for developing the design of biodegradable sensors with designed degradation time. In this chapter, *in vitro* degradation behavior of the fabricated fully functional sensors are investigated. Together with the functional performance illustrated in Chapter 6, the complete performance study of this novel biodegradable pressure senor is presented.

7.1 In vitro Degradation Study of Biodegradable Zn/Fe-couple Conductors

Freestanding electroplated Zn/Fe-couple conductors are obtained by dissolving the embossing polymer (PLLA) film bearing the embedded Zn/Fe-couple conductor patterns. The conductors are washed with DCM to remove polymer residues and dried thoroughly before the weight of each specimen is carefully measured. During the degradation test, each specimen is immersed in saline (0.9% NaCl, pH 6.8) and placed in an incubator at a temperature of 37±0.5°C with gentle mechanical agitation (shaker, < 50 rpm). When the specimens are removed from saline for weight measurements, each specimen is rinsed with approximately 50 mL DI water for at least 3 times and dried thoroughly in a 37±0.5°C oven overnight.

7.1.1 Degradation of Electroplated Zn/Fe(bilayer) Conductors

The weight of each electroplated Zn/Fe(bilayer) specimen is measured approximately every 24 hours over a 300-hour time frame. Each specimen is placed in approximately 10 ml of saline, and the saline is refreshed every 24 hours. Figure 121 shows Zn/Fe(bilayer) conductor specimens before the degradation test and after immersion in saline for 24 hours before washing and drying. Similar to that of the Zn/Fe-couple rectangular specimens studied in Chapter 4, a significant quantity of residue is observed on the surface of the specimens. Most of the residue is loosely attached to specimens and can be removed by rinsing the specimens in DI water.

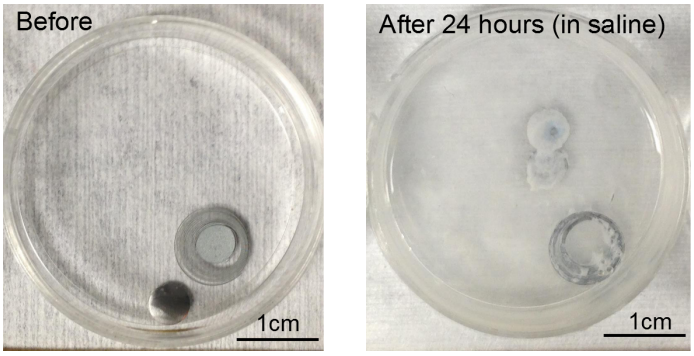

(a) (b)

Figure 121: Electroplated Zn/Fe bilayer freestanding conductors (a) before degradation, and (b) after degrading for 24 hours in 0.9% saline (without washing and drying).

A pictorial history of the Zn/Fe(bilayer) conductors over the 300-hour experiment duration is shown in Figure 121. The behavior is consistent with that of the Zn/Fe rectangular specimens. Initially, a white oxidation product is observed, consistent with Zn oxidation [21]. As the degradation of the Zn/Fe(bilayer) conductors continues, the specimens lose physical integrity, beginning with the thinner coil lines and proceeding to the capacitor plates. As degradation progresses, brown/red iron oxides begin to be observed, consistent with iron oxidation [98], and these oxides are not soluble during rinse.

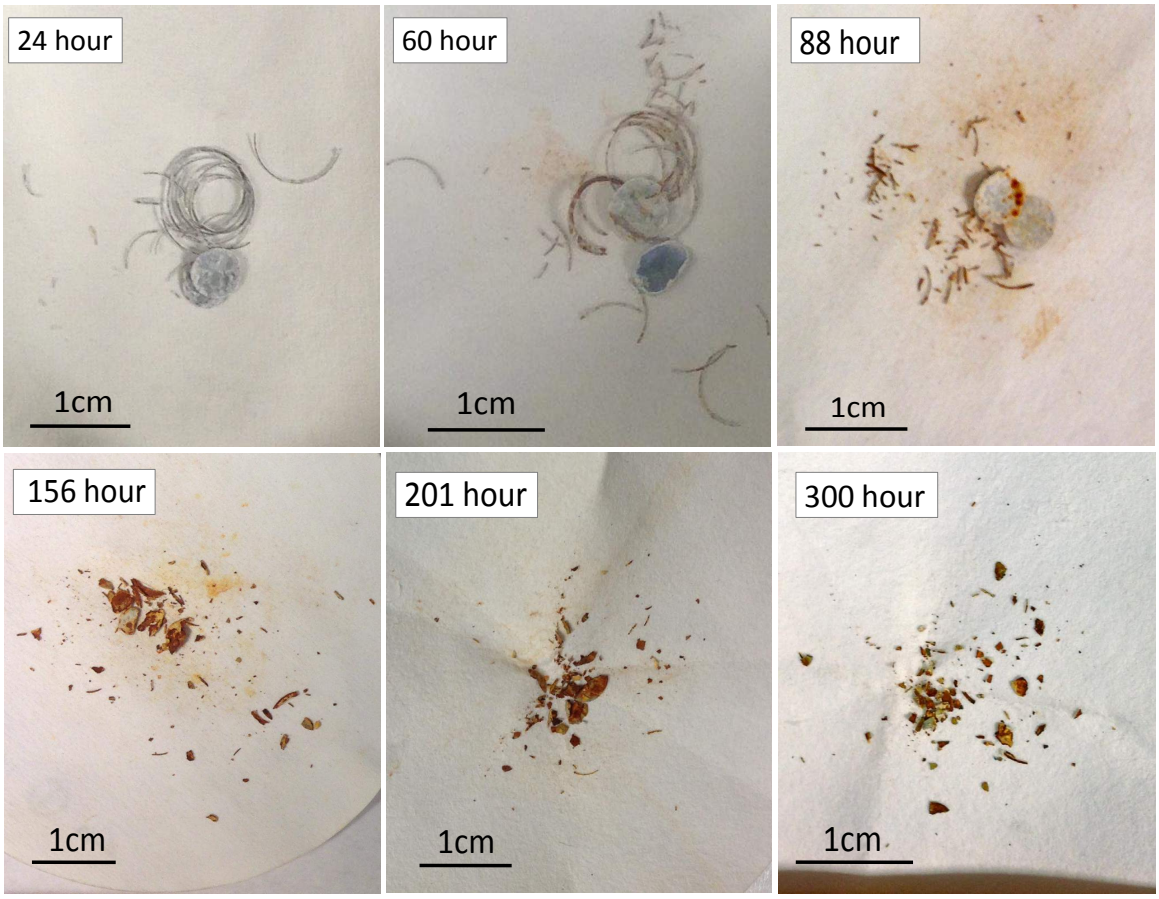

Figure 122: A pictorial history of the Zn/Fe(bilayer) conductors over a 300-hour experiment duration.

Four Zn/Fe(bilayer) specimens of similar nominal initial weight (29 ± 2 mg) are selected for detailed weight loss analysis. The normalized average remaining weight as a function of degradation time is plotted in Figure 123. The four specimens show similar degradation behavior: the weight of the specimens monotonically decreases over 200 hours, reaching an asymptotic residual weight of approximately 20% of the original weight.

To further understand the detail of this degradation behavior, the average weight loss rate (mg/hour, not normalized by Zn area) as a function of degradation time of the Zn/Fe(bilayer) is plotted in Figure 124. The degradation rate can be roughly divided into 3 stages. In the first 72 hours (stage 1), the degradation rate is the most rapid, above 0.15 mg/hour. This stage corresponds to the period that specimens are

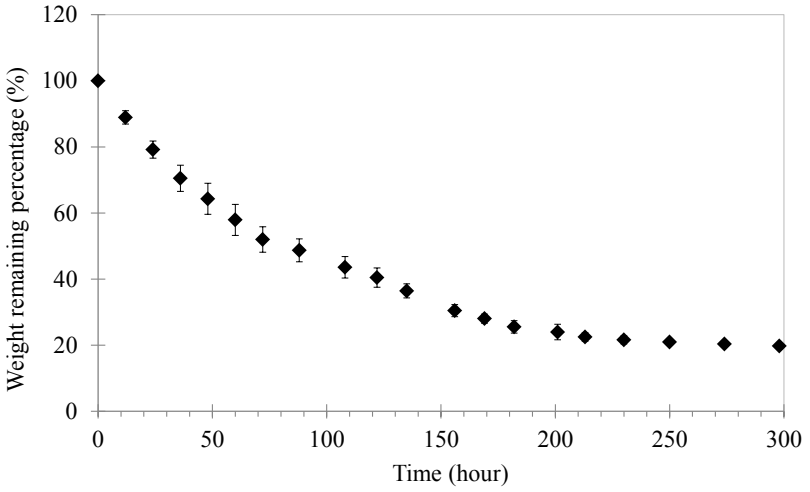

Figure 123: Remaining weight (in percent) of the Zn/Fe(bilayer) conductor specimens as a function of time during the *in vitro* degradation measurement.

either unbroken or broken into relatively large pieces, in which the degradation of the Zn/Fe(bilayer) structure is consistent with a galvanic corrosion mechanism. The original total Zn surface area including the top surface and side-wall is 0.62 cm^2, and the Fe surface is 0.52 cm^2. The calculated weight loss rate per unit area of Zn per hour is between 0.5 to 0.25 mg/(cm^2·hour). This rate is a little lower than the degradation rate model developed in Chapter 4. The main reason might be the different protocol used here: the volume of the saline is smaller and refresh frequency is less. In stage 2, between 84 and 180 hours, the degradation rate of the bilayer specimen is between 0.05-0.1 mg/hour. In this stage, the specimens have broken into much smaller pieces, some of which may no longer have been bearing Zn, and initial formation of iron oxides is observed. This slower iron oxidation, together with the reduced Zn surface area as degradation proceeds, is consistent with the observed reduction in weight loss rate. In stage 3, after 200 hours, the degradation rate of the specimens is very small ($<$ 0.04 mg/hour). In this period, the entire specimen has been broken into very small pieces (Figure 122). Most of the Zn has gone, leaving only the iron oxide. The total weight of the corroded specimens at the end of stage 3 was approximately 20% of the original weight (Figure 123), which is consistent with the expected weight

of remaining iron if it had been transformed into iron oxides. The residue of the corroded iron cannot be dissolved in saline; however, *in vivo* studies of iron implants that have undergone biodegradation have shown both lack of toxicity of any residual iron oxides [113, 114] as well as postulated phagocytic transport of iron oxide particles away from the implant site [100].

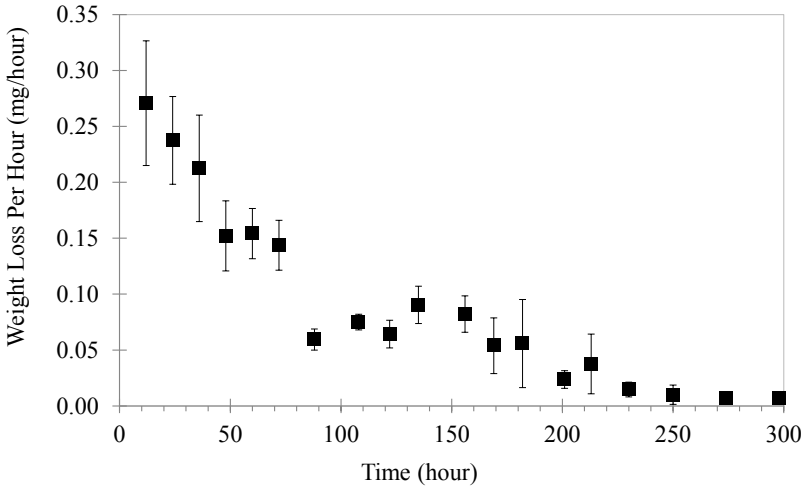

Figure 124: Weight loss rate (mg/hour) of the Zn/Fe(bilayer) conductor specimens as function of degradation time in saline.

7.1.2 Degradation of Zn/Fe(checker) Conductors

A degradation study of the Zn/Fe(checker) conductor that is fabricated by E-beam evaporation of 500 nm Fe on partial portions of the electroplated Zn surface is also performed. To compare the weight loss rate of the Zn/Fe conductor with the model deduced from rectangular Zn/Fe-couple pieces in Chapter 4, a similar protocol is utilized here: the weight of each plated Zn/Fe(checker) specimen is measured approximately every 6 hours over a 60-hour time frame. Each specimen is placed in approximately 10 ml of saline, and the saline is refreshed every 6 hours. A pictorial history of the Zn/Fe(checker) conductors (50% coverage shadow mask coverage) over the 60-hour experiment duration is shown in Figure 125. The behavior is consistent with that

of the electroplated Zn/Fe(bilayer) conductors. Similar to the Zn/Fe(checker) rectangular specimens in Chapter 4, breakage of the windings usually occurs in the Zn area between the Fe coverage, where the most rapid degradation is observed. After 60 hours, no significant amount of iron oxides are observed, suggesting that full degradation of the specimens has not yet occurred.

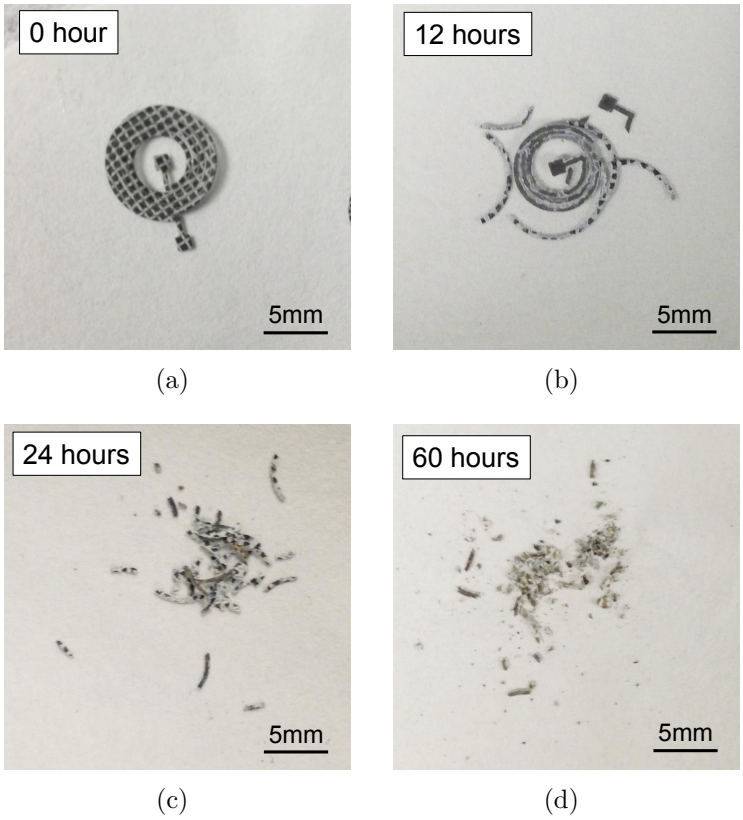

Figure 125: A pictorial history of the Zn/Fe(checker) conductors: (a) before degradation, and (b-d) after degrading *in vitro* for (b) 12 hours, (c) 24 hours, and (d) 60 hours.

Three Zn/Fe(checker) specimens with similar nominal initial weight (27 ± 1 mg) are selected for detailed weight loss rate analysis. The normalized remaining weight percentage and the average rate of weight loss (in mg/hour, not normalized by the aread of Zn) as functions of degradation time are plotted in Figure 126 and Figure 127 respectively. The remaining weight percentage is approximately 49% after *in-vitro* degradation testing for 60 hours. The average weight loss decreases monotonically

from 0.42 mg/hour in the initial 6 hours to 0.1 mg/hour after 60 hours. This is due to the continuous loss of physical integrity, especially after 24 hours. In the initial 12 hours, the average weight loss rate per unit area of initially exposed Zn (0.53 cm^2) is calculated to be between 0.77 and 0.52 mg/(cm^2·hour). This value agrees well with the degradation rate model developed in Chapter 4.

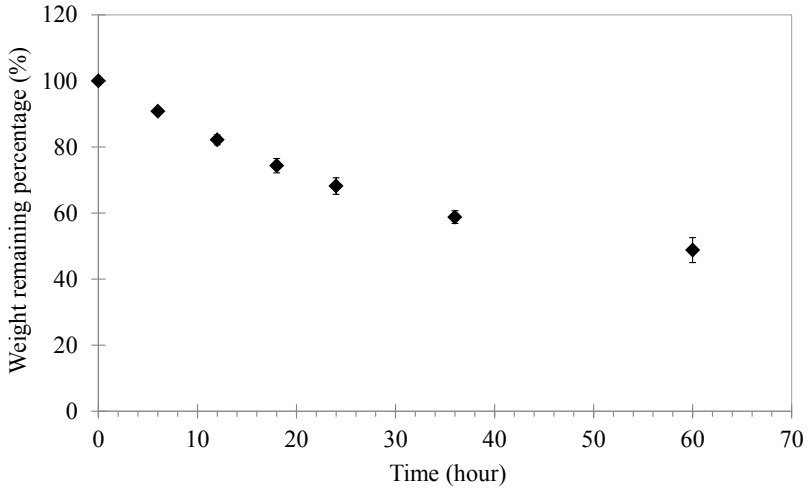

Figure 126: Remaining weight (in percent) of the Zn/Fe(checker) conductor specimens during *in vitro* degradation measurement.

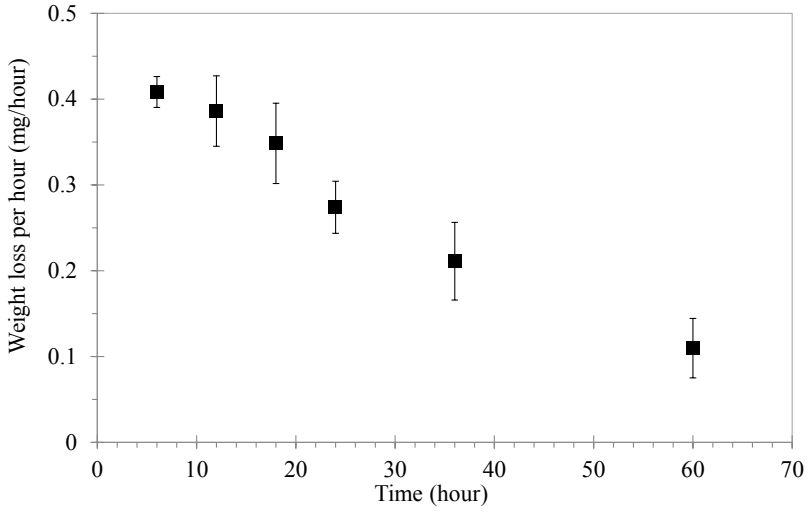

Figure 127: Weight loss rate (mg/hour) of the Zn/Fe(checker) conductor specimens as a function of degradation time in saline.

7.2 *In Vitro Degradation Behavior of Biodegradable Pressure Sensors*

7.2.1 *In Vitro* Degradation of PLLA-based Sensors

After completion of the functionality performance characterization, each PLLA-based sensor is placed in approximately 20 mL of 0.9% saline and stored at 37 ±0.5°C in an incubator. The sensors are removed the saline for weight measurement intermittently. Before each weight measurement, each sensor is rinsed with at least 300 mL DI water, and dried for 48 hours at 37 ±0.5°C. The entire degradation measurements last for approximately 8 months for the PLLA-Zn and PLLA-Zn/Fe(bilayer) sensors, and 60 days for the PLLA-Zn/Fe(checker) sensors. The normalized weight changes of these three kinds of PLLA-based sensors are shown in Figure 128, with pictures of them at different degradation times shown in Figure 129.

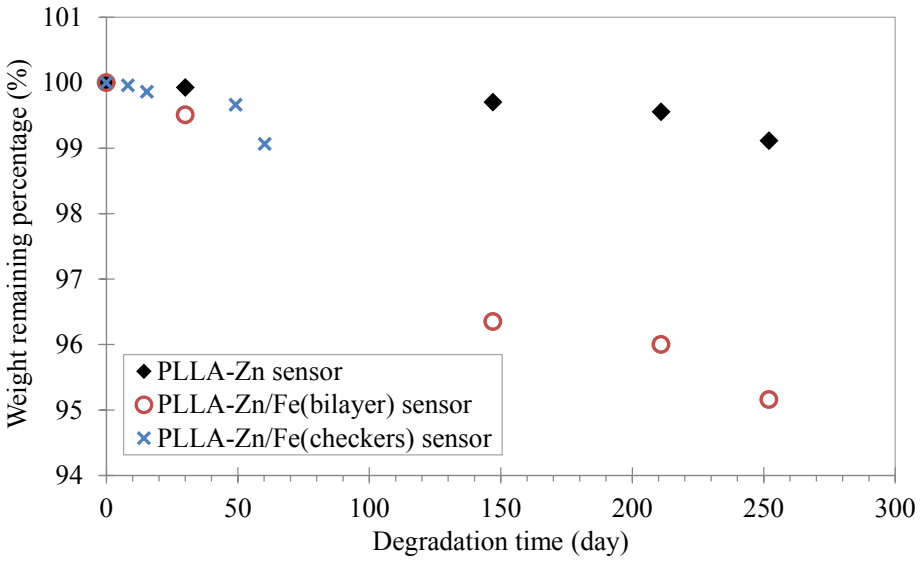

Figure 128: Remaining weight percentage of PLLA-based sensors during *in vitro*degradation characterization.

After 8 months, PLLA sensors with pure Zn and Zn/Fe-couple conductors show less then 2% and 5% weight loss, respectively. This small weight loss is reasonable due to the fact that PLLA, which accounts most of the weight of the sensor, takes years to degrade *in vitro* [9, 141, 142]. However, it is noticeable that the metal conductor

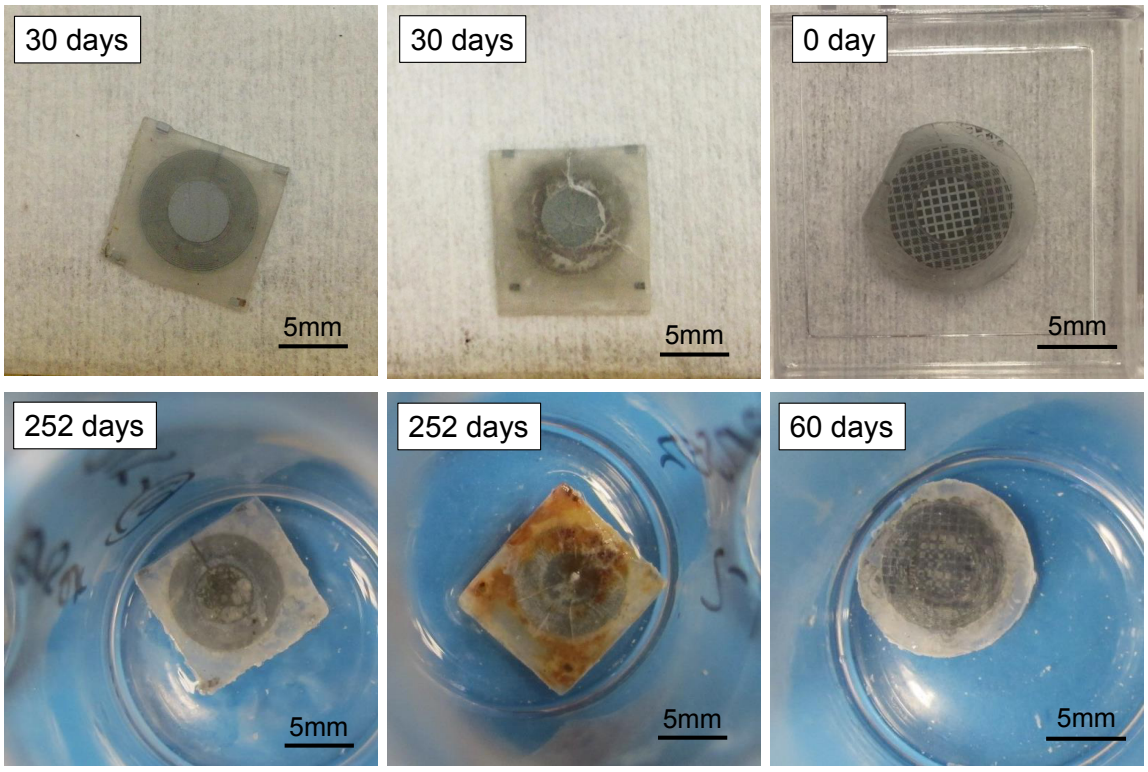

(a) (b) (c)

Figure 129: A pictorial history of PLLA-based sensors with a: (a) pure Zn conductor, (b) Zn/Fe(bilayer) conductor, and (c) Zn/Fe(checker) conductor, before and during the sensor *in vitro* degradation characterization.

begins to degrade during this time period, even they are encapsulated within the PLLA package. Generation of a fair amount of Zn oxides is observed in the sensor with pure Zn conductor (Figure 129(a)) and the sensors with Zn/Fe-couple conductors during the early stages (60 days) (Figure 129(b) and Figure 129(c)). Brown/red Fe oxides are also observed in the sensors with Zn/Fe(bilayer) conductors in the later stages in Figure 129(b). It should be noted that there is still a certain amount of Zn present after the Fe already begins to degrade (Figure 129(b): 252 hours), this might due to the PLLA film restraining the release of the Zn oxides, thereby reducing the efficiency of the Fe-Zn galvanic couple.

7.2.2 *In Vitro* Degradation of PLGA/PVA-based Sensors

In order to understand the degradation lifetime of the PLGA/PVA-based sensors, a prolonged *in vitro* degradation measurement of these sensors in saline is performed after sensor electrical resonance can no longer be detected. Each sensor is kept in its glass vial with approximately 20 ml of 0.9 % saline and stored in the incubator under 37 $\pm$0.5 °C. The weight of each sensor is measured intermittently until the majority of the sensor is degraded. To measure the weight of the sensor, the extra saline inside the vial is removed, and 20 ml of DI water is poured into the vial to rinse the sensor. The sensor is rinsed for at least 5 times, and placed into the 37 $\pm$0.5 °C oven together with the vial container, and dried for 48 hours prior to measurement.

The degradation rate of PLGA/PVA-based sensors are expected to be much more rapid than PLLA devices due to the relatively rapid degradation rate of the PLGA and PVA films. As mentioned in the fabrication of the PLGA/PVA-based sensor in Chapter 5, 165 °C is initially utilized to emboss the metal conductor into the PVA film, and PLLA-PCL spacers are utilized to create the cavity in the sensor. However it is observed that PVA undergoing such high temperature processing will crosslink and subsequently cannot dissolve completely in water at 37 °C. Therefore, 130 °C is utilized as the embossing temperature of PVA film in later studies; and at the same time, non-PLLA spacers are adopted to enable the complete dissolution of the sensor within a short time.

Below, the long term degradation behavior of these two types of sensors (based on the spacer materials utilized) are presented. In each types of sensor, the conductor can be either pure Zn or Zn/Fe-couple. Pictorial history as well as the weight loss results are presented for each type of sensor.

7.2.2.1 In vitro Degradation of PLGA/PVA-based Sensors With PLLA/PCL Spacer and 165 °C PVA Embossing Temperature

Within this type of PLGA/PVA-based sensor (PLLA/PCL spacers and 165 °C PVA embossing temperature), two types of contuctors, pure Zn and Zn/Fe-couple are fabricated and characterized.

(a) Pictorial Histories

The pictorial history of degradation of a such PLGA/PVA-based sensor with Zn conductor is shown in Figure 130. At a time point of 24 hours, in addition to the observation that the edge of the PLGA turns translucent (which usually is accompanied by failure of the sensor), white patches appear in the middle of the sensor (Figure 130(b)). These white patches correspond to the swelling/dissolving of highly crosslinked PVA. As the sensor is immersed in saline for longer times, the area of the white patches increases gradually (Figure 130(c)). By the 3 day time point, the sensor becomes completely white and opaque (Figure 130(d)). The PLGA package finally breaks and the sensor starts to fragment into small pieces; meanwhile, the Zn originally present inside the sensor starts to degrade as well (Figure 130(e)-Figure 130(g)). However, due to the high crosslink density introduced into the PVA during the 165 °C lamination process, the PVA cannot dissolve in the saline completely, as shown by the white residue remaining after 39 days (Figure 130(h)).

Degradation of such a PLGA/PVA based sensor with Zn/Fe(checker) conductors is also studied. Referring to the PLGA/PVA sensor 1 studied in Section 6.3.3. Prolonged degradation testing is performed, and the pictorial history is shown in Figure 131. Before the PLGA package breaks, the sensor with Zn/Fe(checker) conductors exhibits similar degradation phenomena as that of the sensors with pure Zn conductor; thus, the first four days of history are not included in Figure 131. Due to the checker-shape coverage of Fe on the Zn surface, significant amounts of Zn oxides appear in Figure 131(a). As the degradation of the sensor continues, the

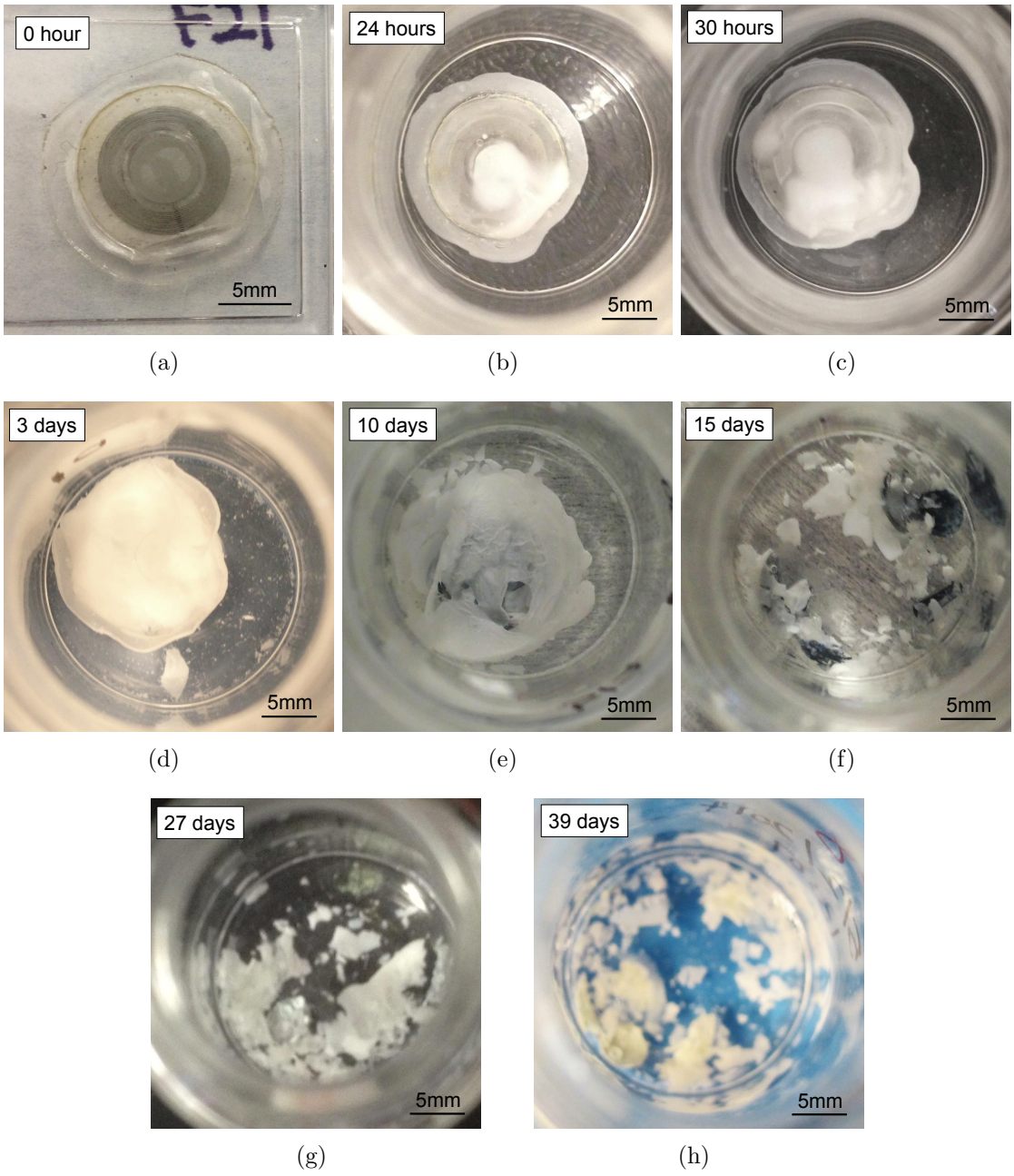

Figure 130: Pictorial history of a PLGA/PVA-Zn sensor with PLLA-PCL spacers and 165 °C PVA embossing temperature (PLGA/PVA sensor 1) *in-vitro* degradation at time points of: (a) 0 hour, (b) 24 hours, (c) 30 hours, (d) 3 days, (e) 10 days, (f) 15 days, (g) 27 days, and (h) 39 days.

metal conductor starts to segment into very small fragments along the boundary of the Zn/Fe junction, and red/brown Fe oxides appear in the late stage after 20 days (Figure 131(b) - Figure 131(d))

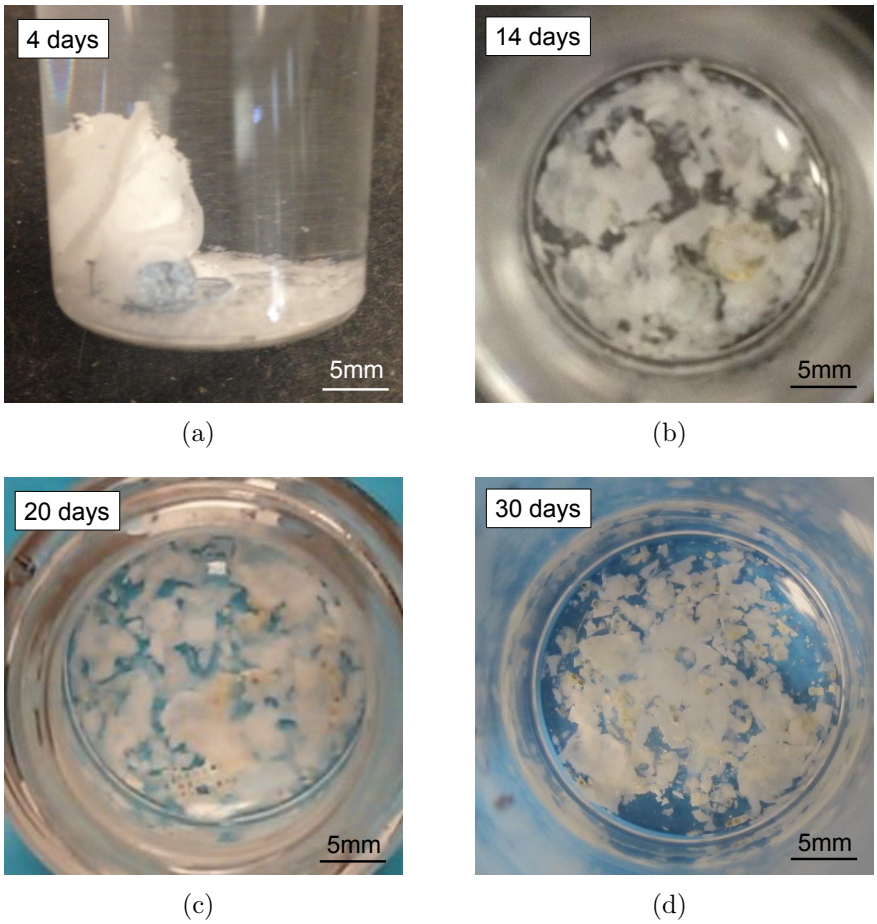

Figure 131: Pictorial *in-vitro* degradation history of a PLGA/PVA-Zn/Fe sensor with PLLA-PCL spacers and 165 °C PVA embossing temperature at time points of: (a) 4 days, (b) 14 days, (c) 20 days, and (d) 30 days.

(b) Weight loss Measurements

In total, weight loss degradation measurements of three representative PLGA/PVA sensors with PLLA/PCL spacers and 165 °C PVA embossing temperature are collected; two with Zn conductors and one with Zn/Fe couple conductors. The weight of each component within the sensor is calculated based on the thicknesses of the polymer films and metal conductors; these thicknesses were measured prior to assembling the sensors. The measured thicknesses of the components, together with the weight percentage normalized by the initial weight of each sensor, are shown in Table 15. Sensor H$_Z n$-1 and H$_Z n$-2 (H represents high PVA embossing temperature)

have pure Zn conductors and H_Zn/Fe has a Zn/Fe(checker) conductor with Fe covering 50% of the area of the Zn on one side. The thicknesses of all the conductors are approximately 65 μm. The PLGA thicknesses of these three sensors are very similar (120 μm for H_{Zn}-1 and H_{Zn}-2, and 100 μm for $H_{Zn/Fe}$), while the PVA thickness varies: approximately 350-380 μm for H_{Zn}-1, 240-260 μm for H_{Zn}-2, and 200-230 μm for $H_{Zn/Fe}$.

Table 15: Measured and calculated parameters of the PLGA/PVA-based sensors with PLLA spacer (165 °C PVA embossing temperature) for degradation study

Parameters		**PLGA/PVA sensor with 165 °C PVA embossing temperature**		
		H_{Zn}-1	**H_{Zn}-2**	**$H_{Zn/Fe}$**
Measured	PVA thickness μm	350-380	240-260	200-230
	PLGA thickness μm	120.00	120.00	100.00
	Metal thickness μm	65.00	65.00	65.00
	Spacer thickness μm	35.00	35.00	25.00
	Sensor weight (mg)	251.93	192.50	168.98
Calculated weight percentage	PVA (%)	57.48	44.35	47.34
	PLGA (%)	31.75	41.56	36.62
	Metal (%)	10.72	14.03	15.98
	PLLA spacer (%)	0.05	0.07	0.06

The measured weight remaining weights of these sensors during the *in vitro* degradation normalized by the initial sensor weights are plotted as function of degradation time in Figure 132. The observed weight change during degradation can be divided in-to 3 stages: slow weight loss in the initial functional stage, principal degradation stage, and then final weight-stable stage, after most of the sensor mass has degraded. During the initial 2 days, all three sensors show less than 3% weight loss. This corresponds to a period in which the sensor is functional for approximately one day, followed by PVA inside the PLGA gradually swelling. After 3 days, the weights of all the sensors decrease dramatically. This stage is the principal degradation of the

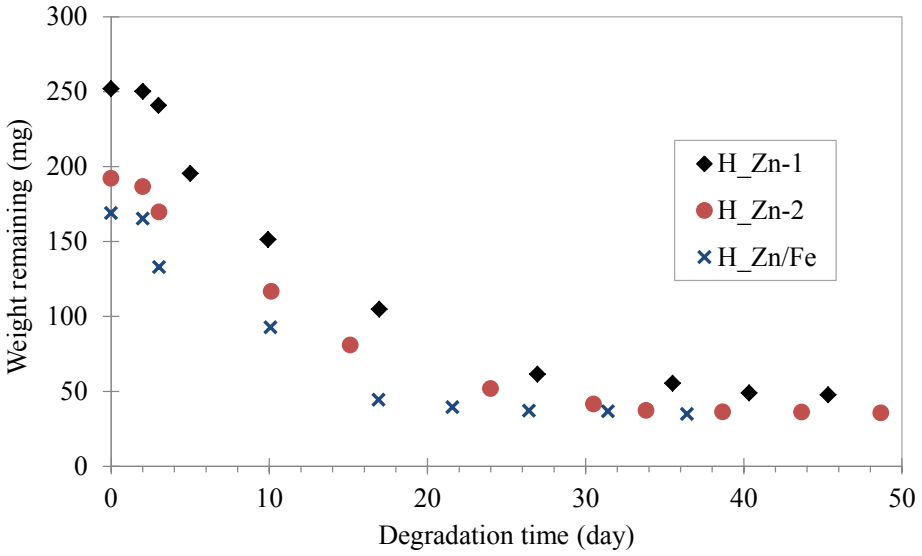

(a)

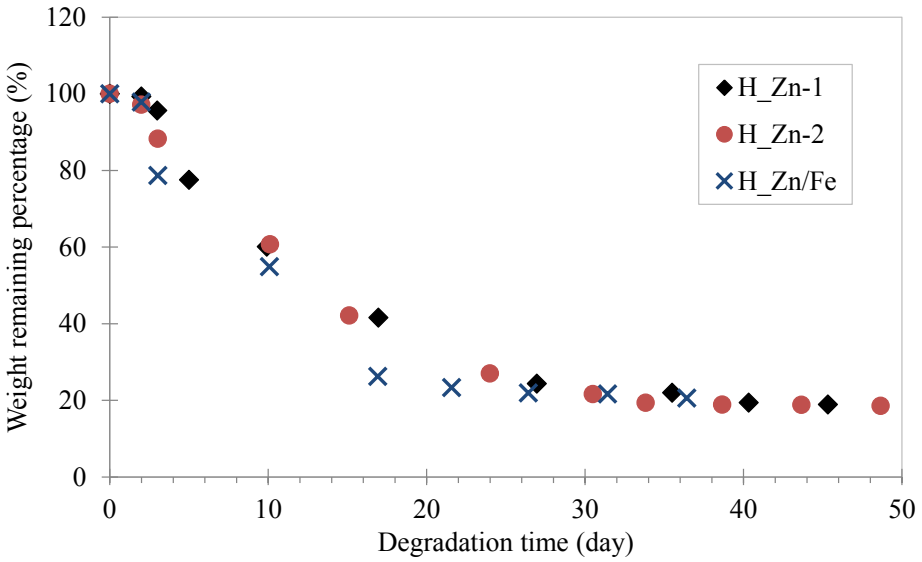

(b)

Figure 132: Remaining weight and normalized percentage of the PLGA/PVA sensors with PLLA spacers and 165 °C PVA embossing temperature during *in-vitro* degradation characterization.

PLGA/PVA sensors. During this stage, the PLGA package brakes, and the PVA originally inside the PLGA shell comes in direct contact with water and dissolves. This behavior is observed in all of the core-shell types of sensors. As the PVA loses its integrity, the metal conductor also comes into contact with saline and begins to

degrade. In parallel, the PLGA package also degrades slowly. Note that the $H_{Zn/Fe}$ specimen exhibits the most rapid degradation among these three sensors during this stage. This is very likely due to the accelerated degradation of the metal due to galvanic corrosion. After approximately 27 days for H_{Zn}-1 and H_{Zn}-2, and 21 days for $H_{Zn/Fe}$, the majority of each sensor has degraded, leaving residual weight that remains relatively constantly for a prolonged time period. This residue includes insoluble highly cross linked PVA, metal and PLLA/PCL spacer material. At this stage, the weight of the residue as a fraction of the original weight is approximately 19% for both sensors H_{Zn}-2 and $H_{Zn/Fe}$, and 21% for sensor H_{Zn}-1. Two sensors with undissolved matter, including undissolved, transparent PLLA/PCL spacers remaining in saline are presented in Figure 133.

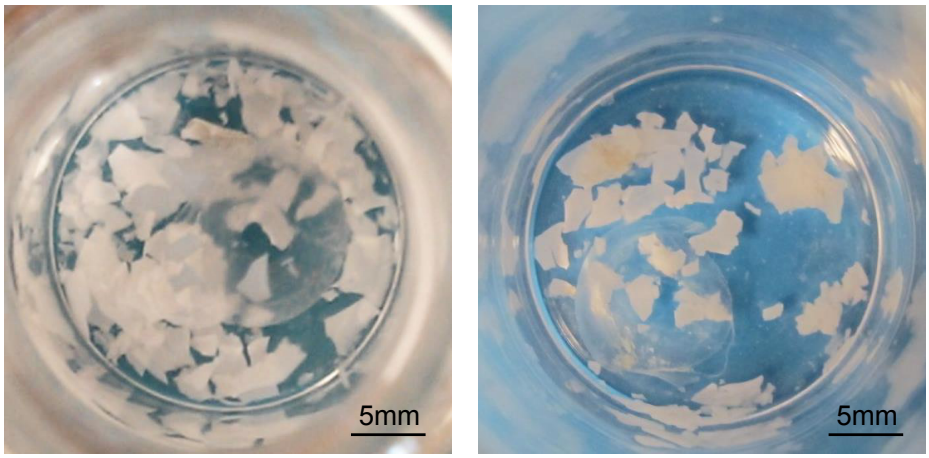

Figure 133: Photographs of two two of the PLGA/PVA sensors with PLLA spacers and 165 °C PVA embossing temperature after 30 days. The undissolved spacers are transparent but can be seen in the photographs.

7.2.2.2 In Vitro Degradation of PLGA/PVA-based Sensor with non-PLLA spacer and 130 °C PVA Embossing Temperature

Based on the above observations, two process modifications could potentially enhance the degradability of these sensors: (1) reducing the embossing temperature to reduce PVA crosslinking; and (2) replacing the PLLA spacers with more easily

degradable material. To test these process modifications, 130 °C embossing temperature is adopted during the PVA embossing process. Further, spacers of PVA/PLGA and pure PLGA are also utilized in the sensor. The degradation behavior of these these sensors are presented below.

(1) PLGA/PVA-based sensor with PVA/PLGA spacers

Two types of PLGA/PVA-based sensor with PVA-PLGA spacers and 130 °C PVA embossing temperature are fabricated and studied here: one with pure Zn conductors and one with Zn/Fe-couple conductors.

(1-a) Pictorial Histories

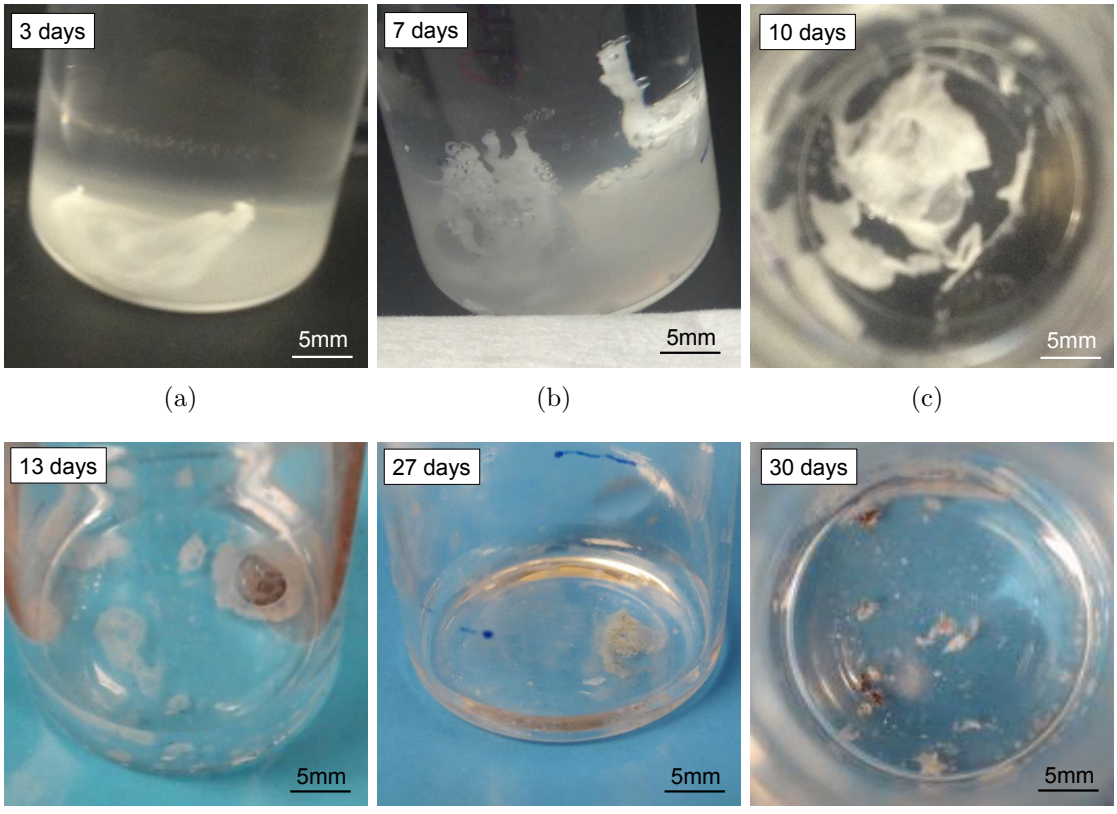

Figure 134: A pictorial *in vitro* degradation history of a PLGA/PVA-Zn/Fe sensor with PVA-PLGA spacers and 130 °C PVA embossing temperature at time points of : (a) 27 hours , (b) 3 days, (c) 6 days, (d)13 days, (e) 18 days, and (f) 23 days.

Pictorial histories of *in vitro* degradation a PVA/PLGA spacers sensor with pure

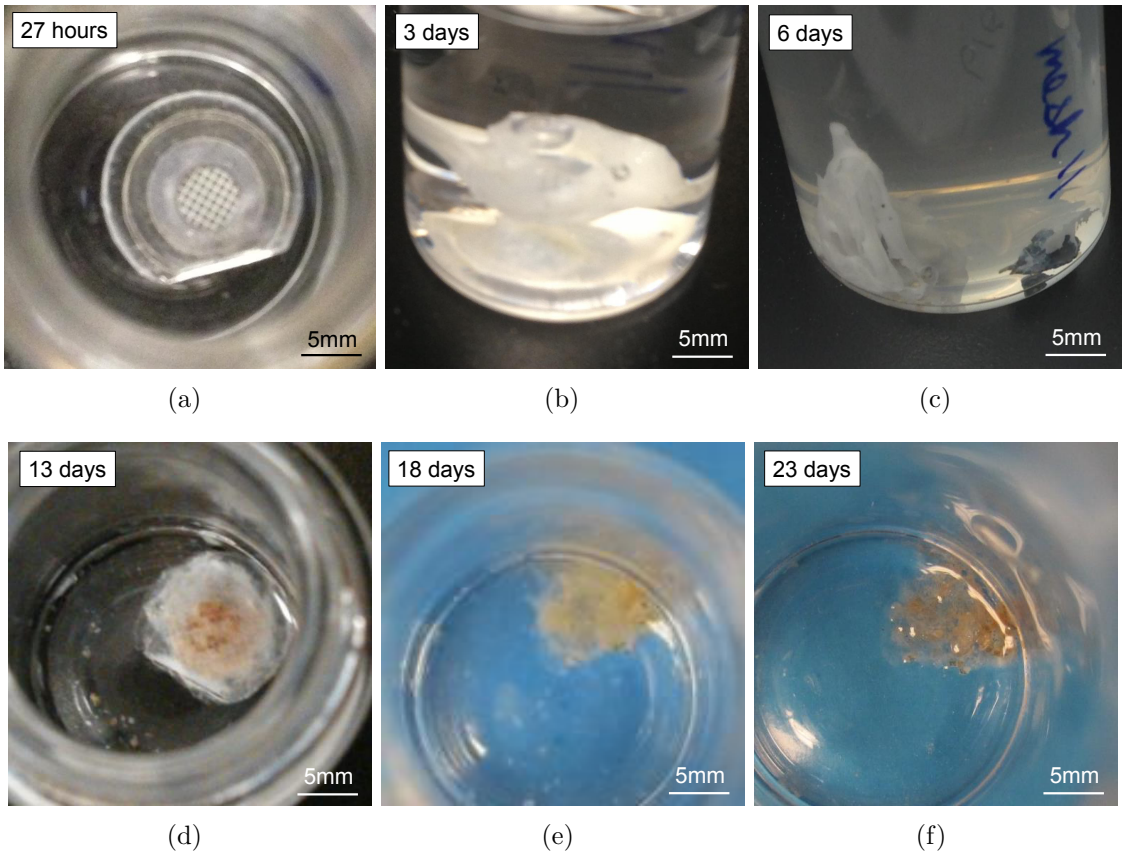

Figure 135: A pictorial *in-vitro* degradation history of a PLGA/PVA-Zn/Fe sensor with PLLA spacers and 165 °C PVA embossing temperature at time points of : (a) 4 days, (b) 14 days, (c) 20 days, and (d) 30 days.

Zn conductor and a sensor with Zn/Fe-couple conductor are shown in Figure 134 and Figure 135 respectively. Both the sensor with pure Zn conductor and Zn/Fe couple conductors show similar behavior. The sensors are greatly twisted/deformed at approximately 3 days, and start to lose physical integrity. The PVA and metal conductors start to degrade once they come in contact with liquid water. The white areas in the sensor photographs before the 7 day degradation time point is an indication of dissolving PVA. At the 13 day time points, most of the PVA has dissolved. The PLGA and metal(s), undergo slow degradation during the following approximately 20 days, ultimately leaving minimal residual traces. During the degradation, the metal conductors can either fall out of the polymer package (Figure 135(c)) or remain inside

of the broken polymer package (Figure 134(d)). If the conductors remain inside of the polymer package, the metal still degrades gradually, possibly with slower degradation rate. In Figure 135, at 6 day time point (Figure 135(c)), one Zn/Fe metal capacitor plate has fallen out of the polymer package while the other remains inside. At the 13 day time point, as shown in Figure 135(d), the Zn/Fe(checker) capacitor plate outside the polymer is almost gone, while the plate inside the polymer still has some residual presence, indicated by the red/brown residue with clear checker-shape in the whitish polymer. Note that the polymers in Figure 135(f) are transparent because this picture is taken after the specimen is dried; PLGA appears whitish when saturated in saline and transparent when dry.

(1-b) Weight Loss Measurements

The degradation results of five PLGA/PVA sensors with PVA as the inner spacer and PLGA as the outer spacer are presented here. Three sensors (labeled as V_Zn-1, V_Zn-3 and V_Zn-3) have pure electroplated Zn conductors, while two senosrs (labelled as V_Zn/Fe-1 and V_Zn/Fe-1) have Zn/Fe(checker) conductors with Fe covering 50% of the area of the Zn on one side. The measured polymer film thicknesses and the initial weight of the sensors, together with the calculated weight percentage of each component, are listed in Table 16. The thicknesses of the metal conductors and spacers for all these sensors are similar, while the thicknesses of the polymer package vary. The thickness of the PVA and PLGA package are between approximately 250 μm to 350 μm and 170 μm to 250 μmrespectively.

The percentage weights of the PLGA/PVA sensors with PVA/PLGA spacers are recoreded during the degradation test, and the data are present in Figure 136. The degradation can be divided into three stages. The weight of the sensors remains relatively stable for the initial 4 days (less than 5% weight loss), decreases dramatically during the middle stage (4 to 19 days), and decreases very slowly in the final stage when the remaining weight is less than 10%. After the degradation time point of

Table 16: Measured and calculated parameters of the PLGA/PVA-based biodegradable sensors with PVA/PLGA spacers

Parameters	**PLGA/PVA based sensors with PVA/PLGA spacers**				
	V_{Zn}-1	**V_{Zn}-2**	**V_{Zn}-3**	**$V_{Zn/Fe}$-1**	**$V_{Zn/Fe}$-2**
Measured thickness (t) and sensor weight					
PVA t (μm)	320-360	270-300	240-260	320-350	260-280
PLGA t (μm)	230	240	250	170	190
Metal t (μm)	65	65	65	65	65
Spacer t (μm)	30	40	30	35	40
Sensor weight (mg)	293.27	274.92	262.96	248.43	238.80
Calculated weight					
PVA (%)	40.9	37.1	31.9	47.7	40.1
PLGA (%)	49.9	53.1	57.8	41.4	48.6
Metal (%)	9.2	9.8	10.3	10.9	11.3

26 days, the remaining weights of all the sensors are less than 5%. There is no significant difference between the weight change of sensors with Zn conductors and Zn/Fe-couple conductors, mainly due to the relatively small amount of metal (27 mg, less than 12% of the entire sensor). Meanwhile, similar degradation time is observed for all these sensors despite their differing polymer thickness; this is due to the fact that both the dissolution of PVA and degradation of PLGA proceed by bulk erosion and are therefore independent of their thickness. It can be concluded that the degradation lifetime of the fabricated PLGA/PVA sensors with PVA/PLGA spacers is approximately 26 days, and independent of the polymer thickness for the thicknesses studied here.

To better understand the *in-vitro* degradation process of the sensor, the degradation rates of the sensors with Zn and Zn/Fe-couple conductors are plotted as functions of degradation time in Figure 137. Every sensor exhibit an increase - peak- decrease pattern of degradation rate during the *in-vitro* degradation. Based on the observation

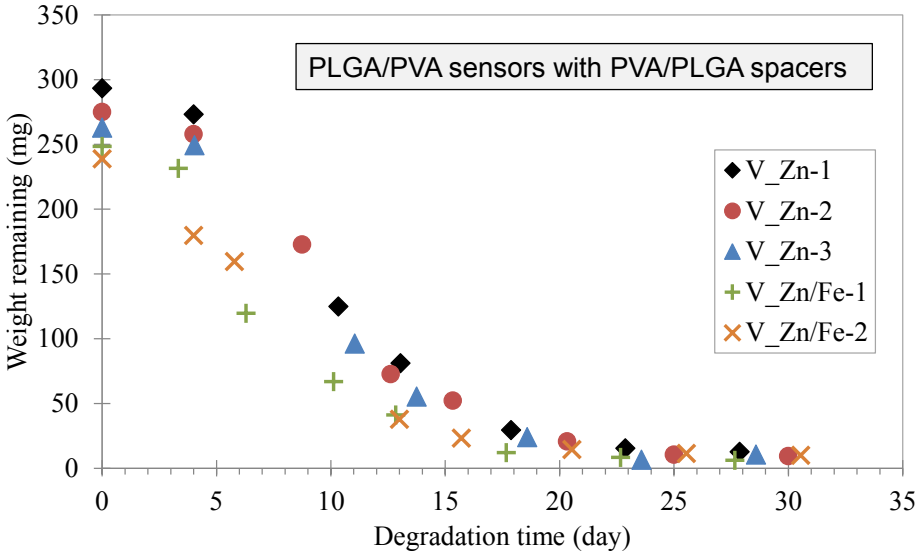

(a)

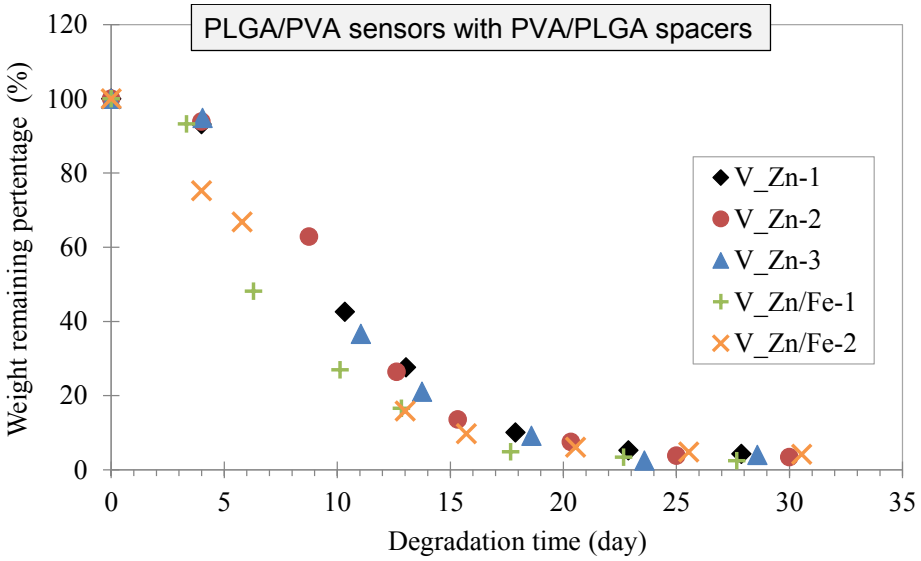

(b)

Figure 136: Remaining weight and normalized percentage of the PLGA/PVA sensors with PVA/PLGA spacers during *in vitro* degradation.

of the appearance change of the sensors during the degradation, this degradation rate peak should correspond to the fracture of the PLGA package and rapid dissolution of PVA, which constitutes a significant proportion of the total weight of the sensor. The peak appears earlier for the sensors with Zn/Fe-couples (between 4 to 10 days) than for the sensors with Zn conductors (between 9 and 13 days). This is likely due

to the relatively larger PLGA thickness (which, even in the case of bulk erosion, may withstand mechanical stress and fracture for a longer time) for the sensors with Zn conductors, rather than the effect of the galvanic corrosion of the metal. The highest rate of the sensor $V_{Zn/Fe}$-1 is also mainly due to the high ratio of PVA in the sensor. During the middle stage when the degradation rate is relatively high (4 to 19 days), the degradation of the sensor includes dissolving PVA, and degradation of metal and PLGA. However, due to the fact that the weight measurements cannot be performed continuously, it is difficult to extract an accurate model for the degradation rate of the sensor based on these limited data.

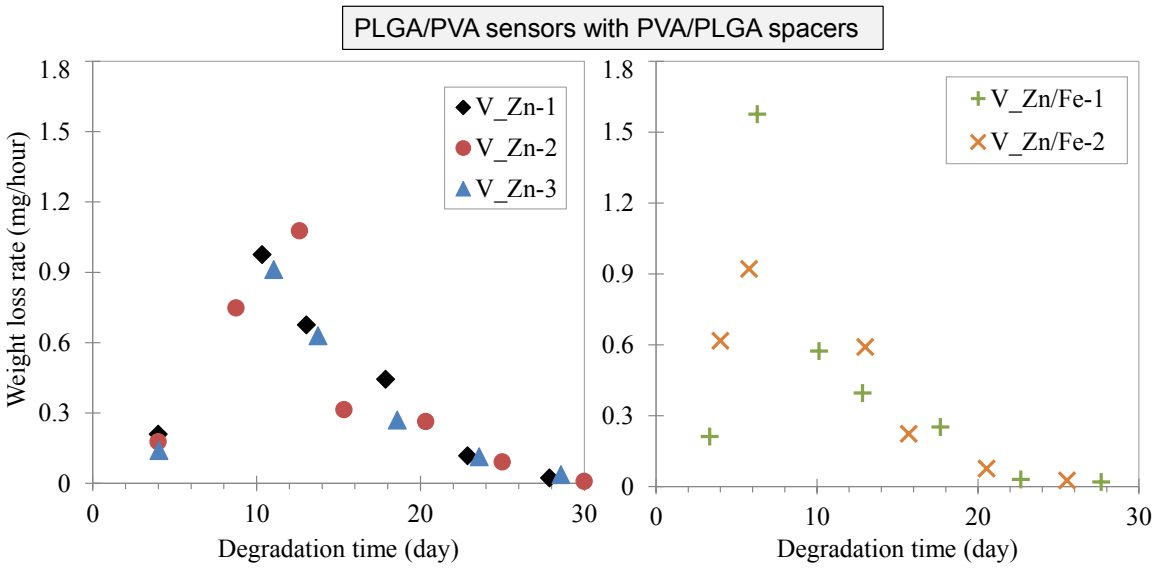

Figure 137: *In-vitro* degradation rate of the PLGA/PVA sensors with PVA/PLGA spacers at different time points

(2)PVA/PLGA-based sensor with pure PLGA spacer

In PLGA/PVA-based sensor with pure PLGA spacer, only pure Zn is utlized as the conductor materials

(2-a) Picture Histories

A pictorial history of *in vitro* degradation of a PVA/PLGA sensor with pure PLGA spacer is shown in Figure 138. The degradation appearance is similar to that of the PVA/PLGA sensors with PVA/PLGA spacers. The PLGA turns white and

opaque during long-term immersion in saline without volume change in the first 7 days (Figure 138(b)). After 10 days, the sensor loses its physical integrity (Figure 138(c)), and the total materials volume of the sensor start to decrease. After a degradation time of 30 days, only trace of residues of Zn and PLGA remains.

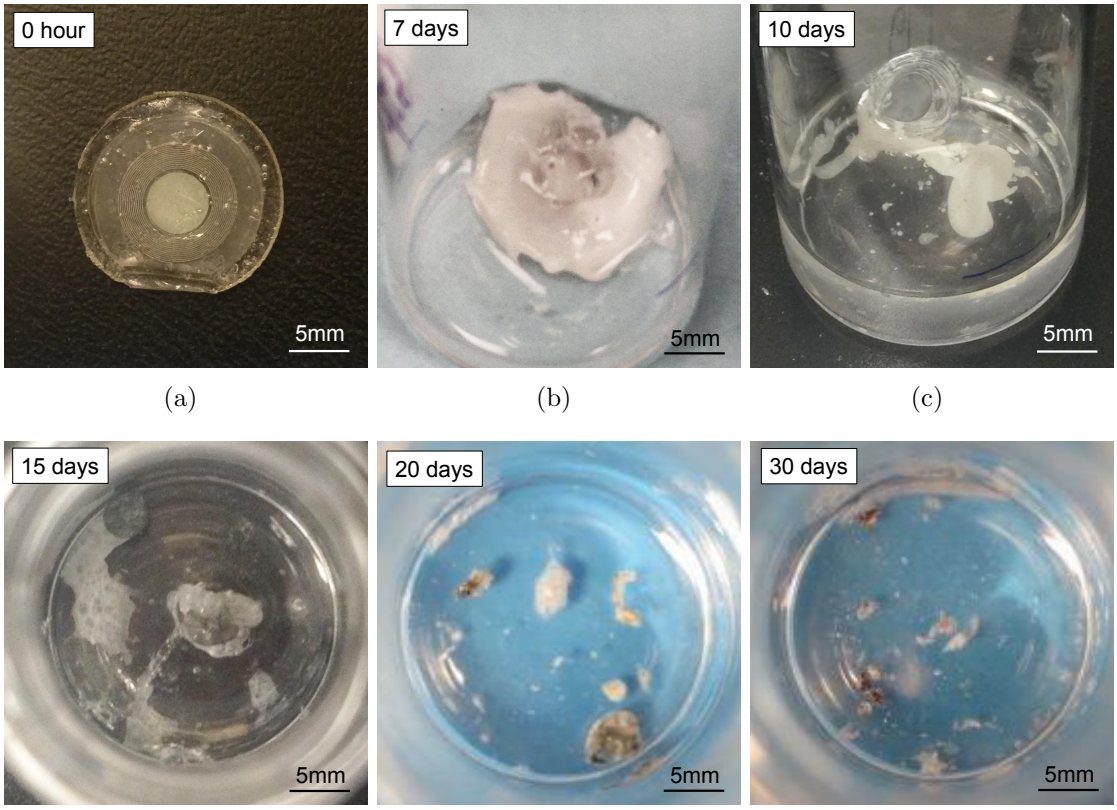

Figure 138: A pictorial *in vitro* degradation history of a PLGA/PVA-Zn/Fe sensor with PLGA spacer and 130 °C PVA embossing temperature at time points of : (a) 0 hour, (b) 7 days, (c) 10 days, (d) 15 days, (e) 20 days, and (f) 30 days.

(2-b) Weight Loss Measurements

The results of two PLGA/PVA sensors with pure PLGA spacer and Zn conductors are studied here. These sensors are labelled as G-1 and G-2. The measured polymer films thicknesses and the initial weight of the sensors, together with the calculated weight percentage of each component are listed in Table 17. The initial weight of sensor G-1 is much higher than that of sensor G-2, due to the thicker PLGA and

PVA films.

Table 17: Measured and calculated parameters of the PLGA/PVA-based biodegradable sensors with pure PLGA spacers

Parameters		**PLGA/PVA sensor with pure PLGA spacer**	
		G-1	G-2
Measured	PVA thickness (μm)	300 330	270-290
	PLGA thickness (μm)	300	200
	Metal thickness (μm)	65	65
	Spacer thickness (μm)	45	45
	Sensor weight (mg)	336.20	249.38
Calculated weight percentage	PVA (%)	32.5	39.3
	PLGA (%)	59.5	49.9
	metal (%)	8.0	10.8

The percentage remaining weight of the PLGA/PVA sensors with PLGA spacers are recorded during the degradation test and are shown in Figure 139. The degradation can also be divided into three stages. In the first approximately 5 days, the weight of the sensors remains relatively constant (less than 4% weight loss). Between 5 days to 20 days, the weight of the sensors decreases dramatically, with approximately 7 % of the total weight remaining. After the majority of the sensor is gone, the degradation rate decreases, until after 25 days, only approximately 3% of the initial sensor weight remains. Similar total degradation time is observed despite the different polymer thickness of the two sensors, again due to the fact that both the dissolution of PVA and degradation of PLGA (bulk erosion) are independent of the thickness. Based on this result, the total *in-vitro* degradation life time of PLGA/PVA based biodegradable sensors with PLGA spacers is approximately 30 days and independent of the polymer thickness.

The degradation rate of the PLGA/PVA sensors with PLGA spacer is plotted

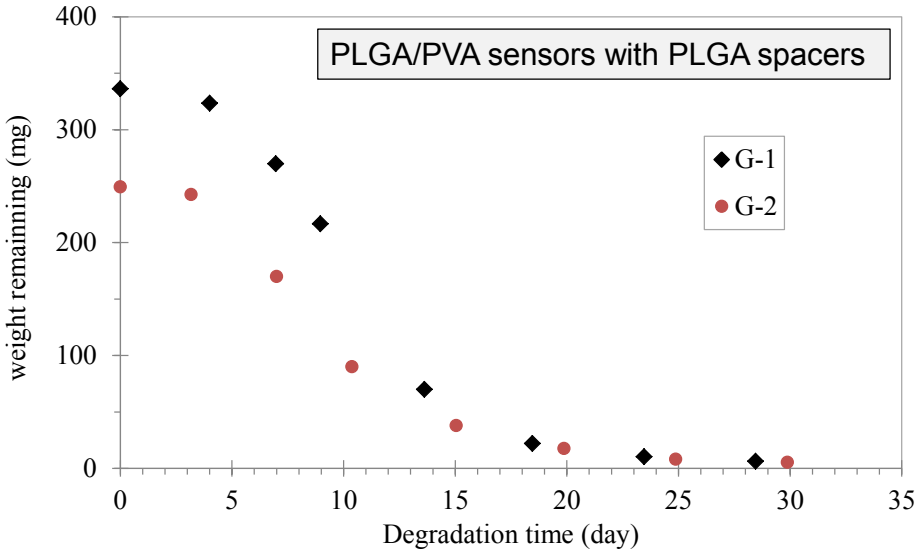

(a)

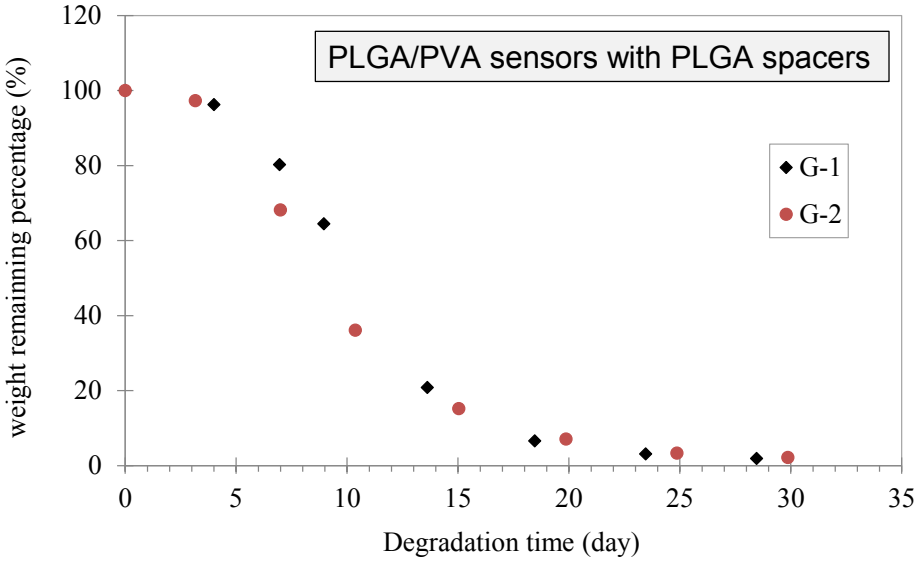

(b)

Figure 139: Weight remaining and normalized percentage of the PLGA/PVA sensors with PLGA spacers during *in vitro* degradation.

in Figure 140. A similar peak to that of the sensors with PVA/PLGA spacers is also observed. The degradation time point of the maximum degradation rate also correlates to the thickness of the PLGA package. The degradation peak is between 9 to 14 days for sensor G-1 (300 μm PLGA package), and between 7 to 10 days for sensor G-2 (200 μmPLGA package). This result agrees with the result obtained from

PLGA/PVA sensors with PVA/PLGA spacers studied above.

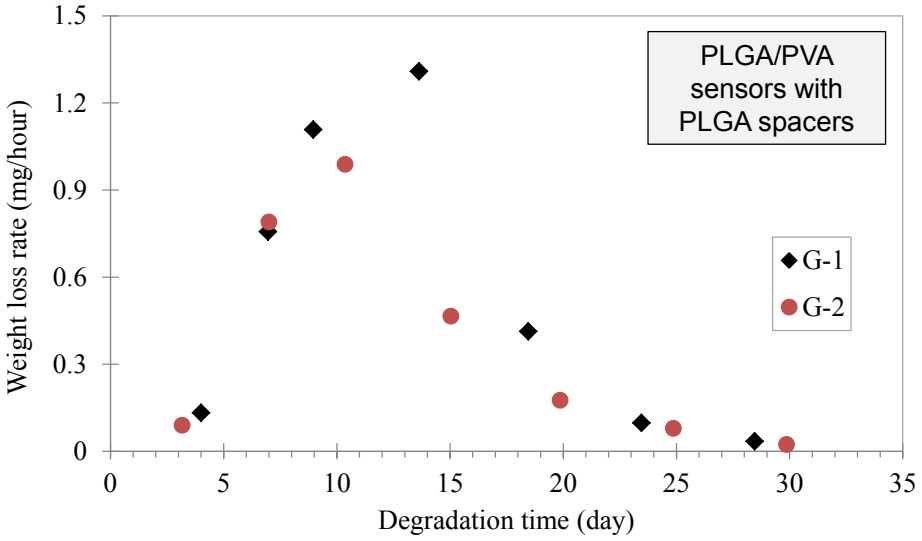

Figure 140: *In-vitro* degradation rate of the PLGA/PVA sensors with PLGA spacer at different time points.

7.3 Functional Lifetime vs. Degradation Lifetime of the Biodegradable Sensors

Functional lifetime, degradation lifetime, as well as the functional time ratio (i.e., ratio of these two times) are three important parameters that can be used to evaluate the performance of biodegradable sensors. Figure 141 depicts a typical schematic performance of a biodegradable sensor. The functional lifetime is the time period that the sensor is fully and stably functional. If there is an equilibration time, this time should be excluded from the functional lifetime. The degradation lifetime is the total duration from the time point that the sensor is placed in contact with saline to the time point at which the sensor completely degrades (or degrades to some acceptable value; for example, in this work, the sensor is considered to be completely degraded if at least 95% of the weight has dissolved). The functional time ratio is defined as the functional lifetime divided by the degradation lifetime, and and can be expressed as a percentage. Ideally, the sensor should disappear

immediately after the sensor finishes its job and is no longer functionally required (i.e., a functional time ratio of 100%). However, in reality, such a case is likely impossible because the degradation of materials will likely have to undergo some unstable stage before disappearing. Further, for short functional lifetime applications, it is possible that a correspondingly short degradation lifetime would result in local toxicity due to the environment surrounding the sensor changing rapidly. Therefore, the desired performance for a degradable sensor would be long functional lifetime, with a functional time ratio as high as possible while remaining biocompatible.

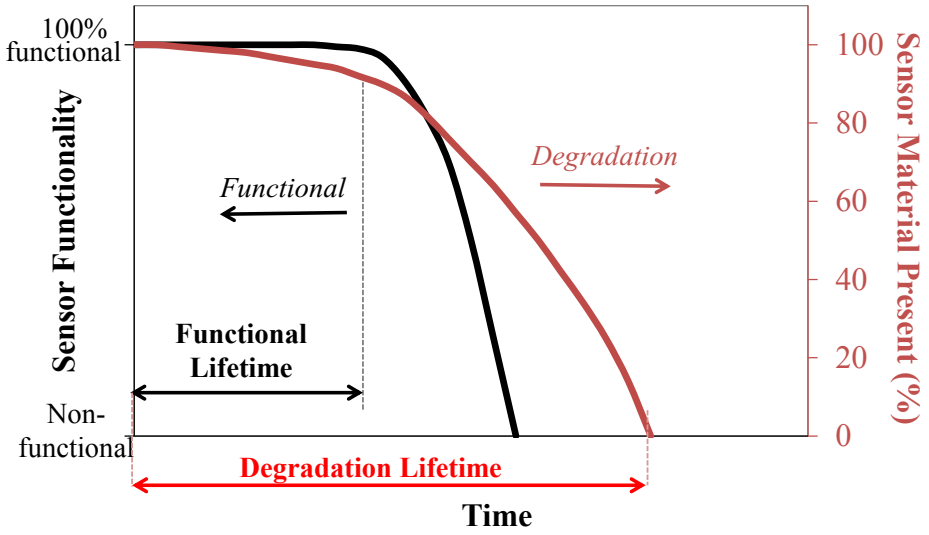

Figure 141: Functional life time vs. degradation life time

Among all the sensors that have been fabricated and studied, the functional lifetime and degradation lifetime of those that possessed satisfactory performance are collected and compared in Table 18. The exact degradation lifetime of the PLLA based sensors sensors unfortunately exceeded the period of time available for its study in this work. Therefore, the degradation time of the PLLA polymer based on its data sheet ($>$ 24 months) is adopted as the degradation lifetime of the PLLA based biodegradable sensors.

The functional lifetimes of the PLLA based sensors are 4 to 15 days, depending on the thickness of the PLLA package. However, their fairly long degradation life time

Table 18: Functional life time vs. degradation life time of the biodegradable sensors

Performance	**PLLA based sensor**		**PLGA based sensor**	
	with 200 μm PLLA	with 400 μm PLLA	with PVA/PLGA spacers	with PLGA spacer
Equilibration time	22 hours	33 hours	1.5 hours	1.5 hours
Functional lifetime	4 days	15 days	17 hours	24 hours
Degradation lifetime	$>$ 2 years	$>$ 2 years	26 days	25 days
Functional time ratio (%)	$<$ 0.5%	$<$ 2.1%	2.7%	4.0%

(more than 1.5 years) make their functional time ratio quite low (the best case is still lower than 2.1%). On the other hand, the biodegradable sensor with PLGA/PVA bilayer package can be fully functional for less than one day and degrade completely within 26 days; in this case, the functional time ratio is increased. In the future, it is expected that this functional time ratio of the PLGA/PVA-based sensor can be increased even further if the fabrication challenge of trapping bubbles can be solved.

CHAPTER VIII

CONCLUSION

8.1 Summary of the Research

Implantable sensors have been extensively investigated to facilitate diagnosis or to provide a means to generated closed loop control of therapy by yielding *in vivo* measurements of physical, chemical and biological signals. MEMS technology has demonstrated significant value in this application mainly due to its micro-scale size, low weight, low power consumption, potential for low fabrication cost, superior functionality or performance, and ability to be combined with biotechnology and molecular biology. Among those, biodegradable sensors which degrade gradually after they are no longer functionally needed exhibit great potential in acute or shorter-term medical diagnostic and sensing applications due to the advantages of (a) exclusion of the need to a secondary surgery for sensor removal, and (b) reduction of the risk of long-term infection.

The objective of this research is to design and characterize microfabricated RF wireless pressure sensors that are made of completely biodegradable materials and degrade at time-controlled manner. This will be achieved by means of investigation of appropriate biodegradable materials and development of appropriate fabrication processes for these non-standard MEMS materials. To achieve this goal, four subareas of research will be performed: (1) design of sensors that operate wirelessly and are made of biodegradable materials; (2) investigation of the biodegradable materials in the application of implantable biodegradable wireless sensors to achieve controllable degradation lifetimes; (3) development of new fabrication processes that allow the handling of delicate biodegradable materials; and (4) testing the pressure response

functionality and studying the degradation behavior of the wireless biodegradable pressure sensors.

The structure of the wireless sensor consists of a very compact and relatively simple design of a passive LC resonant circuit embedded in a polymer dielectric package. A sensing cavity, which is bounded by two metal plates, forms a variable capacitor and is interconnected with planar inductor coil(s). The inductor and the capacitor can be either connected with a conducting via, or can be capacitively and inductively coupled without a conducting via. When pressure is applied to the sensor, the gap between the two capacitive electrodes is reduced and the capacitor value increases. The resulting pressure-induced LC resonant frequency change can be measured wirelessly using an external coil. To design the sensor with a particular resonant frequency range, the inductance and capacitance of the sensor is predicted using an analytical model based on the literature. An electromagnetic model of the sensor is also developed to analyze the wireless sensing mechanism. A mechanical model for circular plate bending is also presented to understand the deflection of the capacitor plates. Then, the electromagnetic and mechanical models are integrated to predict the pressure-dependent capacitance change. The geometry of the sensor is finally established based on the analytical and finite element simulations results.

Among various biodegradable materials, including both polymers and metals that have been reviewed for biomedical applications, only FDA-approved and commercialized biodegradable polymers are considered as candidates in this pioneer work of completely biodegradable wireless sensors. To explore the feasibility of both slow degradation sensors (expected degradation time on the order of years), and rapid degradation sensors (expected degredation time on the order of months), poly(L-lactic acid) (semi-crystalline, degradation time $>$ 2 years) and a "shell-core" structure of poly(lactic-co-glycolic acid) (amorphous, degradation time $<$ 1 month) and polyvinyl alcohol (water soluble) are utilized as the dielectric package. To form the

required electrical conductors, biodegradable metallic zinc and zinc/iron couples with appropriate electrical properties (e.g., conductivity and AC resistance) and ease of fabrication are chosen. In the metallic couples, a bulk biodegradable metal (zinc) that degrades relatively slowly is electrically connected to a small amount of more active biodegradable metal (iron). This approach allows acceleration and tailoring of the degradation rate of the entire metal by galvanic corrosion. The *in vitro* degradation rate of the pure zinc and zinc/iron-couples with different metal surface area ratio are studied through both electrochemical testing and physical weight loss measurements. Further, due to the absence of degradation data of poly(lactic-co-glycolic acid) utilized in the degradable sensor, the degradation behavior of this polymer is studied *in vitro*.

To exploit the advantages of microelectromechanical systems (MEMS) technology in fabricating miniaturized devices, while protecting vulnerable biodegradable materials from the strong and/or hazardous chemicals that are commonly used in conventional MEMS fabrication process, novel fabrication processes that combine conventional MEMS technology with non-wet processes have been developed in this study. These new processes enable the fabrication of biocompatible and biodegradable 3-D devices with embedded, near-hermetic cavities. The bulk metal conductors are electrodeposited through photoresist molds; for the case of the metal couples, a thin layer of more active metal is either evaporated or electrodeposted on this bulk conductor. The metal conductor is then embossed into biodegradable polymer sheets, followed by multilayer polymer lamination with or without folding to create the final devices with or without a conducting via.

The fabricated biodegradable pressure sensors are characterized wirelessly in air and through a long-term immersion test *in vitro* until no resonance can be detected by the external coil. During the entire *in vitro* functionality measurements, the impedance phase and magnitude of individual sensors without applied pressure

are recorded to determine the resonant frequency and quality factor, and pressure response tests are performed intermittently to determine the sensitivity. *In vitro* degradation tests continue after the sensor stops resonating with the external coil and last for 7 months for the slow degradation sensors, and less than 35 days for the rapid degradation sensors. All the sensors exhibit three stages of behavior *in vitro*: equilibration, functional lifetime, and performance degradation. During the functional lifetime, most sensors exhibit fully stable functionality: relatively steady resonant frequency and slight decrease of quality factor with zero applied pressure, as well as comparable sensitivities at different time points. The slow degradation sensors exhibit functional lifetimes of several days and show no significant total weight loss but do show an obvious physical appearance change of the metal-couple conductors within 7 months. These slow degradation sensors are expected to fully degrade after 2 years, based on the degradation of the polymer package. The rapid degradation sensors exhibit functional lifetimes of no more than 1 day and can degrade completely within 26 days. Compared with that of slow degradation sensors, the rapid degradation sensors present improved functional time ratio (functional lifetime/degradation lifetime $\times 100\%$) of 2.7% to 4.0%.

8.2 Contributions

A series of novel completely biodegradable RF wireless LC resonant pressure sensors utilizing slow degradation polymer PLLA, and rapid degradation polymer PLGA combined with water soluble polymer PVA as dielectrics, and electrodeposted Zn and Zn-Fe couples as conductors, are successfully designed, microfabricated and characterized.

Based on the *in vitro* degradation study results using both electrochemical testing and physical weight loss of pure electroplated Zn and Zn/Fe couples with different area ratio, a model has been developed to predict the degradation rate of Zn/Fe-couples

with Fe : Zn area ratio less than 1.

The degradation of Zn/Fe-couple metallic conductors is shown to be accelerated by a galvanic corrosion mechanism. This exploitation of galvanic corrosion, a normally undesirable behavior in structural engineering, for the application of acceleration of biodegradable metals, suggests the potential for expending the number of candidate degradable metals.

Microfabrication processes that combine MEMS technology and non-wet processes were developed for fabricating completely biocompatible and/or biodegradable miniature implantable sensors that involve delicate and sensitive polymers. By first microfabricating structures on relatively robust substrates and then transferring these structures to biodegradable polymers, flexible electronics can be achieved. By adopting folding and multiple-layer polymer lamination, 3-D device with quasi-hermetic cavities embedded inside can be achieved.

A modified model taking into account the fabrication-induced pre-bending of the capacitor plate is proposed to accurately predict the resonant frequency and sensitivity of the sensor. By calculating an equivalent absolute applied pressure to realize the observed pre-bending center deflections of capacitor plates using COMSOL, the simulated sensitivities of the sensors under relative pressure agree well with the experimental results. Therefore, pre-bending can be intentionally introduced to alter the sensitivity of the sensor.

Fabricated sensors exhibit full functionality in both air and in saline under 37 °C. All the sensors show three stages of behavior *in vitro*: equilibration stage, functional lifetime, and performance degradation. During the functional lifetime, most successful sensors exhibit fully stable functionality: relatively steady resonant frequency and slight decrease of quality factor with zero applied pressure, as well as comparable sensitivities at different time points. By adopting a "shell-core" structure of rapid

degradation polymer and water soluble polymers as the package, the rapid degradation sensor can degrade completely within 26 days with improved functional time ratio (functional lifetime/degradation lifetime $\times 100\%$) of 2.7 % to 4.0 %. Further improvements can be expected if the fabrication challenge of trapping bubbles can be solved.

8.3 Future Outlook

This work on completely biodegradable wireless pressure sensors demonstrated the feasibility of biodegradable passive *LC* resonant circuits packaged in biodegradable polymers and offers the potential for application of these structures as implantable sensors. While this work is focused on pressure sensing, it is likely that this idea of integrating biodegradable metals and polymers and the developed fabrication process can be utilized to design and fabricate completely biodegradable wireless sensors in other miniature implantable applications (e.g. strain sensors, active sensors.)

Functionality and degradation behavior have been demonstrated in this work; however, further investigation of the possible factors affecting the mechanism of sensor equilibration and failure in saline are still needed to help precisely design the functional lifetime and degradation lifetime of the sensors.

Improvements can be made to the fabrication process to achieve better control of the resonant frequency and sensitivity of the sensor. Possible means include more precise control of the polymer film thickness uniformity, improvements in lamination to achieve consistently, completely laminated structures, approaches for complete removal of bubbles, and utilizing precise control of the cooling temperature range after releasing the embossing pressure before folding and lamination to eliminate or make more reproducible the observed pre-bending.

With some optimizations of the geometry design, these biodegradable sensors can be utilized in urodynamic applications for diagnosing urinary incontinence *in vitro*

and *in vivo*. The sensor geometry of the sensor need to be more compatible with catheter delivery, e.g. being foldable and/or reduced the size.

More biodegradable materials can also be investigated as candidates for biodegradable wireless sensors to achieve superior performance and increase the functional life ratio. For instance: magnesium alloy or Zn-Mg couples can be utilized as the biodegradable conductor to obtain rapid degradation and possibly higher quality factor. Since the failure of the sensor is very likely due to the invasion of water (or water vapor), to achieve minimum functionality fluctuation before the sensor fails and controllable degradation, the package of the biodegradable sensor can also adopt the core-shell structure similar to the PLGA/PVA bilayer package in this work, while substituting PLGA with better "water-proof" biodegradable materials. Possible shell-material candidates include surface erodible polymers, silk and some biodegradable polymers that require enzymes for fast degradation.

APPENDIX A

PROCESS RECIPES

A.1 Process Recipe of NR21 - 20000 on Kapton® Film with 90 μm Thickness

1. Clean the surface of the wafer with acetone.
2. Spin coat NR9-1500PY on the surface of water with spin rate of 1200 rpm for 10 seconds.
3. Attach the Kapton® film with seed layer to the wafer.
4. Place the wafer with Kapton® film on top on the hotplate under 80 °C for 2 minutes and then 150 °C for approximatly 5 mintues. Remove the bubbles generated beneath the Kapton® film gently.
5. Cover the surface of Kapton® film with a non-adhesive clean wafer and press gently while removing the wafer with Kapton® film from the hotplate.
6. After the wafer is compeletely cooled down, clean the Kapton® film surface with acetone in spin coater with spin rate of 1200 rpm.
7. Tape the edge with single layer of Kapton® tape if necessary.

A.2 Hot-plate Photolthography Recipe of NR21-20000P on Kapton® Film with 90 μm thickness

(Note: the Kapton® film has Ti-Cu-Ti seed layer and is bonded to a wafer)

1. Clean the surface of the Kapton® film with acetone in spin coater with spin rate of 1200 rpm.
2. Spin coat NR21-20000P with spin rate of 1200 rpm for 10 seconds.

3. Rest the specimen on a levelled surface for 5 minutes.
4. Soft bake on 80 °C hot plate for 10 minutes and then ramp up the temperature to 150 °C with speed of 35 °C/min, and baked for 9 minutes (including the ramp-up time), and ramp down the temperature to room-temperature with speed of -30 °C/min.
5. Rest the specimen for at least 2 hours.
6. Expose with dose of 4000 mJ.
7. Post bake on hot-plate for 12 minutes starting at 40 °C with ramp-up speed of 40 °C/min to 80 °C, and ramp down the temperature to room-temperature with speed of -30 °C/min.
8. Rest the specimen for at least 3 hours.
9. Develop in RD-6 with gentally shaking until all the unexposed photo-resist is gone, rinse with water and dry with nitrogen air gun.
10. O_2 RIE for 30 seconds modify the photoresist surface to hydrophilic.

A.3 Oven Photolthography Recipe of NR21-20000P on Kapton® film with 90 μm thickness

(Note: the Kapton® film has Ti-Cu-Ti seed layer and is bonded to a wafer)

1. Repeat procedures steps 1-3 from above in Section A.2.
2. Soft bake in oven for 60 minutes, starting at 80 °C with ramp-up speed of 40 °C/min to 130 °C. Ramp down the temperature to room-temperature with speed of -30 °C/min.
3. Repeat procedures steps 5-6 from above in Section A.2.
4. Post bake in oven for 30 minutes under 85 °, and ramp down the temperature to room-temperature with speed of -30 °C/min.

5. Repeat procedures steps 8-10 from above in Section A.3.

A.4 Oven Photolthography Recipe of NR22-20000P on Kapton® film with 40 μm thickness

(Note: the Kapton® film has Ti-Cu-Ti seed layer and is bonded to a wafer)

1. Clean the surface of the Kapton® film with acetone in spin coater with spin rate of 1200 rpm.
2. Spin coat NR22-20000P with spin rate of 1500 rpm for 10 seconds.
3. Rest the specimen on a levelled surface for 5 minutes.
4. Soft bake in oven for 45 minutes, starting at 80 °C with ramp-up speed of 40 °C/min to 130 °C. Ramp down the temperature to room-temperature with speed of -30 °C/min.
5. Rest the specimen for at least 2 hours.
6. Expose with dose of 2500 mJ.
7. Repeat the procedures steps 4-5 from above in Section A.2.

APPENDIX B

COMSOL SIMULATION PARAMETERS

B.1 Moving Mesh Module

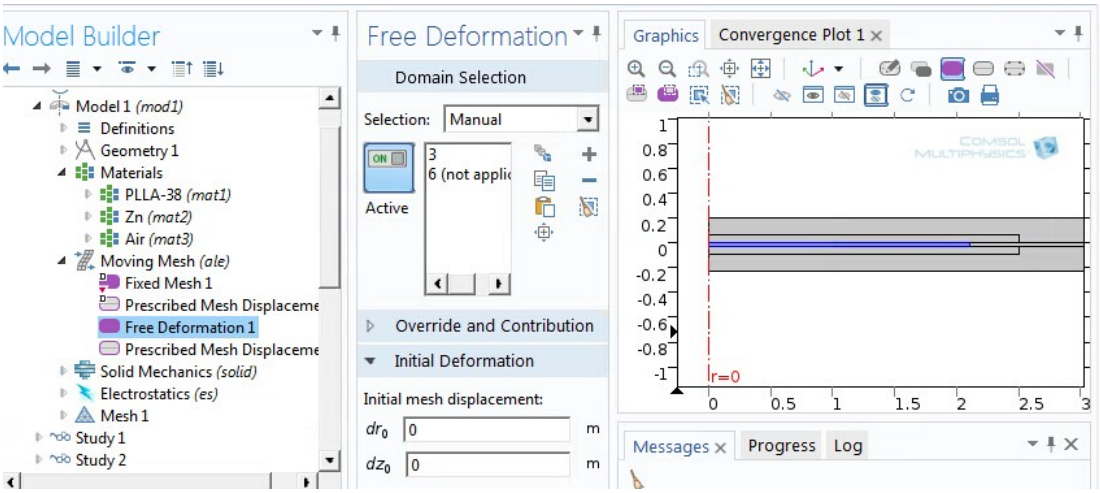

Figure B.1: Define the free deformation Domain in moving mesh module

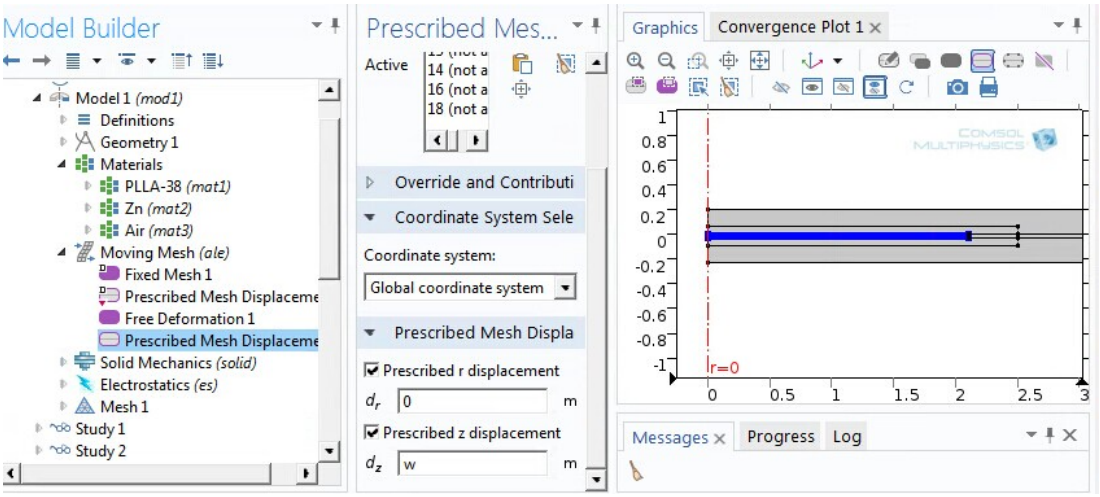

Figure B.2: Define the frescribed mesh displacement boundary in moving mesh module

B.2 Solid Mechanics Module

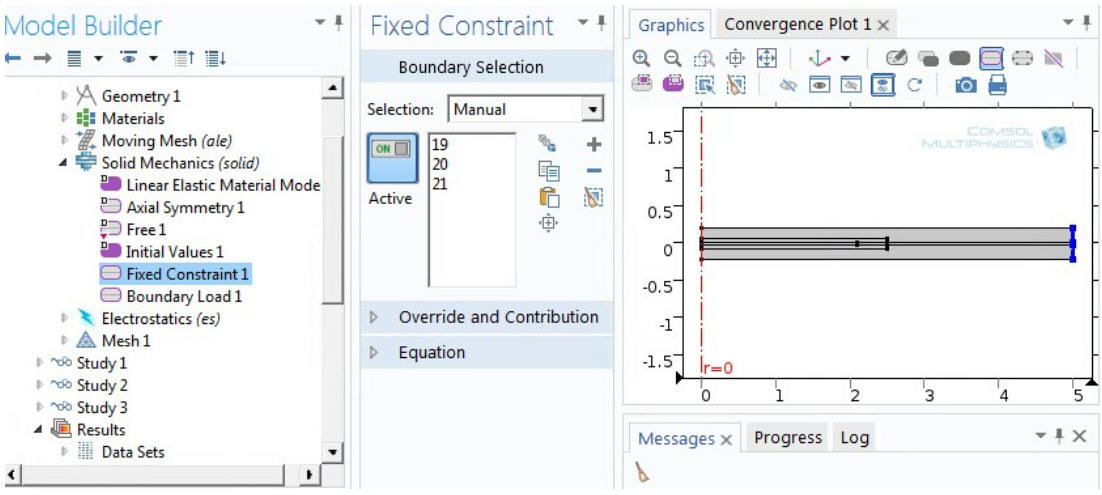

Figure B.3: Define fixed constraint boundary in solid mechanics module

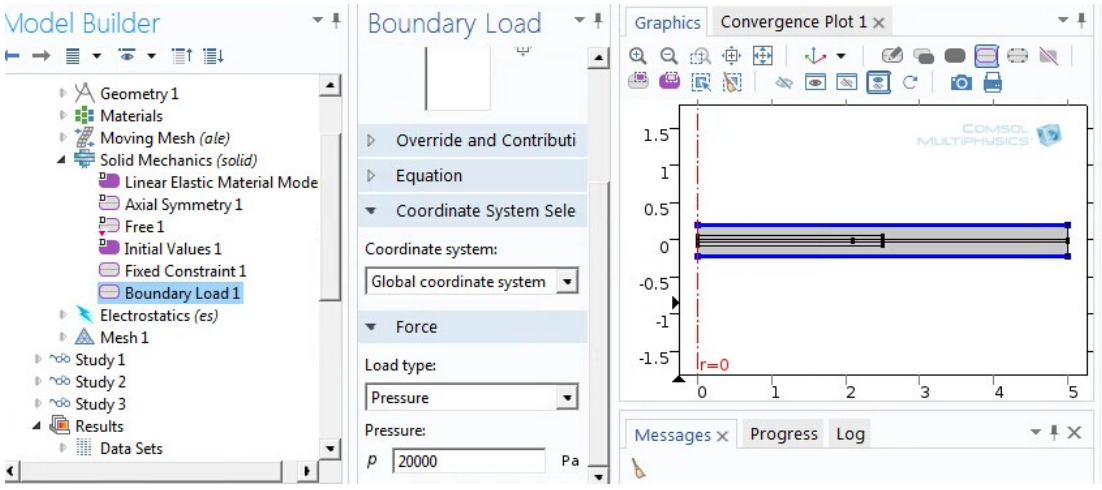

Figure B.4: Define bondary load (pressure) boundary in solid mechanics module

B.3 Electrostatics Module

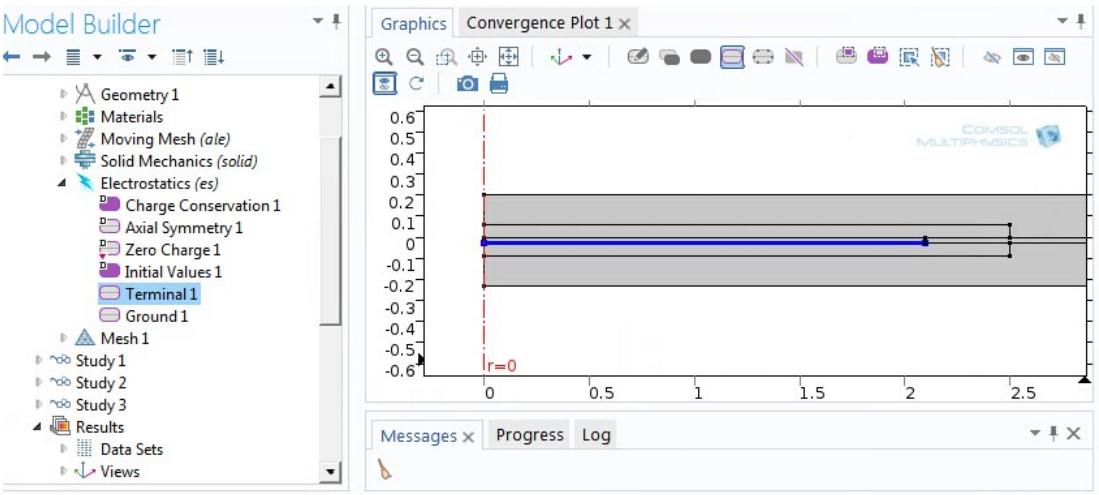

(a)

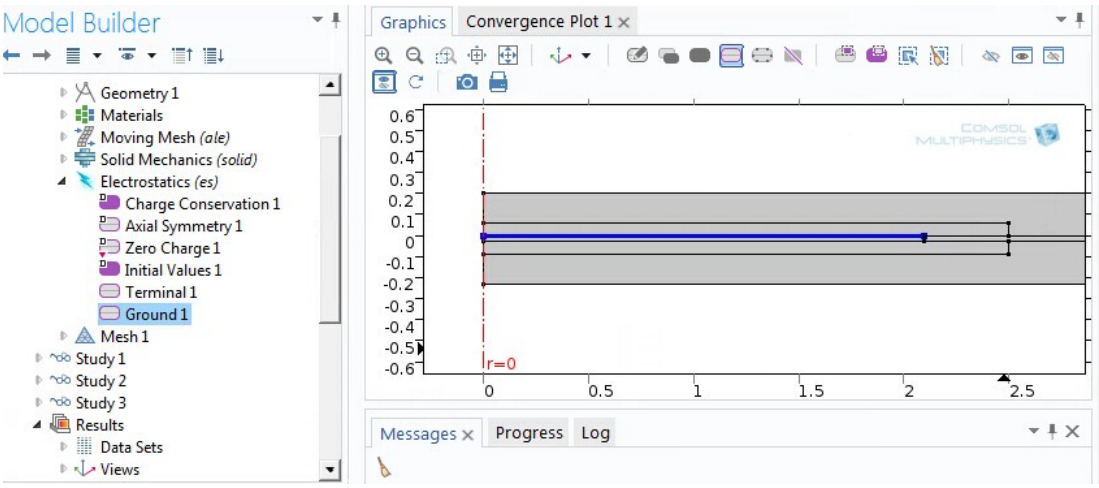

(b)

Figure B.5: Define the terminal and ground bondary in electrostatics module

B.4 Comsol Simulation Output

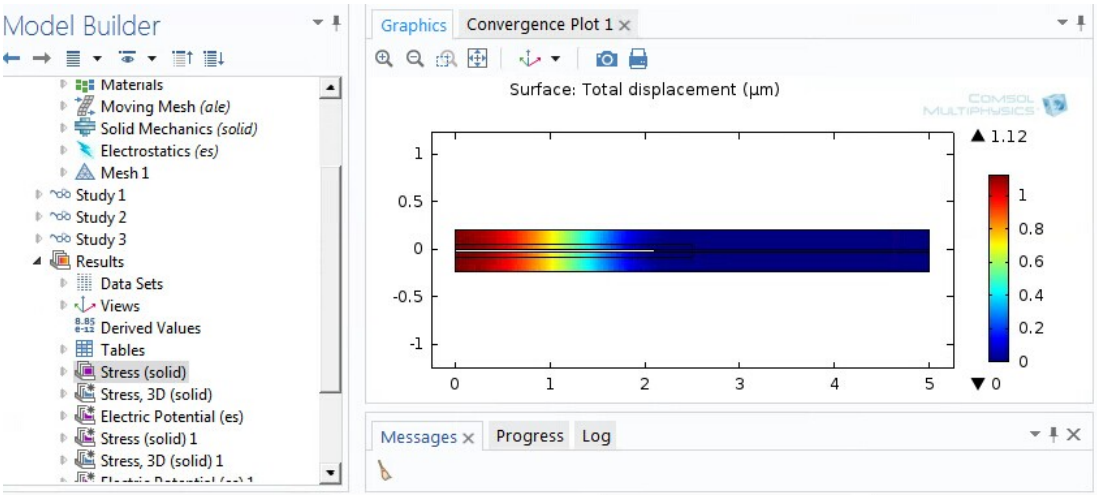

Figure B.6: Surface displacement output (P= 20kPa

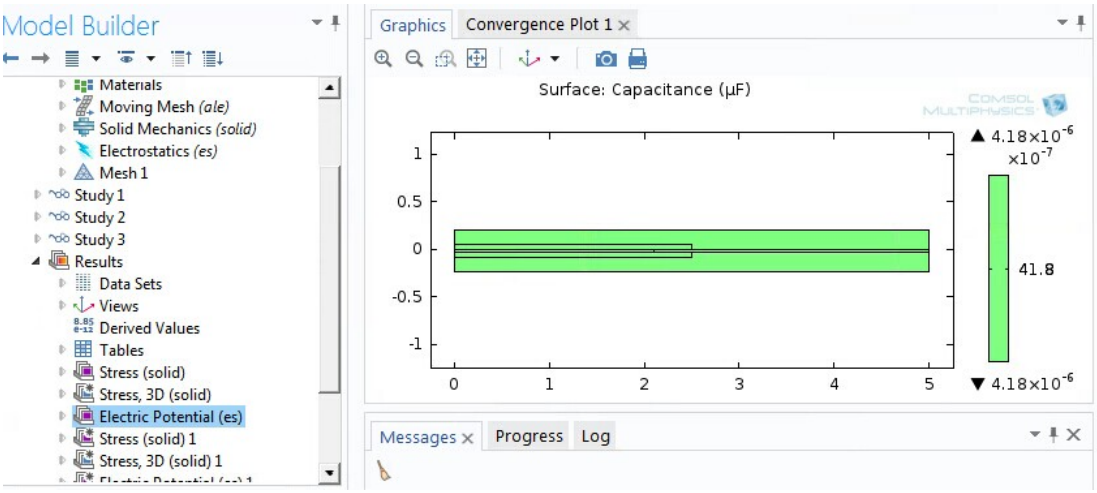

Figure B.7: Capacitance (center circular) output (P= 20kPa)

REFERENCES

[1] Agrawal, C., Haas, K., Leopold, D., and Clark, H., "Evaluation of poly (l-lactic acid) as a material for intravascular polymeric stents," *Biomaterials*, vol. 13, no. 3, pp. 176–182, 1992.

[2] Allen, M. G., "Micromachined endovascularly-implantable wireless aneurysm pressure sensors: from concept to clinic," in *Solid-State Sensors, Actuators and Microsystems, 2005. Digest of Technical Papers. TRANSDUCERS'05. The 13th International Conference on*, vol. 1, pp. 275–278, IEEE, 2005.

[3] Arshak, A., Arshak, K., Waldron, D., Morris, D., Korostynska, O., Jafer, E., and Lyons, G., "Review of the potential of a wireless mems and tft microsystems for the measurement of pressure in the gi tract," *Medical engineering & physics*, vol. 27, no. 5, pp. 347–356, 2005.

[4] Bashirullah, R., "Wireless implants," *Microwave Magazine, IEEE*, vol. 11, no. 7, pp. S14–S23, 2010.

[5] Benicewicz, B. C. and Hopper, P. K., "Polymers for absorbable surgical sutures. i," *Journal of bioactive and compatible polymers*, vol. 5, no. 4, pp. 453–472, 1990.

[6] Bergmann, C. and Stumpf, A., "Biomaterials," in *Dental Ceramics*, Topics in Mining, Metallurgy and Materials Engineering, pp. 9–13, Springer Berlin Heidelberg, 2013.

[7] Bergsma, J., Rozema, F., Bos, R., Boering, G., De Bruijn, W., and Pennings, A., " *In vivo* degradation and biocompatibility study of *in vitro* pre-degraded as-polymerized polylactide particles," *Biomaterials*, vol. 16, no. 4, pp. 267–274, 1995.

[8] Borden, M., Attawia, M., Khan, Y., and Laurencin, C. T., "Tissue engineered microsphere-based matrices for bone repair:: design and evaluation," *Biomaterials*, vol. 23, no. 2, pp. 551–559, 2002.

[9] Bos, R., Rozema, F. B., Boering, G., Nijenhius, A., Pennings, A., Verwey, A., Nieuwenhuis, P., and Jansen, H., "Degradation of and tissue reaction to biodegradable poly (l-lactide) for use as internal fixation of fractures: a study in rats," *Biomaterials*, vol. 12, no. 1, pp. 32–36, 1991.

[10] Boutry, C. M., Chandrahalim, H., Streit, P., Schinhammer, M., Hänzi, A. C., and Hierold, C., "Towards biodegradable wireless implants," *Philosophical Transactions of the Royal Society A: Mathematical, Physical and Engineering Sciences*, vol. 370, no. 1967, pp. 2418–2432, 2012.

[11] Boutry, C. M., Chandrahalim, H., Streit, P., Schinhammer, M., Hänzi, A. C., and Hierold, C., "Characterization of miniaturized rlc resonators made of biodegradable materials for wireless implant applications," *Sensors and Actuators A: Physical*, vol. 189, pp. 344–355, 2013.

[12] Boutry, C., Chandrahalim, H., and Hierold, C., "Characterization of rf resonators made of biodegradable materials for biosensing applications," *Procedia Engineering*, vol. 25, pp. 1529–1532, 2011.

[13] Bowen, P. K., Drelich, J., and Goldman, J., "Zinc exhibits ideal physiological corrosion behavior for bioabsorbable stents," *Advanced Materials*, vol. 25, no. 18, pp. 2577–2582, 2013.

[14] Brannon-Peppas, L., "Recent advances on the use of biodegradable microparticles and nanoparticles in controlled drug delivery," *International Journal of Pharmaceutics*, vol. 116, no. 1, pp. 1–9, 1995.

[15] Briscoe, B., Luckham, P., and Zhu, S., "The effects of hydrogen bonding upon the viscosity of aqueous poly (vinyl alcohol) solutions," *Polymer*, vol. 41, no. 10, pp. 3851–3860, 2000.

[16] Cai, W. and Liu, L., "Shape-memory effect of poly (glycerol–sebacate) elastomer," *Materials Letters*, vol. 62, no. 14, pp. 2171–2173, 2008.

[17] Chen, Q.-Z., Bismarck, A., Hansen, U., Junaid, S., Tran, M. Q., Harding, S. E., Ali, N. N., and Boccaccini, A. R., "Characterisation of a soft elastomer poly (glycerol sebacate) designed to match the mechanical properties of myocardial tissue," *Biomaterials*, vol. 29, no. 1, pp. 47–57, 2008.

[18] Chen, Q.-Z., Ishii, H., Thouas, G. A., Lyon, A. R., Wright, J. S., Blaker, J. J., Chrzanowski, W., Boccaccini, A. R., Ali, N. N., Knowles, J. C., and others, "An elastomeric patch derived from poly (glycerol sebacate) for delivery of embryonic stem cells to the heart," *Biomaterials*, vol. 31, no. 14, pp. 3885–3893, 2010.

[19] Chung, S., Lin, A., Chang, J., and Shih, H., "Exafs study of atmospheric corrosion products on zinc at the initial stage," *Corrosion science*, vol. 42, no. 9, pp. 1599–1610, 2000.

[20] Cole, I., Muster, T., Furman, S., Wright, N., and Bradbury, A., "Products formed during the interaction of seawater droplets with zinc surfaces: I. results from 1- and 2.5- day exposures," *Journal of The Electrochemical Society*, vol. 155, no. 5, pp. C244–C255, 2008.

[21] Cole, I., Muster, T., Lau, D., Wright, N., and Azmat, N. S., "Products formed during the interaction of seawater droplets with zinc surfaces ii. results from short exposures," *Journal of the Electrochemical Society*, vol. 157, no. 6, pp. C213–C222, 2010.

[22] Collins, C. C., "Miniature passive pressure transensor for implanting in the eye," *Biomedical Engineering, IEEE Transactions on*, no. 2, pp. 74–83, 1967.

[23] Cook, W., Cameron, J., Bell, J., and Huang, S., "Scanning electron microscopic visualization of biodegradation of polycaprolactones by fungi," *Journal of Polymer Science: Polymer Letters Edition*, vol. 19, no. 4, pp. 159–165, 1981.

[24] Daniels, A., Chang, M. K., Andriano, K. P., and Heller, J., "Mechanical properties of biodegradable polymers and composites proposed for internal fixation of bone," *Journal of Applied Biomaterials*, vol. 1, no. 1, pp. 57–78, 1990.

[25] Dario, P., Carrozza, M. C., Benvenuto, A., and Menciassi, A., "Micro-systems in biomedical applications," *Journal of Micromechanics and Microengineering*, vol. 10, no. 2, p. 235, 2000.

[26] Edlund, U. and Albertsson, A.-C., "Degradable polymer microspheres for controlled drug delivery," in *Degradable aliphatic polyesters*, pp. 67–112, Springer, 2002.

[27] Engelberg, I. and Kohn, J., "Physico-mechanical properties of degradable polymers used in medical applications: a comparative study," *Biomaterials*, vol. 12, no. 3, pp. 292–304, 1991.

[28] Erbel, R., Di Mario, C., Bartunek, J., Bonnier, J., de Bruyne, B., Eberli, F. R., Erne, P., Haude, M., Heublein, B., Horrigan, M., and others, "Temporary scaffolding of coronary arteries with bioabsorbable magnesium stents: a prospective, non-randomised multicentre trial," *The Lancet*, vol. 369, no. 9576, pp. 1869–1875, 2007.

[29] Evans, A. and Hutchinson, J., "The thermomechanical integrity of thin films and multilayers," *Acta Metallurgica et Materialia*, vol. 43, no. 7, pp. 2507–2530, 1995.

[30] Feng, J.-H. and Dogan, F., "Aqueous processing and mechanical properties of plzt green tapes," *Materials Science and Engineering: A*, vol. 283, no. 1, pp. 56–64, 2000.

[31] Finamore, B., Fedder, G., Khairi, A., Paramesh, J., Schultz, L., Burgess, J., Campbell, P., and Weiss, L., "Development of an implantable biodegradable electrical stimulator for bone repair," in *Biomedical Engineering Society Fall Meeting*, 2009.

[32] Finch, C. A. and others, *Polyvinyl alcohol: properties and applications*. Wiley London, 1973.

[33] Fonseca, M. A., "Polymer/ceramic wireless mems pressure sensors for harsh environments: high temperature and biomedical applications," *Ph.D. dissertation, Georgia Institute of Technology, Atlanta, GA, USA*, 2007.

[34] Fonseca, M. A., Allen, M. G., Kroh, J., and White, J., "Flexible wireless passive pressure sensors for biomedical applications," in *Tech. Dig. Solid-State Sensor, Actuator, and Microsystems Workshop (Hilton Head 2006)*, 2006.

[35] Fonseca, M. A., English, J. M., Von Arx, M., and Allen, M. G., "Wireless micromachined ceramic pressure sensor for high-temperature applications," *Microelectromechanical Systems, Journal of*, vol. 11, no. 4, pp. 337–343, 2002.

[36] Fosmire, G. J., "Zinc toxicity," *The American journal of clinical nutrition*, vol. 51, no. 2, pp. 225–227, 1990.

[37] Frankel, G. S., "Electrochemical techniques in corrosion: status, limitations, and needs," *Journal of ASTM International*, vol. 5, no. 2, pp. 1–27, 2008.

[38] Fraschini, C., Plesu, R., Sarasua, J.-R., and Prud'Homme, R. E., "Cracking in polylactide spherulites," *Journal of Polymer Science Part B: Polymer Physics*, vol. 43, no. 22, pp. 3308–3315, 2005.

[39] Frazza, E. and Schmitt, E., "A new absorbable suture," *Journal of biomedical materials research*, vol. 5, no. 2, pp. 43–58, 1971.

[40] Gilding, D. and Reed, A., "Biodegradable polymers for use in surgerypolyglycolic/poly (actic acid) homo-and copolymers: 1," *Polymer*, vol. 20, no. 12, pp. 1459–1464, 1979.

[41] Göpferich, A., "Mechanisms of polymer degradation and erosion," *Biomaterials*, vol. 17, no. 2, pp. 103–114, 1996.

[42] Göpferich, A., "Polymer bulk erosion," *Macromolecules*, vol. 30, no. 9, pp. 2598–2604, 1997.

[43] Göpferich, A. and Tessmar, J., "Polyanhydride degradation and erosion," *Advanced Drug Delivery Reviews*, vol. 54, no. 7, pp. 911–931, 2002.

[44] Graedel, T., "Gildes model studies of aqueous chemistry. i. formulation and potential applications of the multi-regime model," *Corrosion science*, vol. 38, no. 12, pp. 2153–2180, 1996.

[45] Grayson, A. R., Shawgo, R. S., Johnson, A. M., Flynn, N. T., Li, Y., Cima, M. J., and Langer, R., "A biomems review: Mems technology for physiologically integrated devices," *Proceedings of the IEEE*, vol. 92, no. 1, pp. 6–21, 2004.

[46] Grijpma, D. W. and Pennings, A. J., "(co) polymers of l-lactide, 1. synthesis, thermal properties and hydrolytic degradation," *Macromolecular Chemistry and Physics*, vol. 195, no. 5, pp. 1633–1647, 1994.

[47] Grimes, C. A., Kouzoudis, D., Ong, K. G., and Crump, R., "Thin-film magnetoelastic microsensors for remote query biomedical monitoring," *Biomedical Microdevices*, vol. 2, no. 1, pp. 51–60, 1999.

[48] Gunatillake, P., Mayadunne, R., and Adhikari, R., "Recent developments in biodegradable synthetic polymers," *Biotechnology annual review*, vol. 12, pp. 301–347, 2006.

[49] Hack, H. P., *Corrosion tests and standards: application and interpretation*, vol. 20. ASTM international, 2005.

[50] Hambidge, K. M. and Krebs, N. F., "Zinc deficiency: a special challenge," *The Journal of nutrition*, vol. 137, no. 4, pp. 1101–1105, 2007.

[51] Hench, L. L., "Biomaterials: a forecast for the future," *Biomaterials*, vol. 19, no. 16, pp. 1419–1423, 1998.

[52] Hennig, B., Toborek, M., McClain, C. J., and Diana, J. N., "Nutritional implications in vascular endothelial cell metabolism.," *Journal of the American College of Nutrition*, vol. 15, no. 4, pp. 345–358, 1996.

[53] Hermawan, H., *Biodegradable Metals*. Springer, 2012.

[54] Hermawan, H., Dubé, D., and Mantovani, D., "Development of degradable fe-35mn alloy for biomedical application," *Advanced Materials Research*, vol. 15, pp. 107–112, 2007.

[55] Herrault, F., Yorish, S., Crittenden, T. M., Ji, C.-H., and Allen, M. G., "Parylene-insulated ultradense microfabricated coils," *Microelectromechanical Systems, Journal of*, vol. 19, no. 6, pp. 1277–1283, 2010.

[56] Hihara, L. H. and Latanision, R., "Galvanic corrosion of aluminum-matrix composites," *Corrosion*, vol. 48, no. 7, pp. 546–552, 1992.

[57] Holland, S. J., Tighe, B. J., and Gould, P. L., "Polymers for biodegradable medical devices. 1. the potential of polyesters as controlled macromolecular release systems," *Journal of Controlled Release*, vol. 4, no. 3, pp. 155–180, 1986.

[58] Horan, R. L., Antle, K., Collette, A. L., Wang, Y., Huang, J., Moreau, J. E., Volloch, V., Kaplan, D. L., and Altman, G. H., "In vitro degradation of silk fibroin," *Biomaterials*, vol. 26, no. 17, pp. 3385–3393, 2005.

[59] Hsueh, C., Luttrell, C., and Becher, P., "Modelling of bonded multilayered disks subjected to biaxial flexure tests," *International journal of solids and structures*, vol. 43, no. 20, pp. 6014–6025, 2006.

[60] Hwang, S.-W., Tao, H., Kim, D.-H., Cheng, H., Song, J.-K., Rill, E., Brenckle, M. A., Panilaitis, B., Won, S. M., Kim, Y.-S., and others, "A physically transient form of silicon electronics," *Science*, vol. 337, no. 6102, pp. 1640–1644, 2012.

[61] Ikada, Y. and Tsuji, H., "Biodegradable polyesters for medical and ecological applications," *Macromolecular rapid communications*, vol. 21, no. 3, pp. 117–132, 2000.

[62] Jaafar, I. H., Ammar, M. M., Jedlicka, S. S., Pearson, R. A., and Coulter, J. P., "Spectroscopic evaluation, thermal, and thermomechanical characterization of poly (glycerol-sebacate) with variations in curing temperatures and durations," *Journal of materials science*, vol. 45, no. 9, pp. 2525–2529, 2010.

[63] Jones, D. A., "Polarization studies of brass-steel galvanic couples," *Corrosion*, vol. 40, no. 4, pp. 181–185, 1984.

[64] Jow, U.-M. and Ghovanloo, M., "Modeling and optimization of printed spiral coils in air, saline, and muscle tissue environments," *Biomedical Circuits and Systems, IEEE Transactions on*, vol. 3, no. 5, pp. 339–347, 2009.

[65] Kawamoto, T. and Sugahara, T., "Examination of properties of bioabsorbable osteosynthetic material using finite element method," *Journal of Hard Tissue Biology*, vol. 14, no. 2, pp. 65–66, 2005.

[66] Kelly, R. G., Scully, J. R., Shoesmith, D., and Buchheit, R. G., *Electrochemical techniques in corrosion science and engineering*. CRC Press, 2002.

[67] Kemppainen, J. M. and Hollister, S. J., "Tailoring the mechanical properties of 3d-designed poly (glycerol sebacate) scaffolds for cartilage applications," *Journal of Biomedical Materials Research Part A*, vol. 94, no. 1, pp. 9–18, 2010.

[68] Klocke, B., Diener, T., Fringes, M., and Harder, C., "Degradable metal stent having agent-containing coating," Jan. 7 2014. US Patent 8,623,073.

[69] Knani, D., Gutman, A. L., and Kohn, D. H., "Enzymatic polyesterification in organic media. enzyme-catalyzed synthesis of linear polyesters. i. condensation polymerization of linear hydroxyesters. ii. ring-opening polymerization of -caprolactone," *Journal of Polymer Science Part A: Polymer Chemistry*, vol. 31, no. 5, pp. 1221–1232, 1993.

[70] Kricheldorf, H. R., Kreiser-Saunders, I., Jürgens, C., and Wolter, D., "Polylactides-synthesis, characterization and medical application," *Macromolecular Symposia*, vol. 103, no. 1, pp. 85–102, 1996.

[71] Kumar, N., Langer, R. S., and Domb, A. J., "Polyanhydrides: an overview," *Advanced drug delivery reviews*, vol. 54, no. 7, pp. 889–910, 2002.

[72] Labrecque, L., Kumar, R., Dave, V., Gross, R., and McCarthy, S., "Citrate esters as plasticizers for poly (lactic acid)," *Journal of Applied Polymer Science*, vol. 66, no. 8, pp. 1507–1513, 1997.

[73] Lalot, T. and Marechal, E., "Enzyme-catalyzed polyester synthesis," *International Journal of Polymeric Materials*, vol. 50, no. 3-4, pp. 267–286, 2001.

[74] Laurencin, C., Gerhart, T., Witschger, P., Satcher, R., Domb, A., Rosenberg, A., Hanff, P., Edsberg, L., Hayes, W., and Langer, R., "Bioerodible polyanhydrides for antibiotic drug delivery: in vivo osteomyelitis treatment in a rat model system," *Journal of orthopaedic research*, vol. 11, no. 2, pp. 256–262, 1993.

[75] Le Duigou, A., Davies, P., and Baley, C., "Interfacial bonding of flax fibre/poly (l-lactide) bio-composites," *Composites Science and technology*, vol. 70, no. 2, pp. 231–239, 2010.

[76] Ledbetter, H., "Elastic properties of zinc: A compilation and a review," *Journal of Physical and Chemical Reference Data*, vol. 6, no. 4, pp. 1181–1203, 1977.

[77] Ledet, E. H., DLima, D., Westerhoff, P., Szivek, J. A., Wachs, R. A., and Bergmann, G., "Implantable sensor technology: from research to clinical practice," *Journal of the American Academy of Orthopaedic Surgeons*, vol. 20, no. 6, pp. 383–392, 2012.

[78] Lenz, R. W., "Biodegradable polymers," in *Biopolymers I*, pp. 1–40, Springer, 1993.

[79] Leong, K., Brott, B., and Langer, R., "Bioerodible polyanhydrides as drug-carrier matrices. i: Characterization, degradation, and release characteristics," *Journal of biomedical materials research*, vol. 19, no. 8, pp. 941–955, 1985.

[80] Leong, K., Kost, J., Mathiowitz, E., and Langer, R., "Polyanhydrides for controlled release of bioactive agents," *Biomaterials*, vol. 7, no. 5, pp. 364–371, 1986.

[81] Li, M. C., Jiang, L. L., Zhang, W. Q., Qian, Y. H., Luo, S. Z., and Shen, J. N., "Electrochemical corrosion behavior of nanocrystalline zinc coatings in 3.5% nacl solutions," *Journal of Solid State Electrochemistry*, vol. 11, no. 9, pp. 1319–1325, 2007.

[82] Li, S. and Vert, M., "Biodegradation of aliphatic polyesters," in *Degradable polymers: principle and applications*, pp. 71–131, Springer, 2002.

[83] Ligier, V., Wery, M., Hihn, J.-Y., Faucheu, J., and Tachez, M., "Formation of the main atmospheric zinc end products: $Nazn_4cl\ (oh)_6so_4{\cdot}6h_2o$,

zn_4so_4 $(oh)_6{\cdot}nh_2o$ and zn_4cl_2 $(oh)_4so_4{\cdot}5h_2o$ in $[cl^-][so_4^{2-}][hco_3^-][h_2o_2]$ electrolytes," *Corrosion science*, vol. 41, no. 6, pp. 1139–1164, 1999.

[84] Liu, B. and Zheng, Y., "Effects of alloying elements (mn, co, al, w, sn, b, c and s) on biodegradability and in vitro biocompatibility of pure iron," *Acta biomaterialia*, vol. 7, no. 3, pp. 1407–1420, 2011.

[85] Liu, H., "Biodegradable metals and responsive biosensors for musculoskeletal applications," in *Nanotechnology Enabled In situ Sensors for Monitoring Health*, pp. 115–137, Springer, 2011.

[86] Löfgren, A., Albertsson, A.-C., Dubois, P., and Jérôme, R., "Recent advances in ring-opening polymerization of lactones and related compounds," *Journal of Macromolecular Science, Part C: Polymer Reviews*, vol. 35, no. 3, pp. 379–418, 1995.

[87] Lu, H. H., Cooper Jr, J. A., Manuel, S., Freeman, J. W., Attawia, M. A., Ko, F. K., and Laurencin, C. T., "Anterior cruciate ligament regeneration using braided biodegradable scaffolds: in vitro optimization studies," *Biomaterials*, vol. 26, no. 23, pp. 4805–4816, 2005.

[88] Lu, Y. and Chen, S., "Micro and nano-fabrication of biodegradable polymers for drug delivery," *Advanced drug delivery reviews*, vol. 56, no. 11, pp. 1621–1633, 2004.

[89] Luo, M., Martinez, A., Song, C., Herrault, F., and Allen, M., "A microfabricated wireless rf pressure sensor made completely of biodegradable materials," *Microelectromechanical Systems, Journal of*, vol. 23, pp. 4–13, Feb 2014.

[90] Mani, G., Feldman, M. D., Patel, D., and Agrawal, C., "Coronary stents: a materials perspective," *Biomaterials*, vol. 28, no. 9, pp. 1689–1710, 2007.

[91] Mansfeld, F., "Area relationships in galvanic corrosion," *Corrosion*, vol. 27, no. 10, pp. 436–442, 1971.

[92] Marten, F. L., "Vinyl alcohol polymers," *Kirk-Othmer Encyclopedia of Chemical Technology*, 2002.

[93] Maurus, P. B. and Kaeding, C. C., "Bioabsorbable implant material review," *Operative Techniques in Sports Medicine*, vol. 12, no. 3, pp. 158–160, 2004.

[94] McNichols, R. J. and Cote, G. L., "Optical glucose sensing in biological fluids: an overview," *Journal of Biomedical Optics*, vol. 5, no. 1, pp. 5–16, 2000.

[95] Middleton, J. C. and Tipton, A. J., "Synthetic biodegradable polymers as orthopedic devices," *Biomaterials*, vol. 21, no. 23, pp. 2335–2346, 2000.

[96] Miller, R. A., Brady, J. M., and Cutright, D. E., "Degradation rates of oral resorbable implants (polylactates and polyglycolates): rate modification with changes in pla/pga copolymer ratios," *Journal of biomedical materials research*, vol. 11, no. 5, pp. 711–719, 1977.

[97] Mohan, S. S., del Mar Hershenson, M., Boyd, S. P., and Lee, T. H., "Simple accurate expressions for planar spiral inductances," *Solid-State Circuits, IEEE Journal of*, vol. 34, no. 10, pp. 1419–1424, 1999.

[98] Moravej, M., Purnama, A., Fiset, M., Couet, J., and Mantovani, D., "Electroformed pure iron as a new biomaterial for degradable stents: *In vitro* degradation and preliminary cell viability studies," *Acta biomaterialia*, vol. 6, no. 5, pp. 1843–1851, 2010.

[99] Moravej, M. and Mantovani, D., "Biodegradable metals for cardiovascular stent application: interests and new opportunities," *International journal of molecular sciences*, vol. 12, no. 7, pp. 4250–4270, 2011.

[100] Mueller, P. P., Arnold, S., Badar, M., Bormann, D., Bach, F.-W., Drynda, A., Meyer-Lindenberg, A., Hauser, H., and Peuster, M., "Histological and molecular evaluation of iron as degradable medical implant material in a murine animal model," *Journal of Biomedical Materials Research Part A*, vol. 100, no. 11, pp. 2881–2889, 2012.

[101] Muster, T. H. and Cole, I. S., "The protective nature of passivation films on zinc: surface charge," *Corrosion science*, vol. 46, no. 9, pp. 2319–2335, 2004.

[102] Nair, L. S. and Laurencin, C. T., "Polymers as biomaterials for tissue engineering and controlled drug delivery," in *Tissue engineering I*, pp. 47–90, Springer, 2006.

[103] Nair, L. S. and Laurencin, C. T., "Biodegradable polymers as biomaterials," *Progress in polymer science*, vol. 32, no. 8, pp. 762–798, 2007.

[104] Nakagawa, T., Nakiri, T., Hosoya, R., and Tajitsu, Y., "Electrical properties of biodegradable polylactic acid film," *Industry Applications, IEEE Transactions on*, vol. 40, no. 4, pp. 1020–1024, 2004.

[105] Neagu, C., Jansen, H., Smith, A., Gardeniers, J., and Elwenspoek, M., "Characterization of a planar microcoil for implantable microsystems," *Sensors and Actuators A: Physical*, vol. 62, no. 1, pp. 599–611, 1997.

[106] Nie, F., Zheng, Y., Wei, S., Hu, C., and Yang, G., "In vitro corrosion, cytotoxicity and hemocompatibility of bulk nanocrystalline pure iron," *Biomedical Materials*, vol. 5, no. 6, p. 065015, 2010.

[107] Nijst, C. L., Bruggeman, J. P., Karp, J. M., Ferreira, L., Zumbuehl, A., Bettinger, C. J., and Langer, R., "Synthesis and characterization of

photocurable elastomers from poly (glycerol-co-sebacate)," *Biomacromolecules*, vol. 8, no. 10, pp. 3067–3073, 2007.

[108] Nix, F. C. and MacNair, D., "The thermal expansion of pure metals: Copper, gold, aluminum, nickel, and iron," *Phys. Rev.*, vol. 60, pp. 597–605, Oct 1941.

[109] Oldfield, J. W., "Electrochemical theory of galvanic corrosion," *Galvanic Corrosion*, pp. 5–22, 1988.

[110] Papavinasam, S., *Electrochemical Polarization Techniques for Corrosion Monitoring*. Elsevier, 2008.

[111] Paradossi, G., Cavalieri, F., Chiessi, E., Spagnoli, C., and Cowman, M. K., "Poly (vinyl alcohol) as versatile biomaterial for potential biomedical applications," *Journal of Materials Science: Materials in Medicine*, vol. 14, no. 8, pp. 687–691, 2003.

[112] Pawlikowski, G. T., "Effects of polymer material variations on high frequency dielectric properties," in *The MRS Spring Meeting*, Cambridge Univ Press, 2009.

[113] Peuster, M., Wohlsein, P., Brügmann, M., Ehlerding, M., Seidler, K., Fink, C., Brauer, H., Fischer, A., and Hausdorf, G., "A novel approach to temporary stenting: degradable cardiovascular stents produced from corrodible metalresults 6–18 months after implantation into new zealand white rabbits," *Heart*, vol. 86, no. 5, pp. 563–569, 2001.

[114] Peuster, M., Hesse, C., Schloo, T., Fink, C., Beerbaum, P., and von Schnakenburg, C., "Long-term biocompatibility of a corrodible peripheral iron stent in the porcine descending aorta," *Biomaterials*, vol. 27, no. 28, pp. 4955–4962, 2006.

[115] Pillai, O. and Panchagnula, R., "Polymers in drug delivery," *Current opinion in chemical biology*, vol. 5, no. 4, pp. 447–451, 2001.

[116] Pitt, C. G. and Zhong-wei, G., "Modification of the rates of chain cleavage of poly (ϵ-caprolactone) and related polyesters in the solid state," *Journal of controlled release*, vol. 4, no. 4, pp. 283–292, 1987.

[117] Puers, R., "Linking sensors with telemetry: impact on the system design," *Sensors and Actuators A: Physical*, vol. 52, no. 1, pp. 169–174, 1996.

[118] Rai, R., Tallawi, M., Grigore, A., and Boccaccini, A. R., "Synthesis, properties and biomedical applications of poly (glycerol sebacate)(pgs): a review," *Progress in Polymer Science*, vol. 37, no. 8, pp. 1051–1078, 2012.

[119] Receveur, R. A., Lindemans, F. W., and de Rooij, N. F., "Microsystem technologies for implantable applications," *Journal of Micromechanics and Microengineering*, vol. 17, no. 5, p. R50, 2007.

[120] Reed, A. and Gilding, D., "Biodegradable polymers for use in surgerypoly (glycolic)/poly (lactic acid) homo and copolymers: 2. *In vitro* degradation," *Polymer*, vol. 22, no. 4, pp. 494–498, 1981.

[121] Reilly, P. and Bullock, R., "Head injury: Pathophysiology and management of severe closed injury," *European Journal of Emergency Medicine*, vol. 5, no. 3, pp. 367–368, 1998.

[122] Revie, R. W., *Corrosion and corrosion control*. John Wiley & Sons, 2008.

[123] Ribas, R. P., Lescot, J., Leclercq, J.-L., Karam, J. M., and Ndagijimana, F., "Micromachined microwave planar spiral inductors and transformers," *Microwave Theory and Techniques, IEEE Transactions on*, vol. 48, no. 8, pp. 1326–1335, 2000.

[124] Romig Jr, A., Dugger, M. T., and McWhorter, P. J., "Materials issues in microelectromechanical devices: science, engineering, manufacturability and reliability," *Acta Materialia*, vol. 51, no. 19, pp. 5837–5866, 2003.

[125] Rosen, H. B., Chang, J., Wnek, G., Linhardt, R., and Langer, R., "Bioerodible polyanhydrides for controlled drug delivery," *Biomaterials*, vol. 4, no. 2, pp. 131–133, 1983.

[126] Rosengren, L., Backlund, Y., Sjostrom, T., Hok, B., and Svedbergh, B., "A system for wireless intra-ocular pressure measurements using a silicon micromachined sensor," *Journal of Micromechanics and Microengineering*, vol. 2, no. 3, p. 202, 1992.

[127] Schäfer, W., Abrams, P., Liao, L., Mattiasson, A., Pesce, F., Spangberg, A., Sterling, A. M., Zinner, N. R., and Kerrebroeck, P. v., "Good urodynamic practices: Uroflowmetry, filling cystometry, and pressure-flow studies**," *Neurourology and urodynamics*, vol. 21, no. 3, pp. 261–274, 2002.

[128] Schinhammer, M., Hänzi, A. C., Löffler, J. F., and Uggowitzer, P. J., "Design strategy for biodegradable fe-based alloys for medical applications," *Acta Biomaterialia*, vol. 6, no. 5, pp. 1705–1713, 2010.

[129] Sedra, A. S. and Smith, K. C., *Microelectronic Circuits Revised Edition*. Oxford University Press, Inc., 2007.

[130] Sieiro, J., López-Villegas, J. M., Cabanillas, J., Osorio, J. A., and Samitier, J., "A physical frequency-dependent compact model for rf integrated inductors," *Microwave Theory and Techniques, IEEE Transactions on*, vol. 50, no. 1, pp. 384–392, 2002.

[131] Sinha, V., Bansal, K., Kaushik, R., Kumria, R., and Trehan, A., "Poly-ϵ-caprolactone microspheres and nanospheres: an overview," *International Journal of Pharmaceutics*, vol. 278, no. 1, pp. 1–23, 2004.

[132] Staiger, M. P., Pietak, A. M., Huadmai, J., and Dias, G., "Magnesium and its alloys as orthopedic biomaterials: a review," *Biomaterials*, vol. 27, no. 9, pp. 1728–1734, 2006.

[133] Su, K. L.-c., *Fundamentals of circuits, electronics, and signal analysis*. Houghton Mifflin, 1978.

[134] Sundback, C. A., Shyu, J. Y., Wang, Y., Faquin, W. C., Langer, R. S., Vacanti, J. P., and Hadlock, T. A., "Biocompatibility analysis of poly (glycerol sebacate) as a nerve guide material," *Biomaterials*, vol. 26, no. 27, pp. 5454–5464, 2005.

[135] Suzuki, I., "The behavior of corrosion products on zinc in sodium chloride solution," *Corrosion science*, vol. 25, no. 11, pp. 1029–1034, 1985.

[136] Tamada, J. and Langer, R., "Erosion kinetics of hydrolytically degradable polymers.," *Proceedings of the National Academy of Sciences*, vol. 90, no. 2, pp. 552–556, 1993.

[137] Thomas, S., Birbilis, N., Venkatraman, M., and Cole, I., "Corrosion of zinc as a function of ph," *Corrosion, The Journal of Science and Engineering*, vol. 68, no. 1, pp. 015009–1, 2012.

[138] Timoshenko, S., Woinowsky-Krieger, S., and Woinowsky-Krieger, S., *Theory of plates and shells*, vol. 2. McGraw-hill New York, 1959.

[139] Trollsås, M., Lee, V. Y., Mecerreyes, D., Löwenhielm, P., Möller, M., Miller, R. D., and Hedrick, J. L., "Hydrophilic aliphatic polyesters: design, synthesis, and ring-opening polymerization of functional cyclic esters," *Macromolecules*, vol. 33, no. 13, pp. 4619–4627, 2000.

[140] Tsai, M.-H. and Whang, W.-T., "Low dielectric polyimide/poly (silsesquioxane)-like nanocomposite material," *Polymer*, vol. 42, no. 9, pp. 4197–4207, 2001.

[141] Tsuji, H. and Ikada, Y., "Properties and morphology of poly (l-lactide) 4. effects of structural parameters on long-term hydrolysis of poly (l-lactide) in phosphate-buffered solution," *Polymer Degradation and Stability*, vol. 67, no. 1, pp. 179–189, 2000.

[142] Tsuji, H., Mizuno, A., and Ikada, Y., "Properties and morphology of poly (l-lactide). iii. effects of initial crystallinity on long-term in vitro hydrolysis of high molecular weight poly (l-lactide) film in phosphate-buffered solution," *Journal of Applied Polymer Science*, vol. 77, no. 7, pp. 1452–1464, 2000.

[143] Tsuji, H. and Muramatsu, H., "Blends of aliphatic polyesters. iv. morphology, swelling behavior, and surface and bulk properties of blends from hydrophobic poly (l-lactide) and hydrophilic poly (vinyl alcohol)," *Journal of applied polymer science*, vol. 81, no. 9, pp. 2151–2160, 2001.

[144] Uhrich, K. E., Cannizzaro, S. M., Langer, R. S., and Shakesheff, K. M., "Polymeric systems for controlled drug release," *Chemical reviews*, vol. 99, no. 11, pp. 3181–3198, 1999.

[145] Umbrecht, F., Wendlandt, M., Juncker, D., Hierold, C., and Neuenschwander, J., "A wireless implantable passive strain sensor system," in *Sensors, 2005 IEEE*, pp. 4–pp, IEEE, 2005.

[146] Vert, M., "Bioresorbable polymers for temporary therapeutic applications," *Die Angewandte Makromolekulare Chemie*, vol. 166, no. 1, pp. 155–168, 1989.

[147] Vojtěch, D., Kubásek, J., Šerák, J., and Novák, P., "Mechanical and corrosion properties of newly developed biodegradable zn-based alloys for bone fixation," *Acta biomaterialia*, vol. 7, no. 9, pp. 3515–3522, 2011.

[148] Waksman, R., "Biodegradable stents: they do their job and disappear.," *The Journal of invasive cardiology*, vol. 18, no. 2, pp. 70–74, 2006.

[149] Waksman, R., "Current state of the absorbable metallic (magnesium) stent.," *EuroIntervention: journal of EuroPCR in collaboration with the Working Group on Interventional Cardiology of the European Society of Cardiology*, vol. 5, pp. F94–7, 2009.

[150] Wang, Y., Ameer, G. A., Sheppard, B. J., and Langer, R., "A tough biodegradable elastomer," *Nature biotechnology*, vol. 20, no. 6, pp. 602–606, 2002.

[151] Ward, W. K., Jansen, L. B., Anderson, E., Reach, G., Klein, J.-C., and Wilson, G. S., "A new amperometric glucose microsensor: *in vitro* and short-term *in vivo* evaluation," *Biosensors and Bioelectronics*, vol. 17, no. 3, pp. 181–189, 2002.

[152] Watanabe, Y., Hamada, N., Morita, M., and Tsujisaka, Y., "Purification and properties of a polyvinyl alcohol-degrading enzyme produced by a strain of¡ i¿ pseudomonas¡/i¿," *Archives of biochemistry and biophysics*, vol. 174, no. 2, pp. 575–581, 1976.

[153] Weast, R. C., Astle, M. J., and Beyer, W. H., *CRC handbook of chemistry and physics*, vol. 69. CRC press Boca Raton, FL, 1988.

[154] Webster, T. J., *Nanotechnlogy Enabled In situ Sensors for Monitoring Health*. Springer, 2011.

[155] Wheeler, H. A., "Simple inductance formulas for radio coils," *Radio Engineers, Proceedings of the Institute of*, vol. 16, no. 10, pp. 1398–1400, 1928.

[156] Williams, D. F., *The Williams dictionary of biomaterials*. Liverpool University Press, 1999.

[157] Williams, D., "Enzymic hydrolysis of polylactic acid," *Engineering in Medicine*, vol. 10, no. 1, pp. 5–7, 1981.

[158] Wise, D. L., McCormick, G. J., Willet, G. P., and Anderson, L. C., "Sustained release of an antimalarial drug using a copolymer of glycolic/lactic acid," *Life Sciences*, vol. 19, no. 6, pp. 867–873, 1976.

[159] Witte, F., Fischer, J., Nellesen, J., Crostack, H.-A., Kaese, V., Pisch, A., Beckmann, F., and Windhagen, H., "*In vitro* and *in vivo* corrosion measurements of magnesium alloys," *Biomaterials*, vol. 27, no. 7, pp. 1013–1018, 2006.

[160] Wright-Charlesworth, D. D., Miller, D. M., Miskioglu, I., and King, J. A., "Nanoindentation of injection molded pla and self-reinforced composite pla after in vitro conditioning for three months," *Journal of Biomedical Materials Research Part A*, vol. 74, no. 3, pp. 388–396, 2005.

[161] Xu, L., Yu, G., Zhang, E., Pan, F., and Yang, K., "In vivo corrosion behavior of mg-mn-zn alloy for bone implant application," *Journal of Biomedical Materials Research Part A*, vol. 83, no. 3, pp. 703–711, 2007.

[162] Yu, C. P., Ryu, C., Lau, J., Lee, T. H., and Wong, S., "A physical model for planar spiral inductors on silicon," in *International electron devices meeting*, pp. 155–158, Citeseer, 1996.

[163] Yue, C. P. and Wong, S. S., "Physical modeling of spiral inductors on silicon," *Electron Devices, IEEE Transactions on*, vol. 47, no. 3, pp. 560–568, 2000.

[164] Zartner, P., Cesnjevar, R., Singer, H., and Weyand, M., "First successful implantation of a biodegradable metal stent into the left pulmonary artery of a preterm baby," *Catheterization and Cardiovascular Interventions*, vol. 66, no. 4, pp. 590–594, 2005.

[165] Zhang, X., "Galvanic corrosion," *Uhlig's Corrosion Handbook*, vol. 51, p. 123, 2011.

[166] Zhang, X. G., *Corrosion and electrochemistry of zinc*. Springer, 1996.

[167] Zhang, X., Wyss, U. P., Pichora, D., and Goosen, M. F., "An investigation of poly (lactic acid) degradation," *Journal of bioactive and compatible polymers*, vol. 9, no. 1, pp. 80–100, 1994.

VITA

Mengdi Luo was bron in Shiyan, Hubei province, China. She received B.S. and M.S. degrees in materials science and engineering from Tongji Univerisity, Shanghai, China, in June of 2005 and March of 2008, respectively. Mengdi's M.S. thesis advisor is Dr. Hongting Pu, and the thesis title is "solid anhydrous proton exchange membranes (PEMs) based on N-heterocyclic polymer/monomer for fuel cell and solid-state electrochromic device applications".

Mengdi came to Georgia Institute of Technology in fall 2008 pursuing her PhD degree in school of Polymer, Textile &Fiber Engineering (merged in to school of Materials Science and Engineering in July 2010). She worked in Dr. Vladimir Tsukruk's group on the project of "PECVD polymerized robust plasma polymerized organic-inorganic Janus microparticles" for one year, before she joined Dr. Mark G. Allen's group in October of 2009. Her research areas are design, microfabrication and characterization of completely biodegradable wireless sensors, MEMS-enabled biodegradable metals, and wireless corrosion sensors.